PREPARATION, CHARACTERIZATION, AND APPLICATIONS OF

POLYSACCHARIDE-STABILIZED METAL NANOPARTICLES

FOR REMEDIATION OF CHLORINATED SOLVENTS

IN SOILS AND GROUNDWATER

Except where reference is made to the work of others, the work described in this dissertation is my own or was done in the collaboration with my advisory committee. This dissertation does not include proprietary or classified information.

_____
Feng He

Certificate of approval:

_____
Thomas Albrecht-Schmitt
Professor
Chemistry and Biochemistry

_____
Dongye Zhao, Chair
Associate Professor
Civil Engineering

_____
Mark O. Barnett
Associate Professor
Civil Engineering

_____
T. Prabhakar Clement
Professor
Civil Engineering

_____
Christopher B. Roberts
Professor
Chemical Engineering

_____
George T. Flowers
Interim Dean
Graduate School

PREPARATION, CHARACTERIZATION, AND APPLICATIONS OF

POLYSACCHARIDE-STABILIZED METAL NANOPARTICLES

FOR REMEDIATION OF CHLORINATED SOLVENTS

IN SOILS AND GROUNDWATER

Feng He

A Dissertation

Submitted to

the Graduate Faculty of

Auburn University

in Partial Fulfillment of the

Requirements for the

Degree of

Doctor of Philosophy

Auburn, Alabama
December 17, 2007

PREPARATION, CHARACTERIZATION, AND APPLICATIONS OF

POLYSACCHARIDE-STABILIZED METAL NANOPARTICLES

FOR REMEDIATION OF CHLORINATED SOLVENTS

IN SOILS AND GROUNDWATER

Feng He

_____
Signature of Author

_____
Date of Graduation

VITA

Feng He was born in a small village in Shexian, Anhui Province, China, on October 22, 1978, the son of Guoqiang He and Yunlv Hong. After completing his studying at Shexian High School in Shexian, China, he entered Zhejiang University in Hangzhou, China, in 1995, where he received both his B.S. and M.S. degree in Environmental Engineering. From 2002 to 2003, he was a lecturer in Zhejaing Wanli University, Ningbo, China, where he met his beloved wife Na Zhou. They got married in 2004. In August, 2003, he flew across the Ocean to pursue his Ph.D. degree at Auburn University, Auburn, Alabama. During his study at Auburn, he coauthored two U.S. patents and published three peer-reviewed papers. Three more papers are under review and three more papers are in preparation. He also delivered fourteen presentations at various local/national/international conferences. He was a recipient of the 2006 ACS Graduate Student Award sponsored by American Chemical Society and a winner of Auburn-CH2M HILL Outstanding Ph.D. Student Fellowship Award (2005), Alabama Water Resources Conference Best Poster Award (2nd place, 2006), and American Water Works Association (AWWA) AL/MS Section Outstanding Graduate Student Scholarship Award (2007).

DISSERTATION ABSTRACT

PREPARATION, CHARACTERIZATION, AND APPLICATIONS OF

POLYSACCHARIDE-STABILIZED METAL NANOPARTICLES

FOR REMEDIATION OF CHLORINATED SOLVENTS

IN SOILS AND GROUNDWATER

Feng He

Doctor of Philosophy, December 17, 2007
(M. S. Zhejiang University, China, 2002)
(B. S. Zhejiang University, China, 1999)

277 Typed Pages

Directed by Dongye Zhao

Removal of chlorinated solvents in groundwater and soils represents one of the most challenging environmental issues. Highly reactive palladized iron (Fe-Pd) nanoparticles offer the potential to migrate in the soil and rapidly degrade the contaminants in source zones and became an attractive alternative for chlorinated solvent remediation. However, due to their high surface energy, Fe-Pd nanoparticles prepared using current methods tend to agglomerate immediately to form large agglomerates, rendering them undeliverable to the targeted area. This study reports that select food-grade starch and carboxymethyl cellulose (CMC) can be used as green stabilizers to produce highly dispersible Fe-Pd nanoparticles, which are reactive and mobile in soil and suitable for in situ injection.

Transmission electron microscopy (TEM) showed that the average particle sizes of both starch- and CMC- stabilized iron nanoparticles were less than 20 nm. Fourier transform infrared (FTIR) spectroscopy results suggested that stabilizer molecules were adsorbed to iron nanoparticles resulting in a steric layer, and thereby, preventing the nanoparticles from agglomeration. The stabilized iron nanoparticles were mobile in the porous media. For example, the CMC-stabilized iron nanoparticles had a low sticking efficiency of 0.0025 in the sand. Meanwhile, the stabilized nanoparticles displayed remarkably greater reactivity than non-stabilized particles. Batch tests demonstrated that the CMC-stabilized nanoparticles degraded trichloroethene (TCE) 17 times faster than non-stabilized counterparts. Further studies showed that CMC may inhibit TCE degradation at a stabilizer-to-Fe molar ratio greater than 0.0124. Within the same homologous series, CMC of greater molecular weight resulted in more reactive nanoparticles. Through selecting the type of stabilizers and synthesizing conditions, the size of the stabilized ZVI nanoparticles were also controlled.

Two field tests carried out in California and Alabama confirmed the unprecedented soil mobility and dechlorination reactivity of the CMC-stabilized Fe-Pd nanoparticles. Groundwater samples from the Alabama site also showed significant promotion of enhanced biodegradation of chlorinated solvent contaminants up to 4 months after injection.

The feasibility of using CMC for synthesis of highly reactive Pd nanoparticles was also investigated in this study. The resultant CMC-Pd nanoparticles exhibited rather high catalytic activity for hydrodechlorinatino of TCE ($k_{obs} > 828$ $L \cdot g_{Pd}^{-1} \min^{-1}$) and hold the promise for future applications in chlorinated solvent remediation.

ACKNOWLEDGEMENTS

My sincerest gratitude goes to my advisor, Dr. Dongye Zhao. I have been fortunate to have an advisor who gave me the freedom to explore on my own, and at the same time the guidance to recover when my steps faltered. He taught me not only to be an experimentalist but also an independent thinker. I thank everything he has done for me. I gratefully acknowledge all the members of my committee, Dr. Albrecht-Schmitt, Dr. Barnett, Dr. Clement, and Dr. Roberts, who have given their time to read this manuscript and who have also offered valuable advice and provided instrumentation helps during my graduate study at Auburn. Sincere appreciation is also extended to Dr. Gupta, who helped me with the DLS analyses and served in the committee as the outside reader.

Best regards to all members of Dr. Zhao's research group for their friendship and helps. I gratefully acknowledge Dr. Zhenli Fu, who inspired me with the idea of starched iron, Dr. Lange and Mr. Jinling Zhuang who helped me with instrumentation. In addition, I wish to thank Dr. Juncheng Liu for his help with experiments and nanoparticle characterization, the results of which are partially presented in Chapter 9.

I am especially indebted to my wife Na Zhou, who has continually offered her understanding, support, and care with her infinite love to accompany me through the study. I'll never thank her enough. Finally, I wish to thank my parents, Na's parents, and other family members for their support. It is their continuous encouragement that made this dissertation possible.

Style manual or journal used   Auburn University manuals and guides for the

preparation of theses and dissertations: Organizing the manuscript – publication format

Computer software used   Microsoft Word & Excel 2002; SigmaPlot 8.0; Mathtype 5.0

TABLE OF CONTENTS

LIST OF TABLES

LIST OF FIGURES

xxiii

CHAPTER 1. GENERAL INTRODUCTION

1.1 Groundwater and Soil Contamination by Chlorinated Solvents

Chlorinated solvents are among the most widely detected contaminants in soil and groundwater at thousands of priority sites. The United States Environmental Protection Agency (EPA) estimates that 8336 Department of Defense (DoD) sites requires cleanup, in which 5418 sites have been impacted by chlorinated solvents (U. S. EPA, 1997; NRC, 1994; Quinn et al., 2005). A number of these sites have chlorinated solvents present as free-phase, dense nonaqueous phase liquids (DNAPLs) that act as a long-term source of contamination to groundwater due to their limited aqueous solubility (on the order of hundreds to thousands of mg/L). Among the most commonly detected chlorinated organics in soil and groundwater are trichloroethene (TCE), and polychlorinated biphenyls (PCBs) (ATSDR, 2007).

TCE is an organic solvent widely used for dry cleaning and metal rinsing. For decades, large amounts of spent TCE were discharged into the environment. As a result, high concentrations of TCE have been widely detected in areas adjacent to dry cleaners, automobile manufacturers or shops, asphalt processing plants, and military bases. For example, TCE has been found in at least 852 of the 1,430 National Priorities List (NPL) sites (ATSDR, 2007).

PCBs are mixtures of various congeners with the general formula $C_{12}H_{10-x}Cl_x$ (NRC, 2001). PCBs were used in a variety of industrial applications (e.g., in electrical transformers, paints and plastics) (Alford-Stevens, 1986; Grittini et al., 1995). Over 1.5 billion pounds of PCBs were manufactured in the U.S. from its first use in 1927 to the cessation of production in 1977. The U.S. EPA estimates that about half of the total domestically consumed PCBs (625,000 tons) found their way into the environment before the enactment of the federal regulations in 1976 (U.S. EPA, 2000). As a result, PCBs have been found in at least 500 of the 1,598 the NPL sites (ATSDR, 2007).

Exposure to chlorinated hydrocarbons can seriously impair human health. It is evident that drinking or breathing tetrachloroethene (PCE) or TCE can cause malfunction of the nervous system, liver and lung damage, abnormal heartbeat, coma, and even death (ATSDR, 2007). PCBs have been associated with acne-like skin diseases in adults and neurobehavioral and immunological changes in children (ATSDR, 2007). PCBs are also known to cause cancer in animals (ATSDR, 2007). In addition, biogeochemical transformation of TCE and PCBs may lead to the production of highly toxic intermediate products such as vinyl chloride (VC) and dioxin, which are potent carcinogens.

The economic impact of chlorinated hydrocarbons in groundwater is substantial. The U.S. government estimated that it will cost $750 billion (or ~$8,000 per American family) over the next 30 years to clean up the nation's contaminated groundwater (Moran, 2004). In Montgomery, AL, a newly discovered PCE/TCE site known as "the capital city plume" site, which was proposed to the NPL in 2000 (U.S. EPA, 2000), demanded a $18.6 million clean-up action to restore the city's drinking water resources. One example of the legacy on PCBs contamination is the site at Anniston, AL, which was discovered

2

in 1993. In 1990 the Environmental Defense Fund Scorecard ranked Calhoun County, where Anniston is located, among the worst 20% of all counties in the US in terms of an average person's added cancer risk from hazardous wastes. The discovery of PCBs in Anniston triggered a costly and lengthy legal battle involving the local community, industry, state courts, state government, and U.S. EPA (Hogue, 2002). In 2003, the firms were ordered to pay a combined $600 million to settle claims of over 20,000 affected residents (Hogue, 2003).

1.2 Current Remediation Methods for Chlorinated Solvents Contaminated Groundwater and Soils

1.2.1 Pump and treat

Pump and treat method is the conventional and most widely used approach to remediate sites contaminated with chlorinated solvents present as DNAPL or dissolved in groundwater (Wong et al., 1997; Suthersan, 1997). Pump and treat systems operate by pumping contaminated groundwater to the surface, removing the contaminants, and then either recharging the treated water back into the ground or discharging it to a surface water body or municipal sewage plant. There are many treatment methods that can be used either to destroy the chlorinated solvents or to remove them for proper disposal, including air stripping, activated carbon treatment, biodegradation, and chemical reduction and oxidation and so on. However, pumping depresses the groundwater level, leaving chlorinated solvents residuals sorbed to organic matters in the soil. After the groundwater level returns to its normal level, the sorbed chlorinated solvents become dissolved again. Pump and treat systems often take a long operational time to meet

cleanup goals (at least 5-10 years, but usually last for decades). Therefore, the consequent

costs for operation and maintenance (O&M) over the life of remediation are usually high.

1.2.2 In situ thermal treatment

In situ thermal treatment includes technologies that employ heat in the source

zone to volatilize or mobilize DNAPL (Wong et al., 1997; Suthersan, 1997). Various

approaches have been used, including steam injection, electrical resistive heating, thermal

conductive heating, hot water injection, hot air injection, and radio frequency heating. In

some applications, high temperature conditions have been created that destroy DNAPLs

in place through pyrolysis. Compared to the pump and treat approach, thermal treatment

is a short or mid-term process, which indicates a lower cleanup costs (Wong et al., 1997).

However, the costs for using this process are still around $25 to $100 per cubic yard.

Thermal treatment is not efficient for the treatment of chlorinated solvents dissolved in

groundwater. Other disadvantages of this approach may include remobilization of

chlorinate solvents in the soil and the possible destruction of microbes in subsurface.

1.2.3 In situ chemical oxidation

This approach includes technologies that involve injecting chemical oxidants or

other amendments directly into the source zone to destroy DNAPL constituents in place

(Wong et al., 1997; Suthersan, 1997). Three of the most common chemical oxidants used

for DNAPL treatment are permanganate (either sodium or potassium permanganate),

hydrogen peroxide (when used with iron catalysts, this is generally referred to as

Fenton's chemistry or Fenton's reagent), and ozone. The injected oxidants react with the

contaminant, breaking chemical bonds and producing degradation products such as

carbon dioxide, water, and chloride. The greatest advantages of chemical oxidation approach are the rapid treatment time (in minutes) and the ability to treat contaminants present at high concentrations. However, oxidation is nonselective. As such, the oxidants will not only react with target chlorinated solvents but also with substance in the soil that can be readily oxidized, which can cause serious problems for destroying soil environment.

1.2.4 Surfactant/Co-solvent flushing

Surfactant/Co-solvent flushing includes technologies that enhance DNAPL removal through injection and subsequent extraction of chemicals to solubilize and/or mobilize DNAPL constituents (Wong et al., 1997; Suthersan, 1997). The chemicals typically used are aqueous surfactant solutions, co-solvents that lower the interfacial tension (including alcohols such as ethanol or isopropyl alcohol), or electrolytes that aid in contaminant solubilization. The chemicals are injected into a system of wells designed to "sweep" the DNAPL zone within the aquifer. The chemical "flood" and the solubilized or mobilized DNAPL are extracted from the subsurface and are separated and treated aboveground. Surfactant/Co-solvent flushing is a short or mid-term process which lasts from a few weeks to several months depending on the soil permeability. The disadvantages of this approach include that surfactant flow may mobilize contaminants deeper into the aquifer or off-site if inadequate hydraulic control is maintained and residual surfactants in the subsurface can have toxic effects. The costs using this process for DNAPL remediation are around \$200 to \$1400 per cubic yard (Wong et al., 1997; Suthersan, 1997).

1.2.5 In situ bioremediation

This includes technologies that use engineered conditions to enhance the biological activity of subsurface microbial populations (Wong et al., 1997; Suthersan, 1997). Typically, electron donor substrates such as lactate, molasses or oil (EOS$^{®}$) are introduced into the subsurface, stimulating native microbes to degrade contaminants through the process of reductive dechlorination. Non-indigenous microbes also have been introduced into the subsurface (referred to as bioaugmentation). Although more commonly applied to dissolved-phase plumes, *in situ* bioremediation has been used at sites with DNAPL sources. Bioremediation is still at an early stage of development. The key attraction of this technology is its potential for cost reduction in O&M. Bioremediation is a relatively long-term process with operation time at least several years. Chlorinated intermediates such as vinyl chloride (VC) are usually generated during the bioremediation process. VC is even more toxic (less biodegradable) than the parent chlorinated solvents such as TCE. Therefore, VC is usually accumulated during the bioremediation process unless further biodegradation can be achieved.

1.2.6 Zero valent iron (ZVI) permeable reactive barriers (PRBs)

In recent years, abiotic dechlorination using zero-valent iron (Fe^0) particles has enticed increasing interest (Reynolds et al., 1990; Matheson and Tratnyek, 1994; Gavaskar et al., 1998). Over the past decade, the ZVI technology has been applied at over 120 sites worldwide PRBs (ITRC, 2005). The PRB systems are simple and cost effective to implement at shallow depths and for relatively low concentrations of chlorinated hydrocarbons. However, challenges with implementation and cost increase in deeper

aquifers and at higher chlorinated hydrocarbon concentration (Gavaskar et al., 2005). Furthermore, due to limited reactivity, the dechlorination rate using these iron particles is often too slow and toxic intermediate by-products such as VC were often detected (Orth and Gillham, 1996; Arnold and Roberts, 2000). Because of the high persistency, PCBs can only be degraded under extreme conditions, e.g. at temperatures greater than 300 ^{o}C when using Fe^{0} as the reducing agent (Chuang et al., 1995). There is an urgent need for developing cost-effective, in-situ treatment technologies for destruction of PCBs in soils and water (Magar, 2003).

1.3 Nanoscale ZVI Particles for Chlorinated Solvents Cleanup

Nanoscale ZVI technology is an extension of the PRBs technology. In 1997, researchers in Lehigh University determined that nanoscale ZVI had ~ 35 times greater surface area than granular ZVI and may be 10 to 1,000 times more reactive than granular ZVI toward trichloroethene (TCE) (Wang and Zhang, 1997). Compared to conventional granular iron particles, ZVI nanoparticles offer the potential of being deliverable into contaminated soils, and thus, can be applied in situ. This advantage can potentially eliminate the need for excavation, and relieve remediation practices from the limitations of depth, site topography, and facility operations. Another potential advantage of ZVI nanoparticles is their high reactivity. The degradation rate of the target contaminants determines the site cleanup time and consequently the remediation cost. The high reactivity of ZVI nanoparticles could tremendously reduce the cleanup time of the target compounds and consequently the remediation cost.

7

However, due to their high surface energy, ZVI nanoparticles tend to agglomerate in water rapidly to form micron-scale or larger aggregates, which renders them undeliverable to the target area. This technology barrier has held back the field-scale application of nanoscale ZVI for over a decade.

1.4 Objectives of this Research

The overall objective of this research is to develop an on-site ZVI nanoparticle injection technology for in-situ destruction of chlorinated hydrocarbons. The **specific objectives** are to:

1) To develop a new class of iron-based nanoparticles that are physically more dispersible and chemically more reactive than current iron-based nanoparticles by use of select low-cost and 'green' polysaccharides (starch and cellulose) and their derivatives as a stabilizer;

2) Elucidate the underlying particle-stabilizing mechanisms through physical, optical and spectroscopic characterization of the stabilized nanoparticles under various conditions;

3) Test the effectiveness of using the stabilized nanoparticles for in-situ reductive destruction of chlorinated hydrocarbons (TCE and PCBs as model contaminants) in water, soils, and sediments;

4) Investigate the effect of parameters such as temperature, pH, ionic strength, stabilizer iron ratio, and stabilizer molecular weight on the size and reactivity of the stabilized nanoparticles;

5) Study the transport of the stabilized nanoparticles in the porous media and their application to in situ destruction of DNAPL; and

6) Pilot-test the technical feasibility of using the stabilized nanoparticles as a novel remediation technology.

CHAPTER 2. PREPARATION AND CHARACTERIZATION OF STARCH-STABILIZED BIMETALLIC NANOPARTICLES FOR DEGRADATION OF CHLORINATED SOLVENTS IN WATER

This chapter studied the feasibility of using starch as a novel and green stabilizer to synthesize highly dispersed Fe-Pd bimetallic nanoparticles. The resultant nanoparticles were characterized using UV-Vis spectroscopy and transmission electron microscopy (TEM). The reactivity of the nanoparticles was evaluated through the degradation of TCE and PCBs in water.

2.1 Introduction

Trichloroethene (TCE) is one of the most commonly detected chlorinated organic compounds in soil and groundwater. TCE has been widely detected in areas adjacent to dry cleaners, automobile manufacturers or shops, asphalt processing plants, and military bases. Polychlorinated biphenyls or PCBs are mixtures of various anthropogenic organic chemicals with the general formula $C_{12}H_{10-x}Cl_x$. For their excellent dielectric properties and their resistance to heat and chemical degradation, PCBs were widely employed in electrical transformers (Alford-Stevens, 1986; Grittini et al., 1995). Both TCE and PCBs are potent carcinogens and are persistent to natural degradation. Cleanup of soils and groundwater contaminated by chlorinated hydrocarbons such as TCE and PCBs has been a challenging task for decades.

Various technologies have been explored for dechlorination of TCE and PCBs, including bioremediation, thermal treatment, and permeable reactive barriers (Wong et al., 1997). Among many technologies tested so far, abiotic dechlorination using zero-valent iron, Fe^0, particles appears to be one of the most promising technologies (Matheson and Tratnyek, 1994; Wang and Zhang, 1997). For instance, commercial granular iron was used in ~70 permeable reactive barriers (PRB) by 2003 to degrade chlorinated hydrocarbons (Gillham, 2003). However, due to the limited reactivity, the TCE reduction rate of granular iron particles has been found very slow, with half lives in the order of days or longer (Johnson et al., 1996; Sayles et al., 1997). As a result, toxic intermediate by-products such as vinyl chloride (VC) are often detected (Arnold and Roberts, 2000; Orth and Gillham, 1996). Because of the high persistency, PCBs can only be degraded under extreme conditions, e.g. at temperatures greater than 300 ^{o}C when using Fe^0 as the reducing agent (Chuang et al., 1995). There is an urgent need for developing cost-effective, in-situ treatment technologies for destruction of PCBs in soils and water (Magar, 2003).

Various strategies have been explored to enhance the dechlorination rates using Fe^0-based particles (Zhang et al., 2002). Since dechlorination of chlorinated compounds by Fe^0-based particles is a surface-mediated process, increasing the surface area of iron will increase the dechlorination rate (Wang and Zhang, 1997). Therefore, reducing particle size can greatly enhance the degradation rate (Wang and Zhang, 1997). Coating iron particles with a second catalytic metal such as Pd, Pt, Ag or Ni can also accelerate the dechlorination process and thereby prevent formation of toxic byproducts (Wang and Zhang, 1997; Schrick et al., 2002; Xu and Zhang, 2000; Zhang et al., 1998). Wang and

11

Zhang (1997) reported that reducing Pd-coated iron particle size from millimeters to nanometers (10-100 nm) increased TCE degradation rate by 10-100 times and could enhance degradation of PCBs.

Typically, Fe^0-based nanoparticles were prepared by reducing Fe(II) or Fe(III) in aqueous solution using a strong reducing agent (e.g., sodium borohydride, $NaBH_4$). However, due to the extremely high reactivity, the initially formed nanoparticles tend to either react rapidly with surrounding media (e.g., dissolved oxygen (DO) or water) or agglomerate rapidly, resulting in formation of much larger (in the micron to millimeter scale) particles or flocs and rapid loss in reactivity.

To prepare physically more stable and chemically more reactive Fe^0-based nanoparticles, Mallouk and co-workers employed carbon nanoparticles and poly(acrylic acid) (PAA) as supports for iron and bimetallic nanoparticles (Ponder et al., 2000; Ponder et al., 2001; Schrick et al., 2002). These supports prevent iron particles from agglomeration and thereby prolong the reactivity of the particles. Significant enhancement of permeability was also observed when the supported particles were used in both sands and soils (Schrick et al., 2004). Using micro-emulsion method instead of conventional solution method, Li et al. synthesized smaller iron nanoparticles (< 10 nm) under the protection of a micro-emulsion mixture (Li et al., 2003). The initial TCE degradation rate coefficient for micro-emulsion product was found 2.6 times higher than that for conventional solution products.

Polyhydroxylated macromolecules, which contain size-confined, nanoscale pools of inter- and intramolecular origin, can be used for synthesis of various nanoscale particles (Lehman, 1998). In a recent study, Raveendran et al. (2003) showed that starch

can serve as a good template or dispersant for preparing nanoscale Ag particles in aqueous media. They observed that starched Ag nanoparticles can be well dispersed in water without agglomeration. Compared to other dispersants, starch is much cheaper and 'greener' for environmental applications.

The primary objective of this work was to prepare a new class of Fe^0-based nanoparticles for degradation of chlorinated hydrocarbons such as TCE and PCBs. Inspired by the work of Raveendran et al., a water-soluble starch was used as the dispersant in the preparation of the nanoparticles. The specific objectives were to: 1) prepare the nanoparticles in the presence of a water soluble starch and under inert conditions; and 2) characterize the resultant nanoparticles with respect to their physical stability and chemical reactivity for degradation of TCE and PCBs in water.

2.2 Experimental Section

2.2.1 Chemicals

The following chemicals were used as received: trichloroethylene (TCE) (>99%, spectrophotometric grade, Aldrich, Milwaukee, WI); 1,1-dichloroethylene (1,1-DCE) (99.9%, Acros Organics, Morris Plains, NJ); *cis*-dichloroethylene (*cis*-DCE) (97%, Acros Organics, Morris Plains, NJ); *trans*-dichloroethylene (*trans*-DCE) (100 mg L^{-1} in methanol, Ultra Scientific, N. Kingstown, RI); vinyl chloride (VC) (100 mg L^{-1} in methanol, Ultra Scientific, N. Kingstown, RI); hexane (pesticide grade, Fisher, Fair Lawn, NJ); PCBs mixture (Aroclor 1254) (100 mg L^{-1} in methanol, Ultra Scientific, N. Kingstown, RI); potassium hexachloropalladate (K_2PdCl_6, 99%, Acros Organics, Morris Plains, NJ); ferric chloride ($FeCl_3$, Fisher, Fair Lawn, NJ); sodium borohydride ($NaBH_4$,

13

ICN Biomedicals, Aurora, Ohio); sodium carbonate (Certified A.C.S anhydrous, Fisher, Fair Lawn, NJ); sodium bicarbonate (Certified A.C.S, Fisher, Fair Lawn, NJ); a water soluble starch (Alfa Aesar, Ward Hill, MA); and a nanoscale iron powder (100 nm, Argonide, Sanford, FL).

2.2.2 Preparation of nanoparticles

Unlike conventional methods, we applied a water soluble starch in the preparation. The starch serves as a stabilizer and dispersant that prevents the resultant nanoparticles from agglomeration, thereby prolonging their reactivity and maintaining the physical integrity. Preparation of mono- or bimetallic Fe^0 nanoparticles follows the schematic below:

Step 1. Prepare a starch-Fe solution containing 0.2 or 0.8% (w/w) starch and Fe^{3+} at a desired concentration (0.1 or 1.0 g L^{-1} as Fe)

← System under vacuum and non-magnetic shaking

Step 2. Reduce Fe^{3+} to Fe^0 using stoichiometric amounts of BH_4^-

← System under vacuum and non-magnetic

Step 3. Coat Fe^0 particles with a second metal (Pd) (for bimetallic particles only)
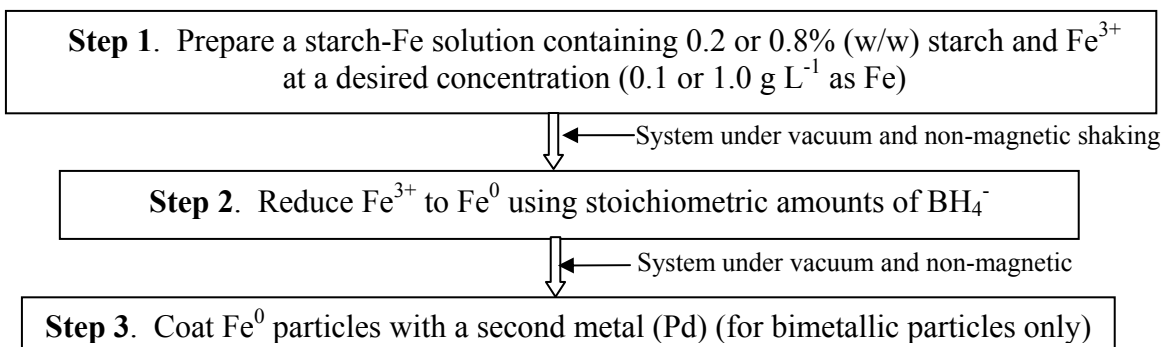
The preparation was carried out in a 250 mL flask attached to a vacuum line. Before use, deionized (DI) water and starch solution were purged with purified N_2 for two hours to remove dissolved oxygen (DO). In a typical preparation, $FeCl_3$ stock solution was added to a starch solution through a burette to yield a solution with desired Fe and starch concentrations. Fe concentration used in this study varied from 0.1 to 1 g L^{-1}. Accordingly, starch concentration was either ~0.2% (w/w) for 0.1 g L^{-1} Fe or ~0.8% (w/w) for 1 g L^{-1} Fe solution. The ratio of Fe to starch was not optimized in this study.

In step 2, Fe^{3+} is reduced to Fe^0 using stoichiometric amounts of sodium borohydride. To ensure efficient use of the reducing agent BH_4^-, the reactor system was operated under inert conditions through continuously vacuuming. The flask was shaken by hands (magnetic stirring was avoided to reduce magnetically induced aggregation of the resultant iron particles) during the reaction. Ferric iron was reduced by borohydride according to the following reaction stoichiometry (Glavee et al., 1995),

$$Fe(H_2O)_6^{3+} + 3BH_4^- + 3H_2O \rightarrow Fe^0 + 10\frac{1}{2}H_2 + 3B(OH)_3 \qquad (2\text{-}1)$$
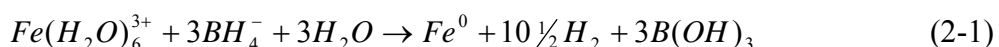
When gas (hydrogen) evolution ceased (after ~15 min), the Fe^0 nanoparticles were either used directly as a mono-metallic agent or loaded with a second metal (Pd) to yield Fe-Pd bimetallic nanoparticles. Loading of Pd to the starched Fe^0 particles was accomplished by adding known quantities of K_2PdCl_4 into the starch- Fe^0 solution and allowing for reaction for 15 minutes under vacuum. The amount of Pd added in this study was 0.1% (w/w) of Fe. Palladium was deposited on the iron surface through the following redox reaction (2-2),

$$Pd^{4+} + 2Fe^0 \rightarrow Pd^0 + 2Fe^{2+} \qquad (2\text{-}2)$$
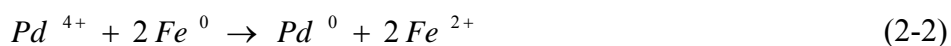
For comparison, non-starched Fe nanoparticles were also prepared following similar procedures but in the absence of starch.

2.2.3 Physical characterization

Transmission electron micrographs were obtained using a Zeiss EM10 Transmission Electron Microscope (TEM) (Zeiss, Thornwood, NJ) operated at 25 kv and 40 kv. The following general procedures were followed for the TEM measurements. First, a 30 μL of aqueous sample containing the nano-particles was placed on a formvar-

carbon coated copper grid. The droplet was then allowed for full contact/spreading on the grid. Then the bulk droplet was wicked away with filter paper to remove the excess volume of the sample, and the grid was allowed to air-dry for 5 minutes. The residual nano-particles attached to the grid were then imaged and photographed using the TEM.

The TEM image was analyzed using a specialty image processing software named ImageJ to obtain the particle size distribution. ImageJ was developed and maintained by the National Institute of Mental Health, Bethesda, MD. In brief, a binary (black and white) TEM image was selected and imported to ImageJ. Particles on the image were then segmented by adjusting the segmentation threshold value to ~ 178, which resulted in the best segmentation of particles from the background. The segmented particles were then analyzed by ImageJ, which indicated a total particle number of ~286 with a particle size ranging from 4 to 60 nm.

2.2.4 Degradation of TCE

Batch experiments were conducted in 65 mL serum bottles containing 63 mL of a solution with a given type of nanoscale particles. The degradation was initiated by adding 2 mL of TCE stock solution, which resulted in an initial TCE concentration of 25 mg L^{-1}, to the solution with the nanoparticles (no headspace). The bottles were then capped with Teflon Mininert valves and mixed on a rotary shaker (40 rpm) at 22 ± 1 ^{o}C in an incubator. At selected time intervals, 0.25 mL of the aqueous sample was withdrawn using a 250 μL gas-tight syringe. Then the sample was transferred into a 2 mL GC vial containing 1 mL of hexane for extraction of TCE. Upon phase separation, the extract was analyzed for TCE using a HP 6890 GC equipped with an electron capture detector (ECD). Control experiments (without the addition of the nanoparticles) were

carried out in parallel. The slight reduction (~3%) in solvent extraction efficiency due to the use of starch was corrected through blank tests. All experimental points were duplicated.

To examine the completeness of TCE dechlorination, coupled TCE degradation and chloride production were followed in a separate set of sacrificial batch experiments conducted in 43 mL vials containing 43 mL of a solution per vial with starched Fe-Pd nanoparticles. To ensure chloride detection, the initial TCE concentration was increased to ~52 mg L^{-1} (or 42 mg L^{-1} as Cl). At selected time intervals, duplicate vials were sacrificially sampled, and samples were extracted with hexane and analyzed for TCE remaining in water in the same manner as before. In addition, the solution was filtered by 0.22 μm membrane (Millipore, Billerica, MA). The filtrate was analyzed for chloride using a Dionex Ion Chromatography (DX-120).

2.2.5 Degradation of PCBs

Sacrificial batch experiments were conducted in 2 mL GC vials with Teflon-lined crimp caps. The degradation was initiated by injecting 25 μL Aroclor 1254 (100 mg L^{-1}) into 1 mL solution per vial containing 1 g L^{-1} as Fe of a certain type of nanoparticles. The initial concentration of the mixture PCBs was 2.5 ppm. The vials were then sealed and mixed on a rotary shaker (40 rpm) at 22±1 °C in an incubator. At predetermined time intervals, solution in selected vials (duplicates each time) was transferred into 1 mL hexane in 10 mL GC vials for extraction of PCBs. To avoid any loss of PCBs due to precipitation or sorption, the emptied vials were rinsed using hexane twice in a row (2 mL hexane in wash 1 and 1 mL in wash 2) and during the first wash the vials were also sonicated for 10 minutes to thoroughly remove PCBs from the vials. The rinsing hexane

17

was then added into the 10 mL vial containing the solution. Upon mixing and sonication for 5 minutes, the vial was centrifuged for 5 minutes at 1500 rpm (219 g) to allow for phase separation. PCBs in the hexane phase were then analyzed using an HP 6890 GC with ECD. All experimental points were duplicated.

2.2.6 Analytical methods

TCE in hexane was analyzed using a HP 6890 GC equipped with an RTX-624 capillary column (32 m long and 0.32 mm ID, Restek Co. Bellefonte, PA, USA) and an ECD. The initial oven temperature was set at 35 $^{\mathrm{o}}$C for 8 minutes and ramped to 60 $^{\mathrm{o}}$C at 5 $^{\mathrm{o}}$C/min, then to 200 $^{\mathrm{o}}$C at 17 $^{\mathrm{o}}$C/min, and then to 250 $^{\mathrm{o}}$C at 50 $^{\mathrm{o}}$C/min. Injector and detector temperatures were both at 250 $^{\mathrm{o}}$C. The carrier gas was helium at a flow rate of 1.7 mL/min and make-up gas was Argon+CH_4 at a flow rate of 58.3 mL/min. The detection limit was 5 μg L^{-1} for TCE, 15 μg L^{-1} for 1,1-DCE, 50 μg L^{-1} for VC, and ~1 mg L^{-1} for *cis*-DCE or *trans*-DCE.

PCBs were analyzed using a HP 6890 GC equipped with a HP5 capillary column (30 m long and 0.25 mm ID, Agilent, Santa Clara, CA, USA) and an ECD. The initial oven temperature was set at 100 $^{\mathrm{o}}$C for 2 min and ramped to 160 $^{\mathrm{o}}$C at 15 $^{\mathrm{o}}$C/min, and then to 270 $^{\mathrm{o}}$C at 5 $^{\mathrm{o}}$C/min. Injector and detector temperatures were 225 $^{\mathrm{o}}$C and 300 $^{\mathrm{o}}$C, respectively. The carrier gas was helium at a flow rate of 2.3 mL/min and make-up gas was Argon+CH_4 at a flow rate of 20 mL/min. Quantification of total Aroclor 1254 was based on the calibration with Aroclor 1254 using 5 major congeners following EPA Method 8082A.

Chloride was analyzed using a Dionex Ion Chromatography (DX-120) with an AS14 column, an AG14 guard column and a 100 μL sample loop. The eluant used was a mixture of sodium carbonate (3.5×10^{-3} M) and sodium bicarbonate (1.0×10^{-3} M).

2.3 Results and Discussion

2.3.1 TEM characterization

Figure 2-1 compares the transmission electron micrographs of the Fe-Pd nanoparticles prepared in the absence **(a)** or presence **(b)** of 0.2% (w/w) of the starch stabilizer. **Figure 2-1 (a)** shows that in the absence of the stabilizer the resultant particles do not appear as discrete nanoscale particles, but form much bulkier dendritic flocs with varying density. The size of some denser flocs can be well greater than 1 μm. This type of aggregation was attributed to the magnetic forces among the primary metal (Fe) particles (Zhang and Manthiram, 1997). Possibly owing to the absence of magnetic stirring and dissolved oxygen during the preparation, the resultant flocs in **Figure 2-1 (a)** appear to be looser in structure and finer in individual tentacles compared to those reported by others (Wang and Zhang, 1997; Schrick et al., 2002). Therefore, greater surface area and reactivity are expected. In contrast, the starch-stabilized Fe-Pd particles shown in **Figure 2-1 (b)** appear to be clearly discrete and well-dispersed. Similar TEM image of discrete particles was observed by others for non-magnetic nanoparticles such as copper (Zhang and Manthiram, 1997). Evidently, the presence of starch prevented agglomeration of the resultant iron particles and thus maintained the high surface area and reactivity of the particles.
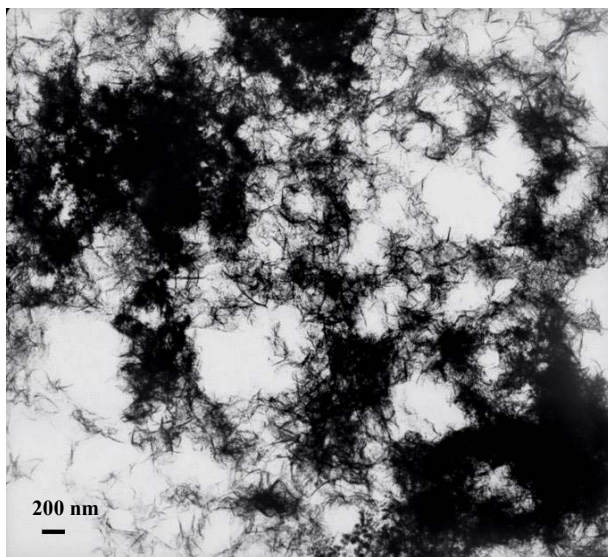
(a)
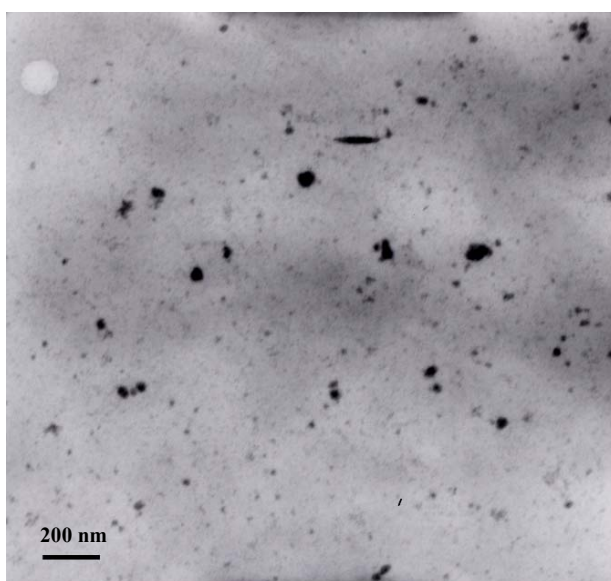
(b)

Figure 2-1. (a) TEM image of Fe-Pd nanoparticles prepared without starch but under inert conditions. (The scale bar represents 200 nm). **(b)** TEM image of Fe-Pd nanoparticles prepared with starch and under inert conditions (The scale bar represents 200 nm).
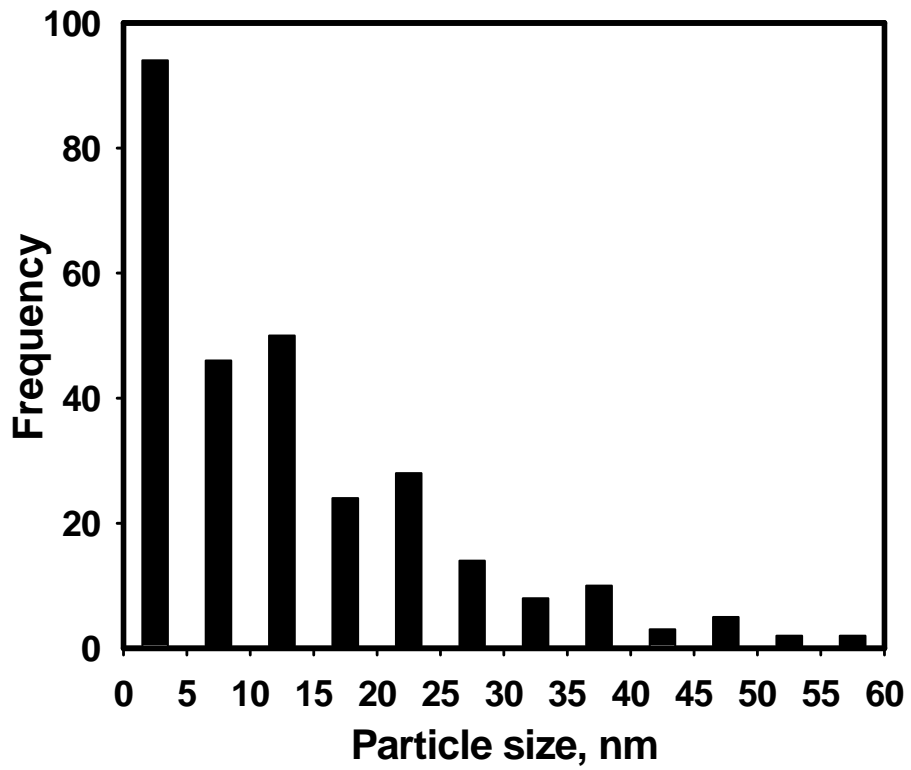
Figure 2-2. Histogram showing the size distribution of starched iron nanoparticles for a random sample of 286 particles.

Figure 2-2 shows the particle size distribution for the 286 starched nanoparticles. The mean particle size was calculated to be 14.1 nm with a standard deviation 11.7 nm. The maximum particle size observed was ~ 60 nm. For discrete, nonporous nanoparticles such as those shown in **Figure 2-1 (b)**, the surface area (S) is inversely related to the particle radius (r) through eqn (2-3) (Kecskes et al., 2003),

$$r = 3[\rho * S]^{-1} \tag{2-3}$$

where ρ is the density of Fe (7,870 kg m^{-3}). Based on a mean radius of 7.0 nm, the surface area for the starch-stabilized iron particles was calculated to be ~ 55 m^2 g^{-1}.

After 24 hours of storage, the stabilized nanoparticles remained suspended in water. Although some precipitation was found after 48 hours, the precipitated particles was easily re-dispersed in water by sonication, and the re-dispersed particles remained suspended for about 3 hours. In contrast, the non-stabilized Fe-Pd particles agglomerated and precipitated nearly completely in a few minutes after the particles were prepared.

2.3.2 Role of starch

The above results indicated that the water soluble starch matrix played an important role in stabilizing the iron nanoparticles. Starch is a branched, hydrophilic polymer that typically contains ~20% amylose. The weak complexation between starch and Fe^{3+} has been well studied through electron paramagnetic resonance (EPR) and conductivity measurements (Ciesielski and Tomasik, 2003; Ciesielski et al., 2003). Results from these studies and our experimental observations suggest that the iron-starch interactions and formation of intra-starch Fe clusters play a fundamental role in dispersing and stabilizing the iron nanoparticles.

When exposed to ferric ions, the hydroxyl groups extensively present in starch facilitated the complexation of ferric ions to the molecular matrix. Upon addition of the strong reducing agent (NaBH₄), the starch complexed Fe^{3+} ions were reduced to Fe^0 (the solution color changed immediately from yellow to dark black). UV-Vis spectra shown in **Figure 2-3** suggest that intra-starch Fe clusters were formed. Before reduction, the solution with starch complexed Fe^{3+} showed a peak at 289 nm wavelength. Upon reduction, the peak disappeared and the spectrum displayed a monotonic and nearly exponential decaying profile as the wavelength increases. This behavior results from the appearance of a new inter-band transition arising from the formation of intra-starch Fe clusters. The exponential shape is characteristic of a band-like electronic structure, which strongly suggests that the reduced Fe does not exist as isolated atoms, but rather as clusters (Kreibig and Vollmer, 1995; Zhao et al., 1998). When Fe clusters are formed in the starch matrix, the hydroxyl groups of starch act as the passivating contacts, thereby preventing the resultant nanoparticles from agglomeration as observed for non-starched particles (Raveendran et al., 2003).

However, even starched iron particles may form flocs over prolonged times (several days). The fact that flocs of starched iron particles can be readily re-suspended through simple sonication suggests that the starch-Fe flocs are rather loosely bonded.
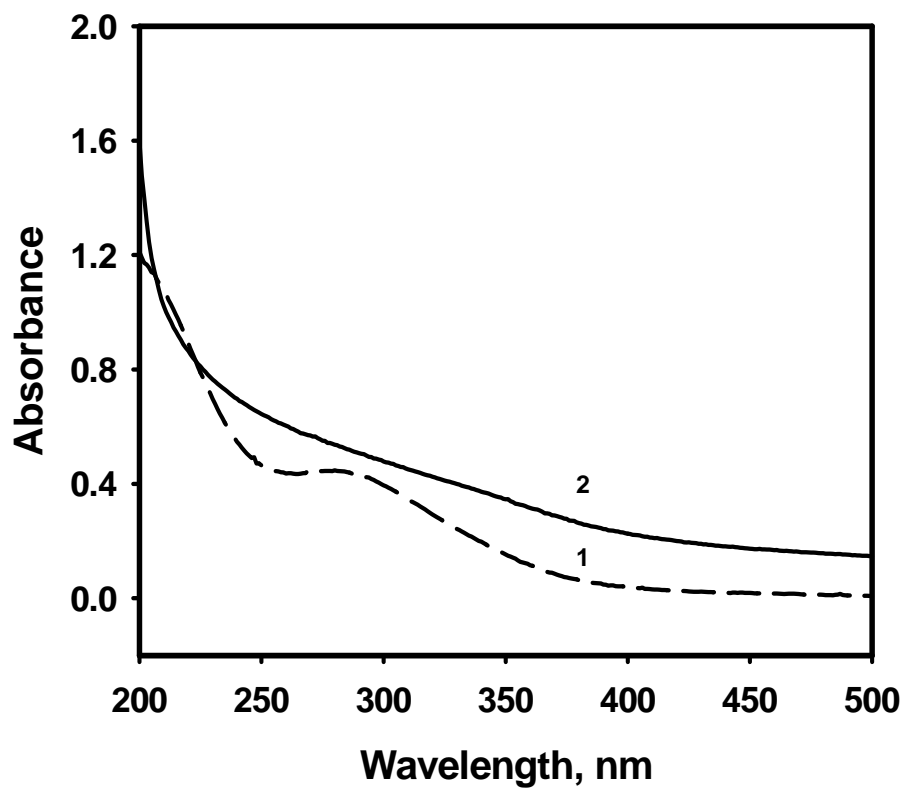
Figure 2-3. Absorption spectra of a solution containing 10 mg L^{-1} Fe^{3+} and 0.2% (w/w) starch before (dashed line, curve 1) and after (solid line, curve 2) reduction with a stoichiometric amount of NaBH$_4$.

2.3.3 Dechlorination of TCE

Figure 2-4 compares TCE degradation efficiency using various Fe(0)-based particles. The initial TCE concentration was ~25 mg L^{-1} in all cases. For comparison, a commercial "nanoscale" iron material was also tested (Note: although the particle size was commercially claimed to be ~100 nm, the actual particle size of the commercial Fe-particles appeared to be in the micron to millimeter range; the particles precipitated in water immediately). Each data point reported in all figures represents the mean of duplicates. The maximum standard deviation was: 0.5% for starched Fe-Pd, 4.5% for non-starched Fe-Pd, 1.2% for starched Fe, 0.5% for non-starched Fe, 0.7% for commercial Fe, 1.5% for commercial Fe-Pd, and 0.3% for control (no iron particles added).

Figure 2-4 (a) shows that the TCE degradation rate was extremely slow when mono-metallic iron nanoparticles were applied. However, the degradation rate was clearly improved when the starch was applied to yield more dispersed iron nanoparticles. Earlier research reported a higher degradation rate for TCE with similar nanoscale Fe^{0} particles but at a 200 times higher iron dose (~20 g L^{-1}) (Wang and Zhang, 1997). The following pseudo-first-order reaction kinetics may be used to describe the initial TCE degradation rate (Johnson et al., 1996b)

$$-\frac{dC}{dt} = k_{SA} a_s \rho_m C = k_{obs} C \qquad (2\text{-}4)$$

(a)

26
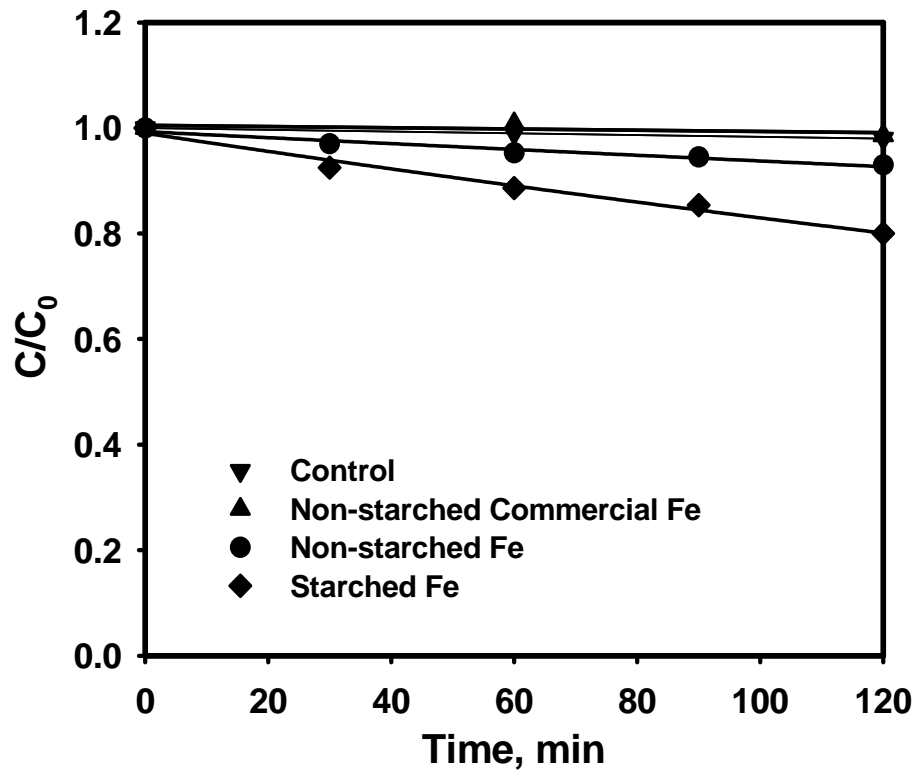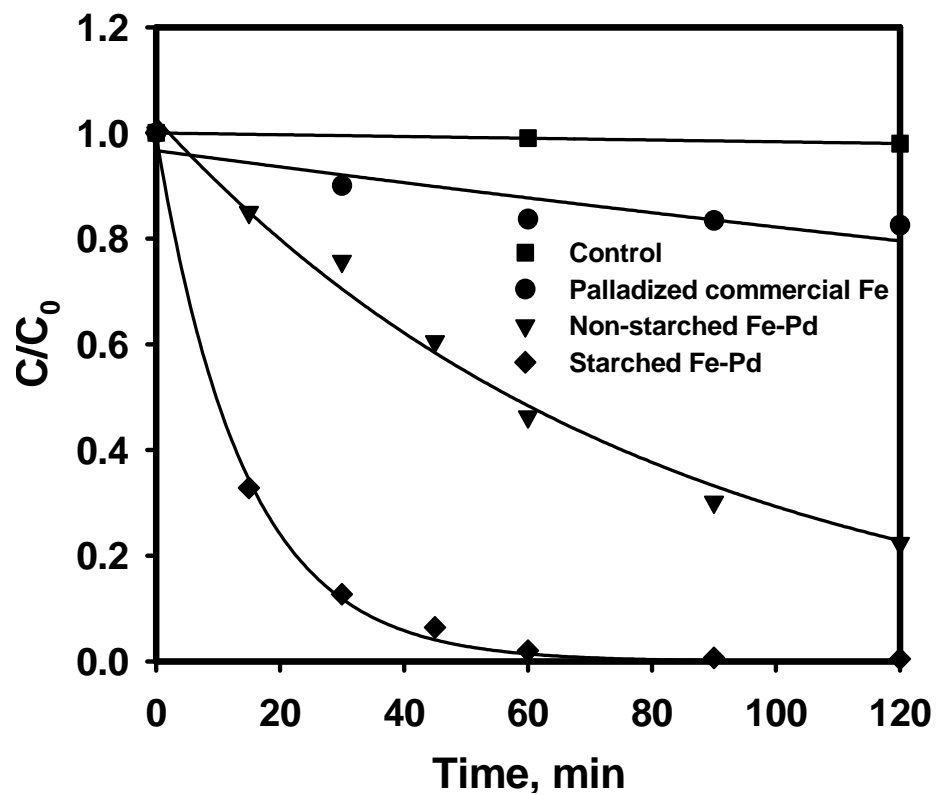
(b)

Figure 2-4. (a) Dechlorination of TCE using commercial iron nanoparticles, non-starched iron nanoparticles prepared in our laboratory, and starched (0.2%, w/w) iron nanoparticles. Iron dose was 0.1 g L^{-1} as Fe in all cases. **(b)** Dechlorination of TCE using palladized iron nanoparticles (Fe-Pd) prepared in our lab, starched (0.2%, w/w) Fe-Pd nanoparticles, and palladized commercial iron particles. Fe dose was 0.1 g L^{-1} in all cases except for palladized commercial iron (1 g L^{-1}). Pd to iron ratio was 0.1/100 (w/w).

where C is TCE concentration (mg L^{-1}) at time t (h), k_{SA} is the specific reaction rate constant based on surface area of the nanoparticles (L h^{-1} m^{-2}), a_s is the specific surface area of the nanoparticles (m^2 g^{-1}), ρ_m is the mass concentration of the nanoparticles (g L^{-1}), and k_{obs} is the observed pseudo-first rate constant. The rate constants (k_{SA} or k_{obs}) can then be determined by fitting the pseudo-first rate expression from eqn (2-4) to the experimental data. The value of k_{obs} was 0.11 h^{-1} for starch-stabilized Fe and 0.034 h^{-1} for non-starch-stabilized Fe particles. The value of k_{SA} was 0.020 L h^{-1}m^{-2} for the starch-stabilized mono-metallic Fe particles. The commercial "nanoscale" iron particles did not show any appreciable degradation of TCE during the course of the experiment (120 minutes). The TCE concentrations in the controls remained unchanged during the course of the experiments.

In accord with prior report (Wang and Zhang, 1997), **Figure 2-4 (b)** shows that degradation of TCE can be greatly enhanced when a small fraction (~0.1 percent of Fe) of Pd was coated on the Fe particles. At the rather modest Fe dose of 0.1 g L^{-1}, even the non-starched nanoscale Fe-Pd particles prepared under inert conditions were able to eliminate ~78 % of TCE in the batch reactor within 2 hours. When the particles were stabilized by starch, ~98 % of TCE was destroyed within 1 hour. In contrast, a TCE degradation of only 18% was observed when the commercial Fe particles were palladized and used at a 10 times higher dose (1 g L^{-1}). The observed k_{obs} value was 3.7 h^{-1} and the k_{SA} value was 0.67 L h^{-1}m^{-2} for the starch-stabilized Fe-Pd nanoparticles. Earlier, Lien and Zhang (2001) reported a k_{SA} value of 0.018 L h^{-1}m^{-2} for their non-stabilized Fe-Pd particles, where the initial TCE concentration was 20 mg L^{-1} and the metal dose was 5 g L^{-1}. The 37-fold difference in k_{SA} suggests that the application of the starch stabilizer not

only increases the specific surface area of the resultant nanoparticles, but also greatly enhances the surface reactivity of the nanoparticles per unit area.

Halogenated intermediates, such as vinyl chloride (VC), *cis*- or *trans*-dichloroethene (DCE), were not detected during the course TCE degradation by either starched or non-starched bimetallic (Fe-Pd) particles. Trace amounts ($< \sim 25$ μg L^{-1}) of 1,1-DCE were detected in the initial stage of TCE degradation using starched Fe-Pd particles. However, 1,1-DCE disappeared after 20 minutes when TCE was lowered to ~ 6 mg L^{-1}, indicating that 1,1-DCE was also destroyed in this reaction period.

The completeness of TCE dechlorination can be reflected by monitoring the coupled TCE degradation and chloride production rates. **Figure 2-5** shows that chloride accumulation rate was nicely coupled with TCE degradation rate during the three-hour degradation of TCE using starched Fe-Pd nanoparticles (Note: TCE remaining is reflected by the amount of TCE-Cl that remains associated with TCE). The nearly perfect chlorine mass balance indicates that for each mg L^{-1} of TCE-Cl depleted, nearly the same amount of chloride was formed, indicating nearly complete dechlorination of TCE. The total Cl (sum of chloride and TCE-Cl) displayed a minor dip in the initial stage (<60 minutes) of TCE reduction, suggesting the formation of small quantities ($<14\%$) of other chlorinated intermediates in the early stage. However, these intermediates were rapidly degraded. At steady state (>120 minutes), the sum of TCE-Cl and Cl$^-$ accounted for more than 95% of the total chlorine in the system.
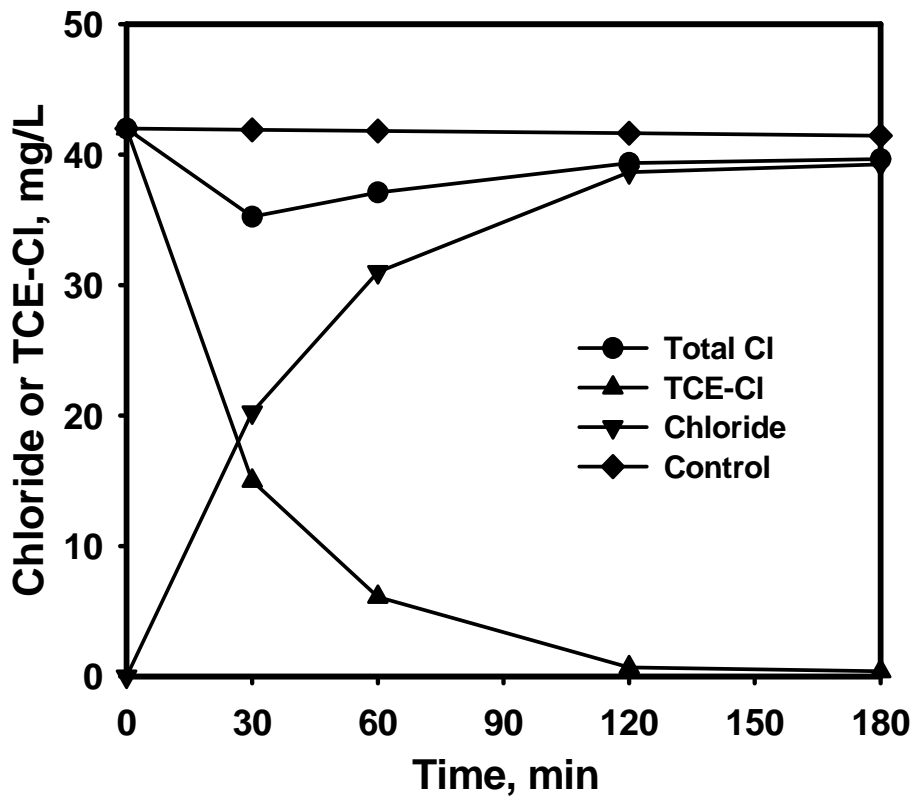
Figure 2-5. Evolution of chloride and TCE-Cl during dechlorination of TCE using starched Fe-Pd nanoparticles. Initial TCE concentration was 52 mg L^{-1} (or 42 mg L^{-1} as Cl). Starch concentration was 0.2% (w/w). Fe to solution ratio was 0.1 g L^{-1}. Pd to iron ratio was 0.1% (w/w).

2.3.4 Dechlorination of PCBs

PCBs are among the most persistent chlorinated hydrocarbons. Degradation of PCBs using Fe^0-based particles has been studied by a number of researchers. However, PCBs were found to be reduced by Fe^0 at high temperature (250 ^{o}C or 300 ^{o}C) and/or high pressure (10 MPa) (Chuang et al., 1995; Yak et al., 1999). **Figure 2-6** compares the degradation rates of a standard mixture of PCBs (Aroclor 1254) measured as five major congeners using four starched or non-starched Fe or Fe-Pd nanoparticles prepared in our laboratory. For the known higher persistency of PCBs over TCE, Fe dose was increased to 1.0 g L^{-1}, whereas the Pd to Fe ratio remained at 0.1%. The data reported represent means of duplicates. The standard deviations were: 2.4% for starched Fe-Pd, 7.6% for non-starched Fe-Pd, 15% for non-starched Fe, and 7.0% for starched Fe.

Figure 2-6 shows that mono-metallic Fe nanoparticles (starch-stabilized or not) did not show any significant degradation of PCBs within the test period of 100 hours. The two nearly flat lines also confirmed the efficiency of the extraction procedures. Therefore, no additional control runs were carried out. The degradation was clearly enhanced when 0.1% (w/w) of Pd was coated on the Fe particles, which resulted in a ~24% reduction of PCBs within 100 hours. In contrast, the starch-stabilized bimetallic (Fe-Pd) particles were able to transform over 80% PCBs under otherwise identical conditions. Again, applying the same pseudo-first-order reaction kinetics to the degradation of PCBs, the observed pseudo-first-order rate constant, k_{obs}, can be determined to be 0.017 h^{-1} for starched Fe-Pd and 0.0029 h^{-1} for non-starched Fe-Pd, a difference of nearly 6-folds.
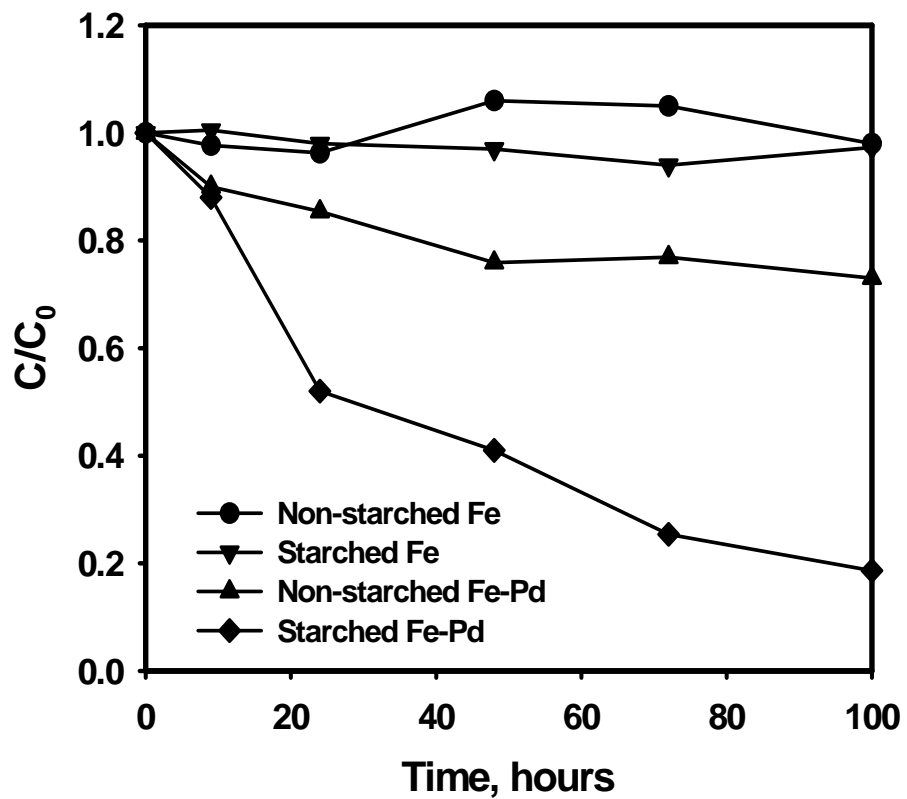
Figure 2-6. Transient dechlorination of PCBs using starched or non-starched nanoscale Fe or Fe-Pd particles. Initial PCBs concentration was 2.5 mg L^{-1}. Metal to solution ratio was 1.0 g L^{-1}. Palladium to iron ratio was 0.1% (w/w). Starch concentration was 0.8% (w/w).

(a)

(b)

34
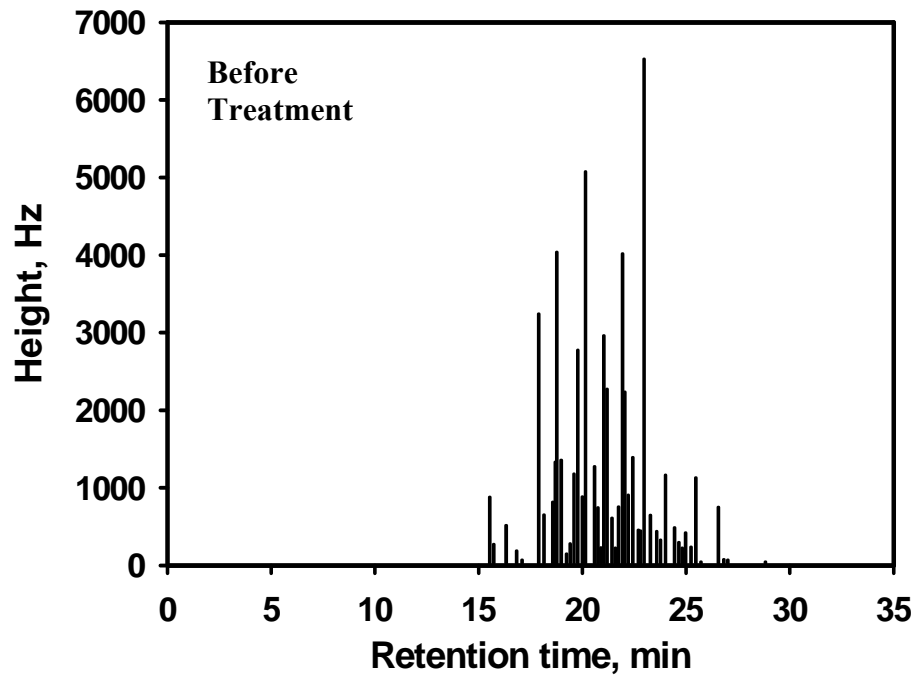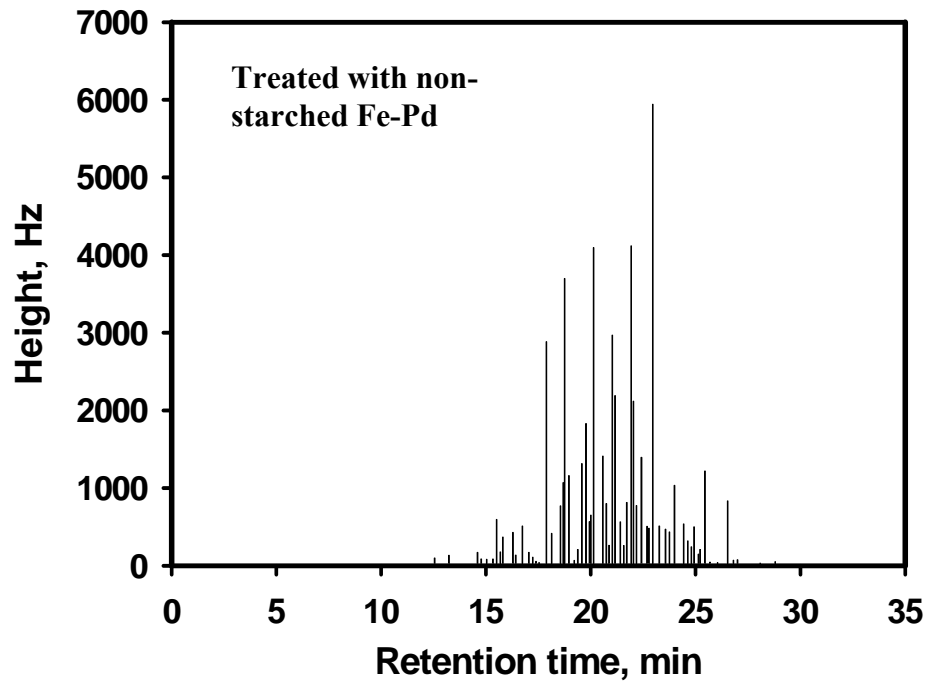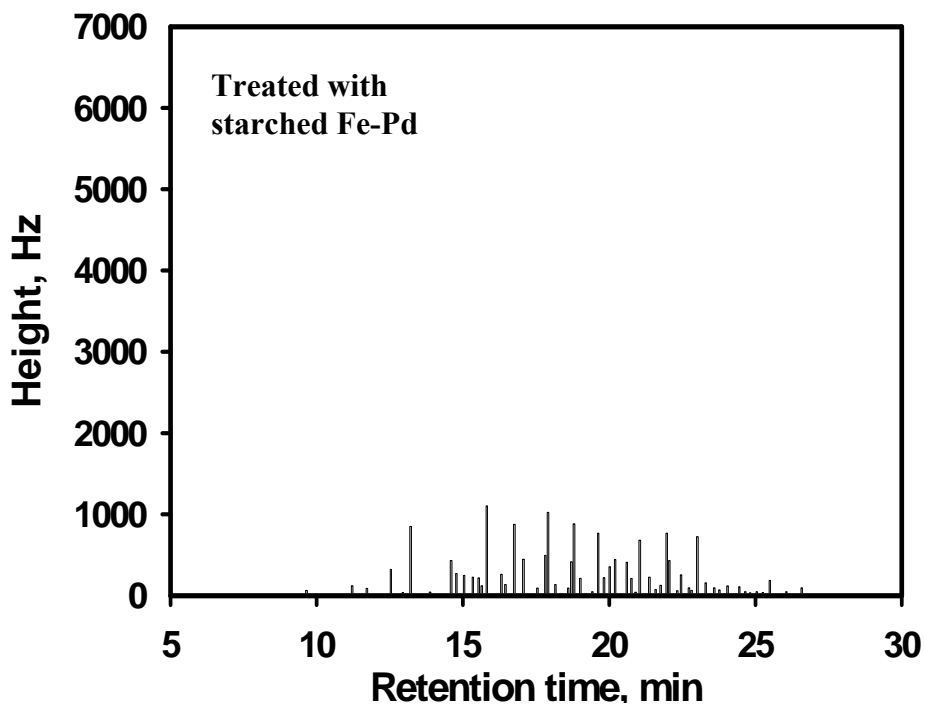
(c)

Figure 2-7. Comparing GC chromatograms for **(a)** a standard Aroclor 1254 sample in water before the treatment, **(b)** the same sample but treated with non-starched Fe-Pd nanoparticles for 72 h, and **(c)** the same sample but treated with starched Fe-Pd nanoparticles for 72 h. Initial PCBs concentration was 2.5 ppm. Metal to solution ratio was 1 g L^{-1}. Pd to Fe ratio was 0.1g/100g.

Figure 2-7 compares the GC chromatograms of PCBs before and after the treatment. **Figure 2-7** suggests that the PCBs were transformed to some lower chlorinated compounds. Namely, some intermediate by-products were produced during the reduction of parent PCBs using the Fe-Pd particles. However, the application of starch as a stabilizer not only substantially enhanced the degradation of parent PCBs, but also resulted in much lower levels of products, evidenced by the new peaks in **Figure 2-7 (c)** that occurred before ~15 minutes. Apparently, these intermediates are expected to continue to be further dechlorinated as the reaction proceeds. In a prior study on the degradation of a single PCB congener (2,3,2',5'-tetrachlorobiphenyl) with palladized iron filings, Korte et al. observed that dechlorination of PCBs occurred in a step-wise fashion with the meta-chlorines being more reactive than ortho-chlorines and less chlorinated by-products being more persistent than their parent congeners (Korte et al., 2002). They also reported that the Fe-Pd particles were able to convert all the congener to biphenyl given sufficient metal dose and reaction time. Due to the lower sensitivity of GC-ECD to the smaller chlorinated congeners (Kubatova et al., 2003) and the complexity and uncertainties associated with the intermediate products, these by-products were not quantified and identified in this study.

CHAPTER 3. STABILIZATION OF FE-PD NANOPARTICLES WITH SODIUM CARBOXYMETHYL CELLULOSE FOR ENHANCED TRANSPORT AND DECHLORINATION OF TCE IN SOIL AND GROUNDWATER

The starched Fe particles started to precipitate after 2 days, which limits their long-term storage and future application in the field. This chapter investigated the feasibility of using carboxymethyl cellulose (CMC) as a novel stabilizer for preparing physically more stable and chemically more reactive Fe-Pd nanoparticles for degradation of TCE in water.

3.1 Introduction

In-situ dechlorination by directly injecting zero-valent iron (ZVI) nanoparticles into the contaminated subsurface has attracted increasing interest in recent years (Gillham, 2003; Moran, 2004; Wang and Zhang, 1997). Compared to the traditional passive processes such as the "funnel and gate' or permeable reactive barrier (PRB) processes, the in-situ injection technology offers a number of key advantages (Gillham, 2003). For example, it can proactively attack contaminant plumes in the source zone and potentially reduce the remediation cost and time substantially (Gillham, 2003).

However, this promising technology has been held back by a key technical barrier that the nanoparticles tend to agglomerate and grow to micron-scale or larger, thereby losing their soil mobility and chemical reactivity rapidly (He and Zhao, 2005; Mondal et al., 2004; Schrick et al., 2004). Typically, Fe(0)-based nanoparticles are prepared by

reducing Fe(II) or Fe(III) in aqueous phase using sodium borohydride (Glavee et al., 1995; Wang and Zhang, 1997). Although other solvent-based methods such as micro-emulsion-based methods (Li et al., 2003), sonication assisted methods (Khalil et al., 2004; Suslick et al., 1996) and sol-gel methods (Wonterghem et al., 1985) have been reported, the water-based approach appears most suitable for environmental applications for its minimal use of environmentally prohibitive solvents or chemicals. However, due to particle agglomeration, the water-based method often fails to produce the desired stable Fe nanoparticles without a stabilizer.

Agglomeration of magnetic metal nanoparticles takes place primarily through direct inter-particle interactions such as van der Waals forces and magnetic interactions (Cushing et al., 2004). Agglomeration reduces the specific surface area and the interfacial free energy, thereby diminishing particle reactivity. A stabilizer can enhance dispersion (or reduce agglomeration) of nanoparticles through: a) electrostatic repulsion (i.e. adsorption of charged stabilizer molecules to the metal core enhances the surface charge, resulting in increased Coulombic repulsion between the capped particles), and b) steric hindrance (i.e. coating the metal core with sterically bulky stabilizers such as polymers impedes particle attractions) (Cushing et al., 2004). In addition to weakening the physical interactions, encapsulating nanoparticles with select stabilizers may also passivate the highly reactive surface from reacting with the media such as dissolved oxygen (DO) and water. Apparently, the surface passivating effect may also inhibit the reaction with target contaminants. However, the net reactivity gain toward a target compound can be substantial due to the tremendous gain in nanoparticle surface area from the particle stabilization.

Extensive studies have been devoted to stabilizing non-ZVI (e.g. Au, Ag and iron oxides) nanoparticles. For instance, to prevent nanoscale iron oxides from agglomeration, various stabilizers have been found to be effective, including thiols (Kataby et al., 1997), carboxylic acids (Kataby et al., 1999), surfactants (Sun and Zeng, 2002) and polymers (Ditsch et al., 2005; Kim et al., 2003; Si et al., 2004). Obviously, not all these stabilizers are applicable to the ZVI nanoparticles of interest. For example, thiols and carboxylic acids may be reduced by ZVI, some polymers may not function properly in water (Khalil et al., 2004), some stabilizers themselves are not environmentally benign, and others are cost-prohibitive. However, the fundamentals and experimental approaches gained from these studies provide a valuable knowledge base for studying the stabilization of ZVI nanoparticles.

In contrast, only limited studies have been reported on stabilizing ZVI nanoparticles. Mallouk et al. employed carbon nanoparticles and poly(acrylic acid) (PAA) as "vehicles" for stabilizing and/or delivering Fe-based nanoparticles (Ponder et al., 2000; Ponder et al., 2001; Schrick et al., 2004). Saleh et al. proposed a new type of sorptive nanoparticles prepared by modifying commercial ZVI nanoparticles with so called 'block copolymer shells' consisting of a hydrophobic inner shell and a hydrophilic outer shell for dechlorination of DNAPLs (Saleh et al., 2005). Sun and Zhang reported that using polyvinyl alcohols can reduce the size of Fe nanoparticles (or their aggregates) from 60 nm to 7.9 nm (Sun and Zhang, 2005).

To implement the in-situ injection of Fe nanoparticles, an ideal stabilizer should be a) able to specifically interact with the nanoparticles and hence suppress their growth; b) environmentally benign; c) cost-effective; and d) mobile in soils. Recently, He and

Zhao reported that a food-grade water-soluble starch can improve both dispersibility and reactivity of Fe nanoparticles (He and Zhao, 2005). Unfortunately, the starched Fe particles became less stable as evidenced by the appearance of floc precipitates after 2 days, thereby limiting long-term storage and commercial application of these Fe nanoparticles. A better stabilizer with stronger interaction with Fe particles needs to be developed that will allow longer-lasting effective stabilization and facilitate environmental applications of these nanoparticles.

Cellulose is a carbohydrate consisting of a series of hydro-glucose units interconnected by an oxygen linkage (known as *beta* linkage) to form a linear molecular chain structure. Cellulose can be easily modified to sodium carboxymethyl cellulose (CMC) by replacing the native CH_2OH group in the glucose unit with a carboxymethyl group. **Figure 3-1** presents a conceptualized representation of the molecular structure of CMC. CMC is water-soluble and is commonly used in food processing (Gilbert, 1994). CMC has been successfully used as an effective stabilizer in preparing nanoparticles such as superparamagnetic iron oxide nanoparticles (SPION) and Ag nanoparticles (Magdassi et al., 2003; Si et al., 2004). Like starch, CMC is also low-cost and environmentally friendly. CMC and starch share a similar macro-molecular skeleton. However, CMC is a polyelectrolyte and carries carboxylate groups in addition to hydroxyl groups. Consequently, CMC is expected to interact with Fe nanoparticles more strongly and stabilize the nanoparticles more effectively.
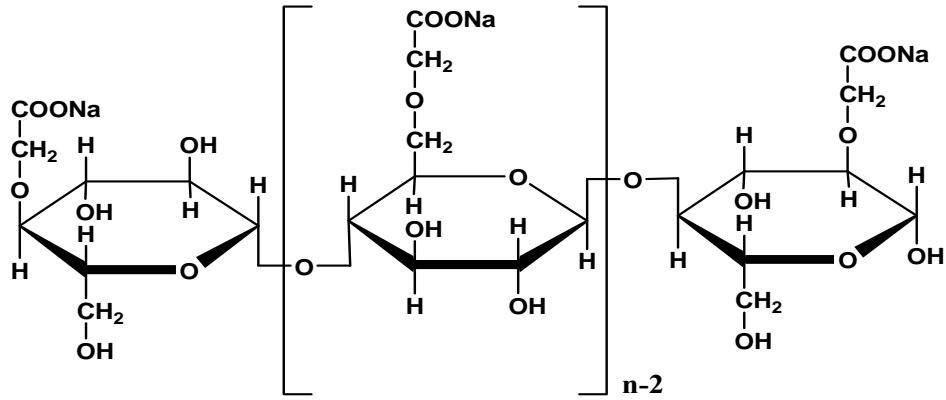
Figure 3-1. A conceptualized representation of the molecular structure of NaCMC.

This work aims to investigate the feasibility of using CMC as a novel stabilizer for preparing physically more stable and chemically more reactive Fe-Pd nanoparticles for degradation of TCE in soils and water. The specific objectives are to 1) prepare a new class of Fe-Pd nanoparticles using CMC as a stabilizer; 2) elucidate the mechanisms governing the particle stabilization; 3) probe the dechlorination reactivity of the nanoparticles with TCE as a model chlorinated hydrocarbon; and 4) preliminarily test the mobility of the CMC-stabilized iron particles in soil.

3.2 Experimental Section

3.2.1 Chemicals

The following chemicals were used as received: TCE (>99%, spectrophotometric grade, Aldrich, Milwaukee, WI); hexane (pesticide grade, Fisher Scientific, Fair Lawn, NJ); K_2PdCl_6 (99%, Acros Organics, Morris Plains, NJ); $FeSO_4 \cdot 7H_2O$ (Acros Organics); sodium carboxymethyl cellulose (NaCMC or CMC, mean M.W. = 90,000, Acros Organics); and sodium borohydride ($NaBH_4$, ICN Biomedicals, Aurora, OH).

3.2.2 Preparation of nanoparticles

Fe-Pd nanoparticles were prepared by modifying a water-based approach (He and Zhao, 2005) with two changes: a) CMC was used as a stabilizer, and b) $FeSO_4 \cdot 7H_2O$ was used as the starting salt for the ZVI nanoparticles. Compared to commonly used $FeCl_3$, $FeSO_4 \cdot 7H_2O$ offers several advantages: 1) it allows for monitoring chloride production during the dechlorination reaction; 2) ferrous ions will form stable complexes with CMC while ferric ions can induce flocculation of CMC; and 3) it consumes less borohydride to reduce ferrous ions. In brief, the preparation was carried out in a 250 mL flask attached to

a vacuum line. Before use, DI water and CMC solution were purged with purified N_2 for 15 minutes to remove DO. In a typical preparation, a 0.21M $FeSO_4 \cdot 7H_2O$ stock solution was prepared right before use, and then was added to the CMC solution through a burette to yield a desired concentration of Fe and CMC. The mixture was purged with N_2 for 15 minutes to complete the formation of Fe-CMC complex. Fe concentration used in this study was 0.1 g/L or 1g/L, whereas the corresponding CMC (in sodium form) concentration was 0.2% (w/w) or 0.8% (w/w).

The Fe^{2+} ions were then reduced to Fe^0 by adding a certain amount of sodium borohydride ($BH_4^-/Fe^{2+} = 2.0$) in the mixture. To ensure efficient use of the reducing agent BH_4^-, the reactor system was operated under inert conditions through continuously vacuuming. The flask was shaken by hands during the reaction. When gas (hydrogen) evolution ceased (after ~15 min), the Fe^0 nanoparticles were loaded with small amount of Pd by adding K_2PdCl_6 (0.027mM) to the CMC-Fe^0 solution (Grittini et al., 1995; Wang and Zhang, 1997). The amount of Pd used in this study was 0.1% (w/w) of Fe. Based on our prior study on starch-stabilized Fe nanoparticles (He and Zhao, 2005), the addition of a small fraction (0.1% w/w Fe) of Pd as a catalyst was able to increase reactivity by ~34 times based on surface area normalized reaction rate. Evidently, because of the chain-like structure and macromolecular nature of CMC, the CMC coating does not prevent the accessibility of the CMC-stabilized core Fe for electron acceptors. It is expected that Pd^{2+} ions are reduced to Pd^0 by the Fe nanoparticles, resulting in the Fe-Pd bimetallic nanoparticles. Evidence for the formation of microscale Fe-Pd bimetallic particles in the absence of a stabilizer has been reported by others (Doong and Lai, 2005; Jovanovic et

al., 2005). In this study, the level of Pd was too low to be discernable from the TEM images.

3.2.3 Physical characterization

TEM micrographs were obtained using a Zeiss EM10 Transmission Electron Microscope (Zeiss, Thornwood, NJ) following a previously reported procedure (He and Zhao, 2005) except that the preparation of the sample grids was carried out in an anaerobic glovebox filled with nitrogen gas.

Dynamic light scattering (DLS) tests were performed with a Nicomp 380 Submicron Particle Sizer (PSS, Santa Barbara, CA) at a measurement angle of 90° (Internal He-Ne laser, wavelength 633 nm). The DLS data were processed with a software package CW380 to yield the number-weighted size distributions. Solution viscosities were measured by a Gilmont falling ball viscometer, and then used to correct for the influence of viscosity on DLS measurements. In all measurements, triplicate samples of 0.1 g/L Fe were analyzed.

FTIR measurements were carried out to explore the modes of interactions between CMC and the nanoparticle surface. The solution containing CMC-stabilized nanoparticles (1.0 g/L) was first high-speed (9000 g) centrifuged. Upon removal of the supernatant, the solid deposit was rinsed with DI water, and then dried under vacuum for 24 hours. The dried sample was mixed with KBr to obtain the KBr pellets consisting of 1.5% (w/w) of the nanoparticles. FTIR spectra of the CMC-stabilized nanoparticles were then recorded by shooting the KBr pellets with a Nicolet AVATAR 360 E.S.P spectrometer (Nicolet, Madison, WI). For comparison, FTIR spectra for CMC were obtained as control.

3.2.4 Degradation of TCE

The TCE degradation effectiveness was tested in a series of duplicated batch experiments. The batch tests were carried out in 43 mL amber glass vials, filled with 43 mL of a solution containing a certain type of nanoscale particles (the headspace was set to nearly zero to minimize volatilization loss of TCE). TCE degradation was initiated by spiking 50 µL of a TCE stock solution (43 g/L TCE in methanol) into the solution containing the nanoparticles, which resulted in an initial TCE concentration of 50 mg/L. The bottles were capped with Teflon Mininert valves and mixed on a rotary shaker (40 rpm) placed in an incubator at 22 ± 1 ^{o}C. At selected time intervals, 0.1 mL of the aqueous sample, which includes the suspended nanoparticles, was withdrawn using a 100 µL gas-tight syringe. Then the sample was transferred into a 2 mL GC vial containing 1 mL of hexane for extraction of TCE. Upon phase separation, the extract was analyzed for TCE using an HP 6890 GC equipped with electron capture detector (ECD).

3.2.5 Analytical methods

TCE was analyzed using a HP 6890 GC equipped with an RTX-624 capillary column (Restek Co, Bellefonte, PA) and an ECD. The detailed procedures were described elsewhere (He and Zhao, 2005). Chloride was analyzed using a Dionex Ion Chromatography (DX-120, Dionex, Sunnyvale, CA) equipped with an AS14 column, an AG14 guard column and a 100 µL sample loop. Iron was analyzed with a flame atomic-absorption spectrophotometer (AAS) (220FS, Varian, Palo Alto, CA).

3.3 Results and Discussion

3.3.1 TEM, DLS and UV-Vis characterization of CMC-stabilized nanoparticles

Figure 3-2 compares the TEM images of the Fe-Pd nanoparticles prepared in the absence of CMC **(a)** and in the presence of CMC **(b)**. **Figure 3-2 (a)** shows that in the absence of the stabilizer the freshly prepared Fe-Pd particles appeared as dendritic flocs rather than discrete particles. This type of aggregation was attributed to the magnetic and/or van der Waals forces between the Fe(0) particles (Zhang and Manthiram, 1997). In contrast, the fresh CMC-stabilized Fe-Pd particles shown in **Figure 3-2 (b)** appeared as much finer nanoparticles with an average particle diameter (D) of 4.3 nm (standard deviation = 1.8 nm). In comparison, the starch stabilized Fe-Pd nanoparticles had a mean size of 14.1 nm (standard deviation = 11.7 nm) (He and Zhao, 2005). Both the smaller mean size and narrower distribution of CMC stabilized particles indicated that CMC better suppressed the growth of the iron nanoparticles and maintained the higher surface area of the particles.

The CMC-stabilized Fe-Pd nanoparticles exhibited superior stability against aggregation in water. Our observation revealed that while non-stabilized particles precipitated in a few minutes, stabilized nanoparticles (0.1g/L) remained fully dispersed in water until they were completely consumed by water after 9 days of aging at room temperature.
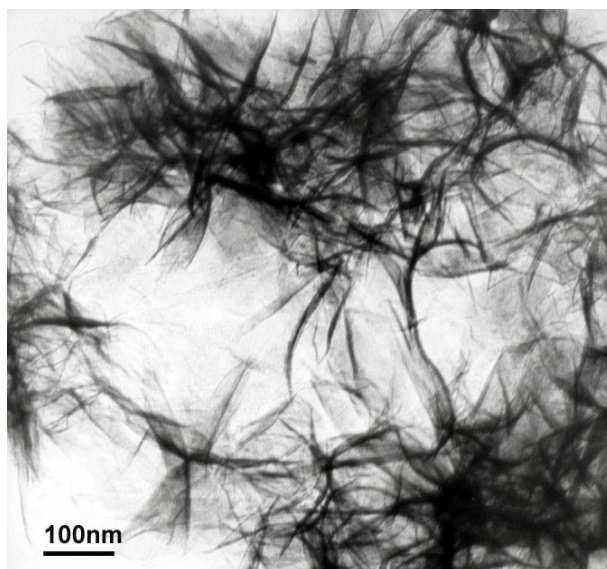
(a)
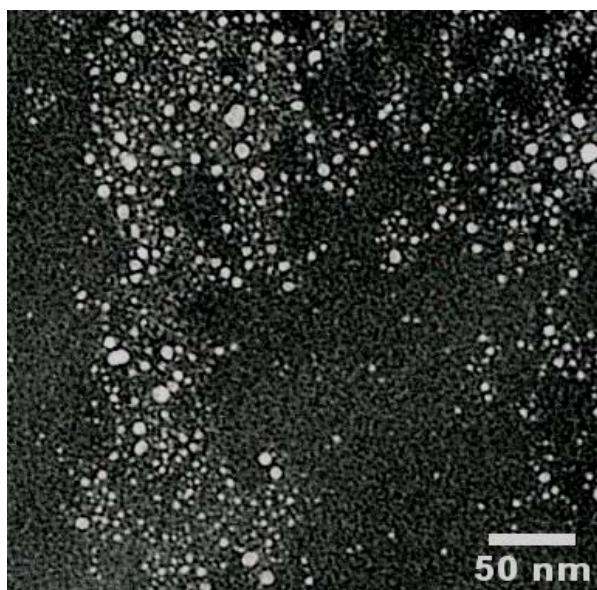
(b)

Figure 3-2. TEM images of 0.1 g/L freshly prepared (a) non-stabilized and (b) 0.2% (w/w) NaCMC stabilized Fe-Pd nanoparticles.

Although TEM images provide direct visualization of the shape and morphology of nanoparticles, estimating the particle size based on TEM images bears with some key assumptions, including a) the particles are spherical; b) the measured dried samples are the same as in the original solution; and c) the population (i.e. number) of TEM samples is large enough and the selection of samples is representative. Clearly, deviations from each of the assumptions can result in significant errors. To facilitate a more accurate measurement of the particle size, DLS was employed to measure the size of the stabilized nanoparticles. Although the assumption of spherical shape remains invoked, DLS offers some key advantages over TEM, including a) it measures the hydrodynamic size of particles in situ (i.e. in the original solution), and b) it measures a much larger sample size (~0.5 mL/sample). The DLS data indicates that the fresh stabilized nanoparticles have a hydrodynamic size of 17.2 nm (standard deviation = 3.2 nm). Considering the DLS and TEM measurements are naturally subjected to inherent sources of random and systematic error (Zheng et al., 2002), the TEM and DLS data appear to agree well.

Colloidal dispersion of metals typically exhibit absorption bands or broad regions of absorption in the ultraviolet-visible range (Creighton and Eadon, 1991). Thus the UV-Vis absorption spectrum gives an instant indication for the formation of metal colloids. The pK_a value of CMC has been reported to be ~4.3 (Magdassi et al., 2003), and the pH of CMC-Fe^{2+} solution (0.2% w/w CMC, 0.1 g/L Fe^{2+}) was measured to be ~6.1. Therefore, the carboxylic groups of CMC are expected to be almost fully disassociated and to interact strongly with the Fe^{2+} cations (Lewis acids). Upon reduction by $NaBH_4$, the solution color rapidly changed from clear to black, visually indicating the formation of Fe nanoparticles (pH after reduction ~8.3). Accordingly, the absorbance intensity rose

48
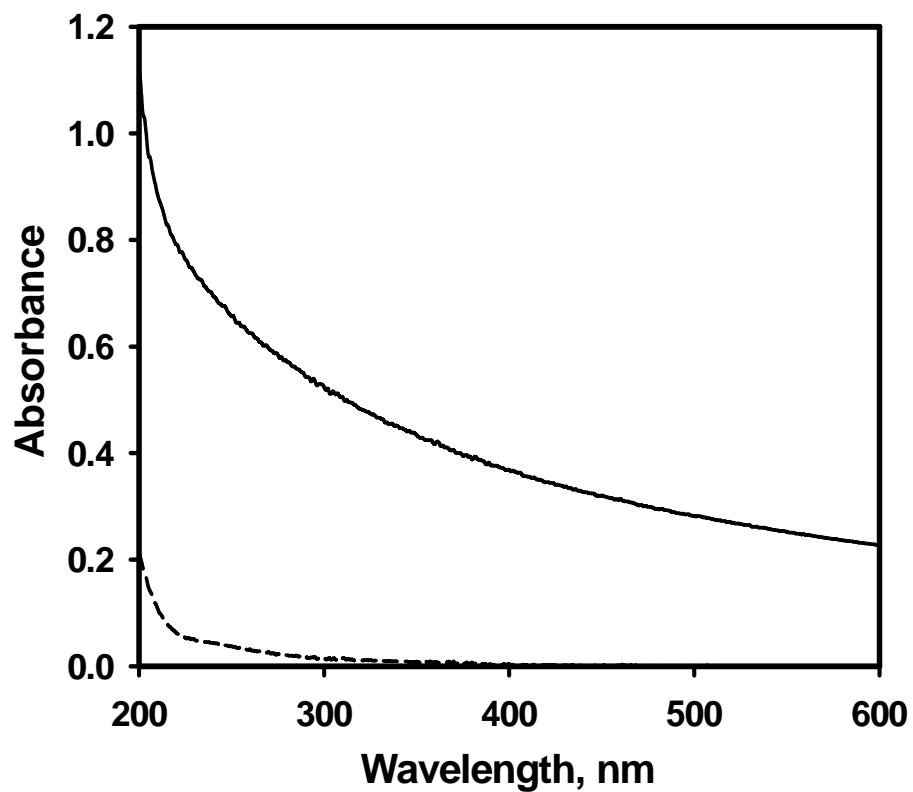
Figure 3-3. UV-Vis absorption spectra of a solution containing 5 mg/L Fe(II) and 0.2%

(w/w) NaCMC before (--- dashed line) and after (— solid line) reduction with NaBH4.

sharply and the UV-Vis spectrum displayed a monotonic and nearly exponential decaying profile as the wavelength increases (**Figure 3-3**). The exponential shape is characteristic of a bandlike electronic structure, which suggests that the reduced Fe does not exist as isolated atoms, but rather as clusters (Creighton and Eadon, 1991; He and Zhao, 2005; Kreibig and Vollmer, 1995; Zhao et al., 1998). Evidently, upon borohydride reduction, CMC-complexed Fe^{2+} ions are reduced to elemental Fe, which further undergoes nucleation and crystal growth (Cushing et al., 2004), resulting in formation of the clustered Fe (i.e. the nanoparticles). In the meantime, however, the surface of the formed nanoparticles will react with water and adsorb CMC molecules, thereby preventing further particle growth.

3.3.2 FTIR characterization of CMC-coated Fe-Pd nanoparticles and the nature of Fe-CMC interactions

To elucidate the stabilization mechanisms and to gain further insight into the interactions between various functional groups of CMC and the nanoparticles, FTIR measurements were carried out on CMC and the CMC-stabilized nanoparticles. **Figure 3-4** compares the characteristic stretching frequencies for CMC alone and for CMC-stabilized iron nanoparticles, and **Table 3-1** gives the assignments of the peaks (Brown et al., 1988). If CMC molecules are adsorbed to the surface of the iron nanoparticles, the stretching frequencies for the functional groups of CMC are expected to shift significantly.

Complexation between a carboxylate group and a metal such as Fe(0) may take place in four fashions: monodentate chelating (I), bidentate chelating (II), bidentate bridging (III) and ionic interactions (Deacon and Phillips, 1980; Wu et al., 2004); the first

three being illustrated in **Figure 3-5**. The separation of the symmetric and asymmetric stretches ($\Delta v = \Delta$ (asym) $- \Delta$ (sym)) of the carboxylate group can be used to identify the bonding mechanism when compared to that of the corresponding carboxylate salt (Deacon and Phillips, 1980; Wu et al., 2004): if $\Delta = 200 \sim 320$ cm^{-1}, the binding is governed by monodentate interaction; if $\Delta < 110$ cm^{-1}, it is by bidentate chelating interaction; and if $\Delta = 140 \sim 190$ cm^{-1}, it is by bidentate bridging.

In the present work, Δv (adsorbed) is determined to be 277 cm^{-1} (1620 cm^{-1} $-$ 1343 cm^{-1}) from **Figure 3-4**. Thus, monodentate interaction is the primary mechanism for binding CMC molecules to Fe nanoparticles. The same type of interaction was also observed by Jones et al. during adsorption of polyacrylate onto hematite (α-Fe$_2$O$_3$) (Jones et al., 1998).

It is also noteworthy that the –OH stretching band shifts from 3447 cm^{-1} for CMC to 3419 cm^{-1} for the CMC-Fe particles. This observation indicates that an enhanced intermolecular hydrogen bond is formed between CMC and Fe particle surface (Sylvestre et al., 2004; Bellamy, 1975). Given the abundance of –OH groups in CMC, this type of hydrogen bonding can be important in binding CMC onto the Fe nanoparticles although the individual bond strength may not be as strong as that between Fe and the carboxylate groups. This is in accordance with our prior observation that a water soluble starch was able to stabilize the iron nanoparticles (He and Zhao, 2005). Since the starch contains no carboxymethyl groups, adsorption of starch molecules onto the nanoparticles is likely facilitated through this type of H-bonding.
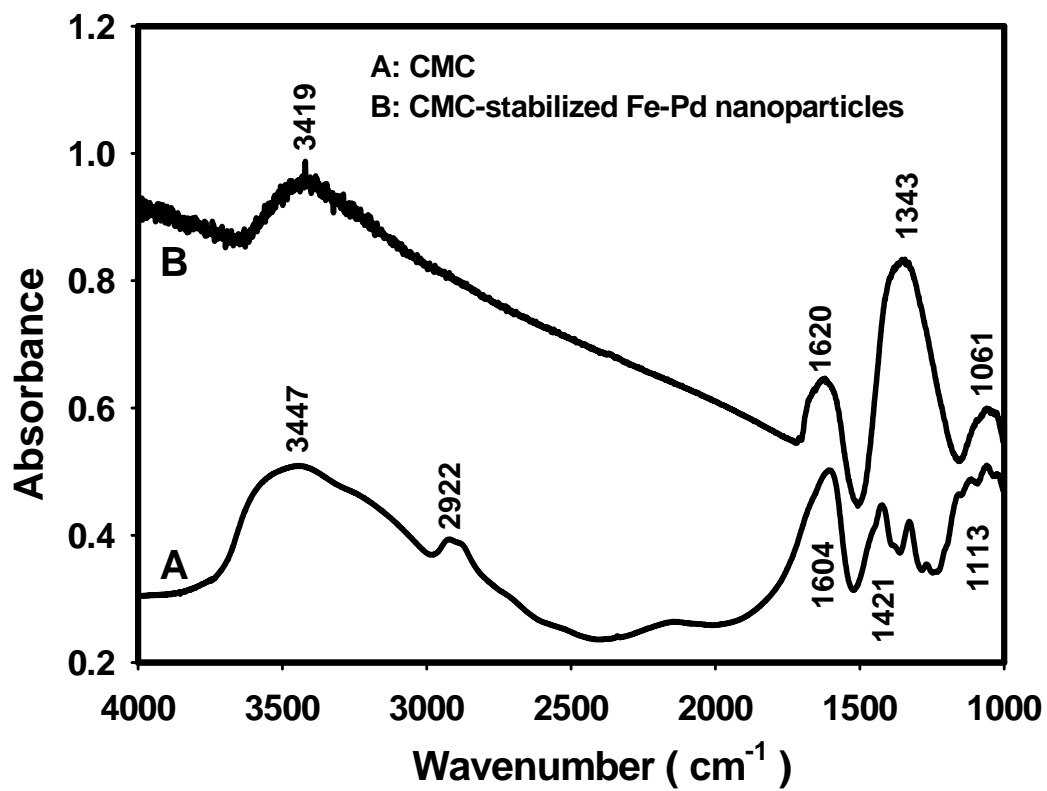
Figure 3-4. FTIR spectra of (A) CMC and (B) CMC-stabilized Fe-Pd nanoparticles.

Table 3-1. FTIR Peak Assignments for CMC and CMC-Stabilized Fe-Pd Nanoparticles.

Peak positions (cm^{-1})		Assignment
CMC Alone	CMC-Coated Iron Nanoparticles	
3447	3419	O-H stretch
2922		Asymmetric CH$_2$ stretch
1604	1620	COO$^-$ (asymmetric)
1421	1343	COO$^-$ (symmetric)
1113		C-O-C stretch (RCH$_2$OCH$_2$R)
1061	1061	C-O stretch (RCH$_2$OH)
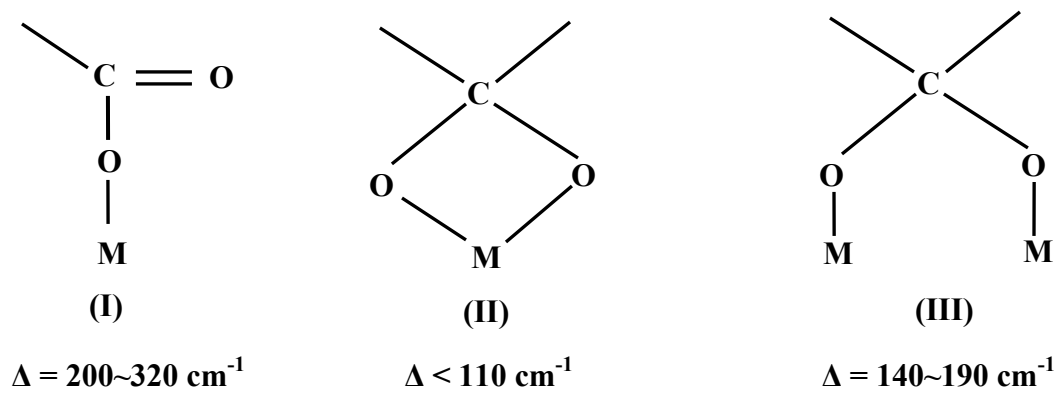
Figure 3-5. Modes of metal-carboxylate complexation: monodentate chelating (I), bidentate chelating (II), and bidentate bridging (III). Δ is the separation of the symmetric and asymmetric stretches of the carboxylate group.

Based on the FTIR results, it appears plausible that the stabilization of the clustered Fe nanoparticles is attributed to the adsorption of CMC molecules to the surface of the nanoparticles. The adsorption process results in the encapsulation of the nanoparticles with a thin layer of negatively charged CMC. It is this protective CMC layer that suppresses the growth of the iron nanoparticles and prevents the particles from agglomeration through the electrostatic repulsion and/or steric hindrance between the CMC-coated nanoparticles (O'Melia, 1972). In a recent study on the aggregation of agitate-coated nanoparticles (Chen et al., 2006), researchers observed that electrostatic or DLVO interactions were the primary mechanism for particle stabilization/aggregation. Consequently, the particle stabilization will be affected by the type and level of cations. In the presence of NaCl, the researchers observed a critical coagulation concentration (CCC) of 180 mM (Na^+), below which there exists a strong electrostatic barrier that prevents the negatively charged nanoparticles from agglomerating. In our study, the total concentration of Na^+ in the nanoparticle suspension ranged from 8.2 to 61.4 mM. In all cases, no electrostatic destabilization of the CMC-stabilized nanoparticles was evident.

3.3.3 Reactivity of CMC stabilized nanoparticles

The reactivity of the nanoparticles was investigated by testing the degradation of TCE. **Figure 3-6** shows the TCE degradation rates with various Fe-Pd particles. Considering that ethane is the primary final dechlorinated product (Liu et al., 2005b), the initial Fe (0.1 g/L) to TCE was 1.17, i.e. Fe was initially in excess in the batch kinetic tests. It is reported that pH is an important factor for iron nanoparticle reactivity (Song and Carraway, 2005).Varying pH from 9 to 6 can increase reactivity by an order of magnitude. In the current study, the initial solution pH for non-stabilized and CMC

stabilized Fe-Pd nanoparticle solution was ~6.8 and ~8.3 respectively. The pH change after TCE degradation reaction was < 0.2 pH unit below the corresponding initial pH in both cases.

Assuming that TCE degradation in the initial stage (<40 min) follows a pseudo-first-order reaction kinetics, the observed initial rate constant can be determined by fitting eqn. (3-1) to the experimental data,

$$-\frac{dC}{dt} = k_{obs}C = k_{SA}a_s\rho_m C \qquad (3\text{-}1)$$

where C is TCE concentration (mg L^{-1}) at time t (h), k_{obs} is the observed pseudo-first rate constant, k_{SA} is surface area-based rate constant (L h^{-1} m^{-2}), a_s is the DLS-based specific surface area of the nanoparticles (m^2 g^{-1}), and ρ_m is the mass concentration of the nanoparticles (g L^{-1}). **Figure 3-6(a)** reveals that the CMC stabilization enhanced the reactivity of the nanoparticles. When 0.2% CMC was added, the value of k_{obs} increased from 0.44 h^{-1} to 7.4 h^{-1} (a factor of 17). Nearly all TCE was destroyed within 40 minutes. Considering the pH difference between non-stabilized and stabilized Fe-Pd nanoparticle solution, the reactivity difference between these two particles could be even greater. Compared to the starch-stabilized Fe-Pd nanoparticles (He and Zhao, 2005), the fresh CMC-stabilized nanoparticles offered a two times greater k_{obs}. The k_{SA} value for CMC-stabilized nanoparticles was 1.0 L h^{-1} m^{-2} based on a DLS diameter of 11.0 nm.

(a)
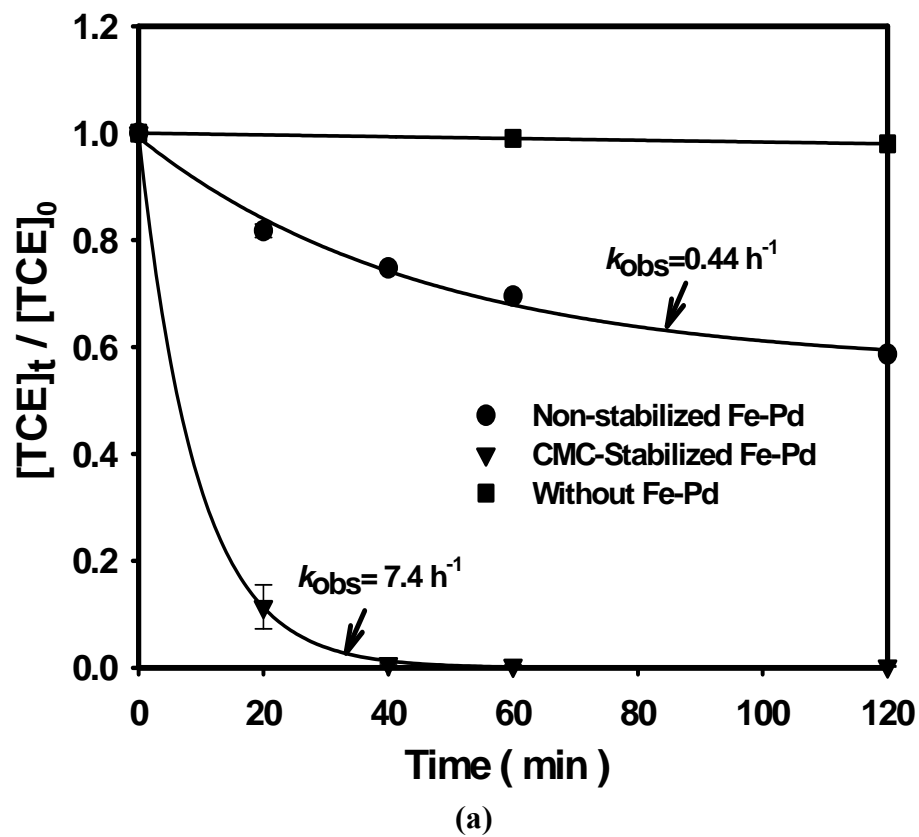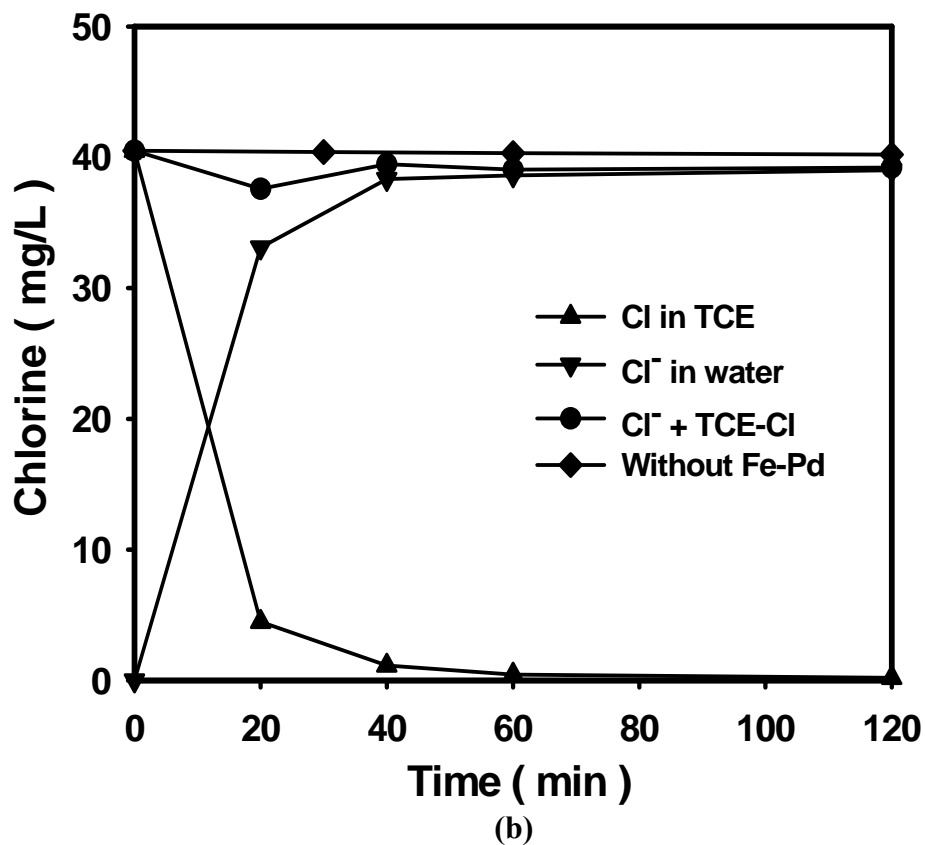
Figure 3-6. (a) Dechlorination of TCE using non-stabilized, or CMC-stabilized Fe-Pd nanoparticles. (b) Evolution of chloride and TCE-Cl during dechlorination of TCE using CMC-stabilized Fe-Pd nanoparticles. Initial TCE concentration = 50 mg L^{-1}. Iron dose = 0.1 g L^{-1} as Fe. Pd:Fe ratio = 0.1/100 (w/w). NaCMC = 0.2% (w/w).

It is well known that TCE degradation undergoes a series of reaction steps, and toxic intermediates such as vinyl chloride (VC) and dichloroethenes (DCE) must be eliminated rapidly, which justifies the pivotal importance of reaction kinetics in the environmental dechlorination processes. During the course of TCE degradation by CMC stabilized Fe-Pd nanoparticles, halogenated intermediates, such as VC, cis- or trans-DCE, were not detected. Trace amounts (~25 μg/L) of 1,1-DCE were detected in the initial stage of TCE degradation, however, it became non-detectable after 20 minutes. **Figure 3-6(b)** shows that the chloride production rate is nearly stoichiometrically coupled with TCE degradation rate during the two-hour degradation of TCE using the CMC-stabilized Fe-Pd nanoparticles (Note: TCE remaining is reflected by the amount of Cl that remains associated with TCE, denoted as TCE-Cl). The nearly perfect chlorine mass balance indicates the rapid and nearly complete dechlorination of TCE.

3.3.4 Soil mobility of CMC-stabilized nanoparticles

To preliminarily test the mobility of the CMC-stabilized and non-stabilized Fe-Pd nanoparticles in soil, simple column breakthrough and elution tests were carried out with a 2.7 mL loamy sand soil bed (obtained from Auburn, AL, USA) packed in a glass column (1 cm I.D.). The salient soil properties are as follows: porosity = 0.35; hydraulic conductivity = 0.25 cm/min; sand content = 84%; silt = 10%; clay = 6%. In the tests, a 2.7 mL portion of a 1 g L^{-1} Fe-Pd suspension (either stabilized with 0.8% (w/w) CMC or non-stabilized) were gravity-fed onto the soil bed and the eluents were collected at the bottom (**Figure 3-7 (a)**). After ~12 minutes, all the suspension was passed through the column (**Figure 3-7 (b)**). Then, ~3 bed volumes of deionized water were passed through the soil bed to elute the particles in the soil bed (**Figure 3-7 (c)**). **Figure 3-7** shows that

while the stabilized Fe-Pd nanoparticles were able to pass through and be completely dispersed in the soil bed, the non-stabilized Fe-Pd particles were retained on the top of the soil bed. When the exited Fe-Pd suspension was collected and analyzed for Fe, ~98% of the Fe introduced was recovered in the CMC-stabilized Fe-Pd suspension eluent, indicating that no nanoparticles were retained irreversibly. However, only ~ 0.2% of the non-stabilized Fe was detected in ~3 bed volumes of the effluent water.

In summary, this study demonstrated that carboxymethyl cellulose can be used for effective stabilization of zero-valent iron nanoparticles to yield stable dispersions with size smaller than 17.2 nm. Compared to non-stabilized iron nanoparticle aggregates, the stabilized nanoparticles displayed greater reactivity for TCE dechlorination, and are highly mobile in a sandy soil. This technology holds the promise to facilitate more effective applications of Fe-Pd nanoparticles for *in-situ* soil and groundwater remediation.
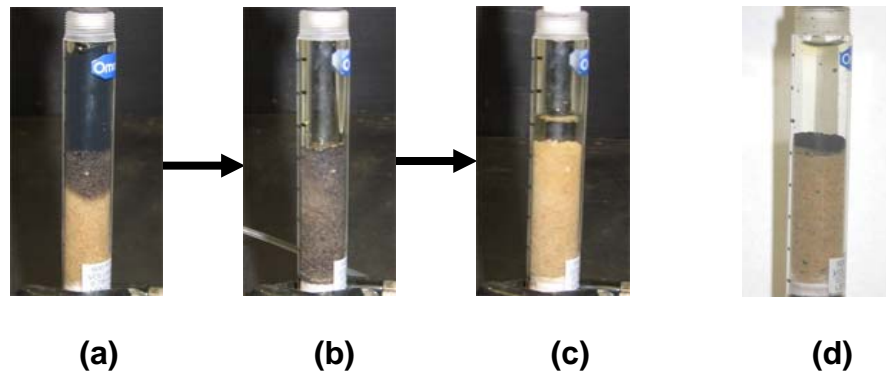
Figure 3-7. Transport of CMC-stabilized Fe-Pd nanoparticles **(a-c)** or non-stabilized Fe-Pd aggregates **(d)** through a loamy sand soil. Note: **(a)** 0.5 minute after 1 bed volume of 1 g/L stabilized Fe-Pd suspension was gravity-fed to the soil bed; **(b)** after all the suspension was passed through the bed; **(c)** after 3 bed volumes of DI-water was passed through the bed shown in **(b)**; and **(d)** after 1 bed volume of 1 g/L of non-stabilized Fe-Pd aggregates suspension was passed through the same soil bed.

CHAPTER 4. MANIPULATING THE SIZE AND DISPERSIBILITY OF ZERO-VALENT IRON NANOPARTICLES BY USE OF CARBOXYMETHYL CELLULOSE STABILIZERS

The soil mobility and dechlorination reactivity of iron nanoparticles are highly size-dependant. The size-controlled synthesis of iron nanoparticles is of great importance for potential effective application of this technology. In this chapter, manipulating the size and dispersibility of iron nanoparticles is practiced by controlling the synthesis conditions, such as iron stabilizer ratio, stabilizer molecular weight and degree of substitution, temperature, pH and ionic strength.

4.1 Introduction

Zero-valent iron (ZVI) particles of the nanometer to millimeter scale have been found effective in degrading various chlorinated hydrocarbons such as trichloroethene (TCE) (Su and Puls, 1999; Arnold and Roberts, 2000; Song and Carraway, 2005). However, field scale applications of ZVI have been limited to granular particles used in permeable reactive barriers (PRB) (Gavaskar et al., 1998; EPA, 1999). While PRBs are found effective for remediation of shallow aquifers, more cost-effective in situ technologies are lacking for rapid and complete destruction of chlorinated contaminants in deep aquifers and in source zones (Gavaskar et al., 2005).

For over a decade, researchers have been testing an in situ remediation strategy where reactive ZVI nanoparticles are directly delivered into the contaminant source zones (Vance, 2005). Compared to the passive technologies such as PRB, in situ active injection of ZVI particles offers some unique advantages, such as 1) applicable to source zones in deep aquifers or to areas where lands are occupied, and 2) much shorter overall remediation time (Wang and Zhang, 1997). However, for this technology to be feasible, the ZVI particles must be small enough (in the nano- to submicron scale) to be mobile in the targeted zones, and the transport behaviors (or size) of the nanoparticles in various soils must be controllable. Yet, there has been no technique available for preparing ZVI nanoparticles of controlled size and transport properties, and a method is lacking to extend the reactive lifetime of these relatively short-lived nanoparticles.

Three major techniques have been employed to prepare ZVI nanoparticles, including a) high-energy ball milling of metallic iron (Zhang, 2005), b) gas-phase reduction of iron oxides with H_2 (e.g. the reactive nano-iron-particles (RNIP) of Toda Kogyo Corporation, Onoda, Japan), and c) aqueous-phase reduction of iron salts with $NaBH_4$ (Wang and Zhang, 1997; Shen et al., 1993). While nano- or micron-scale ZVI particles have been reported to be attainable by these methods, it was recognized that ZVI nanoparticles tend to rapidly agglomerate to form larger aggregates due to Van der Waals and magnetic forces, rendering them undeliverable to the targeted contaminant locations (He and Zhao, 2005; He et al., 2007).

To prevent aggregation of metallic nanoparticles, particle stabilization has been commonly practiced by attaching a stabilizer such as a soluble polymer or surfactant onto the nanoparticles (Cushing et al., 2004). The attached stabilizer molecules are designed to

provide strong inter-particle electrostatic and/or steric repulsions to overweigh the attractive Van der Waals and magnetic forces. To stabilize ZVI nanoparticles, two general strategies have been employed: a) apply stabilizers before the nanoparticles or aggregates are formed (pre-agglomeration stabilization), or b) mechanically break down the formed nanoparticle agglomerates and add stabilizer (post-agglomeration stabilization). Schrick et al. used poly(acrylic acid) (PAA) for (pre-agglomeration) stabilizing Fe-based nanoparticles and observed improved transportability of PAA-stabilized ZVI nanoparticles in soils (Schrick et al., 2004). More recently, He and Zhao employed a food-grade starch and a CMC as pre-agglomeration stabilizers and obtained highly dispersed ZVI nanoparticles (He and Zhao, 2005; He et al., 2007). Saleh et al. synthesized triblock copolymers to (post-agglomeration) stabilize sonicated RNIP particles in aqueous suspension (Saleh et al., 2005).

In the conventional borohydride reduction method (Wang and Zhang, 1997; Shen et al. 1993), ZVI nanoparticles are prepared by reducing ferrous or ferric ions with borohydride in water. A number of physico-chemical processes can affect the formation and size of the resultant ZVI clusters, including inter-particle interactions and particle nucleation. In the absence of a stabilizer, the inter-particle attractive forces prevail, and thus, nanoparticles agglomerate rapidly. When a stabilizer is applied, the stabilizer molecules are adsorbed to the surfaces of the nanoparticles, preventing further agglomeration. In addition, the presence of a stabilizer may facilitate nucleation and growth of iron particles during the formation of nanoparticles (Shimmin et al., 2004). Therefore, the pre-agglomeration stabilization offers the advantage that particle size may be controlled by manipulating the particle synthesizing conditions such as concentration

64

and type of stabilizers, temperature and pH. Given the highly heterogeneous nature of natural soils, and considering that both soil mobility and dechlorination reactivity of ZVI nanoparticles are highly size-dependant, manipulating the size of ZVI nanoparticles offers profound practical convenience for in situ remediation uses.

The overall objective of this study was to investigate factors that affect the size of ZVI nanoparticles when CMC was used as a pre-agglomeration stabilizer. Specifically, the following key factors were investigated: 1) the CMC-to-Fe^{2+} molar ratio and the initial Fe^{2+} concentration; 2) CMC molecular weight and degree of substitution as well as stabilizer type; 3) synthesizing temperature and pH; and 4) concentration of common cations (Na^+ and Ca^{2+}) in water. The results from this study are expected to provide guidelines for controlling the size of ZVI nanoparticles, and thus, optimizing their performances (mobility and reactivity) when used for soil and groundwater remediation.

4.2 Experimental Section

4.2.1 Chemicals

The following chemicals were used as received: $FeSO_4 \cdot 7H_2O$ (Acros Organics, Morris Plains, NJ); sodium carboxymethyl cellulose (CMC): CMC90k (M.W. = 90k, D.S. = 0.7, Acros Organics), CMC250k (M.W. = 250k, D.S. = 0.7, Acros Organics), HP-5A (M.W. = 13k, D.S. = 0.78, Montello, Tulsa, OK), HP-7A (M.W. = 30k, D.S. = 0.74, Montello), and EP-ML (M.W. = 30k, D.S. = 1.2, Montello); 2-hydroxyethyl cellulose (M.W. = 90k, Sigma-Aldrich, St. Louis, MO); Poly(ethylene glycol)-*block*-poly(propylene glycol)-*block*-poly(ethylene glycol) or PEG-PPG-PEG (Mn 8000) (Sigma-Aldrich); a nonionic surfactant, Tween 80 (Sigma-Aldrich); hydrochloric acid

65

(Fisher, Fair Lawn, NJ); CaCl$_2$ (Fisher); Na$_2$SO$_4$ (Fisher); and sodium borohydride (NaBH$_4$, ICN Biomedicals, Aurora, OH).

4.2.2 Preparation of nanoparticles

Various stabilized ZVI nanoparticles were prepared by modifying the borohydride-reduction approach with a CMC as a pre-agglomeration stabilizer (He et al., 2007). In brief, the preparation was carried out in a 250 mL flask attached to a vacuum line. In a typical preparation, FeSO$_4$·7H$_2$O stock solution (10mL) was prepared right before use, and then added to the stabilizer solution (100 mL) to yield a desired concentration of Fe^{2+} and CMC. The mixture was then sparged with N$_2$ for 15 minutes to assure formation of Fe^{2+}-CMC complex and to remove dissolved oxygen. The final Fe^{2+} concentration used in this study was either 0.1 g/L or 1g/L.

ZVI nanoparticles were then formed by reducing Fe^{2+} ions using 10 mL of a borohydride solution (introduced at 5 mL/min) at a BH$_4^-$/Fe^{2+} molar ratio of 2.0. To ensure efficient use of BH$_4^-$, the reactor system was operated under anoxic conditions through continuously vacuuming. The reactor was shaken at 230 rpm until gas (hydrogen) evolution ceased (after ~15 min). The resultant nanoparticle suspension was then sampled and analyzed within one hour to obtain the mean particle size or size distribution.

4.2.3 Physical characterization

The mean hydrodynamic diameter of the prepared ZVI nanoparticles was determined with a dynamic light scattering (DLS) submicron particle sizer (Nicomp 380, PSS, Santa Barbara, CA) at a measurement angle of 90° (Internal He-Ne laser,

wavelength 633 nm). The DLS data were processed with a software package CW380 to yield the volume-weighted size distributions. In all measurements, at least duplicate samples (~1 mL each) of 0.1 g/L Fe were analyzed. Freshly prepared samples of 1 g/L Fe were first diluted to 0.1g/L before the analysis. In this paper, all data on particle size are given as mean ± standard deviation.

In addition, selected samples (fresh) were also dried overnight on Formvar-carbon-coated copper grids under nitrogen gas, and TEM micrographs of the dried ZVI nanoparticles were obtained using a Zeiss EM10 Transmission Electron Microscope (Zeiss, Thornwood, NJ). The TEM images were then processed with a specialty software known as ImageJ to give the mean particle size and size distributions. Detailed procedures on TEM analyses have been described elsewhere (He and Zhao, 2005).

4.2.4 Analytical methods

The viscosity of solution containing various types or concentrations of CMC was measured using a Gilmont falling ball viscometer (Pole-Parmer, Vernon Hills, IL). Total iron concentration in various nanoparticle suspensions was analyzed with a flame atomic-absorption spectrophotometer (AAS) (220FS, Varian, Palo Alto, CA). Before the iron analysis, the ZVI nanoparticles were digested with 2M HCl for ~5 min, which was enough to fully dissolve the nanoparticles.

4.3 Results and Discussion

4.3.1 Effect of CMC-to-Fe^{2+} molar ratio on particle size

CMC molecules can be adsorbed to the surface of ZVI nanoparticles, resulting in a layer of negative charges, and thereby, preventing the nanoparticles from agglomeration (He et al., 2007). Our prior FTIR results (He et al., 2007) indicated that both carboxymethyl groups and hydroxyl groups of CMC can interact with ZVI nanoparticles. Consequently, the concentration of CMC in the solution is expected to affect the growth and aggregation of ZVI nanoparticles.

Figure 4-1 shows the volume-weighted mean hydrodynamic diameter and size distribution of ZVI nanoparticles synthesized in the presence of a CMC (M.W. = 90,000) and at various CMC-to-Fe^{2+} molar ratios with a fixed Fe^{2+} concentration of 0.1 g/L. At a CMC-to-Fe^{2+} molar ratio of 0.0124, the volume-weighted distribution consisted primarily (81.0%) of particles of 18.6 nm in diameter, although large aggregates with diameter around 161 nm (5.1%) and 1460 nm (13.9 %) were also observed.

When the CMC-to-Fe^{2+} molar ratio was increased to 0.0186, the mean hydrodynamic diameter of the primary (89.5%) ZVI nanoparticles decreased to 17.6 nm, and the size distribution of the ZVI nanoparticles became narrower (**Figure 4-1**). In this case, no aggregates greater than 1 μm were detected. When the CMC-to-Fe^{2+} molar ratio was further increased to 0.0248, the primary (90.3%) nanoparticles became even smaller (15.3 nm). Conversely, when the CMC-to-Fe^{2+} molar ratio was reduced to 0.0062, ~92.4% of the ZVI particles aggregated to greater than 3 μm.
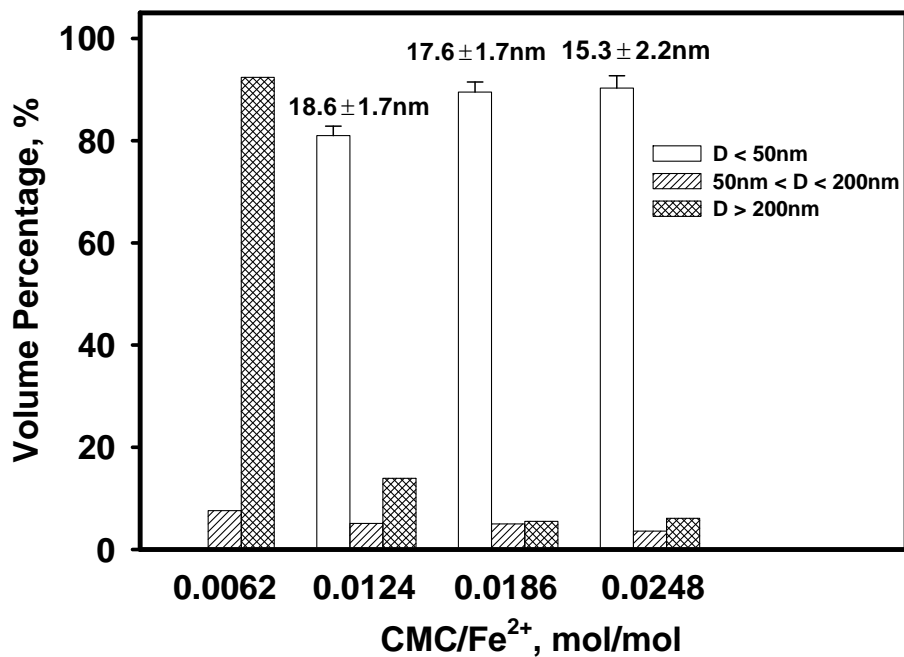
Figure 4-1. Size distribution of ZVI nanoparticles synthesized at various CMC-to-Fe^{2+} molar ratios with a fixed Fe^{2+} concentration of 0.1 g/L (CMC M.W. = 90k, temperature = ~22°C).
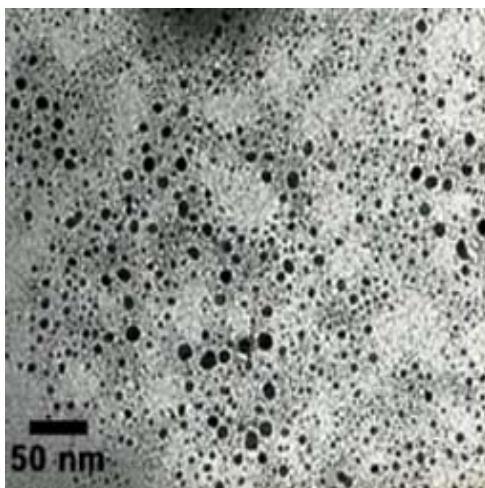
(a)
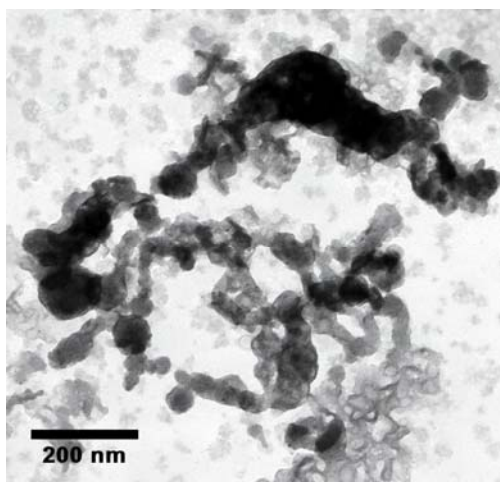
(b)

Figure 4-2. TEM images of nitrogen-dried ZVI nanoparticles: (a). freshly prepared at 0.1 g/L Fe and in the presence of 0.2% (w/w) CMC (M.W. = 90k) or at CMC-to-Fe^{2+} ratio = 0.0124, and (b). in the presence of 0.1% (w/w) CMC (M.W. = 90k) or at CMC-to-Fe^{2+} ratio = 0.0062. The scale bar represents 50 nm in (a) and 200 nm in (b). In image processing, optimal segmentation threshold = 84, and minimum circularity = 0.5.

Figure 4-2 compares the TEM images of the ZVI nanoparticles prepared at a CMC-to-Fe^{2+} molar ratio of 0.0124 (a) and 0.0062 (b). The particles prepared in case (a) appear as discrete nanoparticles with an average size of 4.3±1.8 nm (**Figure 4-2a**), while much larger aggregates were formed at the lower CMC-to-Fe^{2+} ratio (**Figure 4-2b**), indicating a minimum CMC-to-Fe^{2+} ratio is required to achieve effective particle stabilization. Note that the DLS-based particle size of the same nanoparticles prepared at the CMC-to-Fe^{2+} ratio of 0.0124 was 18.6 nm. This discrepancy is due in part to that TEM measures only the electron-dense metal core, while DLS measures both the core and CMC molecules attached thereto (Zheng et al., 2002). The hydrodynamic diameter of the nanoparticles in case (a) did not show any increase over a 7-day period, after which the 0.1g/L nanoparticles were nearly completely oxidized by water under ambient conditions.

Shimmin et al. (2004) investigated the effect of thiol-terminated poly(ethylene glycol) as a stabilizer on the size of Au nanoparticles and suggested that the key effect of the stabilizer on the nanoparticle size lies in the initial particle nucleation stage. They indicated that through weak coordination between Au(0) and the lone pair electrons of the stabilizer, the polymeric structure of the stabilizer enhanced the growth of the attached particles (nucleation) by serving as a 'net' capturing additional gold atoms, which resulted in formation of a larger number of smaller particles. They also claimed that steric hindrance of the capped polymer becomes important only after relatively mature nanoparticles are formed (i.e. after the nucleation is completed). The same argument appears plausible for stabilization of ZVI nanoparticles by CMC. Because of the high Fe^{2+}-complexation capacity of the CMC molecules, Fe^{2+} ions are attracted to and

confined in the network of the CMC molecular structure before they are reduced by borohydride. When the reduction of Fe^{2+} is initiated, nucleation of Fe atoms will take place through formation of multiple nuclei, which are the core for the birth of 'mature' ZVI nanoparticles. However, a thermodynamically stable and a mature nanoparticle can only be formed when a nucleus grows into a cluster that is larger than a certain critical size. Therefore, a fast initial nucleation is critical to the production of stable nuclei and subsequently smaller nanoparticles. Because of the strong "netting' effect of CMC molecules as in the case of Au nanoparticles (Shimmin et al., 2004), the growth of the complexed Fe clusters is accelerated by rapidly supplying Fe atoms to the unstably small Fe clusters before they disintegrate. Later, when the nuclei grow into larger and more stable nanoparticles, CMC molecules become attached to the particle surface, preventing further growth of the nanoparticles through electrostatic repulsion and steric hindrance. When the CMC concentration is insufficient, the effect on the nucleation is insignificant and the amount of CMC adsorbed to the particle surface is not enough to resist the inter-particle attractive forces. As a result, larger aggregates are formed as shown in **Figure 4-2b**.

Figure 4-3 shows that at a 10 times greater concentration of Fe^{2+} (1 g/L), nanoparticles with a mean diameter of 22.8 nm (84.0%) were obtained with a CMC-to-Fe^{2+} molar ratio of as low as 0.0031. Comparing the results in **Figures 4-1** and **4-3** reveals that the stabilization of ZVI nanoparticles by CMC is more effective at higher iron concentrations. Given that nucleation of Fe atoms is accelerated at elevated reagent concentrations (Fe^{2+} and BH_4^-), this observation agrees with the notion that faster growth of large numbers of nuclei favors production of more and smaller nanoparticles. When

the CMC-to-Fe^{2+} ratio was increased further to 0.005 (**Figure 4-3**), the size of primary (89.9%) nanoparticles was decreased to 19.6 nm, and the fraction of particles greater than 50 nm was reduced to 10.1%, which is consistent with the observation in **Figure 4-1** that the higher CMC-to-Fe^{2+} ratio, the smaller and more monodisperse the nanoparticles. More effective stabilization of Ag nanoparticles by CMC (Magdassi et al., 2003) or a surfactant (DAXAD19) (Sondi et al., 2003) in aqueous solution was reported at higher Ag^{+} concentrations.

4.3.2 Effect of CMC molecular weight and degree of substitution

To examine the influence of the chain conformation of CMC molecules on the particle size, ZVI nanoparticles were synthesized in the presence of a CMC of various M.W. and/or D.S. Four representative CMC's were tested for the effect of M.W., including HP-5A, HP-7A, CMC90k and CMC250k. Various concentrations of a CMC were tested for stabilizing Fe nanoparticles at a fixed Fe^{2+} concentration of 0.1 g/L. To compare the permeability of the resultant nanoparticles, the nanoparticle suspension from each synthesis was passed through a Fisher P5 filter paper (particle retention: >1 μm). The effluent Fe concentration history during the filtration was followed and plotted in **Figure 4-4**. Evidently, on an equal weight basis, CMC with greater M.W. is more effective in stabilizing ZVI nanoparticles. For example, it requires 1% of HP5A but only 0.12% of CMC250k to achieve 90% of particle passage.
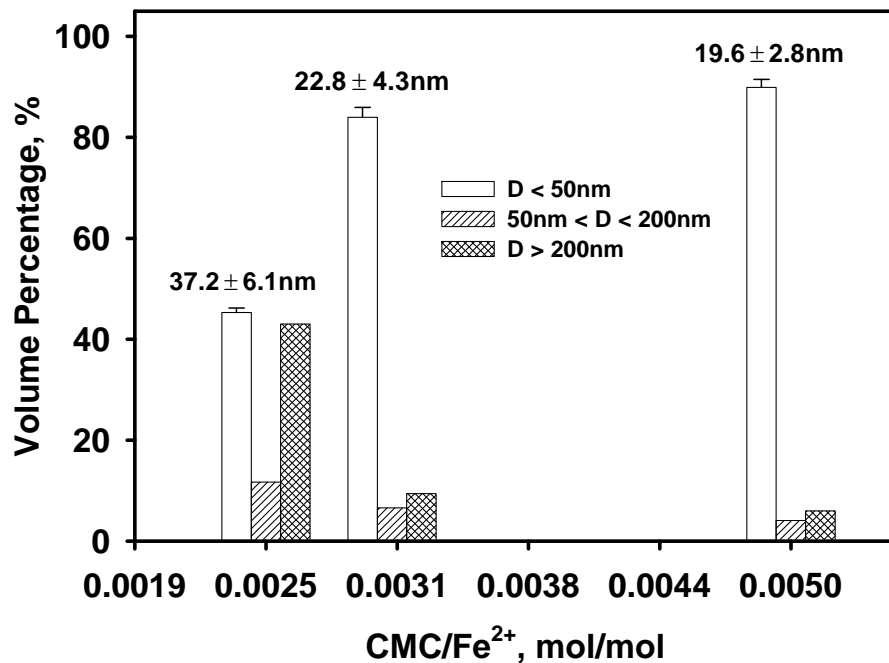
Figure 4-3. Size distribution of ZVI nanoparticles synthesized at various CMC-to-Fe^{2+} molar ratios and at a fixed Fe^{2+} concentration of 1 g/L (CMC M.W. = 90k, temperature = ~22°C).
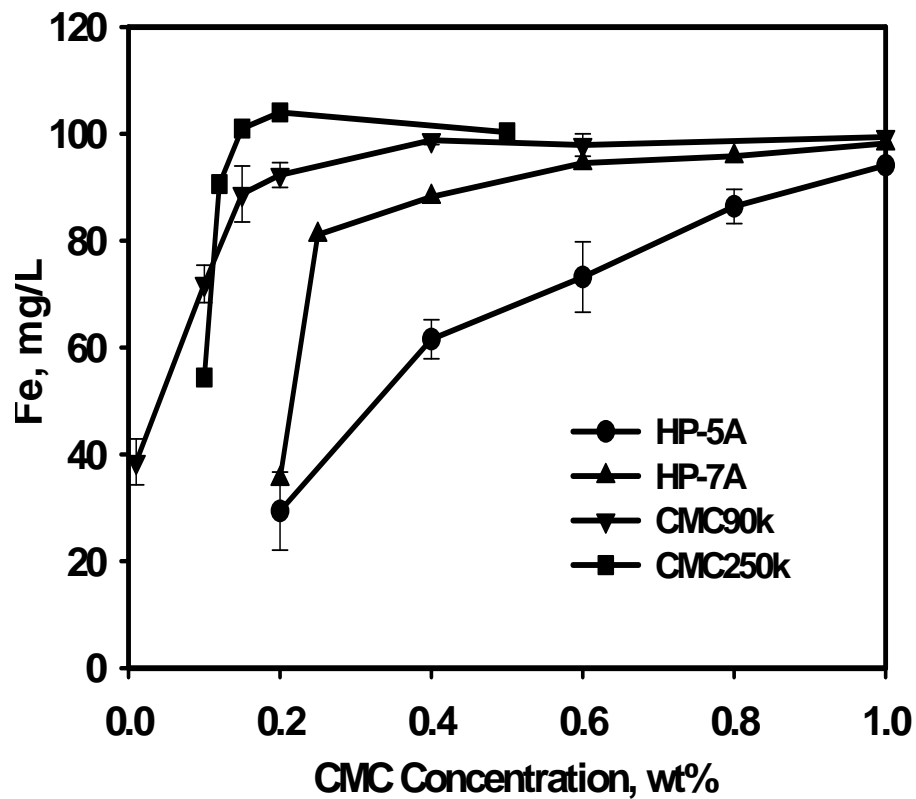
Figure 4-4. Passage of ZVI nanoparticles stabilized with various types and at various concentrations of a CMC through a Fisher P5 filter paper. ZVI nanoparticle concentration before filtration was 100 mg/L in all cases.
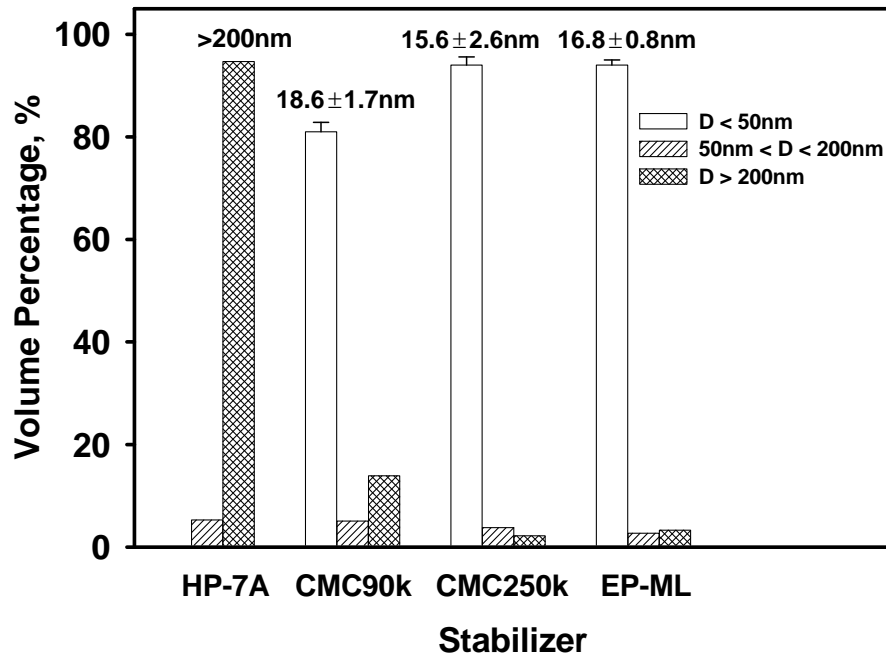
Figure 4-5. Size distribution of ZVI nanoparticles stabilized with CMC of various molecular weight and degree of substitution (Fe = 0.1 g/L, CMC = 0.2% (w/w), temperature = ~22°C).

Figure 4-5 shows that at a fixed CMC concentration of 0.2% (w/w), a CMC with greater M.W. results in smaller ZVI nanoparticles and smaller fractions of larger aggregates (>50 nm). This observation again conforms to the theory by Shimmin et al. (2004). A CMC with greater M.W. exerts stronger 'netting' effects, and thus, more effectively enhances the particle nucleation at the early stage of iron reduction. Once the nanoparticles are formed, CMC molecules are attached to the surface of the ZVI nanoparticles. The larger the CMC molecules, the stronger the repulsive forces as well as the steric hindrance.

Although both -COO⁻ groups and -OH groups of CMC are involved in interacting with the ZVI nanoparticles (He et al., 2007), the -COO⁻ groups are expected to play a more profound role in the particle stabilization for their known stronger binding power with metals. Because the pH (~6.2) of CMC-Fe^{2+} solution (0.2% CMC, 0.1 g/L Fe^{2+}) is higher than the pKa (~4.3) value of CMC, the -COO⁻ groups of CMC are almost fully disassociated, and thus, can interact strongly with the Fe^{2+} cations (Lewis acids). Therefore, the number or density of -COO⁻ groups in a CMC molecule (i.e. D.S.) is expected to affect the ZVI stabilization. To test the effect, three CMC's with similar M.W. of 90k-95k and matrices but different D.S. (CMC90k with a D.S. of 0.7, EP-ML with a D.S. of 1.2, and 2-hydroxyethyl cellulose with no -COO⁻ groups) were compared under otherwise identical conditions. As expected, EP-ML turned out to be more effective than CMC90k and resulted in smaller and more monodisperse nanoparticles (16.0 nm at 94.0% vs 18.6 nm at 81.0%, **Figure 4-5**). While both CMC90k and EP-ML were able to produce highly stable, black suspension of ZVI nanoparticles, a dark green color appeared when $NaBH_4$ was added to the solution containing 2-hydroxyethyl

cellulose and Fe^{2+}, and then large precipitates were observed. Evidently, the -OH groups in the celluloses alone cannot facilitate adsorption of sufficient cellulose molecules onto the nanoparticles. In addition, 2-hydroxyethyl cellulose is much less water soluble (more hydrophobic) compared to the CMC molecules containing $-COO^-$ groups. As the hydrophobic polymer molecules tend to leave water, ZVI nanoparticles associated with the macromolecules would also aggregate. Ditsh et al. studied the stability of Fe oxide nanoparticles stabilized with copolymers and found that to achieve maximum stabilization, stabilizers of greater M.W. are needed if the polymers are more hydrophobic (Ditsch et al., 2005). From a practical viewpoint, application of more hydrophobic stabilizers may promote dissolution and subsequent destruction of the targeted hydrophobic chlorinated solvents by ZVI nanoparticles. Earlier, Saleh et al. reported that several triblock copolymers were able to stabilize commercial Fe^0 (RNIP) nanoparticles and promote particle-solvent contact (Saleh et al., 2005). Our work reveals that to facilitate the optimum stabilization and Fe-solvent contact, a novel stabilizer should offer a delicate architecture with a careful design of hydrophobic-hydrophilic entities as well as well balanced molecular size (weight). For example, we observed that a commercial triblock copolymer (PEG-PPG-PEG) and a surfactant (Tween 80) were not effective for stabilizing the ZVI nanoparticles (data not shown).

4.3.3 Effect of temperature

Figure 4-6 shows that the size of the ZVI nanoparticles is quite sensitive to the solution temperature during the formation of the nanoparticles. Smaller (13.2 nm) and nearly monodisperse (95.0%) nanoparticles were obtained at ~8 ^{o}C. The higher the temperature, the larger and more polydisperse nanoparticles were obtained. At temperatures of 25°C and 30 ^{o}C, the particles of >200 nm accounted for 83.6% and 95.3%, respectively. Solution temperature can affect the reduction of Fe^{2+}, nucleation of Fe atoms/clusters, ZVI-CMC interactions and particle aggregation rate. Sodium borohydride is a strong reducing agent and the reduction of Fe^{2+} is a fast process under mixing. Thus, the change in temperature should not alter the reduction rate to any significant extent (Shen et al., 1993; Liu et al., 2006b). Temperature can affect nucleation and particle growth in several ways. One is that particle growth is usually slower at lower temperatures (Zhou et al., 2002). On the other hand, lower temperatures favor the kinetic stabilization process during nucleation, and promote the growth of unstable smaller nuclei to larger and more stable nano-clusters (Zhou et al., 2002). In addition, at elevated temperatures, sorption of CMC molecules to the nanoparticles is reduced. This effect is comparable to the effect of decreasing the CMC-to-Fe ratio at a given temperature. Jorgensen et al. reported the similar temperature effect on particle size and polydispersivity of alkylthiol-stabilized Au nanoparticles (Jorgensen et al., 2005), and they attributed this effect to the reduced sorption of alkylthiol on the nanoparticles at elevated temperatures.
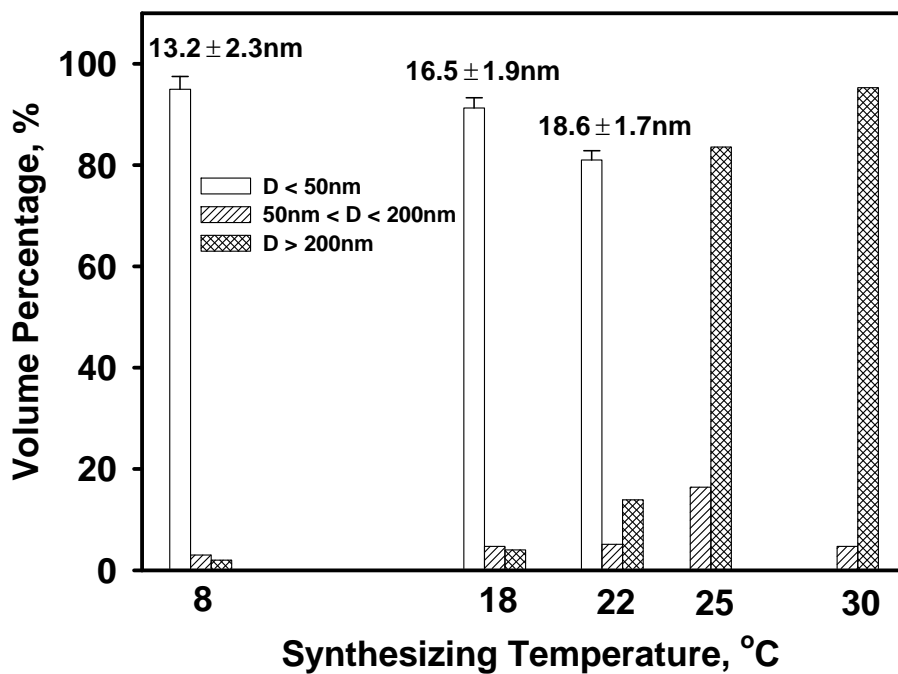
Figure 4-6. Size distribution of CMC-stabilized ZVI nanoparticles prepared at different temperatures (Fe = 0.1 g/L, CMC90k = 0.2% (w/w)).

4.3.4 Effect of pH

The pH value of the CMC-Fe^{2+} solution (0.2% w/w NaCMC (M.W. = 90k) and 0.1 g/L Fe^{2+}) was around 6.2. To test the effect of solution pH, ZVI nanoparticles were prepared based on the same solution but at different solution pH values. The concentration of the resultant ZVI nanoparticles was then measured and compared based on the UV-Vis absorbance of the nanoparticle suspensions at a wavelength of λ=508 nm. The UV-Vis absorbance was found to be a convenient measure for representing the concentration of suspended ZVI nanoparticles in water (Saleh et al., 2005).

When BH_4^- is introduced into the CMC-Fe^{2+} solution, the following two competitive reactions will take place:

$$BH_4^- + H^+ + 3H_2O \longrightarrow H_3BO_3 + 4H_2 \uparrow \qquad (4\text{-}1)$$

$$BH_4^- + 2Fe^{2+} + 4H_2O \longrightarrow 2Fe \downarrow + B(OH)_4^- + 4H^+ + 2H_2 \uparrow \qquad (4\text{-}2)$$
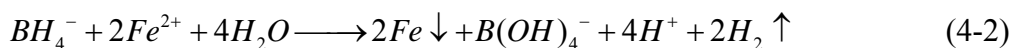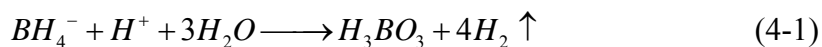
Eqn. (1) indicates that pH or H^+ activity can impact the reduction of Fe^{2+}. At a lower pH ($\leq$6.2), reduction of H^+ is more favored than Fe^{2+} because of the greater electrode potential of $2H^+/H_2$ over that of Fe^{2+}/Fe^0 (Shen et al., 1993). As reduction of H^+ proceeds, the solution pH goes up. When the solution pH reaches 7.3 or higher, reduction of Fe^{2+} becomes more favored (Shen et al., 1993). Thus, a lower pH would consume more BH_4^-, leading to a lower yield of the ZVI nanoparticles. At an initial pH (pH_0) 3.9, the UV-Vis absorbance of the final particle suspension was nearly zero (0.01), indicating that nearly all BH_4^- ions, added at a BH_4^--to-Fe^{2+} molar ratio of 2.0, were consumed by H^+ reduction (eqn. (4-1)), which resulted in a final pH (pH_f) of 6.3. When pH_0 was increased to 4.9, a strong UV-Vis absorbance of 1.40 was observed with a pH_f of 8.1.

Further, at pH_0 6.2, the absorbance was increased to 2.02 (pH_f = 8.4), indicating the reduction of Fe^{2+} was more efficient at pH_0 6.2 although the size of the resultant nanoparticles was comparable (17.9 nm at pH_0 = 4.9 vs 18.6 nm at pH_0 = 6.2).

When pH_0 of the CMC-Fe^{2+} solution was further increased to 8.0, the solution color changed to green instantly, suggesting formation of iron hydroxides (e.g. $Fe(OH)_2$). Upon introduction of borohydride (pH_f = 8.6), the solution turned to dark-green rather than the expected black ZVI, implying that Fe species other than ZVI were formed in the suspension. Apparently, the formation of iron hydroxides diminished the reduction of Fe^{2+} and nucleation of Fe atoms, and thus, the yield of ZVI nanoparticles. Since the resultant particles are no longer pure ZVI nanoparticles, the UV-Vis absorbance and particle diameter were not measured.

4.3.5 Effect of cations

According to the classical double-layer and colloid stability theories (O'Melia, 1972), particle stability can be affected by the valence and concentration of cations (coagulants). In this study, effects of Na^+ and Ca^{2+} were investigated on the CMC solubility and the following ZVI particle stabilization.

First, the presence of elevated concentrations of salts was found to reduce the water solubility of CMC. For example, in the presence of 20 mM Na^+, 0.24% CMC (M.W. = 90k) was fully dissolved in water. However, when the Na^+ concentration was increased to 100 mM, a fraction of the CMC remained undissolved. Second, when Ca^{2+} is added into a CMC (in sodium form) solution, Na^+ ions are replaced by the divalent cations, resulting in CMC-metal precipitates. Indeed, in the presence of 5 mM of Ca^{2+}, CMC-metal precipitates were clearly observed.

82
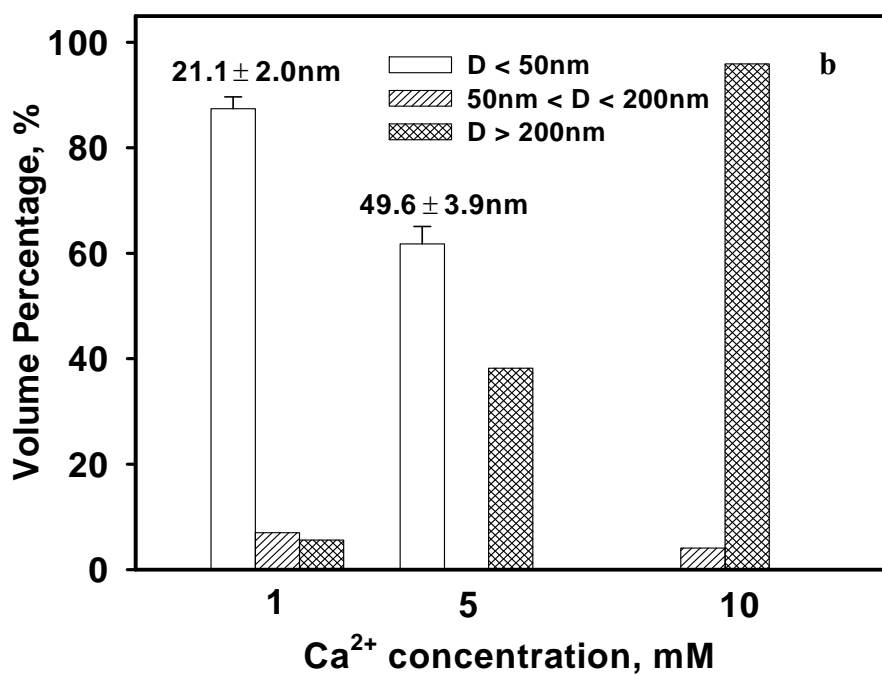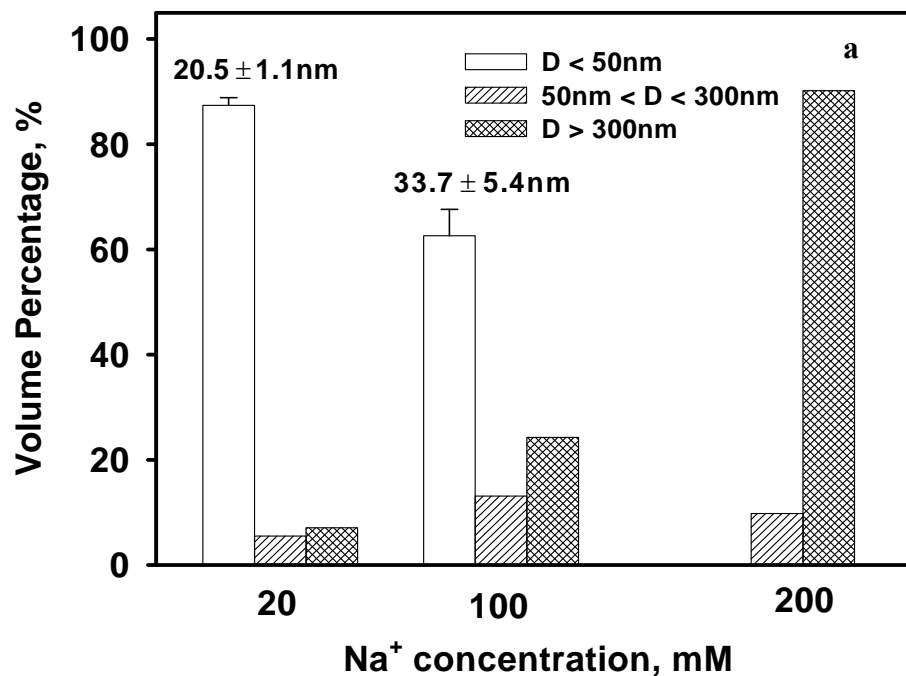
Figure 4-7. Size distribution of ZVI nanoparticles prepared in the presence of various concentrations of Na^+ **(a)** or Ca^{2+} **(b)** (Fe = 0.1 g/L, CMC90k = 0.2% (w/w), temperature = ~22°C, Na^+ was added as Na_2SO_4 and Ca^{2+} as $CaCl_2$).

Figure 4-7 shows the size distribution of ZVI particles prepared at various concentrations of Na^+ or Ca^{2+}. In the presence of 20 mM Na^+, the Fe suspension has a primary (87.4%) particle size of 20.5 nm, slightly larger than that when no Na^+ salt was added. An increase of Na^+ concentration to 100 mM increased the primary (62.6%) particle size to 33.7 nm. At Na^+ = 200 mM, aggregates larger than 3 μm accounted for ~90.2% of the particles. As expected, divalent cations are much more efficient coagulants. In the presence of only 5 mM of Ca^{2+}, nearly 40% of the ZVI particles were greater than 200 nm.

When the concentration of Na^+ is below 100 mM, the CMC is fully soluble. Therefore, the increased aggregation at elevated Na^+ concentration is attributed to compression of the diffusion layer on the nanoparticles. In a recent study on the aggregation of alginate-coated hematite nanoparticles, Chen et al. observed a critical coagulation concentration (CCC) of 180 mM (Na^+), below which there exists a strong electrostatic barrier that prevents the negatively charged nanoparticles from agglomerating (Chen et al., 2006). In this study, the CCC for the ZVI nanoparticles appears to be lower. The incomplete dissolution of CMC in high-Na^+ water and the different molecule properties between CMC and alginate may account for the difference. Based on Figure 7 and work by others (Chen et al., 2006), the effect of Cl^- and SO_4^{2-} is negligible in the concentration range compared to that of the cations.

4.3.6 Implications for in situ remediation

The CMC-stabilization strategy for manipulating the size of ZVI nanoparticles may facilitate more effective applications of ZVI nanoparticles for in situ dechlorination in soils and groundwater. Given the diversity in soil conditions (e.g. porosity,

conductivity, and groundwater flow rate, and sticking coefficient), it is critical to control the size of ZVI particles to assure effective delivery and subsequent dechlorination. This study showed that highly stable ZVI nanoparticles of desired size can be prepared by applying a CMC stabilizer and by manipulating synthesizing conditions. While details on the effects of CMC on the reactivity of the stabilized nanoparticles are yet to be investigated, our prior study (He et al., 2007) indicated that the CMC-stabilized nanoparticles degraded TCE >17 times faster than the non-stabilized counterparts. From a practical standpoint, it is recommended that the nanoparticles be prepared on-site and applied as soon as possible to assure maximum usage of the reactivity of the nanoparticles.

CHAPTER 5. HYDRODECHLORINATION OF TRICHLOROETHENE USING STABILIZED FE-PD NANOPARTICLES: REACTION MECHANISM AND EFFECTS OF STABILIZERS, CATALYSTS AND REACTION CONDITIONS

In this chapter, we investigated the effect of iron stabilizer ratio, stabilizer molecular weight, pH, and ionic strength on the reactivity of the stabilized Fe-Pd nanoparticles. A mechanism on TCE reduction by stabilized Fe-Pd nanoparticles was proposed.

5.1 Introduction

Nanoscale zero-valent iron (ZVI) has attracted growing attention in the past decade or so for remediation of groundwater and soils contaminated with chlorinated solvents (He and Zhao, 2005; He et al., 2007; Liu et al., 2005b; Nurmi et al., 2005; Schrick et al., 2002; Song and Carraway, 2005; Wang and Zhang, 1997; Wei et al., 2006; Wu and Ritchie, 2006; Xu and Bhattacharyya, 2007), heavy metals (Ponder et al., 2000; Xu and Zhao, 2007), arsenic (Kanel et al., 2005; Kanel et al., 2006), nitrate (Liou et al., 2006) and perchlorate (Xiong et al., 2007). Compared to conventional granular iron particles, ZVI nanoparticles offer the advantage of being deliverable into contaminated soils, and thus, can be applied in situ. This advantage can potentially eliminate the need for excavation, and relieve remediation practices from the limitations of depth, site topography, and facility operations. Another potential advantage of ZVI nanoparticles is their high reactivity. The degradation rate of the target contaminants determines the site

cleanup time and consequently the remediation cost. It was reported that ZVI nanoparticles can degrade TCE one order of magnitude faster than iron filings (Schrick et al., 2002). However, because of the very high surface energy, ZVI nanoparticles tend to agglomerate in water rapidly to form micron-scale or larger aggregates, thereby losing their soil mobility and reactivity (He and Zhao, 2005; Li et al., 2006; Saleh et al., 2005; Schrick et al., 2004). For example, the mass-normalized rate constant for dechlorination of trichloroethene (TCE) by aggregated ZVI nanoparticles was reported only in the order of 10^{-2} L g^{-1} h^{-1} (Schrick et al., 2002; Liu et al., 2005b).

To enhance the reactivity of ZVI nanoparticles toward chlorinated solvents, researchers plated trace amounts of a metal catalyst such as Pd, Ni, and Pt onto the ZVI particles, resulting in various bimetallic nanoparticles (He and Zhao, 2005; Schrick et al., 2002; Wang and Zhang, 1997; Wu and Ritchie, 2006; Xu and Bhattacharyya, 2007). Numerous studies have demonstrated that the iron-based bimetallic particles can degrade chlorinated hydrocarbons such as TCE in water much faster than monometallic ZVI particles (Cwiertny et al., 2006; Lien and Zhang, 2001).

Reduction of chlorinated compounds by bimetallic particles is a hydrodechlorination process, where Fe acts as the electron source, and the metal additive as a catalyst. Consequently, the metal additive's capacity to generate and sorb the reactive atomic hydrogen determines the dechlorination reactivity (Cwiertny et al., 2006; Kim and Carraway, 2003a; Lin et al., 2004; Schrick et al., 2002). Researchers claimed that the galvanic couples formed between iron and a metal additive are critical for the generation of the reactive atomic hydrogen in the bimetallic systems (Lin et al., 2004; Schrick et al., 2002). On the other hand, Cwiertny et al. (2006) pointed out that the rate of

Fe corrosion is related to the specific properties and loadings of the metal additives. However, it remains unclear how the metal additives affect the TCE reduction with ZVI-Me (Me = a metal catalyst) nanoparticles.

Our recent work (He and Zhao, 2005; He et al., 2007; He and Zhao, 2007a) indicated that applying a stabilizer not only prevents aggregation of ZVI nanoparticles, but also results in enhanced overall degradation effectiveness due to the greater specific surface area of finer nanoparticles. To this end, some water-soluble polysaccharides (e.g. starch and cellulose) have shown themselves to be among the best stabilizers for their low cost and environmental compatibility. Moreover, it was demonstrated that the stabilizers can be used to regulate the iron nucleation and particle growth during the nanoparticle formation and effectively prevent agglomeration of the resultant ZVI nanoparticles (He and Zhao, 2007a), thus providing a convenient means for manipulating the size and reactivity of ZVI nanoparticles. Yet, detailed investigation into the effect of particle stabilization on the dechlorination reactivity has been lacking. Moreover, as many other factors such as pH, the type and amount of metal additives have been reported to affect the reactivity of non-stabilized bimetallic ZVI nanoparticles (Zhang et al., 1998; Wei et al., 2006), effects of these factors on the particle reactivity in the presence of a stabilizer have not been investigated, and our knowledge on the catalytic degradation of TCE is rudimentary.

The overall objective of this study was to investigate the effects of stabilizers, metal additives, pH and ionic strength on the reactivity of CMC-stabilized bimetallic nanoparticles and to elucidate the underlying TCE reduction mechanisms. Sodium carboxymethyl cellulose (CMC) of various molecular weights (M.W.) were tested as

model stabilizers. The following key factors were investigated: 1) CMC/Fe^{2+} molar ratio and CMC M.W.; 2) loading and type of a metal catalyst; and 3) reaction pH and ionic strength. Moreover, a conceptual model was proposed to elucidate the TCE reduction mechanism with the stabilized bimetallic nanoparticles.

5.2 Experimental Section

5.2.1 Chemicals

The following chemicals were used as received: FeSO$_4$·7H$_2$O (Acros Organics, Morris Plains, NJ, USA); sodium carboxymethyl cellulose (CMC): CMC90k (M.W. = 90k, Degree of Substitution D.S. = 0.7, Acros Organics), CMC250k (M.W. = 250k, D.S. = 0.7, Acros Organics), HP-5A (M.W. = 13k, D.S. = 0.78, Montello, Tulsa, OK, USA); sodium borohydride (NaBH$_4$, ICN Biomedicals, Aurora, OH, USA); Na$_2$PdCl$_4$·3H$_2$O (99%, Strem Chemicals, Newburyport, MA, USA); trichloroethylene (TCE) (>99%, spectrophotometric grade, Aldrich, Milwaukee, WI, USA); hexane (pesticide grade, Fisher, Fair Lawn, NJ, USA); nickel chloride (Fisher); copper chloride dihydrate (Acros Organics); H$_2$PtCl$_6$·6H$_2$O (99.9%, Acros Organics) and HEPES buffer (Fisher).

5.2.2 Preparation of nanoparticles

Various stabilized ZVI nanoparticles were prepared by modifying the borohydride-reduction approach using various CMCs as a stabilizer (He et al., 2007; He and Zhao, 2007a). In brief, the preparation was carried out in a 250 mL flask attached to a vacuum line. In a typical preparation, 10 mL freshly prepared stock solution of 0.21 M FeSO$_4$·7H$_2$O was added to 100 mL of a CMC solution, resulting in a desired concentration of Fe^{2+} and CMC (0-1.0 wt.%). The mixture was then sparged with N$_2$ for

15 minutes to assure formation of Fe^{2+}-CMC complex and to remove dissolved oxygen (DO).

ZVI nanoparticles were then obtained by reducing Fe^{2+} ions using 10 mL of a borohydride solution (introduced at 5 mL min^{-1}) at a BH_4^--to-Fe^{2+} molar ratio of 2.0, which was equivalent to the stoichiometric amount. The final ZVI concentration was 0.1 mg L^{-1}. To ensure efficient use of BH_4^-, the reactor system was operated under anoxic conditions through continuously vacuuming. Following the addition of BH_4^-, the reactor was shaken at 230 rpm for 5 min, and left still for 10 more minutes. Then, the Fe nanoparticles were either tested as monometallic particles or loaded with trace amounts (up to 0.2 wt.% of Fe) of a second metal (Pd, Pt, Ni or Cu) to yield the CMC-stabilized bimetallic nanoparticles. The loading was accomplished by adding known quantities of a metal salt into the CMC-stabilized ZVI nanoparticle suspension (He and Zhao, 2005). To test the effect of residual H_2 from the nanoparticle preparation, select nanoparticle suspensions were sparged with N_2 for 5 min to remove the residual H_2, and then tested. In all cases, the degradation tests were performed within five minutes after preparation. To test pH effect, TCE degradation tests were also carried out at various pH levels (6.0 - 9.0) in the presence of 50 mM of HEPES buffer.

To probe the role of Pd in TCE degradation with the stabilized Fe-Pd nanoparticles, CMC-stabilized mono-metallic Pd nanoparticles were also synthesized by reducing Pd^{2+} ions with sodium borohydride ($NaBH_4$) in an aqueous solution. In a typical preparation, 1 mL aliquot of a 0.05M $Na_2PdCl_4 \cdot 3H_2O$ aqueous solution was added to 250 mL of a 0.15 wt.% CMC aqueous solution. Subsequently, 3.5 mL 0.05 M $NaBH_4$ aqueous solution was added to the system under constant stirring to yield the stabilized

Pd nanoparticles (Liu et al., 2007). The concentration of the resultant Pd nanoparticles was ~0.2 mM. The Pd nanoparticles were characterized or tested within 24 hours.

5.2.3 Physical characterization

TEM micrographs of dried Pd nanoparticles were obtained using a Zeiss EM10 Transmission Electron Microscope (Zeiss, Thornwood, NJ, USA). Detailed procedures on TEM analyses have been described elsewhere (He and Zhao, 2005).

5.2.4 Degradation of TCE

Batch experiments were conducted in 43 mL amber glass vials, filled with 43 mL of a suspension of a certain type of nanoparticles (the headspace was set to nearly zero to minimize volatilization loss of TCE). TCE degradation was initiated by spiking 25 μL of a TCE stock solution (34.4 g L^{-1} TCE in methanol) into the nanoparticle suspensions, which resulted in an initial TCE concentration of 20 mg L^{-1}. The bottles were then capped with Teflon septa and mixed on a rotary shaker (50 rpm) operated at room temperature (~22 ^{o}C). At selected times, 0.1 mL of aqueous samples were withdrawn from the reactors using a 100 μL gas-tight syringe. Then the samples were transferred into 2-mL GC vials, each of which containing 1 mL of hexane for extraction of TCE. Upon phase separation, the extracts were analyzed for TCE using a HP 6890 GC equipped with electron capture detector (ECD). All the experimental points were duplicated in two consecutive experiments.

5.2.5 Analytical methods

TCE was analyzed using an HP 6890 GC equipped with an RTX-624 capillary column (Restek Co, Bellefonte, PA) and an ECD. The detailed procedures have been provided elsewhere (He and Zhao, 2005).

5.3 Results and Discussion

5.3.1 Effects of CMC stabilizers on hydrodechlorination of TCE by stabilized Fe-Pd nanoparticles and role of H_2

Our previous study (He and Zhao, 2007a) showed that the size of CMC-stabilized ZVI nanoparticles can be manipulated by tuning the CMC-to-Fe^{2+} ratio during the particle synthesis. In general, the higher the CMC-to-Fe^{2+} ratio, the smaller and more monodisperse ZVI nanoparticles were obtained. In this study, the reactivity of CMC-stabilized Fe-Pd nanoparticles (synthesized at various CMC-to-Fe^{2+} molar ratios) was investigated through batch TCE degradation tests. **Figure 5-1** shows the TCE degradation kinetic data for the Fe-Pd particles stabilized at various CMC-to-Fe^{2+} ratios. The rate data in **Figure 5-1** are fitted with the following pseudo-first order rate law:

$$-\frac{dC}{dt} = k_{obs}C = k_{SA}a_s\rho_m C \tag{5-1}$$

where C is the aqueous phase TCE concentration (mg L^{-1}) at time t (min), k_{obs} is the observed pseudo-first order rate constant, k_{SA} is the surface area-based rate constant (L min^{-1} m^{-2}), a_s is the specific surface area of the nanoparticles (m^2 g^{-1}), and ρ_m is the mass concentration of the nanoparticles (g L^{-1}).
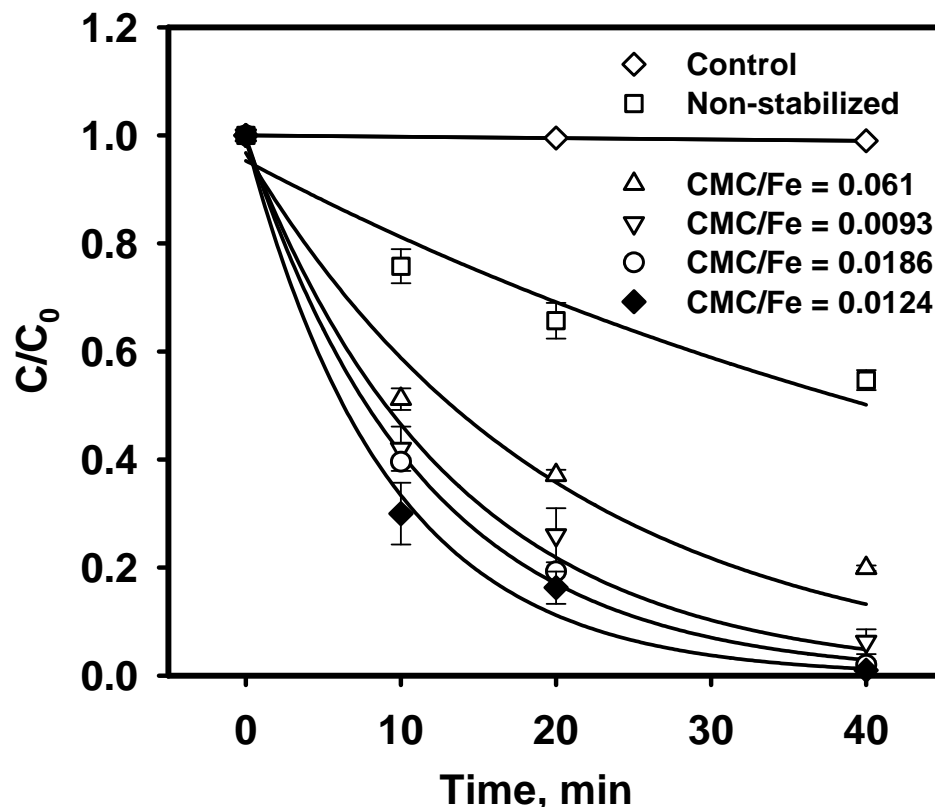
Figure 5-1. Hydrodechlorination of TCE using Fe-Pd nanoparticles stabilized with CMC90k at various CMC-to-Fe (CMC/Fe) molar ratios. Initial TCE concentration (C_0) = 20 mg L^{-1}, Iron dose = 0.1 g L^{-1} as Fe, Pd:Fe mass ratio = 1.0 mg Pd/g Fe, reaction pH = 8.3 ± 0.2. Symbols: mean of experimental duplicates with standard deviation; Lines: the first-order model fittings.

Figure 5-1 shows that the reactivity of Fe-Pd nanoparticles increases as the CMC-to-Fe molar ratio increased from 0 to 0.0124 (i.e. when CMC was increased from 0 to 0.2 wt.% for a fixed ZVI concentration of 0.1 g L^{-1}). However, a further increase of the CMC-to-Fe molar ratio from 0.0124 to 0.0186 slightly inhibited the TCE degradation, especially at the beginning of the reactions. Our previous study showed that the size of ZVI nanoparticles was reduced from >200 nm to ~18.6 nm when the CMC-to-Fe molar ratio was increased from 0.0093 to 0.0124 (He and Zhao, 2007a). Therefore, a >11 times faster TCE reduction rate would be expected as the CMC-to-Fe molar ratio increased from 0.0093 to 0.0124 based on the gain in specific surface area (the estimated specific surface area of ZVI particles with diameter of 200 nm and 18.6 nm is 3.8 m^2 g^{-1} and 41.0 m^2 g^{-1}, respectively). However, the TCE reduction rate (k_{obs}) was increased by only a factor of 1.7 (from 4.1 h^{-1} to 6.8 h^{-1}). Apparently, the increase of the dechlorination reactivity in **Figure 5-1** was not proportional to the gain in the specific surface area of the ZVI nanoparticles. When the CMC-to-Fe molar ratio was further increased from 0.0124 to 0.0186, the ZVI particle size was slightly reduced from 18.6 nm to 17.6 nm (He and Zhao, 2007a). However, the reactivity of the nanoparticles started to decline, and the degradation was further inhibited as the CMC-to-Fe molar ratio was further increased to 0.061 (**Figure 5-1**). Considering that more CMC molecules are adsorbed to the surface of the nanoparticles at higher CMC-to-Fe ratios, this observation suggests that accumulation of CMC molecules on the nanoparticle surface can render a good fraction of the reactive surface unavailable for TCE degradation, and thus, greatly diminish the gained surface area. Evidently, there exists an optimum CMC-to-Fe ratio (~0.0124), where the dechlorination reactivity is maximized and above which the inhibitive effect of CMC

overweighed the positive effect from the reduced particle size. In addition to the direct surface occupation, the sorbed CMC molecules can form a more compact surface coating on the particle surface at elevated CMC concentration, which can hinder the mass transfer of TCE to the reactive sites of the Fe-Pd surface. This observation is consistent with several recent published findings. For example, Doong and Lai (2005) reported that humic acids competed for the reactive sites on the microscale Fe-Pd with tetrachloroethylene (PCE), and thus, lowered the dechlorination rate of PCE. Saleh et al. (2007) reported that the reactivity of monometallic ZVI nanoparticles was reduced due to surface coating with surfactants and copolymers.

It should be noted that during the nanoparticle preparation, a relatively large amount of hydrogen gas is formed according to eqn (5-2),

$$Fe(H_2O)_6^{2+} + 2BH_4^- \rightarrow Fe^0 + 7H_2 + 2B(OH)_3 \tag{5-2}$$
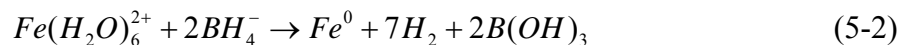
eqn (5-2) indicates that for each mole of Fe^0 formed, seven moles of hydrogen gas is produced. Although the particle preparation was carried out under vacuum, no attempt was made to completely remove the resultant H_2 before the tests in **Figure 5-1** were conducted. However, because the same particle preparation procedure was followed, the initial amount of H_2 for all cases of **Figure 5-1** was considered at a comparable level. In addition to the residual H_2 from Fe^{2+} reduction, H_2 can also be formed from corrosion of the ZVI nanoparticles (see Section 5.3.5 for more details). Our recent study showed that in the presence of CMC-stabilized Pd nanoparticles (2.4 nm, 1 mg L^{-1}), H_2 was able to serve as an effective electron source for rapid and complete degradation of TCE (Liu et al., 2007). Therefore, the TCE degradation in **Figure 5-1** was attributed to reactions with both ZVI nanoparticles and H_2, i.e.

$$C_2HCl_3 + 4Fe^0 + 5H_2O \xrightarrow{\quad Pd \quad} C_2H_6 + 4Fe^{2+} + 3Cl^- + 5OH^- \qquad (5\text{-}3)$$

$$C_2HCl_3 + 4H_2 \xrightarrow{\quad Pd \quad} C_2H_6 + 3H^+ + 3Cl^- \qquad (5\text{-}4)$$
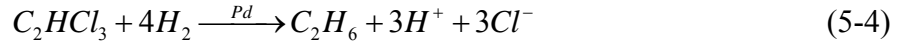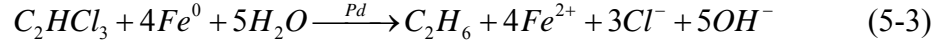
Consequently, the reaction rate law represented by eqn (5-1) is physically incorrect for fitting the TCE degradation data although it has been commonly used to quantify the overall "lumped" degradation rate. In this particular case, fairly significant discrepancies between the model fittings and experimental data were observed. From an electron balance viewpoint, conversion of Fe^0 to H_2 will not affect the amount TCE degraded. However, cautions should be exercised that when the residual H_2 from the particle synthesis is present as in **Figure 5-1**. This excess H_2 may lead to overestimation of the reactivity of the stabilized Fe-Pd nanoparticles. For example, the reported unusually high rate constants for starch-stabilized (He and Zhao, 2005) and CMC-stabilized Fe-Pd nanoparticles (He et al., 2007) were partially attributed to the residual H_2. On the other hand, discarding the H_2 from the particle synthesis (as commonly is the case) represents a tremendous waste of electron source which is equally effective as Fe^0 for TCE degradation, but offers 7 times more electrons (enq (5-2)).

To demonstrate and estimate the magnitude of the added reducing power from the residual hydrogen, TCE degradation tests were carried out at an initial TCE concentration of 100 mg L^{-1} and a ZVI nanoparticle dose of 0.1 g L^{-1}. Based on the reaction stoichiometry, the electrons from the ZVI nanoparticle dose can only transform a maximum of 53.0 mg L^{-1} TCE, i.e. TCE was nearly 2 times in excess of the ZVI nanoparticles. However, **Figure 5-2** shows that 88.5±2.2% of the TCE was degraded at equilibrium (after ~1 day). Considering a TCE loss of 10 mg L^{-1} based on the control tests, an extra 25 mg L^{-1} TCE was degraded in the system. Evidently, the residual H_2
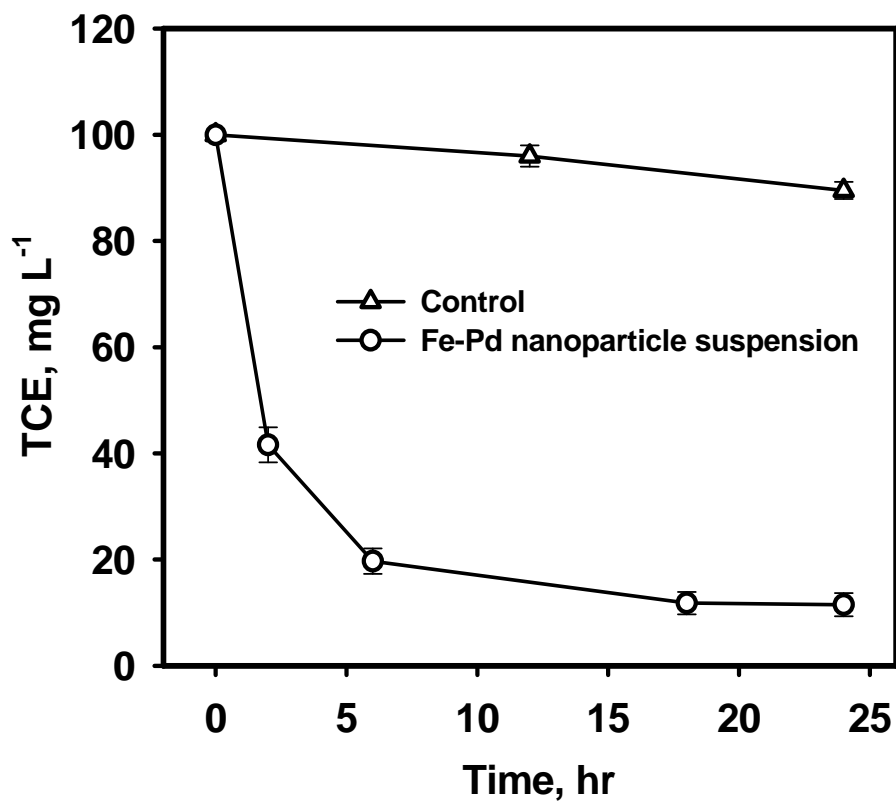
Figure 5-2. Degradation of TCE by CMC-stabilized Fe-Pd nanoparticles and by residual hydrogen from the nanoparticle synthesis. Iron dose = 0.1 g L^{-1} Fe^{0}, C_0 = 100 mg L^{-1} TCE, CMC90k = 0.2 wt.%, Pd:Fe mass ratio = 1.0 mg Pd/g Fe. Data given as mean of experimental duplicates with standard deviation.
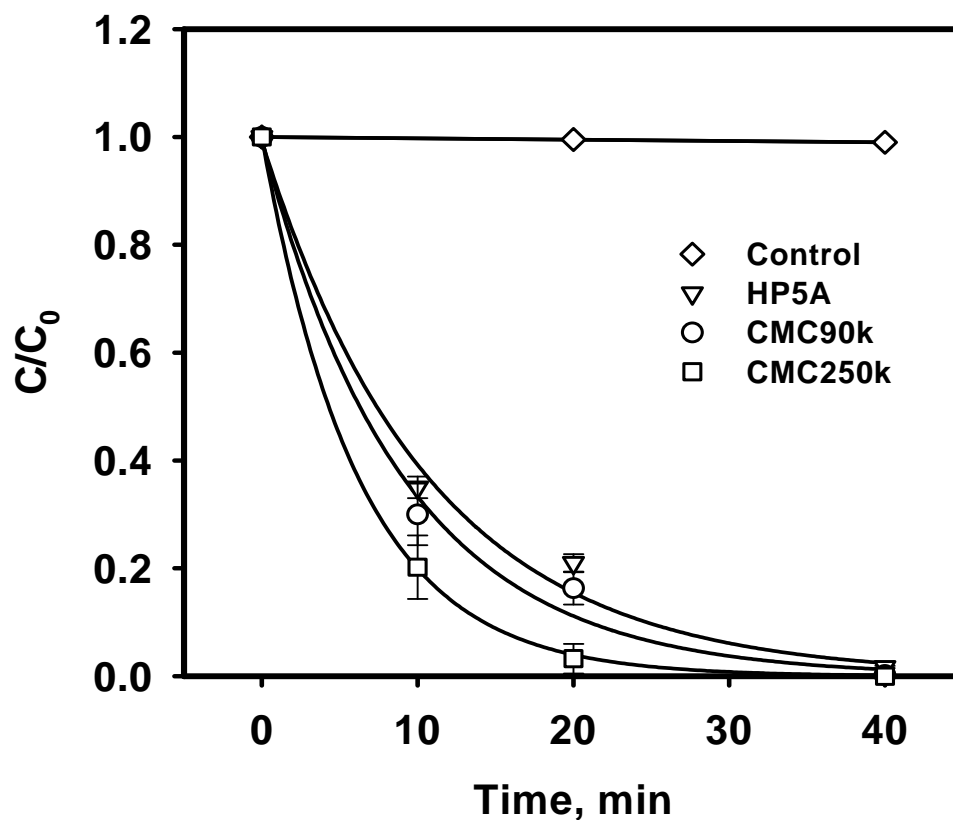
Figure 5-3. Hydrodechlorination of TCE using Fe-Pd nanoparticles stabilized with CMCs of various M.W. Iron dose = 0.1 g L^{-1} Fe, C_0 = 20 mg L^{-1} TCE, CMC = 0.2 wt.% for all cases, Pd:Fe mass ratio = 1.0 mg Pd/g Fe, reaction pH = 8.3 ± 0.2. Symbols: mean of experimental duplicates with standard deviation; Lines: the first-order model fittings.

from the ZVI nanoparticle preparation (eqn. (5-2)) was acting as additional electron donors. Based on electron balance calculations, the extra TCE degraded was equivalent to the solubility of H_2 (0.8 mM or 1.6 mg L^{-1}, in water at 25 $^{\circ}$C (Lide, 1994)), indicating that the freshly prepared Fe-Pd suspension was initially saturated by H_2 before TCE was introduced.

The size of Fe nanoparticles can also be altered by using CMCs of various M.W. or of different functionalities as a stabilizer (He and Zhao, 2007a). At a fixed CMC-to-Fe^{2+} molar ratio of 0.0124, the application of three CMC stabilizers HP5A (M.W. = 13k), CMC90k (M.W. = 90k), and CMC250k (M.W. = 250k) resulted in Fe nanoparticles (0.1 g L^{-1}) of >200 nm, 18.6 nm, and 15.6 nm, respectively. **Figure 5-3** shows that the smaller nanoparticles (stabilized with CMC of greater M.W.) exhibited greater reactivity for TCE degradation. The three CMC stabilizers bear homologous chain-like molecular structures with markedly different molecular size (length) but the same repeating units. Our prior FT-IR (He et al. 2007) studies indicated that the CMC molecules are adsorbed on the ZVI nanoparticle surface via the –COO⁻ and –OH groups. From the standpoint of both the stereochemistry of the CMC molecules and thermodynamic stability of the system, it is plausible that only a fraction of the –COO⁻ and –OH groups in the CMC molecules are involved in interacting with the ZVI particles, and the larger the CMC molecules, the fewer molecules are adsorbed to the nanoparticles (i.e. larger CMC molecules are more effective stabilizers). Therefore, larger CMC molecules occupy fewer reactive sites on Fe surface, leaving more sites available for reactions. From a mass transfer viewpoint, the sorption of larger CMC molecules results in a bulkier and loosely assembled layer of

99

CMC molecules on the particles (as opposed to a more compact layer for smaller CMC molecules), resulting in less mass transfer resistance of TCE to the Fe-Pd surface.

5.3.2 Effects of Pd coated on ZVI and Pd added as separate nanoparticles

Numerous studies have demonstrated the formation of Fe-Pd bimetallic particles with adding Pd^{2+} to microscale ZVI (Doong and Lai, 2005; Jovanovic et al., 2005). In this study, it is expected that Fe-Pd bimetallic nanoparticles were formed upon the addition of Pd^{2+} ions to Fe nanoparticle suspension. To gain a deeper insight into the role of Pd in TCE degradation by stabilized Fe-Pd nanoparticles, monometallic Pd and Fe nanoparticles were first synthesized separately and then mixed and tested for TCE degradation. **Figure 5-4** shows a typical transmission electron microscopy (TEM) image of the CMC-stabilized monometallic Pd nanoparticles. Based on the TEM image, the mean particle diameter was determined to be 2.4 ± 0.5 nm (SD). **Figure 5-5** compares the TCE degradation rates of the separate Fe and Pd nanoparticles versus Fe-Pd bimetallic nanoparticles under otherwise identical conditions.

To eliminate the interference of the residual H_2 from the particle preparation, the nanoparticle suspensions were first purged with N_2 for 5 minutes to remove the H_2 before TCE degradation was initiated. UV-Vis measurement of the nanoparticle suspensions before and after N_2 purging showed only ~5% decrease of the absorbance (A) at a wavelength 600 nm, which indicated that the amount of Fe^0 corroded during the N_2 purging was negligible. The UV-Vis absorbance was found to be a convenient measure for representing the concentration of suspended ZVI nanoparticles in water (Saleh et al., 2005).
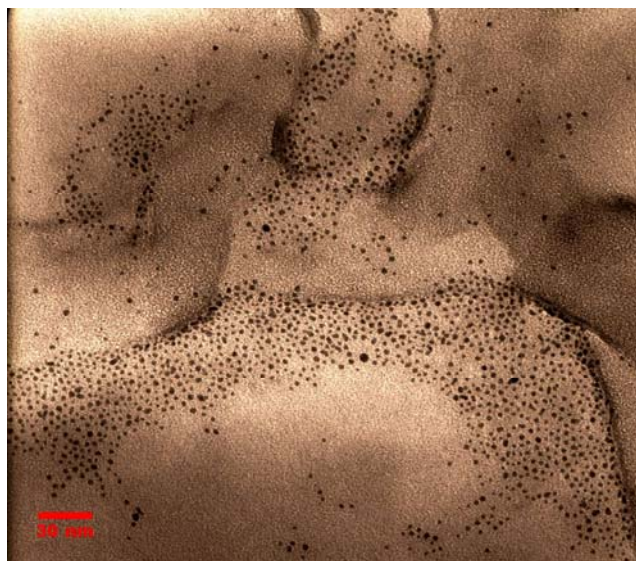
Figure 5-4. Representative TEM image of CMC90k-capped Pd nanoparticles. The scale bar represents 30nm. The average size of 452 particles in this image was determined to be 2.4±0.5 nm (SD) using Image J software.
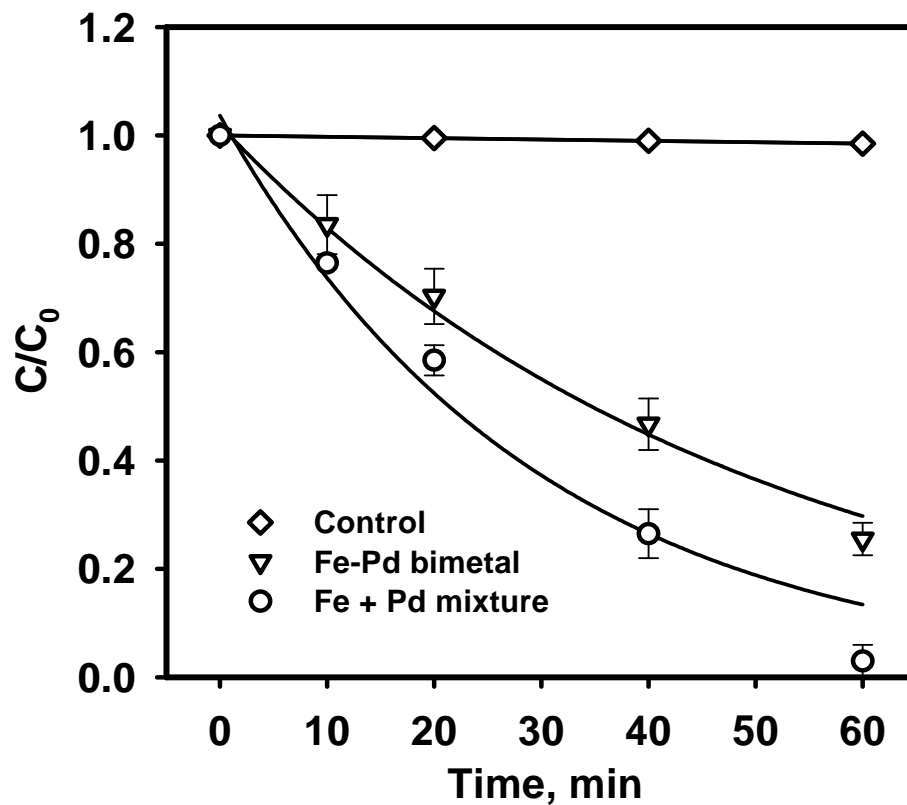
Figure 5-5. Hydrodechlorination of TCE using mixture of separately prepared monometallic Pd and Fe nanoparticles as opposed to Fe-Pd bimetallic nanoparticles. Residual H_2 from particle synthesis was removed for all cases. Iron dose = 0.1 g L^{-1} Fe, C_0 = 20 mg L^{-1} TCE, CMC90k = 0.2 wt.%, Pd:Fe mass ratio = 1.0 mg Pd/g Fe, reaction pH = 8.3 ± 0.2. Symbols: mean of experimental duplicates with standard deviation; Lines: the first-order model fittings.

Figure 5-5 shows that the mixture of CMC-stabilized monometallic Fe and Pd nanoparticles exhibited a nearly two times greater reactivity toward TCE (k_{obs} = 2.0 h^{-1}) than the Fe-Pd bimetallic nanoparticles (k_{obs} = 1.1 h^{-1}). In the former case, the Pd and Fe nanoparticles are separated by the solution, and thus, there exists a huge activation barrier for Pd to directly catalyze the degradation of TCE by the ZVI nanoparticles. However, the highly reactive ZVI nanoparticles can undergo rapid corrosion reaction with water to give off H$_2$. Therefore, the observed highly effective degradation of TCE is attributed to reduction by H$_2$ with the Pd nanoparticles as catalysts. For the bimetallic Fe-Pd nanoparticles, the presence of Pd on the Fe surface is expected to catalyze TCE reduction by both Fe^0 and H$_2$. However, the slower overall TCE degradation rate with the bimetallic nanoparticles indicates that the overall TCE degradation rate is not limited by the Fe corrosion, but rather by the catalytic activity of Pd. Evidently, the highly dispersed monometallic Pd nanoparticles (~2.4 nm) offer greater specific surface area and provide a TCE degradation pathway of lower activation energy compared to Pd that sits on the ZVI nanoparticles. When the results in **Figure 5-1** and **Figure 5-5** are compared, it is evident that the removal of the residual H$_2$ from the particle synthesis reduced the TCE degradation rate (k_{obs}) from 6.8 h^{-1} to 1.1 h^{-1} for the Fe-Pd bimetallic nanoparticles. Based on the data for the Fe-Pd bimetallic nanoparticles in **Figure 5-5** and a mean TEM-based diameter of 4.3 nm (specific surface area: 177 m^2 g^{-1}) (He et al., 2007), the surface area normalized k_{SA} value was calculated to be 0.0064 L h^{-1} m^{-2}.

5.3.3 Effect of Pd loading on TCE hydrodechlorination

As has been widely observed, the presence of trace amounts of Pd can substantially catalyze the hydrodechlorination rate. On the other hand, from both economic and environmental standpoints, the amount of Pd applied should be minimized. To this end, a mechanistic and quantitative analysis of the role of Pd is of critical importance. **Figure 5-6** shows the TCE degradation rates by Fe-Pd bimetallic nanoparticles at various loading of Pd but under otherwise identical conditions. In agreement with our previous study (He and Zhao, 2005), the presence of trace amounts of Pd resulted in much more effective degradation of TCE. At a Pd loading of 0.5 mg Pd/g Fe, a k_{obs} value of 0.84 h^{-1} was obtained, which was one order of magnitude greater than that when only ZVI was used. Further increasing the Pd loading to 1.0 mg Pd/g Fe increased the TCE reduction rate constant to 1.1 h^{-1}. However, when the loading was further increased to 2.0 mg Pd/g Fe, the degradation rate remained nearly unchanged. Kim and Carraway (2003b) studied the reactivity of millimeter-scale Pd-Fe bimetallic particles for TCE degradation as a function of Pd loading. They observed that the k_{SA} value increased linearly over the range of Pd loadings < 0.1 wt.% of Fe (i.e. 1.0 mg Pd/g Fe). However, the increase in k_{SA} became much less considerable when the Pd loading was increased from 0.1 to 0.77 wt.% of Fe. Wei et al. (2006) also observed the increase of k_{obs} for 2, 4-chlorophenol reduction over the investigated range of Pd loadings (<1.0 mg Pd/g Fe) with non-stabilized Fe-Pd particles.
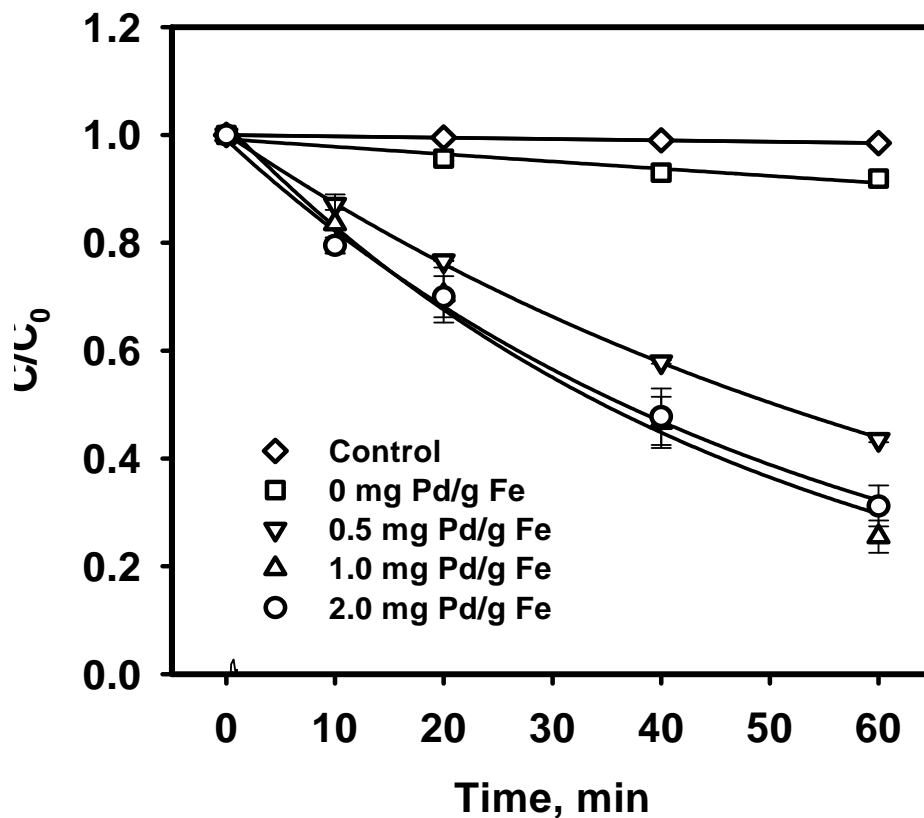
Figure 5-6. Effect of Pd loading on hydrodechlorination of TCE by CMC-stabilized Fe-Pd nanoparticles. Residual H_2 from particle synthesis was removed in all cases. Iron dose $= 0.1$ g L^{-1} Fe, $C_0 = 20$ mg L^{-1} TCE, CMC90k $= 0.2$ wt.%, reaction pH $= 8.3 \pm 0.2$. Symbols: mean of experimental duplicates with standard deviation; Lines: the first-order model fittings.

When trace amounts of Pd^{2+} ions are added to the ZVI nanoparticle suspension, the cations are reduced by the nanoparticles and end up being plated on the iron surface uniformly to form a monolayer of Pd atoms (Bransfield et al., 2006). The theoretical monolayer surface coverage can be estimated by assuming that the Pd overlayer is predominantly in the lowest energy fcc(111) crystallographic orientation (Bransfield et al., 2006). Under these conditions, the surface area of one unit cell is given by (Bransfield et al., 2006)

$$\text{Surface Area per Unit Cell (nm}^2\text{)} = 2 \cdot \sqrt{3} \cdot r^2 \qquad (5\text{-}5)$$

where r is the radius of a Pd atom (0.138 nm) (Tilley, 2004). Based on the specific surface area of the iron calculated based on the mean TEM diameter (4.3 nm, 177 $m^2\ g^{-1}$) (He et al., 2007), a full monolayer of Pd atoms would be equivalent to 0.47 g Pd/g Fe.

Therefore, at a Pd loading of <2.0 mg Pd /g Fe, only a small fraction (<0.43%) of the ZVI surface is covered by the Pd atoms. Conceptually, doubling the Pd loading (e.g. from 1.0 to 2.0 mg Pd/g Fe) will double the number of Fe-Pd galvanic cells, which would generate more atomic hydrogen (the reactive species for TCE degradation), and thus, should speed up the TCE reduction rate. However, the fact that little enhancement in the reaction rate was observed as the Pd loading was increased from 1.0 to 2.0 mg Pd/g Fe indicates that the generation of the reactive atomic hydrogen is not controlled by the Fe-Pd galvanic couples, but rather by the corrosion rate of the bulk ZVI surface. It is also evident from **Figure 5-6** that at a Pd-to-Fe ratio of <1.0 mg Pd/g Fe, the amount of catalyst (Pd) is limiting the degradation rate, whereas the iron corrosion (or formation of atomic hydrogen) becomes the rate-limiting factor when the loading exceeds 1.0 mg Pd/g Fe.

5.3.4 Effect of various types of metal catalysts

In addition to Pd, other transition metals such as Ni, Pt and Cu were studied for their catalytic activity toward TCE degradation with the stabilized ZVI nanoparticles. CMC-stabilized bimetallic Fe-Me (where Me = Ni, Pt or Cu) nanoparticles were prepared following the same procedure as for the stabilized Fe-Pd nanoparticles. For all cases, the Me-to-Fe ratio was fixed at 9.7 μmol Me/g Fe, which is equivalent to 1.0 mg Pd/g Fe for the Fe-Pd nanoparticles. **Figure 5-7** shows that the catalytic activity of Pd far exceeds that of the other metals. **Figure 5-7** reveals the following sequence of dechlorination reactivity for the Me-Fe bimetallic nanoparticles: Fe-Pd >> Fe-Ni > Fe-Pt ≈ Fe-Cu ≈ Fe, which generally agrees with the results for non-stabilized ZVI particles reported by others (Kim and Carraway, 2003a; Lin et al., 2004; Zhang et al., 1998).

5.3.5 Mechanisms of TCE degradation by stabilized Fe-Pd nanoparticles

Based on findings in this work and extensive studies in the open literature, the underlying mechanisms of TCE dechlorination by CMC-stabilized Fe-Pd nanoparticles are elucidated. In a system containing TCE and the aqueous suspension of CMC-stabilized Fe-Pd nanoparticles, the following reactions can take place:

$$Fe^0 \rightarrow Fe^{2+} + 2e^- \tag{5-6}$$

$$2H^+ + 2e^- \rightarrow H_2 \uparrow \tag{5-7}$$

$$H_2 \xrightarrow{Pd} H \cdot + \cdot H \tag{5-8}$$

$$TCE + 8H \cdot \rightarrow ethane + 3H^+ + 3Cl^- \tag{5-9}$$

$$Fe^0 \xrightarrow{Pd} Fe^{2+} + 2e^- \text{ (side reaction)} \tag{5-10}$$

$$TCE + ne^- + mH^+ \rightarrow products + 3Cl^- \text{ (side reaction)} \tag{5-11}$$

107
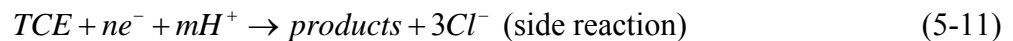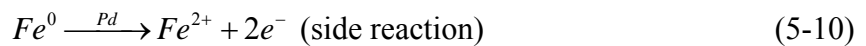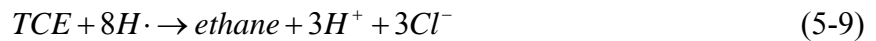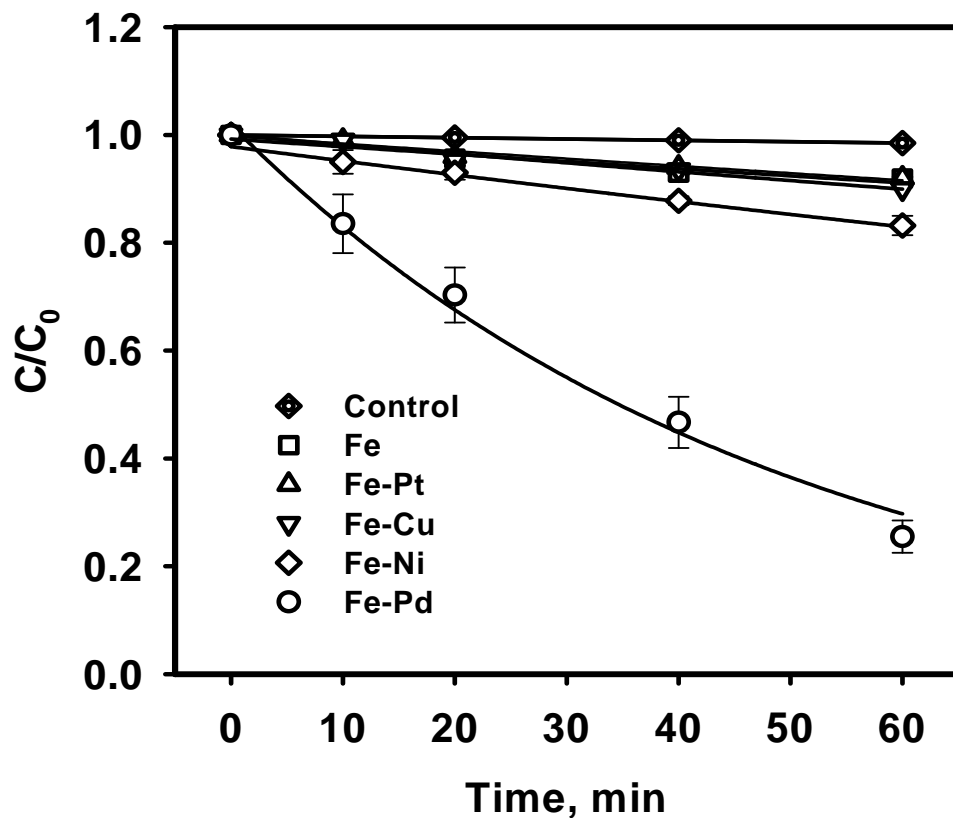
Figure 5-7. Effect of various metal catalysts on hydrodechlorination of TCE by CMC-stabilized bimetallic nanoparticles. Residual H_2 from particle synthesis was removed in call cases. Iron dose = 0.1 g L^{-1} Fe, C_0 = 20 mg L^{-1} TCE, CMC90k = 0.2 wt.%, Metal:Fe molar ratio = 9.7 μmol metal/g Fe, reaction pH = 8.3 ± 0.2. Symbols: mean of experimental duplicates with standard deviation; Lines: the first-order model fittings.

Liu et al. (2005a; 2005b) investigated the dechlorination of TCE by non-stabilized ZVI nanoparticles, and they asserted that the ZVI particles underwent an oxidative dissolution process with Fe^0 in the particles being fully accessible during TCE reduction. They also observed that a portion of the oxidized iron was transformed to crystalline magnetite in solution. For the CMC-stabilized Fe-Pd nanoparticles, Fe^0 may undergo the same oxidative corrosion (reaction with water) (eqn. (5-6)) with the resultant Fe^{2+} released into the solution. However, because of the much smaller size, the reactive lifetime for the CMC-stabilized nanoparticles is expected to be shorter than for the non-stabilized counterparts. In addition, CMC can complex with Fe^{2+} ions, and prevents the resulting iron oxides or iron hydroxides from aggregating and settling down as is the case for non-stabilized iron particles. We observed that under ambient conditions, the stabilized Fe-Pd (0.1 g L^{-1}) nanoparticles were completely oxidized in water after ~ 7 days without precipitates being observed.

Corrosion facilitated by the Fe-Pd galvanic cells should also be concurrently operative (eqn (5-10)). However, the role of this galvanic corrosion appears insignificant as discussed earlier because of the minimal amounts of Pd loaded (<2.0 mg Pd/g Fe). However, the galvanic corrosion can be more profound when the surface loading of the metal is high. For example, Schrick et al. (2002) observed that the galvanic corrosion rate of non-stabilized bimetallic Fe-Ni (Fe:Ni = 3:1 w/w) particles was much faster than the mixture of monometallic Fe or Ni particles. Lin et al. (2005) reported that the corrosion of an Fe powder was promoted as 0.25 wt.% of a noble metal such as Pd, Pt, Au and Ru was plated on the Fe surface. Note that for the Fe powder, this metal loading was enough to form two full atomic layers on the Fe surface because of the much larger particle size

of the Fe powder. For comparison, 0.25 wt.% Pd would only cover ~ 0.54% of the Fe surface for the CMC-stabilized nanoparticles.

As iron corrodes, protons from water are reduced to atomic H and then to molecular hydrogen at the iron surface (eqn (5-7)). The hydrogen is then transferred and sorbed to the palladium lattice where it partially dissociates back to atomic hydrogen (eqn (5-8)), which is the primary reactive species for hydrodechlorination. Note that the residual H_2 from ZVI nanoparticle synthesis process can also undergo the same process and degrade TCE. As TCE is transferred onto the surface of Pd atoms, the cleavage of the C-Cl bonds takes place via hydrodechlorination (eqn (5-9)). **Figure 5-8** depicts the degradation mechanism of TCE in the stabilized Fe-Pd bimetallic systems. Ethane is considered to be the final TCE hydrodechlorination product based on the results from prior studies (Lien and Zhang, 2001; He et al., 2007).

Concurrently, TCE reduction can also occur via direct electron transfer or via adsorbed atomic hydrogen on the Fe surface (eqn (5-10)), as indicated in **Figure 5-7**, though it is not as fast as in the above case. The faster TCE reduction rate in the CMC-stabilized Fe-Pd suspension indicates that hydrodechlorination is the primary mechanism for TCE degradation.

Researchers have attributed the different catalytic activity of various metal catalysts to different 'solubility' of atomic hydrogen in each metal additive (Lin et al., 2004; Cwiertny et al., 2006), although competing theories exist on what represents a metric for hydrogen solubility. Lin et al. (2005) proposed that exchange current densities for hydrogen evolution represent a metric for the hydrogen solubility in metal additives. On the other hand, Cwiertny et al. (2006) postulated that the relative partial molar
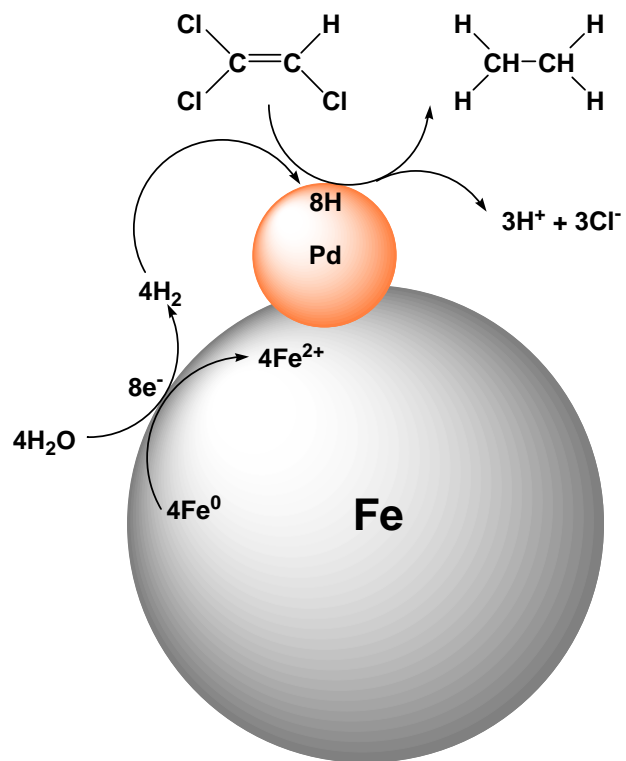
Figure 5-8. Illustrative diagram of TCE hydrodechlorination on the surface of CMC-stabilized Fe-Pd nanoparticles.

enthalpy for an infinitely dilute solution of hydrogen in each additive is a better metric for atomic hydrogen solubility. Despite the different metrics, both theories support the notion that palladium offers the greatest hydrogen solubility of the tested metals. Consequently, palladium is the most efficient metal catalyst for TCE dechlorination.

5.3.6 Effect of pH

Since ZVI corrosion involves reaction with protons, pH is expected to affect the TCE degradation rate with the stabilized Fe-Pd nanoparticles. To investigate pH effects on dechlorination reactivity of the stabilized Fe-Pd nanoparticles, Fe-Pd nanoparticle suspensions at pH ranging from 6 to 9 were prepared by using 50mM HEPES as a buffer. **Figure 5-9 (a)** shows that at a given pH, the degradation of TCE followed a pseudo first-order kinetics. The results also indicate a general trend of decreasing reaction rate with increasing pH. This observation is consistent with the results observed for 2,4-dichlorophenol hydrodechlorination by non-stabilized Fe-Pd nanoparticles (Wei et al., 2006) and reductive dechlorination of TCE and TCA by non-stabilized ZVI nanoparticles (Liu and Lowry, 2006; Song and Carraway, 2005).

In accord with the TCE degradation mechanism discussed above, two reactions can limit the TCE degradation rate in stabilized Fe-Pd nanoparticle system. One is the corrosion of ZVI to produce H_2, which is more favored at lower solution pH; and the other is the hydrodechlorination of TCE by H_2 (or atomic hydrogen) at the Pd surface, which is also favored at lower pH since lowering pH produces more H_2. To gain an insight into the relative corrosion rate, the corrosion rate of the CMC-stabilized Fe-Pd nanoparticles in water (no TCE) was monitored by monitoring the transient change in the UV-Vis absorbance (A) of the nanoparticle suspensions at a wavelength 600 nm (Saleh et

112

(a)

113

(b)

114
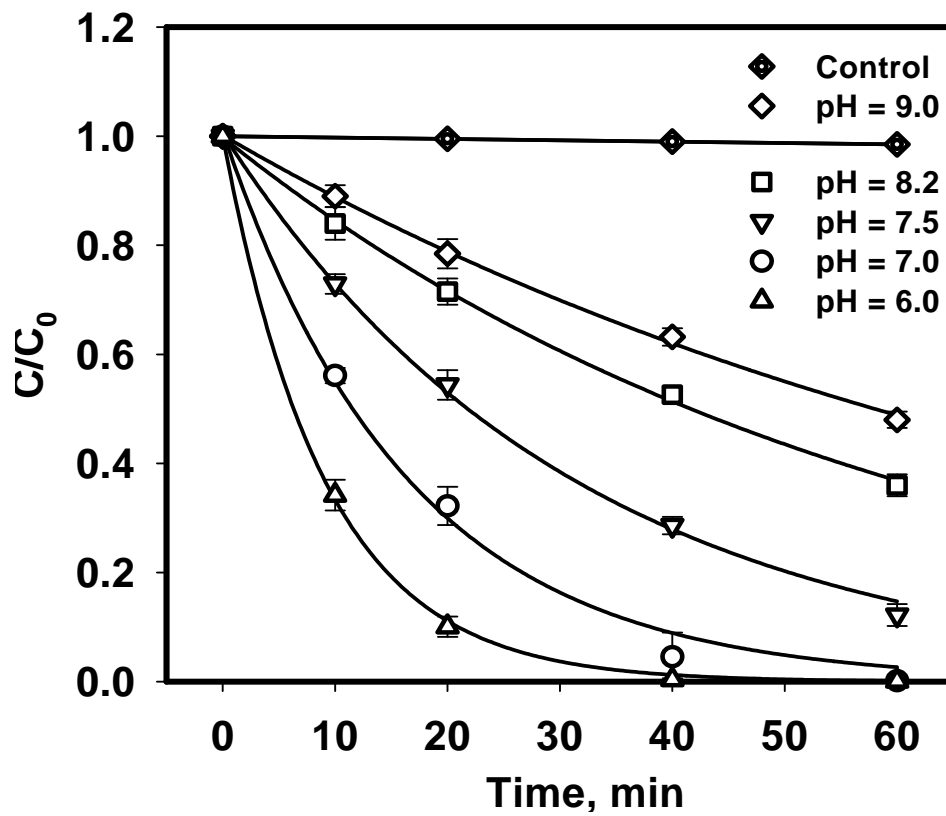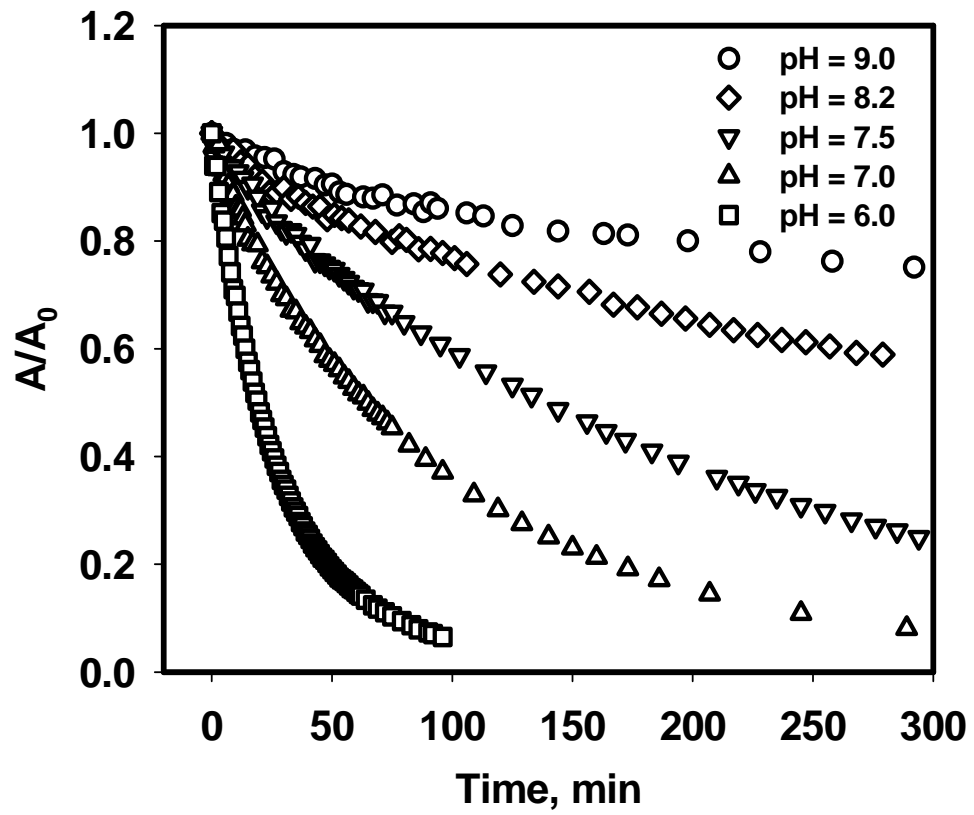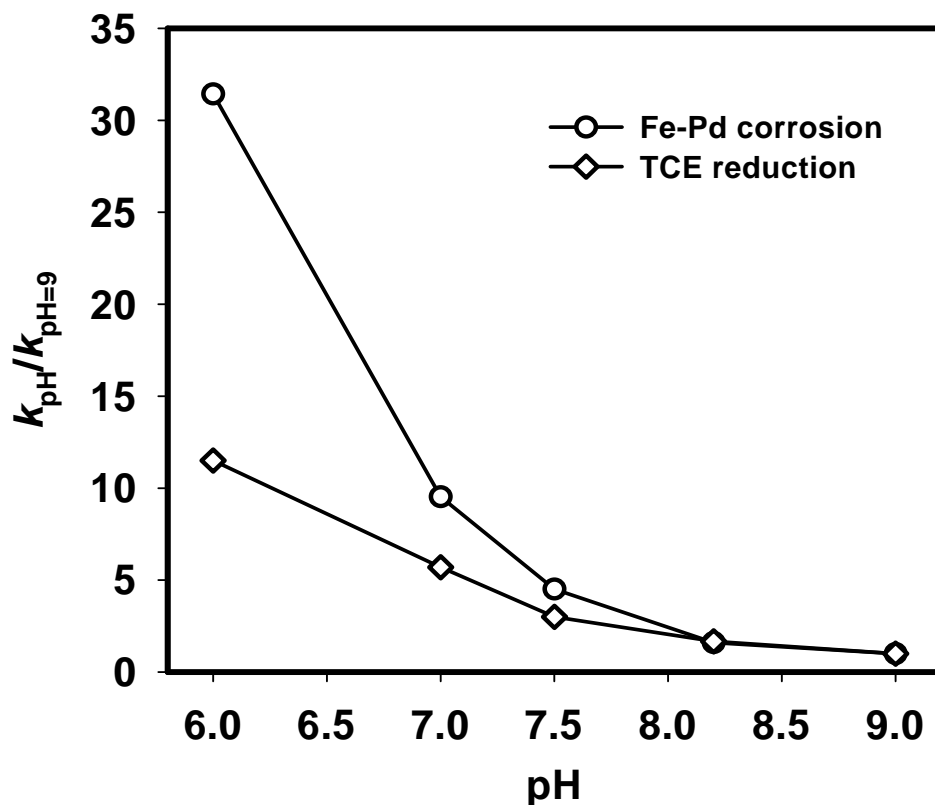
(c)

Figure 5-9. (a) Hydrodechlorination of TCE by CMC-stabilized Fe-Pd nanoparticles at various pH levels in a 50mM HEPES buffer with removal of residual H_2 from particle synthesis; (b) Corrosion of Fe represented by the decrease of suspension UV-Vis absorbance at a wavelength of 600 nm; (c) Normalized TCE reaction rate vs. Fe corrosion rate. In call cases, Iron dose = 0.1 g L^{-1} Fe, C_0 = 20 mg L^{-1} TCE, CMC90k = 0.2 wt.%, Pd:Fe mass ratio = 1.0 mg Pd/g Fe. Symbols: mean of experimental duplicates with standard deviation; Lines in (a): the first-order model fittings.

al., 2005), as shown in **Figure 5-9(b)**. Evidently, the Fe corrosion at a given pH also followed the first-order kinetics, and thus, k_{obs} can be determined for each pH. **Figure 5-9(c)** compares the pseudo first-order corrosion rate constants and the TCE degradation constants at each pH. Note that in **Figure 5-9(c)** the rate constants are normalized to the respective rate constant at pH 9.0. **Figure 5-9(c)** also revealed that there exists a strong correlation between iron corrosion and TCE degradation. As pH was lowered from 9.0 to 8.2, both TCE degradation and Fe corrosion rates were increased by ~ 60%. This observation indicates that at higher pH (e.g. pH > 8.2), Fe corrosion controls the reduction of TCE as a relatively slow process. However, as pH was further decreased from 8.2 to 6.0, the increase in iron corrosion rate far overweighed the TCE reduction rate. For example, from pH 8.2 to 6.0, Fe corrosion rate was increased by ~31.4 times, compared to only 11.5 times for TCE reduction rate. Evidently, as pH decreases, proton supplies become more abundant, and the rate controlling step gradually shifts from iron corrosion to the hydrodechlorination process, which is governed by the activity and concentration of the catalyst (Pd).

Liu and Lowry (2006) reported that for the monometallic reactive nanoiron particles (RNIP), Fe^0 corrosion follows first-order decay kinetics and pH affected Fe^0 corrosion and TCE reduction to a different extent. For example, decreasing solution pH from 8.9 to 6.5 increased the RNIP Fe^0 corrosion rate constant by 27 times, but the TCE dechlorination rate constant only doubled. In comparison, the corrosion rate of the stabilized Fe-Pd nanoparticles was enhanced by ~ 21 times as pH was decreased from 8.9 to 6.5, which appears comparable to the results of RNIP corrosion. However, the gain in TCE reduction rate for the stabilized Fe-Pd nanoparticles was more than five times

greater than that for RNIP in the same pH range. The rather pronounced difference between the RNIP and stabilized Fe-Pd nanoparticles again confirms the critical role of the Pd catalyst, i.e. H_2 produced from iron corrosion can be effectively used by Pd for hydrogenation but cannot be effectively catalyzed by RNIP (Liu et al., 2005a) for reductive dechlorination.

5.3.7 Effect of ionic strength on TCE dechlorination by stabilized Fe-Pd nanoparticles

To test the effect of ionic strength on TCE degradation by the CMC-stabilized Fe-Pd nanoparticles, sodium chloride at 1.0 wt.% (ionic strength = 0.17M) and 3.0 wt.% (ionic strength = 0.51M), respectively, was added into the nanoparticle suspension to simulate conditions of a saline water. **Figure 5-10** shows that the presence of 1.0 wt.% and 3.0 wt.% NaCl only slightly reduced the TCE degradation. For example, at the end of the 1-hour test period, the amount of TCE degraded was 62% and 60% with 1.0 and 3.0 % NaCl, compared to 75% when no NaCl was present. Our prior study showed that the presence of high concentrations of Na^+ can cause partial aggregation of the nanoparticles due to the double layer compression effect on the ZVI nanoparticle surface (He and Zhao, 2007a). For instance, the presence of 100mM (or 0.6 wt.%) NaCl increased the particle size from 18.6 to 33.7 nm. Because of the increased particle size (or reduced specific surface area), the TCE degradation reactivity by the stabilized nanoparticles was slightly reduced. Nevertheless, **Figure 5-10** indicates that the stabilized Fe-Pd nanoparticles remain highly effective for TCE dechlorination even under highly saline conditions. It is also noteworthy that the TCE degradation rate in the initial stage (< 20 min) was slightly enhanced by the high concentration of salts due to the "salting out" effect, i.e. the
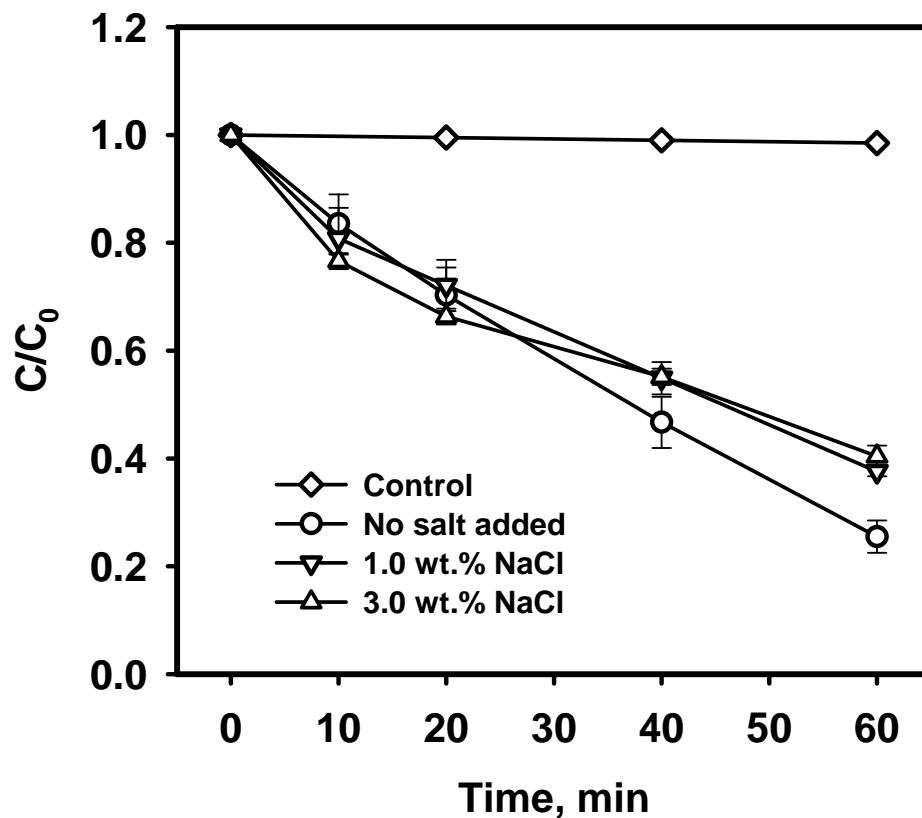
Figure 5-10. Hydrodechlorination of TCE by CMC-stabilized Fe-Pd nanoparticles in the presence of high concentration NaCl. Residual H_2 from particle synthesis was removed in all cases. Iron dose = 0.1 g L^{-1} Fe, C_0 = 20 mg L^{-1} TCE, CMC90k = 0.2 wt.%, Pd:Fe mass ratio = 1.0 mg Pd/g Fe, reaction pH = 8.3 ± 0.2. Data given as mean of experimental duplicates with standard deviation.

hydrophobic TCE molecules are pushed to the nanoparticle surface by the highly polar salt solution. However, this positive effect was shortly outweighed as the particles grew into larger aggregates in the course of the reaction.

5.4 Conclusions

In this study, effects of particle stabilization, metal catalysts, reaction pH and ionic strength on TCE degradation by CMC-stabilized Fe-Pd nanoparticles were investigated. The key findings from this study are summarized as follows:

(1) The concentration, molecular weight and type of stabilizers can affect surface capping chemistry of the Fe-Pd nanoparticles, and thus, the TCE mass transfer behavior on Fe-Pd surface and the TCE reduction rate. Generally, particle stabilization prevented particle agglomeration and resulted in greater particle reactivity. However, CMCs at excessively high concentrations (e.g. CMC-to-Fe molar ratio > 0.0124 for CMC90k) may inhibit the reactivity of the nanoparticles. On an equal equivalent basis, application of CMCs of lower M.W. resulted in slower TCE reduction.

(2) H_2 can serve as an effective electron source for TCE degradation in the presence of a metal catalyst such as Pd. In a closed system, the conversion of the electron sources from ZVI to H_2 during the ZVI corrosion does not diminish the TCE reducing power of the nanoparticles.

(3) Water reduction on the Fe surface instead of galvanic corrosion was the predominant mechanism for the generation of molecular hydrogen with the stabilized Fe-Pd nanoparticles at a Pd loading less than 2.0 mg Pd/g Fe. At a Pd-to-Fe molar ratio lower than 1.0 mg Pd/g Fe, the amount of catalyst (Pd) limited the degradation rate,

119

whereas the iron corrosion became the rate-limiting factor when the loading exceeded 1.0 mg Pd/g Fe.

(4) Decreasing solution pH benefited the TCE reduction in Fe-Pd system but enhanced the corrosion rate to an even greater extent at a Pd loading of 1.0 mg Pd/g Fe. As pH was lowered from 9.0 to 6.0, the rate controlling step of TCE reduction shifted from Fe corrosion to hydrodechlorination.

(5) The stabilized bimetallic nanoparticles can effectively degrade TCE in both fresh and saline water.

CHAPTER 6. TRANSPORT OF CARBOXYMETHYL CELLULOSE STABILIZED ZVI NANOPARTICLES IN POROUS MEDIA AND APPLICATION TO DNAPL DEGRADATION

Transport of ZVI nanoparticles in soil is essential for the in situ application of this technology for soil and groundwater remediation. This chapter evaluated the transport of CMC-stabilized iron nanoparticles in four different porous media. For the first time, the effectiveness of DNAPL remediation in porous media using Fe-Pd nanoparticles was studied.

6.1 Introduction

The use of zero-valent iron (ZVI) as a method for groundwater remediation started in early 1990s when granular ZVI was first employed in permeable reactive barriers (PRBs) systems (Reynolds et al., 1990; Gavaskar et al., 1998). In a ZVI PRB system, groundwater flows passively through an engineered iron wall while contaminants are precipitated, adsorbed or transformed on the iron surface. Over the past decade, the ZVI technology has been applied at over 120 sites worldwide PRBs (ITRC, 2005). While PRBs are found effective for remediation of shallow aquifers with relatively low concentrations of contaminants, challenges with implementation and cost increase in deeper aquifers and at higher contaminant concentration (Gavaskar et al., 2005). As such, nanoscale ZVI technology became an extension of the PRBs technology.

In 1997, researchers in Lehigh University determined that nanoscale ZVI had ~

35 times greater surface area than granular ZVI and may be 10 to 1,000 times more reactive than granular ZVI toward trichloroethene (TCE) (Wang and Zhang, 1997). This fact, combined with the potential for nanoscale particles to migrate in the subsurface, resulted in the ideal concept of injecting nanoscale ZVI into the ground for in situ degradation of chlorinated solvents such as TCE in soil, even potentially dense nonaqueous phase liquid (DNAPL) in source zones.

Over the past 10 years, researches on nanoscale ZVI have been focused on its effectiveness in treating diverse pollutants, including chlorinated solvents, energetic munitions such as TNT and RDX, legacy organohalogen pesticides such as lindane and DDT, as well as inorganic contaminants such as heavy metals, arsenic and anions (Li et al., 2006). However, the transport of ZVI nanoparticles in porous media, which is essential for the in situ remediation, had been neglected for a long period. The fact is that ZVI nanoparticles tend to aggregate rapidly in water to form micron-scale or larger aggregates, rendering them undeliverable in the soil (He and Zhao, 2005).

In recent years, researchers have explored ways to modify the surface of the ZVI nanoparticles using polymers and surfactants (e.g. stabilizers) to enhance their colloid stability and soil mobility (He and Zhao, 2005; He et al., 2007; Kanel et al., 2007; Saleh et al., 2005; Schrick et al., 2004). Among them, sodium carboxymethyl cellulose (CMC) has shown itself one of the most promising selects for its strong chelating ability, low cost and environmental compatibility (He and Zhao, 2007a; He et al., 2007). In our prior study, enhanced transport of CMC-stabilized ZVI nanoparticles in a loamy sand soil was observed (He et al., 2007). However, a detailed and quantitative investigation on their mobility in porous media has been lacking. Furthermore, only few studies have reported

the transport of surface-modified nanoscale ZVI in porous media, and most of them were performed in 1-D columns under fixed physical flow conditions (Kanel et al., 2007; Schrick et al., 2004). However, researches have shown that flow velocities could significantly affect the transport behavior of the colloids (Lecoanet and Weisner, 2004).

The undeliverable property of the bare nanoscale ZVI (e.g. unmodified nanoscale ZVI) has held back the wide application of this technology since its beginning. Due to this, no studies on soil-related chlorinated solvent degradation or DNAPL degradation in porous media with nanoscale ZVI have been reported, although this technology was developed for remediation of contaminants in deep aquifer or DNAPL in source zones. Our prior studies showed that the CMC-stabilized ZVI bimetallic (Fe-Pd) nanoparticles degraded TCE approximately 17 times faster than the non-stabilized counterparts (e.g. bare Fe-Pd nanoparticles) (He et al., 2007). This fact, combined with the observed high mobility of CMC-stabilized Fe-Pd nanoparticles in soil, provide a possibility of proactive attacking of DNAPL in porous media using stabilized Fe-Pd nanoparticles.

The overall objective of this study was to investigate the mobility of the CMC-stabilized ZVI nanoparticles in porous media and its application to DNAPL degradation. The specific objectives were to: 1) investigate the CMC-stabilized ZVI nanoparticles transport in 1-D columns with various porous media under different flow conditions; and 2) assess the feasibility of using CMC-stabilized Fe-Pd nanoparticles for in situ DNAPL remediation in porous media.

6.2 Experimental Procedures

6.2.1 Preparation and characterization of nanoparticles

Stabilized ZVI nanoparticles were prepared by a modified borohydride-reduction approach using CMC as a stabilizer. A detailed protocol for CMC-stabilized ZVI nanoparticle preparation was described in our prior study (He and Zhao, 2007a). The resultant nanoparticle suspension (Fe = 1.0 g/L) was diluted to desired concentrations under the protection of N_2 for particle size analyses (Fe = 0.1 g/L) and for transport tests (Fe = 0.2 g/L).

To test the reactivity of the nanoparticles, trace amount of Pd (Pd/Fe = 0.1 wt.%) was loaded onto the ZVI nanoparticle (Fe = 1.0 g/L) surface to yield the CMC-stabilized bimetallic (Fe-Pd) nanoparticles. The loading was accomplished by adding known quantities of $Na_2PdCl_4 \cdot 3H_2O$ (Strem Chemicals, Newburyport, MA) solution into the CMC-stabilized ZVI nanoparticle suspension. The Fe-Pd bimetallic nanoparticle suspension was then diluted to 0.5 g/L for batch and column degradation tests.

The size of ZVI nanoparticles was studied by transmission electron microscope (TEM) and dynamic light scattering (DLS) tests. TEM micrographs of ZVI nanoparticles were obtained using a Zeiss EM10 TEM (Zeiss, Thornwood, NJ). DLS tests were performed with a Nicomp 380 Submicron Particle Sizer (PSS, Santa Barbara, CA). More details on TEM and DLS analyses have been described elsewhere (He et al., 2007).

6.2.2 Porous medium and treatment

The porous media selected for the column breakthrough experiments were silica glass bead, quartz sand and a loamy sand soil. Two types of glass bead (purchased from

Potters Industries Inc.) were used in the experiments as received. One is A110 with sizes ranging from 1.0 mm to 1.2 mm (coarse type). The other is P0230 with sizes ranging from 0.43 mm to 0.60 mm (fine type).

The quartz sand was Accusand 40/60 with sizes ranging from 0.3 mm to 0.36 mm obtained from Unimin Corporation, Le Sueur, MN. The sand was thoroughly cleaned prior to use. The cleaning procedure consisted of washing with DI water, followed by immersion in sodium dithionite solution (0.1M $Na_2S_2O_4$) for 2h to remove surficial metal oxides. Organic impurities were removed by soaking the sand in hydrogen peroxide (5%) for 3h, followed by a wash with DI water and subsequent soaking in hydrochloric acid (12N HCl) overnight. The sand was then thorough rinsed with DI water and dried in the air for the column tests.

The loamy sand soil was obtained from a local farm in Auburn, AL. Before use, raw soil was sieved in a standard sieve of 2 mm openings and then rinsed with deionized (DI) water to remove any dissolved solids. The salient soil properties are as follows: sand content = 84%; silt = 10%; clay = 6%.

6.2.3 Column breakthrough experiments

The mobility of the CMC-stabilized ZVI nanoparticles in porous media was investigated through a series of fixed-bed column tests. A summary of the experimental conditions maintained for the columns is provided in **Table 6-1**. The column test setup included a solution reservoir, Teflon tubings, an HPLC pump, a glass column (1 cm i.d.; Omnifit, Cambridge, England), and a fraction collector (Eldex Laboratories, Napa, CA). In all tests, the volume of the packed bed was ~ 16.7 mL (21.3 cm height). About 0.3 cm (height) of glass wool was placed on the bottom of the column to support the porous

media bed. When packing a column, a deaerated background solution (0.84 mM NaCl + 0.16 mM NaHCO3, pH 7.5) was preintroduced into the column from its bottom to a certain height, and then the dry glass bead, sand or soil was slowly poured into the solution while the column was being clicked with a plastic rod to ensure uniformity of the packing and to avoid air entrapment in the column.

For each experiment, ~ 15 pore volumes (PVs) of the background solution was first introduced to the column upward from the bottom using HPLC pump to obtain a stable baseline. After that, application of the input was switched to the tracer solution, and later switched back to the background solution to thoroughly flush the column. After the complete elution of the tracer, the input was switched to the nanoparticle suspension (0.2 g/L Fe and 0.16 wt.% NaCMC) to obtain the nanoparticle breakthrough curve. The nanoparticle suspension in the reservoir was purged with N_2 all the time during the experiments to prevent the particles from oxidation.

6.2.4 TCE NAPL degradation in the sand column

To prove the concept of proactive attacking of DNAPL in the subsurface, TCE NAPL degradation by CMC-stabilized Fe-Pd nanoparticles was performed in the glass column packed with sand. The column setups and the packing were as same as those in transport experiments. With the equilibration of the column system (e.g. after ~ 15 PVs background solution introduced), the pumping was stopped and 10 μL pure TCE was slowly injected into the sand bed at 3 cm from the top. After 30min equilibrium time, background solution (control test) or Fe-Pd nanoparticle suspension was introduced to the column downward from the top using HPLC pump to (i) allow enough residential time of TCE and (ii) avoid preferential leaching of TCE from the column. The input of

nanoparticle suspension was composed of 0.5 g/L Fe-Pd nanoparticle (Pd/Fe = 0.1 wt.%) and 0.4 wt.% NaCMC and was under N_2 protection during the experiments. At selected time intervals, 100 μL of effluent sample was collected and transferred into a 2 mL GC vial containing 1 mL of hexane for extraction of TCE. Upon phase separation, the extract was analyzed for TCE using a HP 6890 GC equipped with an electron capture detector (ECD). Fraction collector was used to collect all the effluent solution from the column for Fe and chloride analyses.

6.2.5 Fe-Pd nanoparticle reactivity test in batch experiments

The reactivity of the Fe-Pd nanoparticles used in column tests was evaluated through batch TCE degradation experiments. The experiments were conducted in 43 mL amber glass vials, filled with 43 mL of a suspension of a certain type of nanoparticles (the headspace was set to nearly zero to minimize volatilization loss of TCE). TCE degradation was initiated by spiking 25 μL of a TCE stock solution (172 g L^{-1} TCE in methanol) into the nanoparticle suspensions, which resulted in an initial TCE concentration of 100 mg L^{-1}. The bottles were then capped with Teflon septa and mixed on a rotary shaker (50 rpm) operated at room temperature ($\sim$22 ^{o}C). At selected times, 0.1 mL of aqueous samples were withdrawn from the reactors using a 100 μL gas-tight syringe. Then the samples were transferred into 2-mL GC vials, each of which containing 1 mL of hexane for extraction of TCE. Upon phase separation, the extracts were analyzed for TCE using a HP 6890 GC equipped with electron capture detector (ECD).

127

6.2.6 Analytical methods

Bromide and chloride were analyzed using a Dionex Ion Chromatography (DX-120, Dionex, Sunnyvale, CA) equipped with an AS14 column, an AG14 guard column and a 100 µL sample loop. Total iron concentration was analyzed with a flame atomic-absorption spectrophotometer (AAS) (220FS, Varian, Palo Alto, CA). Before the iron analysis, the ZVI nanoparticles were digested with 2M HCl for ~5 min, which was enough to fully dissolve the nanoparticles. TCE was analyzed using an HP 6890 GC equipped with an RTX-624 capillary column (Restek Co, Bellefonte, PA) and an ECD. The detailed procedures have been provided elsewhere (He and Zhao, 2005).

6.3 Results and Discussion

6.3.1 Characterization of CMC-stabilized ZVI nanoparticles

CMC-stabilized ZVI nanoparticle suspension appears to be inky black without any precipitates observed, as shown in **Figure 6-1(a)**. The particle morphology of the nanoparticles studied by transmission electron microscope is presented in **Figure 6-1(b)**. The colloids were of spheroidal to pseudocubic shape and exhibited certain degree of surface roughness. The mean size of the freshly prepared CMC-stabilized nanoparticles was estimated to be 11.2 ± 7.9 nm (standard deviation). Meanwhile, DLS tests were also carried out to obtain the hydrodynamic diameter of the particles. The DLS results gave a particle diameter of 18.1 ± 2.5 nm (99.9% particles by number), from which the thickness of the CMC layer was estimated to be 3.5 nm.

Table 6-1. Parameters of the Tracer Experiments.

Porous media	saturation %	bulk density g/mL	porosity	pore velocity cm/s	dispersion cm^2/h	r^2
Coarse glass bead	100	1.49	0.421	0.0302	26.2	0.993
Fine glass bead	100	1.57	0.388	0.0327	21.3	0.993
Sand	100	1.73	0.360	0.0353	18.1	0.990
Loamy sand soil	100	1.74	0.355	0.0358	25.9	0.978
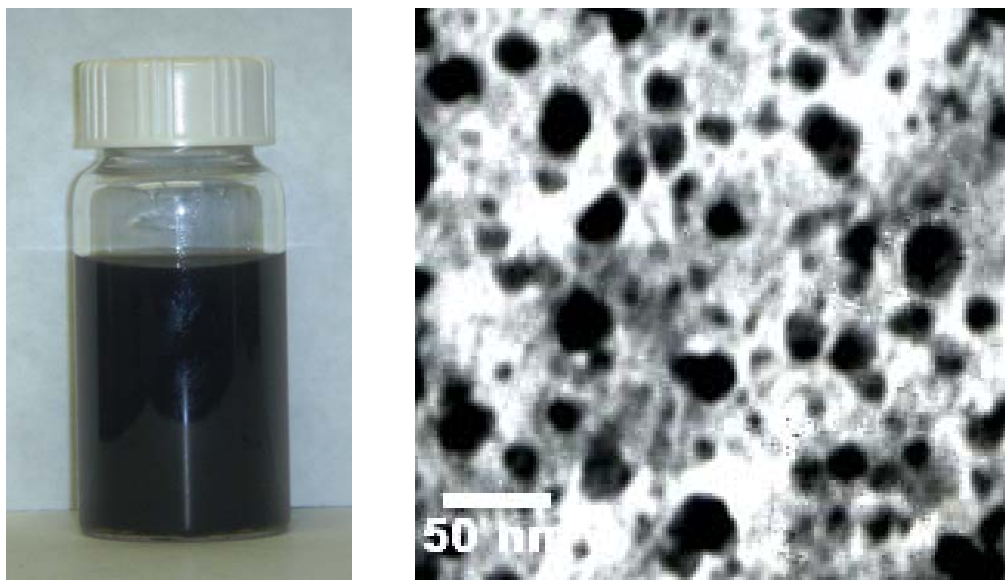
(a)	**(b)**

Figure 6-1. Digital photograph of the CMC-stabilized ZVI nanoparticle (Fe = 0.2g/L; CMC = 0.16 wt.%) suspension **(a)** and a representative TEM image **(b)** showing the morphology of the particles (Scale bar: 50nm).

6.3.2 Transport of CMC-stabilized ZVI nanoparticles in 1-D porous media

Breakthrough curves of bromide in all studied porous media are plotted in **Figure 6- 2**. Stability of the tracer breakthrough suggests that the flow conditions were controlled very well for the experiments. The dispersion coefficients (*D*) obtained using CXTFIT (STANMOD software, USDA) as well as the experimental conditions are presented in **Table 6-1**.

Figure 6-3 shows breakthrough curves of CMC-stabilized ZVI nanoparticles in different porous media. In all cases, the effluent Fe concentrations rapidly raised and reached a constant level at ~1.5 pore volumes (PVs) and remained for the duration of the experiments. This behavior indicates that the removal of CMC-stabilized ZVI nanoparticles in porous media was controlled by a first-order kinetic mechanism. Therefore, the transport of ZVI nanoparticles in porous media can be described by a convention-dispersion equation (CDE) including a term to account for the first-order removal (Chu et al., 2000):

$$R\frac{\partial C}{\partial t} = D\frac{\partial^2 C}{\partial z^2} - V\frac{\partial C}{\partial z} - k_d C \qquad (6\text{-}1)$$

In which, C (mg/L) is the liquid-phase Fe concentration, D (cm^2/h) is the hydrodynamic dispersion coefficient, V (cm/h) is the pore fluid velocity, R is the retardation factor, and k_d (h^{-1}) is the first-order removal rate coefficient. From the non-reactive tracer test, the dispersion coefficient D of the porous media was obtained (**Table 6-1**). The retardation factor R and the first-order removal rate coefficient k_d were then estimated by fitting the breakthrough data using CXTFIT.
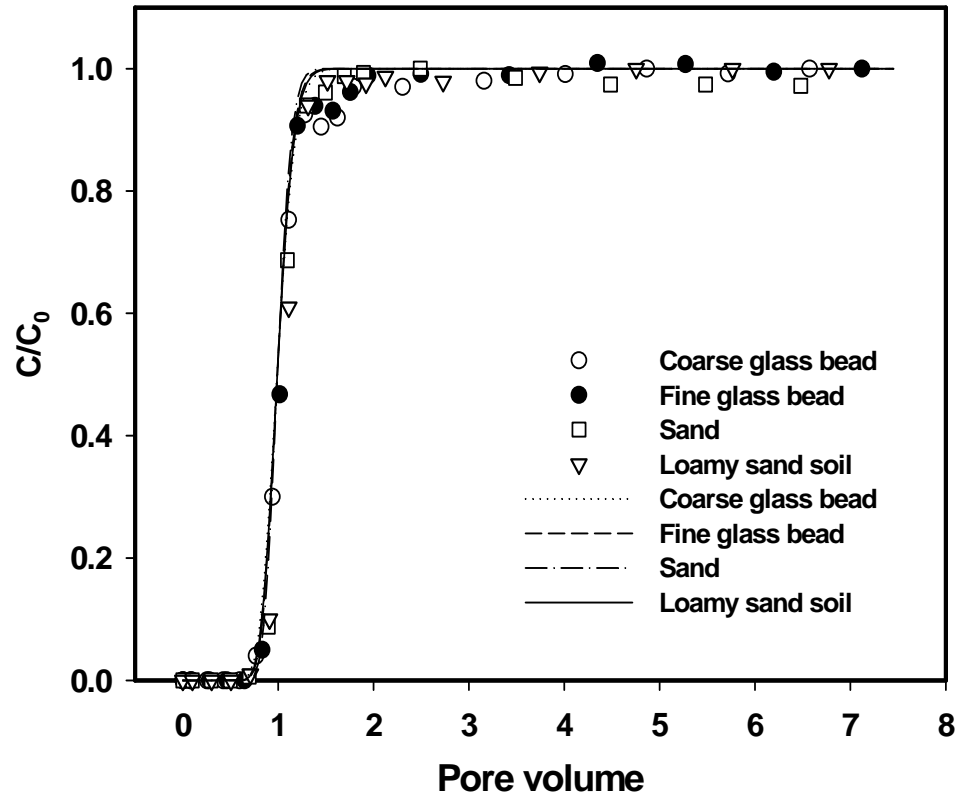
Figure 6-2. Bromide breakthrough curves in different porous media.
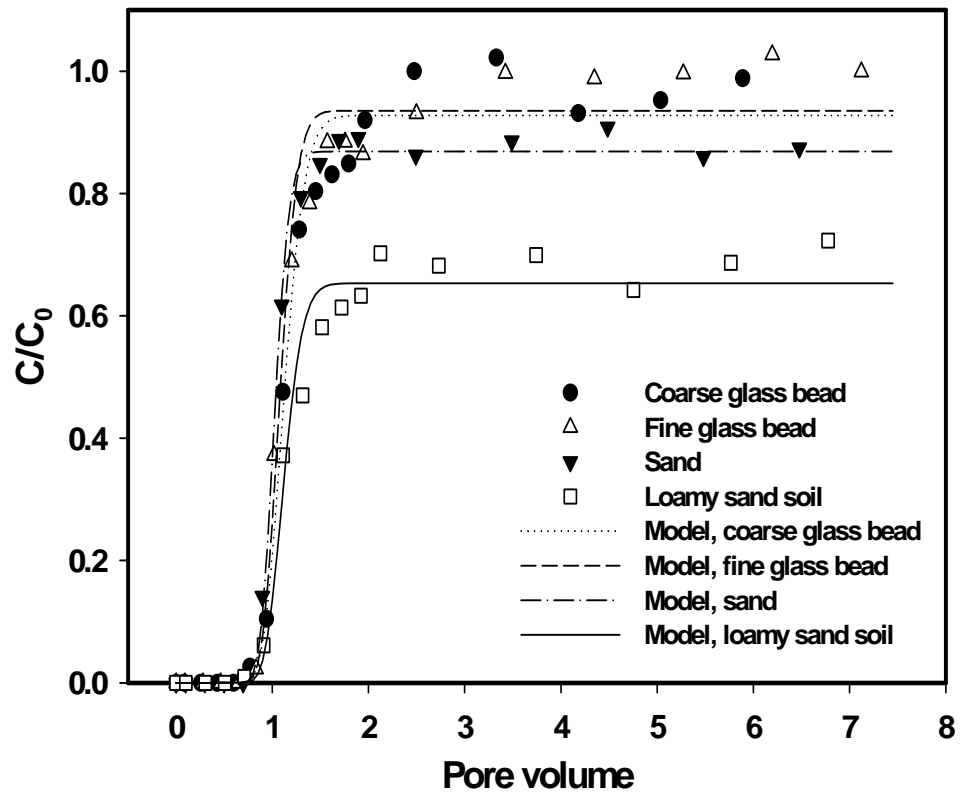
Figure 6-3. Breakthrough curves of CMC-stabilized ZVI nanoparticles in various porous

media. Iron concentration was 0.2 g/L, the flow rate for all cases was 0.6 mL/min.

Table 6-2. Parameters of the CMC-stabilized ZVI Nanoparticle Breakthrough Experiments

Porous media	Pore velocity cm/s	C/C_0	R	k_d h^{-1}	r^2
Coarse glass bead	0.0302	0.93	1.11	0.38	0.986
Fine glass bead	0.0327	0.94	1.11	0.36	0.981
Sand	0.0176	0.83	1.13	0.57	0.997
	0.0353	0.87	1.10	0.83	0.997
	0.0706	0.95	1.11	0.55	0.988
Loamy sand soil	0.0358	0.65	1.11	2.54	0.977

Figure 6-3 shows that ZVI nanoparticle breakthrough curves could be fitted well by equilibrium CDE model using CXTFIT (e.g. $r^2 > 0.98$). The estimated R and k_d as well as the stable outflow concentration C/C_0 are summarized in **Table 6-2**. According to **Table 6-2**, the transport of ZVI nanoparticles was slightly retarded in all cases with a similar R of 1.11. Comparing **Figure 6-2** with **Figure 6-1** also shows no earlier breakthrough of ZVI particles than that of bromide. This behavior indicates that CMC-stabilized ZVI nanoparticles didn't experience the preferential transport due to size exclusion, which was commonly observed for nanoparticles with size > 100nm (Kretzschmar and Sticher, 1997; Zhuang et al., 2005). Furthermore, the first-order removal rates of ZVI nanoparticles varied in different porous media with a trend of coarse glass bead ≈ fine glass bead < sand < loamy sand soil. Evidently, ZVI nanoparticles experienced various degrees of liquid-solid interfacial attachment in porous media.

Colloid deposition on porous media includes two steps: (i) transport of colloid particles to matrix surfaces by Brownian diffusion, interception, or gravitational sedimentation resulting in collisions and (ii) attachment of colloidal particles to the matrix surfaces (Kretzschmar et al., 1999). The physical factors such as colloid size and density, fluid velocity, pore structure, and the accessible surface area of the matrix affect the kinetics of the transport step. In contrast, the solution and surface chemistry determine the kinetics of the attachment step. In **Figure 6-3**, the colloid size and density, fluid velocity and solution chemistry being equal, the pore structure, accessible matrix surface area and surface chemistry should be the factors affecting the deposition rate of ZVI nanoparticles on the porous media. For example, the glass bead column contains big

pores and low accessible matrix surface area, which make the ZVI nanoparticles easily passed without significant retention. As the matrix grain size gets smaller (e.g. sand), more retention of nanoparticles was obtained due to the increase of collector (e.g. matrix) surface area. Worthy noting here is that the silica glass bead and the clean quartz sand have the similar surface composition (e.g. silica) and therefore similar surface chemistry.

Interestingly, much more retention of ZVI nanoparticles was observed in the loamy sand soil although the porosities of the soil column and sand column are comparable. This may due to that the surface of soil grain is geochemically heterogeneous with oxide of iron, aluminum and manganese coated on silicate mineral grains or as separate accessory minerals (Johnson et al., 1996a). Literatures show that the isoelectric points of silica sand and iron oxyhydroxide are around 2 and 6, respectively (Johnson et al., 1996a). Under experimental conditions used in the column tests (pH = 8.1), both of the sand surface and soil surface should be negatively charged but in different degree.

To further examine the transport behavior of stabilized ZVI nanoparticles in porous media, filtration theory is used to analyze the particle deposition with respect to different transport mechanisms: Brownian diffusion, interception, and gravitational sedimentation. As described by Tufenkji and Elimelech (2004), the overall single-collector contact efficiency (η_0) equals to the sum of the single-collector contact efficiency by diffusion (η_D), by interception (η_I), and by gravitational sedimentation (η_G). Using the method of Tufenkji and Elimelech, η_D, η_I, and η_G are obtained and summarized in **Table 6-3**. The attachment efficiency is then calculated from:

$$\alpha = -\frac{2}{3}\frac{d_c}{(1-f)L\eta_0}\ln(C/C_0) \qquad (6\text{-}2)$$

where f is the porosity, d_c is the grain diameter, and L is the porous medium packed length. Results from **Table 6-3** indicate that Brownian diffusion was the dominant mechanism for CMC-stabilized ZVI nanoparticles removal in all the tested porous media. In addition, it is also noteworthy that ZVI nanoparticle removal by gravitation was significant in tested porous media due to the high density of the iron particle (e.g. $\rho_p =$ 7,680 kg/m^3). Particularly, in coarse glass bead column, the gravitation accounted for 34% of the single-collector contact efficiency. This behavior of ZVI nanoparticles is rather different from that of extensively studied latex microsphere particles with similar diameter, in which gravitation was negligible for particle removal in the porous media (Zhuang et al., 2005).

As shown in **Table 6-3**, the loamy sand soil had higher attachment efficiency than sand if their grain sizes were assumed to be equal. This is because oxide minerals on the soil grain surface decreased the negative charge on the collector surface and therefore lowered the energy barrier. As such, the deposition of ZVI nanoparticles onto soil collector surface was more favorable than onto sand surface according to DLVO theory. Surprisingly, the observed attachment efficiency of ZVI nanoparticles on coarse glass bead was also higher than that on sand and fine glass bead as the solution and surface chemistry of the three systems were similar. We notice that C/C_0 of 0.93 from CXTFIX model was used as the stable ZVI effluent concentration through coarse glass bead. If α of 0.0025 (e.g. α in sand) is applied, a stable C/C_0 value of 0.98 is predicted according to the filtration theory. Therefore, the CXTFIT model may underestimate the breakthrough

concentration of ZVI nanoparticles through glass bead as it appears from **Figure 6-3**, where C/C_0 of 0.98 is closer to the analytical values of ZVI concentration in the effluent.

Fluid velocity effect on the nanoparticle transport was also investigated. In sand column, increasing the fluid pore velocity from 0.0353 cm/s to 0.0706 cm/s increased the ZVI nanoparticle breakthrough concentration from 0.87 to 0.95, as shown in **Figure 6-4** and **Table 6-3**. Conversely, when the flow rate was reduced to 0.0176 cm/s, more retention of ZVI nanoparticles was observed. For eqn 6-1, if the retardation is negligible, the k_d can be simply obtained from

$$k_d = -\frac{V}{L}\ln(C/C_0)$$ (6-3)

Therefore, assuming the k_d is a constant at different velocity, higher C/C_0 is expected when the nanparticle suspension flow rate is increased and vice versa. The observed passage of ZVI nanoparticles from **Figure 6-3** is consistent with this prediction as the fitted k_d at different pore velocities being similar (**Table 6-2**). Filtration theory is applied here to further examine the fluid velocity effect on particle transport. The obtained results (summarized in **Table 6-3**) clearly show that CMC-stabilized ZVI nanoparticles had higher collision rate onto grain surface at lower velocity due to higher Brownian diffusion (η_D) and gravitation (η_G). Since the attachment efficiencies were similar at different velocities (**Table 6-3**), more attachment of nanoparticles onto porous media surface was expected at lower velocity. Here, the similar α obtained from the experiments at different velocities agrees well with the filtration theory that the attachment efficiency is a function of solution and surface chemistry, which were constants in these experiments.

Table 6-3. Filtration Theory Analysis of CMC-Stabilized ZVI Nanoparticle Deposition onto Porous Media

Porous media	Pore velocity cm/s	dc 10^{-3} m	C/C_0	η_D	η_I 10^{-6}	η_G	η_0	α
Coarse glass bead	0.0302	1.1	0.93	0.031	0.29	0.016	0.047	0.0079
Fine glass bead	0.0327	0.52	0.94	0.054	1.2	0.013	0.067	0.0024
Sand	0.0353	0.33	0.87	0.076	3.2	0.012	0.088	0.0025
	0.0706	0.33	0.95	0.046	2.9	0.006	0.052	0.0016
	0.0176	0.33	0.83	0.12	3.5	0.026	0.15	0.0021
Loamy sand soil	0.0358	0.33*	0.65	0.077	3.3	0.012	0.089	0.0079

Parameter values used in the calculation: Hamaker constant A = 1 × 10^{-20} J; Boltzmann constant k = 1.38 × 10^{-23} J/K; fluid absolute temperature T = 295 K; fluid viscosity μ = 1.3 × 10^{-3} kg/m/s; fluid density ρ_f = 1000 kg/m^3; particle density ρ_p = 7680 kg/m^3. *: the diameter of the soil grain is assumed to be 0.33.
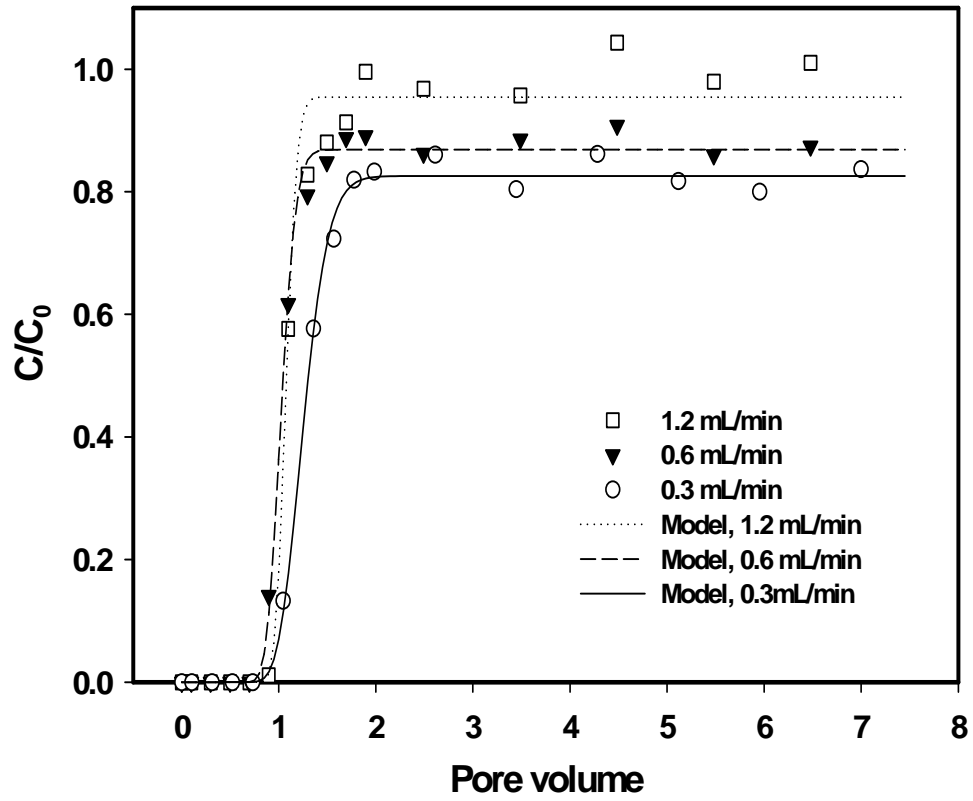
Figure 6-4. Effect of pore velocity on transport of CMC-stabilized ZVI nanoparticles.

Some studies have been conducted to evaluate the mobility of the other surface-modified ZVI nnaoparticles in porous media. Schrick et al. (2004) reported α value of 0.36 for polyacrylic acid (PAA) coated ZVI nanoparticle and 0.07 for hydrophilic carbon supported ZVI nanoparticles in Ottawa sand. Kanel et al. (2007) reported α values of 0.21 and 0.18 for surfactant (Tween 20) coated ZVI nanoparticles in unbaked and baked sand. The 1-2 magnitude lower α value of CMC-stabilized ZVI nanoparticles in the sand medium indicates higher mobility of the CMC-stabilized ZVI nanoparticles in sand porous medium. Our prior study suggested that CMC molecules are adsorbed on the surface of ZVI nanoparticles, resulting in a bulky layer of negative charges. As such, a high energy barrier for particle depositing on the collector surface (e.g. low α) is expected for CMC-stabilized ZVI nanoparticles.

In recent years, health concerns have been raised for the potential risk of in situ injection of ZVI nanoparticles into the ground. Using the filtration theory and Tufenkji and Elimelech method, we calculated the transport distance over which 99% removal of CMC-stabilized ZVI nanoparticles would occur in the silica sand. As α of 0.0025 is used, the relationship between the transport distance and CMC-stabilized ZVI nanoparticle suspension flow velocity is plotted in **Figure 6-5** (assuming that the properties of the porous media and the nanoparticles are unchangeable). At a typical groundwater flow velocity of 0.1m/day (e.g. 1.16×10^{-6} m/s), the transport distance of CMC-coated ZVI nanoparticles is calculated to be only 19.0 cm. This result indicates that human exposure to Fe nanomaterial resulting from remediation application of CMC-stabilized ZVI nanoparticles will be minimal. When an injection pressure is applied, the stabilized ZVI nanoparticles can move much further than under the typical groundwater conditions. For

instance, as the velocity increased to 1×10^{-3} m/s, the nanoparticles can transport as far as 34.0 m. Therefore, controlling the pressure of ZVI nanoparticle injection could control the transport distance of the iron, which offers profound practical convenience for in situ remediation uses. As the injection pressure released in the subsurface, the ZVI nanoparticles would be easily trapped by the aquifer within a very short distance (for example, 19.0 cm in sand).

6.3.3 Degradation of TCE DNAPL by CMC-stabilized Fe-Pd nanoparticles in a sand column.

The application of CMC-stabilized Fe-Pd nanoparticles for in situ remediation of TCE NAPL in subsurface was investigated in a sand column. The TCE elution curves with the injection of background solution (control test) and CMC-stabilized Fe-Pd nanoparticle suspension are presented in **Figure 6-6**. In the control test, the elution of TCE started at 0.5 PV and achieved a stable peak concentration from 2.5 PV to 5.0 PV. The TCE peak concentration was around 300 ppm (<< TCE solubility ~1100 ppm), indicating the slow dissolution of TCE NAPL phase under the experimental conditions. When the exited solution was collected and analyzed for TCE, ~ 96.4% of the TCE injected was recovered in the effluent, suggesting that the TCE loss during the experiment was minimal. Interestingly, the TCE elution curves for the control and Fe-Pd nanoparticle suspension almost coincided before 5.0 PV. After that, the TCE concentration in the Fe-Pd suspension effluent sharply decreased compared to that in control effluent, suggesting the degradation of TCE. In this case, ~ 58.3% of the TCE injected was recovered in the effluent. Therefore, ~ 39.5% of the TCE was degraded with the injection of Fe-Pd nanoparticles.

142
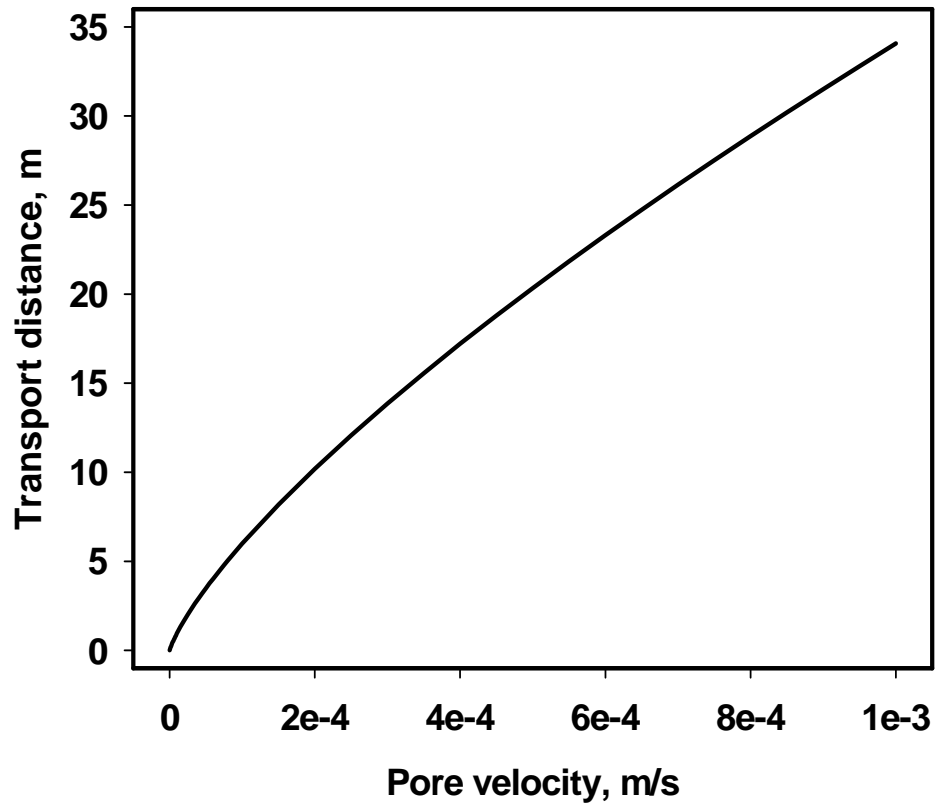
Figure 6-5. Calculated distance over which 99% of CMC-stabilized nanoparticles are removed in the sand at different pore velocities.
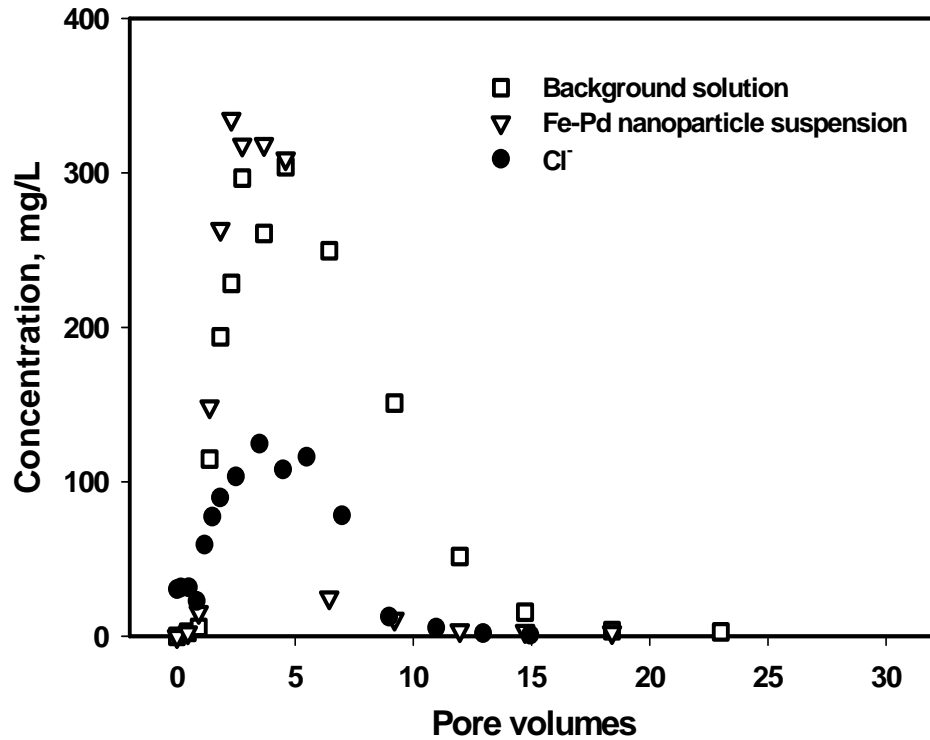
Figure 6-6. Degradation of TCE DNAPL and generation of Cl$^-$ in a sand column with injecting of CMC-stabilized Fe-Pd nanoparticles (TCE = 14.6 mg, Fe = 0.5 g/L, Pd/Fe = 0.1 wt.%, CMC = 0.4 wt.%, suspension pore velocity = 0.0118 cm/s, Empty Bed Contact Time (EBCT) = 84 min). The initial Cl$^-$ in the effluent samples was from the background solution resided in the column.
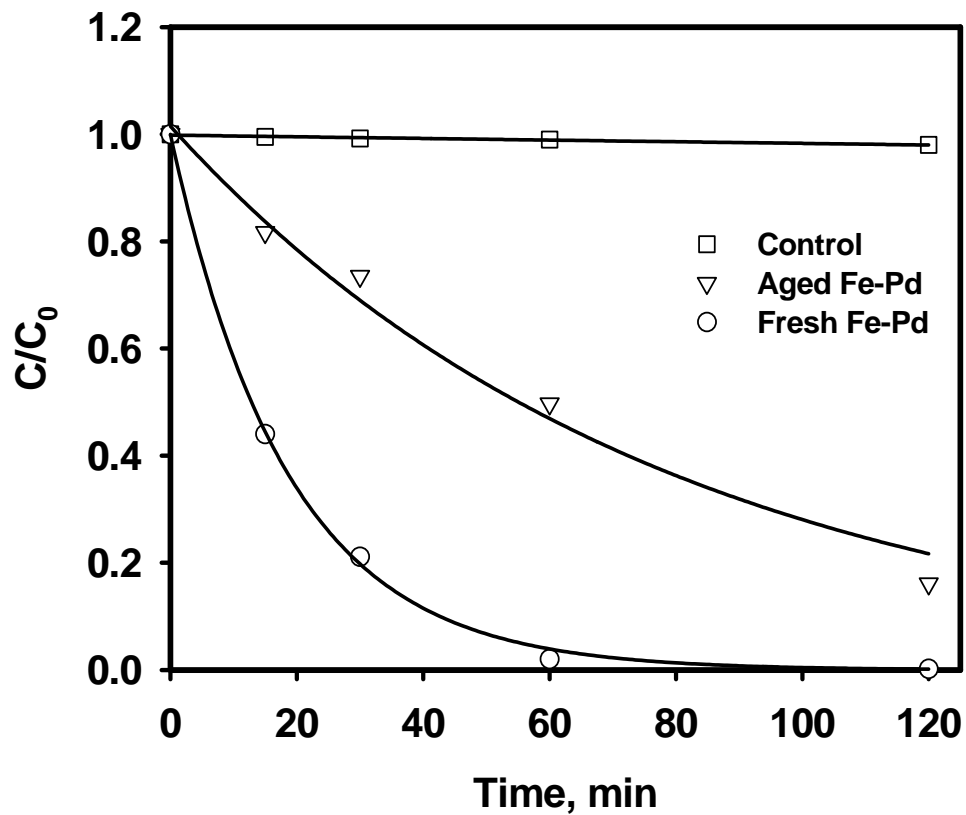
Figure 6-7. Dechlorination of TCE in aqueous phase by CMC-stabilized Fe-Pd nanoparticle suspension before (e.g. fresh) and after the column test (e.g. ~ 8 hr aged). The initial TCE concentration was 100 mg/L.

The coinciding of TCE elution curves for the control and nanoparticle suspension before 5.0 PV further suggests that the dissolution of TCE controlled the TCE elution behavior in the column, which resulted in consistent TCE evolutions in aqueous phase. This behavior also suggests that the TCE degradation in the column may mainly undergo near the NAPL phase, where a concentration gradient was maintained and rapid supplement of TCE from NAPL to aqueous phase was achieved.

The reactivity of the Fe-Pd nanoparticle suspension before and after column test (e.g. fresh and ~ 10h aged Fe-Pd) was investigated through batch TCE degradation. **Figure 6-7** shows that both the newly synthesized and aged Fe-Pd nanoparticles were highly reactive toward TCE in aqueous phase. The degradation of TCE in Fe-Pd suspension exhibit a first-order kinetics with reaction rates of 0.065 min^{-1} and 0.011 min^{-1} for the fresh and aged Fe-Pd nanoparticles, respectively. The loss of particle reactivity during injection is attributed to the corrosion of Fe, in which H_2 was produced and then purged out by the N_2. The high reactivity of CMC-stabilized Fe-Pd nanoparticles would ensure the effective degradation of DNAPL in porous media as the nanoparticles passing through.

The degradation of TCE NAPL phase in the sand column was further confirmed by the significant production of chloride in the Fe-Pd suspension effluent. The Cl$^-$ collected from the effluent samples (Note: Cl$^-$ from background solution was eliminated) accounted to approximately 96.0% of the TCE degraded, which suggests the complete degradation of TCE in the porous media without accumulation of other chlorinated intermediates such as dichloroethene (DCE) and vinyl chloride (VC). The complete degradation of TCE was further confirmed by the GC analysis where no VC and DCE

146

were detected in effluent samples. It is noteworthy that the chloride production curve also exhibits a concentration peak from 2.5 PV to 5.5 PV, consistent with the TCE elution curves. Interestingly, the highest Cl^- accompanied with the highest TCE concentration in the effluent, which further suggested that the TCE degradation near the NAPL phase was dominant.

6.3.4 Implications for in situ remediation

The successful demonstration of DNAPL degradation in porous media using stabilized Fe-Pd nanoparticles may facilitate the application of this technology to DNAPL remediation in source zones, which may significantly cut down the overall cost and time required for remediation of contaminated aquifers. The relatively "limited" mobility of CMC-stabilized Fe-Pd nanoparticles in subsurface makes the human exposure resulting from remediation application of ZVI nanoparticles likely be minimal. However, though controlling the injection pressure, the transport distance of CMC-stabilized Fe-Pd nanoparticles could be controlled, which offers practical convenience for in situ remediation uses.

CHAPTER 7. PUSH-PULL TESTS TO FIELD DEMONSTRATE THE MOBILITY AND REACTIVITY OF CMC-STABILIZED FE-BASED NANOPARTICLES IN SOIL

This chapter described the results of the first field-scale demonstration to evaluate the potential effectiveness of CMC-stabilized ZVI and bimetallic Fe-Pd nanoparticles as a remediation technology. Four push-pull tests (PPTs) were performed to determine the soil mobility of the stabilized ZVI (or Fe-Pd) nanoparticles at a PCE/TCE contaminated site in California and to assess the reactivity of the nanoparticles towards these contaminants.

7.1 Introduction

Chlorinated solvents are present in groundwater at an overwhelming number of contaminated sites in U.S. (Moran et al., 2007; Quinn et al., 2005). For example, tetrachloroethene (PCE) and trichloroethene (TCE) are among 29 of the chemicals, metals, and other substances most commonly found at USEPA Superfund sites. Due to their low solubility in groundwater, the chlorinated solvents may be present as dense nonaqueous phase liquids or associated with soil in the subsurface. Conventional treatment technologies such as pump-and-treat are usually not efficient for chlorinated solvent remediation and require long operational terms to meet the clean up requirement.

Significant attention has been attracted over the past decade to research and field application of in situ dechlorination using zero-valent iron (ZVI) nanoparticles (Elliott

and Zhang, 2001; He et al., 2007; He and Zhao, 2005; Quinn et al., 2005; Wang and Zhang, 1997). The high reactivity of nanoscale ZVI particles combined with their potential to migrate in the ground make them an ideal alternative for rapid and effective destruction of chlorinated solvents in contaminated groundwater and soil. However, the wide application of this promising technology has been held back due to the rapid aggregation of these nanoparticles, which renders them undeliverable to the target area (He et al., 2007; He and Zhao, 2005). Recently, our research group developed a new class of highly dispersed ZVI nanoparticles that were stabilized by low-cost and "green" carboxymethyl cellulose (CMC) (He et al., 2007; He and Zhao, 2007a). Our prior studies showed that these stabilized nanoparticles were highly reactive and readily dispersible in the soil. However, because of their high reactivity, the reactive lifetime of the CMC-stabilized nanoparticles may be short. To ultimately apply this promising technology in the field, pilot-test is a critical and logical step, and will yield critical information on the technical and cost effectiveness and necessary design and operating parameters.

Single-well injection-withdrawal tests or push-pull tests (PPTs) involve injecting a test solution containing a chemical of interest and a conservative tracer into a well, where the injected test solution mixes with groundwater and reacts with groundwater and soil chemicals in the vicinity of the well. The injected solution/groundwater mixture is then recovered by pumping from the well. Samples of the recovered solution/groundwater mixture are collected periodically during extraction for analysis of tracer, chemical of interest, and reaction products. Transport properties and reactivity of the chemical of interest are inferred by comparing tracer concentrations to concentrations of the chemical of interest and reaction product concentrations in recovered water. PPTs

have been used by a number of researchers to determine the hydraulic properties of aquifers (Gűven et al., 1985; Hall et al., 1991), degradation rates of contaminants (Field et al., 1999; Istok et al., 2002; Pitterle et al., 2005), as well as the microbial degradation pathways (Reinhard et al., 1997; Schroth et al., 1998). The analysis of PPT is relatively simple and requires no previous knowledge of region groundwater flow or hydraulic parameters (Haggerty et al., 1998; Snodgrass et al., 1998).

The objective of this project was to assess the effectiveness of CMC-stabilized Fe-based nanoparticles as a potential remediation technology for chlorinated solvent contaminants. To the best of our knowledge, PPTs have not been applied to assess the mobility and reactivity of Fe-based nanoparticles at field scale. The specific objectives of this study were to (i) assess the feasibility of preparing CMC-stabilized Fe-based nanoparticles on site and being injected as soon as possible to maximally maintain the particle reactivity; (ii) assess the in situ transport characteristics of stabilized suspension of Fe-based nanoparticles; and (iii) assess the reactivity of freshly prepared CMC-stabilized ZVI nanoparticles, with and without palladium catalyst, for treating chlorinated solvents in situ.

7.2 Experimental Section

7.2.1 Site description

The site selected for the pilot test is an existing aerospace facility near San Francisco Bay located in Palo Alto, CA. The area is underlain by alluvial sediments, predominantly silts and clays, with coarse-grained sediments deposited along ancient stream beads. Coarse-grained channel deposits are the primary water-bearing zones

beneath the area, where the uppermost water-baring zone is generally encountered between 10 and 15 feet below ground surface (bgs). The test area is located within one of the relatively well-characterized source zones. An injection well, denoted I-1, served as the point of injection and withdrawal for the PPTs. Four PPTs were conducted in I-1 at different screened intervals.

7.2.2 Field preparation of stabilized nanoparticles

The preparation of ZVI nanoparticles was achieved by reducing ferrous ions with borohydride in aqueous phase on the site. Three batches were prepared: Batch 1 was approximately 31 gallons of ~ 1.0 g/L ZVI nanoparticle suspension stabilized by 0.8 wt.% NaCMC; Batch 2 was approximately 29 gallons of ~ 0.2 g/L ZVI nanoparticle suspension stabilized by 0.4 wt.% NaCMC; and Batch 3 was prepared as a 29 gallon batch Fe-Pd bimetallic nanoparticle suspension with a total iron content of ~ 1.0 g/L and Pd/Fe weight ratio of 0.1% (NaCMC: 0.8 wt.%). This batch was then diluted to approximately 87 gallons using deaerated tap water. The final suspension was composed of ~ 0.33 g/L Fe (Pd/Fe = 0.1 wt.%) and ~ 0.27 wt.% NaCMC. The detailed synthesis processes are described below.

Approximately 28 gallons of tap water were placed in a 55 gallon reactor and rapidly stirred with a 1/3 horsepower motorized impeller. The sodium carboxymethyl cellulose (NaCMC) powder 282 g to 564g was then added near the impeller while mixing, and the solution was mixed until no visible clumps were observed (~ 3 hrs). During mixing, the nitrogen gas was also supplied to purge the oxygen out of the reactor and help mixing. After the completion of NaCMC dissolution, approximately 113g to 564g $FeSO_4 \cdot 7H_2O$ (Fisher, Fair Lawn, NJ) (dissolved in ~ 1 gallon tap water) was added into

the reactor. As the stirring and N_2 purging were continuing, approximately 29.2g to 146g NaBH$_4$ (98%, Acros Organics, Morris Plains, NJ) was dissolved in ~ 1 gallon tap water and then added into the reactor. A minimum reaction time of 30 minutes was allowed during each preparation. The solution in the tank turned from a milky white to inky black as the nanoparticles were produced.

Palladium catalyst was added to form bimetallic ZVI nanoparticle suspension during preparation of Batch 3. Briefly, about 0.36 g Na$_2$PdCl$_4$·3H$_2$O (Strem, Newburyport, MA) was dissolved in 100ml tap water and slowly added into ZVI nanoparticle suspension in the reactor. In this way, Pd was coated on the surface of ZVI nanoparticles to form bimetallic ZVI nanoparticles. The 1g/L Fe-Pd suspension was then pumped into a 100gallon reactor for dilution, in which 58 gallon tap water had been purged with N_2 for 3 hours. Before the injection, sodium bromide (NaBr) was added to each freshly prepared batch of nanoscale ZVI particles for use as a conservative tracer.

7.2.3 Push-pull test (PPT) procedures

Four push-pull tests were conducted in this study. A "control" test was performed where potable water was injected in the uppermost screened interval of the injection well I-1 (e.g. PPT-1, April 6, 2006). Three push-pull tests were conducting using nanoscale ZVI from April 25, 2006 to May 2, 2006 in the uppermost (e.g. PPT-2), second (e.g. PPT-3), and third (e.g. PPT-4) screened intervals of injection well I-1. Inflatable straddle packers were installed in well I-1 to isolate the test interval for each test as shown in **Figure 7-1**. The details of the push-pull tests are summarized in **Table 7-1**.
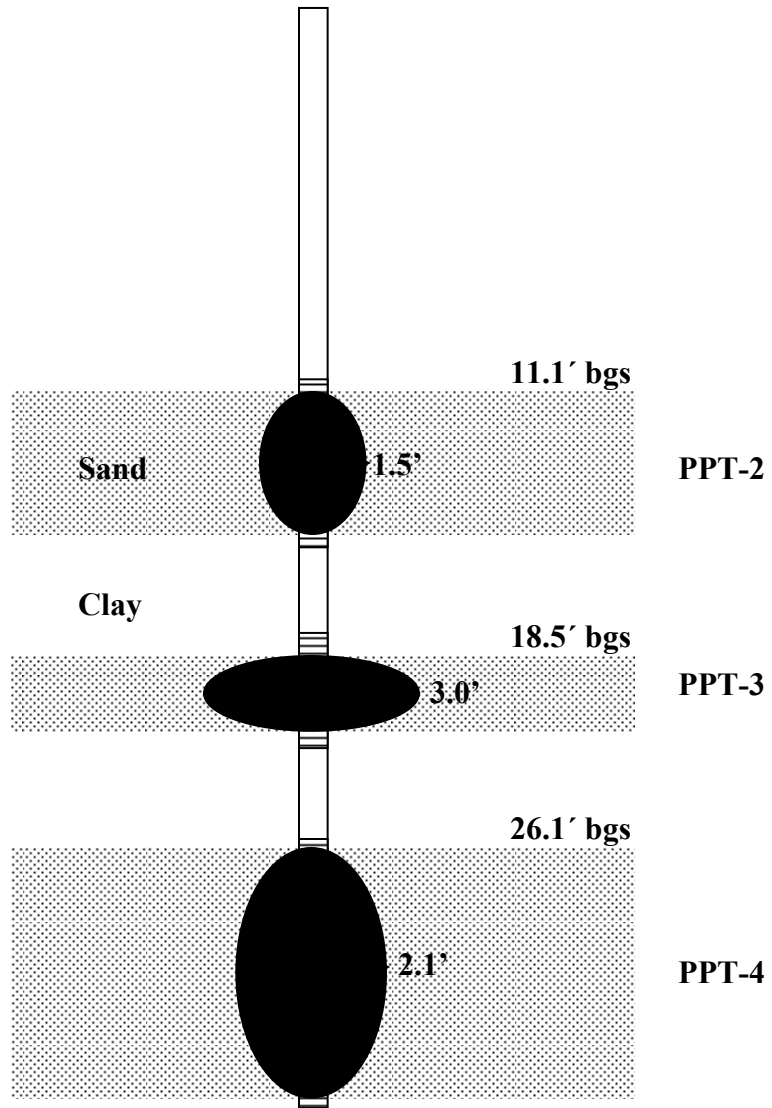
Figure 7-1. Schematic of the push-pull tests performed in injection well I-1.

Table 7-1. Push-Pull Test Details

Injection details	PPT-1	PPT-2	PPT-3	PPT-4
Date of injection	04/06/06	04/25/06	04/26/06	05/01/06
Solution composition	tap water	nZVI suspension	nZVI suspension	nZVI-Pd suspension
Reactive solute	none	nZVI (960 mg/L)	nZVI (210 mg/L)	nZVI-Pd (340 mg/L)
Conservative tracer	specific conductance (144 µS/cm)	Br^- (285 mg/L)	Br^- (284 mg/L)	Br^- (140 mg/L)
Screened interval of injection well (ft below top of casing)	11.1-15.3	11.1-15.3	18.5-20.6	26.1-33.1
Approximate vertical thickness of water-bearing zone (ft)	3.5	3.5	0.6	3
Soil type intercepted by well screen	poorly graded sand	poorly graded sand	silty sand	poorly graded sand
Volume of test solution injected (L)	699	117	113	329
Injection start time	10:12	19:25	15:46	20:57
Injection end time	12:24	20:00	17:23	23:04
Filter pack and casing volume (L)	36	36	18	40
Composition of chase solution	groundwater from test interval	deoxygenated tap water	deoxygenated tap water	deoxygenated tap water
Volume of chase solution (L)	53	111	19	19
Average injection rate (L/min)	5.3	3.4	1.2	2.6
Estimated distance traveled outside injection well (ft)	2.9	1.5	3.0	2.1
Extraction details				
Date of extraction	04/06/06	04/26/06	04/26-04/27/06	05/01-05/02/06
Volume extracted (L)	1440	659	286	756
Extraction start time	12:38	8:56	04/26/06 17:43	05/01/06 23:28
Extraction end time	16:15	12:11	04/27/06 12:11	05/02/06 5:30
Average extraction rate (L/min)	6.6	3.4	0.3	2.1

154

Table 7-2. Push-Pull Test Baseline Conditions

Baseline	PCE	TCE	cis-DCE	trans-DCE	VC	Methane	Ethene	Ethane	Total Iron	Boron	Bromide	Chloride	TOC
	μg/L	μg/L	μg/L	μg/L	μg/L	mg/L	μg/L	μg/L	mg/L	mg/L	mg/L	mg/L	mg/L
PPT-1	64	71	74	< 1.7	300	12	6	< 5	0.3	NA	0.65	52	NA
PPT-2	64	71	74	< 1.7	300	12	6	< 5	0.3	NA	0.65	52	NA
PPT-3	< 2	30	320	7	1600	13	18	< 5	4.4	0.6	0.68	74	NA
PPT-4	15	24	330	< 10	1300	6	9	< 5	18	1.4	1.1	87	550

Prior to injection, background samples were collected from the injection well intervals for analysis of bromide, total iron and VOCs. During PPT-1, the tap water was injected directly into the uppermost screened interval of injection well I-1 after passing the water through a flow-through cell containing a YSI multi-parameter probe, and a totalizer. Water levels were monitored during the injection process and did not increase by more than 0.15 feet during injection. The ZVI nanoparticle suspensions (with tracer NaBr) used for PPT-2, PPT-3, and PPT-4 were injected using a peristaltic pump that extracted liquid from the bottom of the batch reactor and injected it at the wellhead after passing through a totalizer and flow-through cell containing a YSI meter. A "chase" solution was added after the injection of each push-pull test to displace the residual test suspension from the well casing and into the surrounding filter-pack and soil (**Table 7-1**). Estimated travel distances (from simple volume-based radius of influence calculations) for the leading edge of the injection suspension, neglecting mechanical dispersion, ranged from 1.5 to 3 feet (**Figure 7-1** and **Table 7-1**).

After injection, water was extracted from each test interval using a peristaltic pump. Extracted volumes were 1.9 to 2.9 times larger than the injected volume. All water extracted during the push-pull tests was transferred to a storage tank on site for disposal. The extraction details are also summarized in **Table 7-1**.

7.2.4 Field measurements

Colorimetric methods (Standard Methods 3500Fe-D) were used to measure total iron concentrations in aqueous samples using a Hach® DR/2010 spectrophotometer at 590 nm. The tracer concentration (Br^-) was monitored with an ion-specific electrode (ISE; TempHion Water Quality Sensors, Instrumentation Northwest®). Measurements of

dissolved oxygen (DO), pH, specific electrical conductance (SC), temperature, and oxidation-reduction potential (ORP) were performed using a multi-parameter meter (YSI® Instruments Model 556 MPS).

7.2.5 Lab analyses

The following analyses were performed by Curtis and Tompkins Limited, a California-certified analytical laboratory, on samples of prepared suspensions and extracted water: 1) Total iron and boron in accordance with U.S. EPA Method 6010B; 2) ferrous iron in accordance with Method SM3500-Fe; 3) VOCs (PCE, TCE, cDCE, tDCE, and vinyl chloride) in accordance with U.S. EPA Method 8260B; 4) dissolved hydrocarbon gases (methane, ethene, and ethane) in accordance with Method RSK-175; 5) Cl⁻ and Br⁻ in accordance with U.S. EPA Method 300.0; and 6) total organic carbon (TOC) in accordance with U.S. EPA Method 415.2 (Note: all the data from Curtis and Tompkins were provided by Geomatrix Consultants, Inc.).

7.3 Results and Discussion

7.3.1 Baseline chemical conditions

Table 7-2 summarizes the PPT tests baseline sampling results. All baseline groundwater samples were reported to contain higher concentrations of reductive dechlorination breakdown products (cis-DCE and vinyl chloride) relative to parent chlorinated compounds (PCE and TCE), in conjunction with relatively high methane concentrations (6 to 12 mg/L), suggesting that baseline conditions were favorable for in situ bioremediation processes, perhaps due to the carbohydrate injection at another injection well, located approximately 20 feet east of injection well I-1. Dissolved total

iron concentrations ranged from 0.3 to 21 mg/L in baseline samples. The baseline sample for PPT-4 was analyzed for TOC and was reported to contain TOC at a concentration of 550 mg/L.

7.3.2 Field characterization of the ZVI nanoparticle suspension

Before injection, each batch of ZVI nanoparticle suspension was passed through a 10 μm filter as a field evaluation of particle size. PPT batches #2 and #3 passed through the filter with no visible retention of solid particles. However, after the filter test was performed on batch #4 (prior to dilution to 87 gallons), black staining was visible on the filter. Field testing indicated that the iron content of the filtrate was approximately 80% of the unfiltered concentration, suggesting that approximately 20% of the particles were aggregated to be larger than the desired size. Our prior lab studies showed that many factors such as CMC/Fe ratio, Fe concentration, temperature, pH and cations could affect the iron atom nucleation rate and consequently the particle size. In general, faster nucleation rate results in smaller nanoparticles. The aggregation here was possibly due to the slower adding rate of $NaBH_4$ during the preparation of this batch compared to others, which slowed down the reduction of Fe^{2+} and therefore the nucleation of the Fe atoms.

7.3.3 Assessment of tracer recovery, dilution, and desorption in the absence of ZVI nanoparticles

PPT-1 was conducted with tap water to act as a control for comparing chemical changes in extracted groundwater with those of subsequent tests using nanoscale ZVI. The tap water had a low specific conductance (SC) (144 μS/cm) compared to that of groundwater (average = 1,538 μS/cm). This low SC was used as a conservative tracer for

determining the proportion of the original injection solution from the "push" phase of the test compared to samples of water recovered during the "pull" phase, according to the following relationship:

$$SC^*(t) = \frac{SC_t - SC_{gw}}{SC_{inj} - SC_{gw}}$$

Where $SC^*(t)$ is the relative specific conductance at time t; SC_t is the measured specific conductance at time t; SC_{gw} is the specific conductance of ambient (background) groundwater; and SC_{inj} is the specific conductance of injected tap water.

Therefore, $SC^*(t)$ could be used as a dilution factor and $1-SC^*(t)$ reflects how much SC is from the groundwater. The $1-SC^*(t)$ of PPT-1 is plotted in **Figure 7-2**. Since groundwater was used as the chase solution in this test, the extracted water initially had a high $1-SC^*(t)$ and shortly the $1-SC^*(t)$ sharply decreased as the tap water was recovered from the well. Then the $1-SC^*(t)$ steadily increased as the groundwater was replacing the tap water in the well. Approximately twice the injected volume of solution was extracted (**Table 7-1**) before SC appeared to stabilize towards initial pre-test values suggesting that extraction volumes of approximately twice the injection volume would be sufficient for performing subsequent tests. Samples of extracted water were collected periodically during the extraction phase for analysis. VOCs and $1-SC^*(t)$ were plotted against time since injection to assess the effects of dilution and desorption on concentration (**Figure 7-2**). As expected, **Figure 7-2** suggests that the primary control on concentration of groundwater constituents in extraction samples is dilution, although some retardation of cis-DCE and VC were observed. Therefore, the comparison between VOCs especially

PCE and TCE curves and dilution curve in the subsequent nanoscale ZVI tests can be a criterion for evaluating the degradation of PCE and TCE.

7.3.4 Assessment of nanoscale ZVI transport

Transport properties of nanosclae ZVI particles were assessed by comparing the mass recovery of injected Fe relative to tracer Br⁻. The results from the extraction phase of PPT-2, PPT-3, and PPT-4 are plotted in **Figures 7-3**, **7-4**, and **7-5**. The masses of Fe and Br⁻ recovered during PPT-2, PPT-3, and PPT-4 were estimated from the area under the Concentration versus Volume Extracted curves shown in **Figures 7-3**, **7-4**, and **7-5**.

As shown in **Figure 7-3**, only ~ 2.6% of injected iron was recovered during PPT-2, compared to ~ 61% Br⁻ recovery, suggesting that the ZVI nanoparticles had become essentially immobile over the lag time of approximately 13 hours between the end of the injection and the beginning of the extraction phase of PPT-2 (**Table 7-1**). Greater Fe recovery (approximately 21%) was observed during PPT-3, where the majority of Fe recovery occurred during the extraction of approximately 60 L of water (approximately half of the injection volume of the ZVI nanoparticle suspension) shortly after the injection phase. After extracting ~ 60 L, a lag time of approximately 13 hours was allowed before extraction was re-initiated. Very little Fe was recovered after this lag time (**Figure 7-4**). Fe recovery was highest for PPT-4 (approximately 31%), compared to 76% for Br recovery (**Figure 7-5**). Higher recoveries may be due to that the extraction was initiated after injection with very little lag time and occurred continuously, without major intervening lag times.
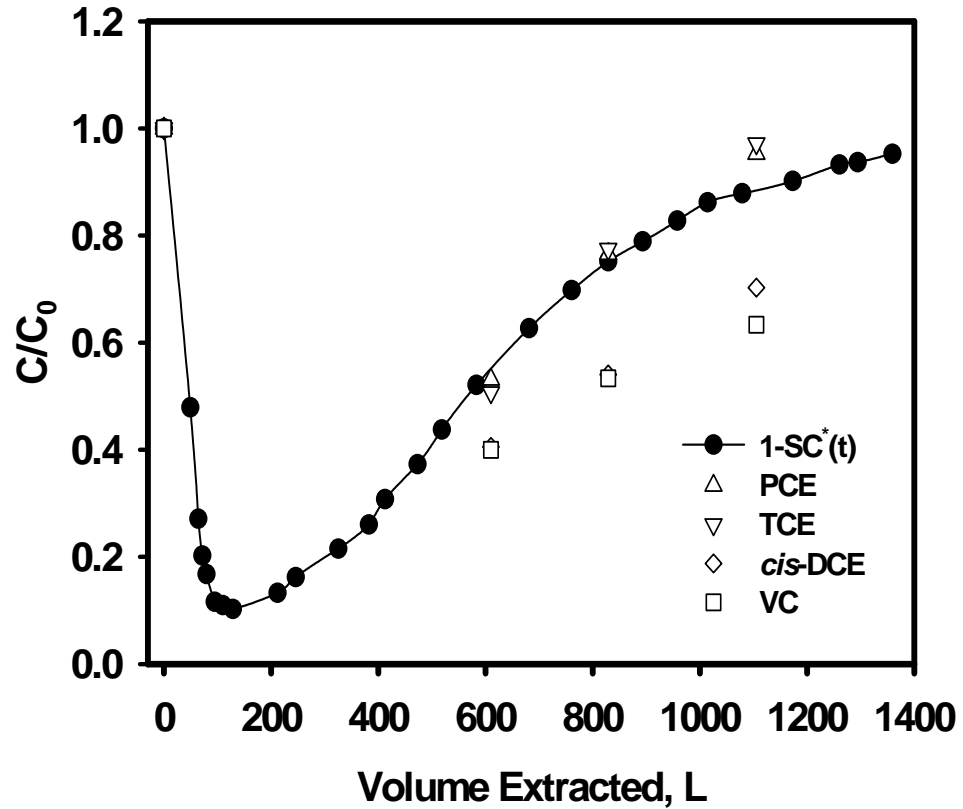
Figure 7-2. Evolution of VOCs and 1-SC*(t) in extracted groundwater samples during PPT-1. Experimental conditions are: V_{inj} = 752 L, V_{ext} = 1,440 L, SC (groundwater) = 1,538 μS/cm, SC (tap water) = 144 μS/cm, C_0 (PCE) = 64 μg/L, C_0 (TCE) = 71 μg/L, C_0 (cis-DCE) = 74 μg/L, C_0 (VC) = 300 μg/L.
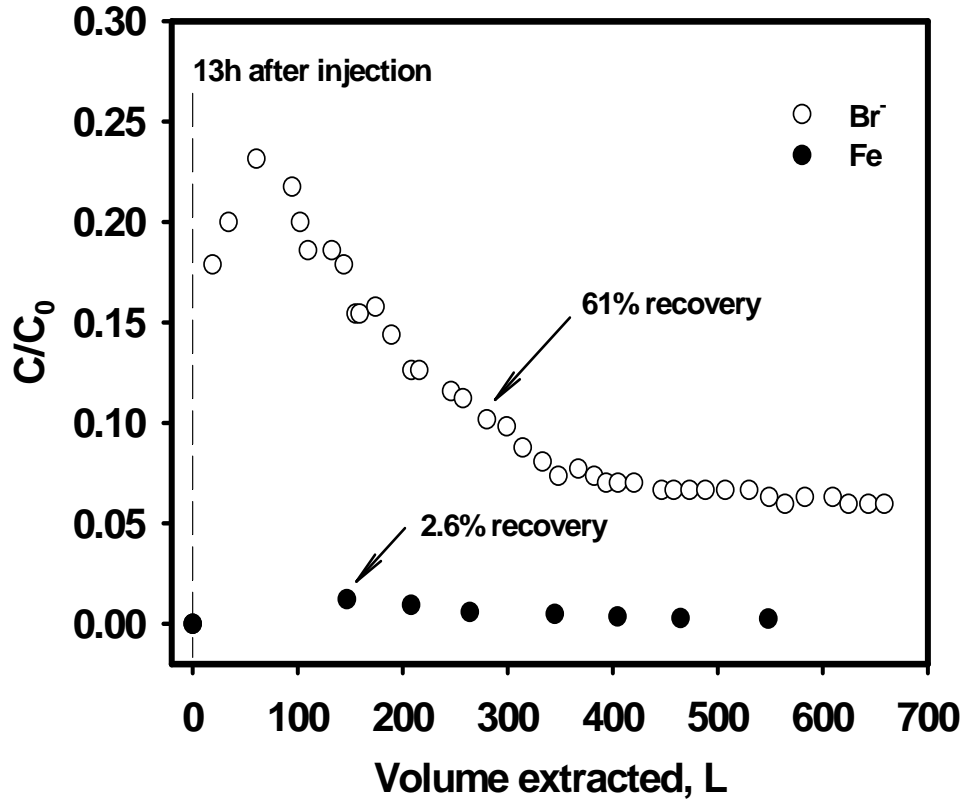
Figure 7-3. Mass recovery of Fe relative to tracer Br$^-$ in extracted groundwater during PPT-2 (13 hr lag time between injection and extraction), V_{inj} = 128 L, V_{ext} = 659 L, Fe_{inj} = 960 mg/L, Br_{inj} = 285 mg/L.
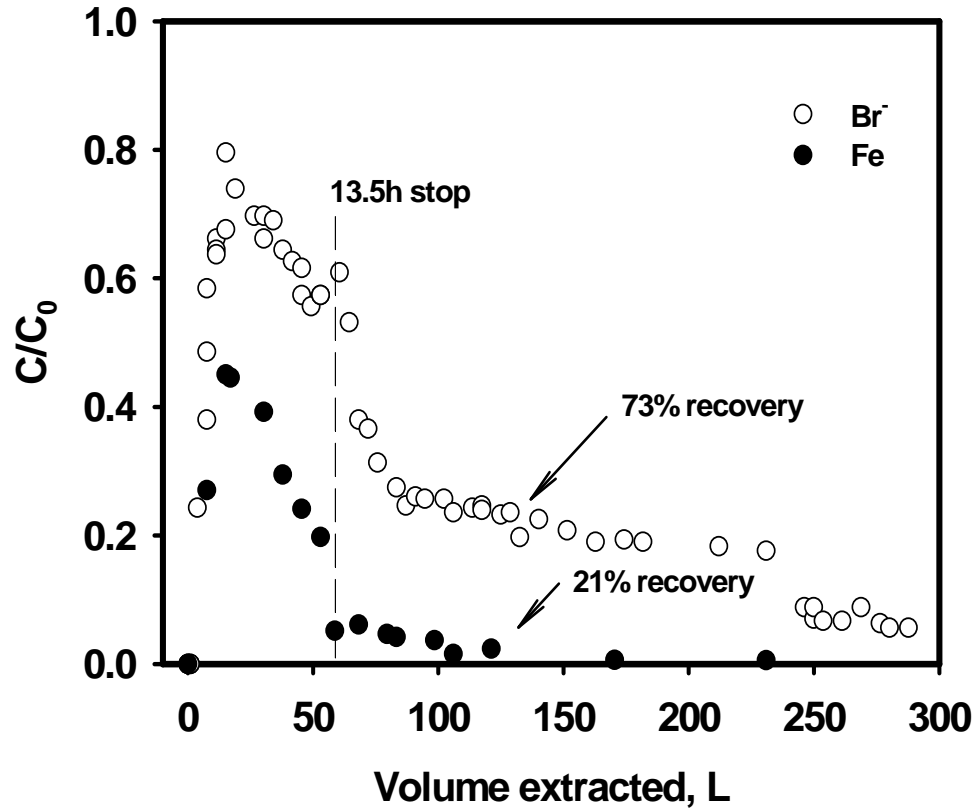
Figure 7-4. Mass recovery of Fe relative to tracer Br⁻ in extracted groundwater samples during PPT-3 (13.5 hr lag time after extracting 60 L). V_{inj} = 132 L, V_{ext} = 286 L, Fe_{inj} = 210 mg/L, Br_{inj} = 284 mg/L.
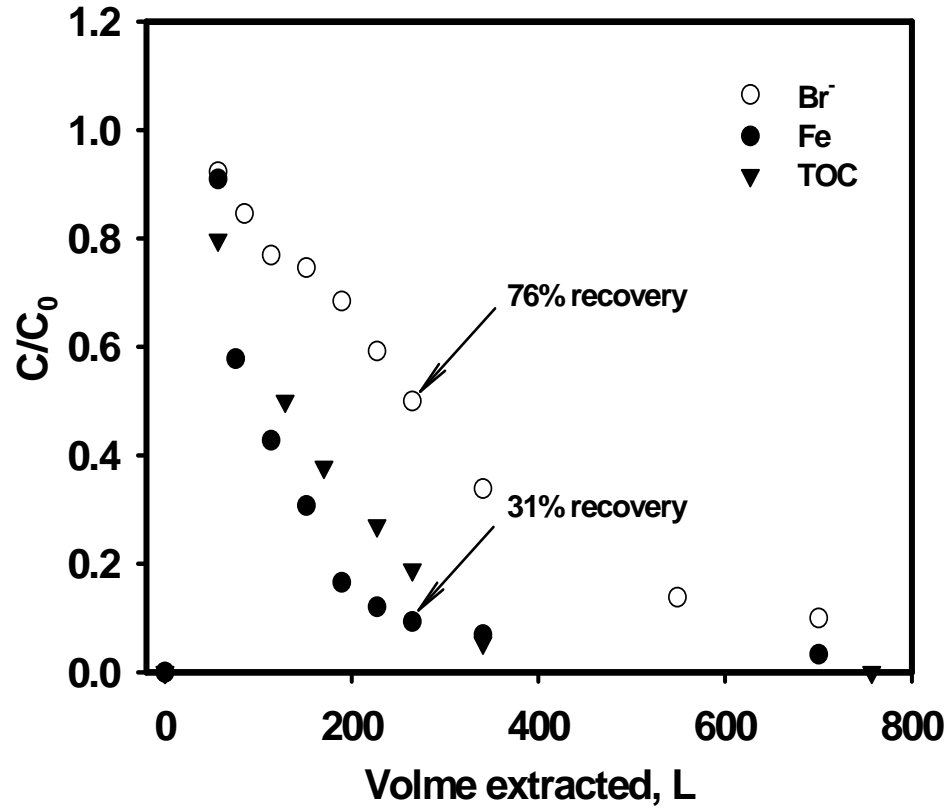
Figure 7-5. Mass recovery of Fe relative to tracer Br$^-$ in extracted groundwater samples during PPT-4 (no lag time). V_{inj} = 369 L, V_{ext} = 756 L, Fe_{inj} = 340 mg/L, Br_{inj} = 140 mg/L, TOC (background) = 550 mg/L.

The filtration of colloids within porous media is generally determined by three major mechanism: 1) Brownian or molecular diffusion by which random motion of colloidal particle is brought about by thermal effects; 2) convective fluid flow wherein particles flow with water; and 3) gravitational effects producing vertical movement of particles (Elliott and Zhang, 2001). Filtration caused by Brownian motion tends to dominate for small particles (e.g. <0.1 μm) whereas filtration induced by gravity outweighs Brownian diffusion for large particles (e.g. > 1μm). The hydrodynamic diameter of CMC-stabilized Fe nanoparticles is lab-determined to be ~ 20nm. Therefore, Brownian motion should be the primary mechanism of Fe nanoparticle filtration in the soil at the initial push-pull stage. However, the Fe nanoparticles may undergo aggregation under the subsurface environment with time. For example, the bacteria in the soil can biodegrade the polysaccharide stabilizer and cause aggregation. Although it is not possible that the bacteria can complete biodegrade the CMC to CO_2 and H_2O in a short residence time of 13h, it is likely that the bacteria can break down the long chain of the CMC molecule, which could significantly decrease the stabilization ability of the CMC molecule and cause particle aggregation (He and Zhao, 2007a). Moreover, the high ionic strength and cations in the groundwater could also cause the aggregation of nanoparticle to micro-scale, where the gravitational effect would dominate the filtration of the particles (He and Zhao, 2007a). No matter what is the main mechanism of filtration, Fe nanoparticles exhibit apparent timeframe for mobility, which implies that human exposure resulting from remediation applications of nZVI is likely to be minimal.

From **Figure 7-5**, it is also noteworthy that the total organic carbon (TOC) in extracted water from PPT-4 decreased at similar apparent rates with Fe concentration.

These results imply that the majority of the CMC was attached on the Fe particles and also intercepted by the soil bed as the particles were blocked. The corrosion of Fe continuously releases H_2, which is the preferred electron donor for microorganisms that biodegrade chlorinated solvents (Seshadri et al., 2005). At the meanwhile, the polysaccharide stabilizer provides the ideal carbon source for bacteria. Therefore, the Fe transported into the soil can not only reduce the chlorinated solvents abiotically but also can significantly enhance the biodegradation of chlorinated solvents in the groundwater, which could increase the attractiveness of NZVI for chlorinated solvents remediation.

7.3.5 Effects of nanoscale ZVI injection on groundwater chemistry

During PPT-2, the ORP of water extracted decreased to values below -500 millivolts (mV) (**Figure 7-6**) compared to baseline ORP values of -173 to -234 mV. The ORP remained low at the end of the extraction phase of PPT-2, after most of the injected suspension had been recovered. Calculations suggest that over 100 grams of nanoscale ZVI particles were immobilized and would, therefore, remain in the soil and create the strong reducing environment. ORP also significantly decreased during the initial extraction phases of PPT-3 and PPT-4, and increased during later stages of extraction (**Figures 7-6**). The more Fe was injected, the lower ORP was generated in the extracted water. The decrease of ORP is attributable to the consumption of oxidants by the nanoparticles as they migrated within the aquifer. The decreasing of ORP provided a favorable environment for reductive dechlorination, which further indicates the potential of biodegradation enhancement of chlorinated solvents with injection of nanoscale ZVI.
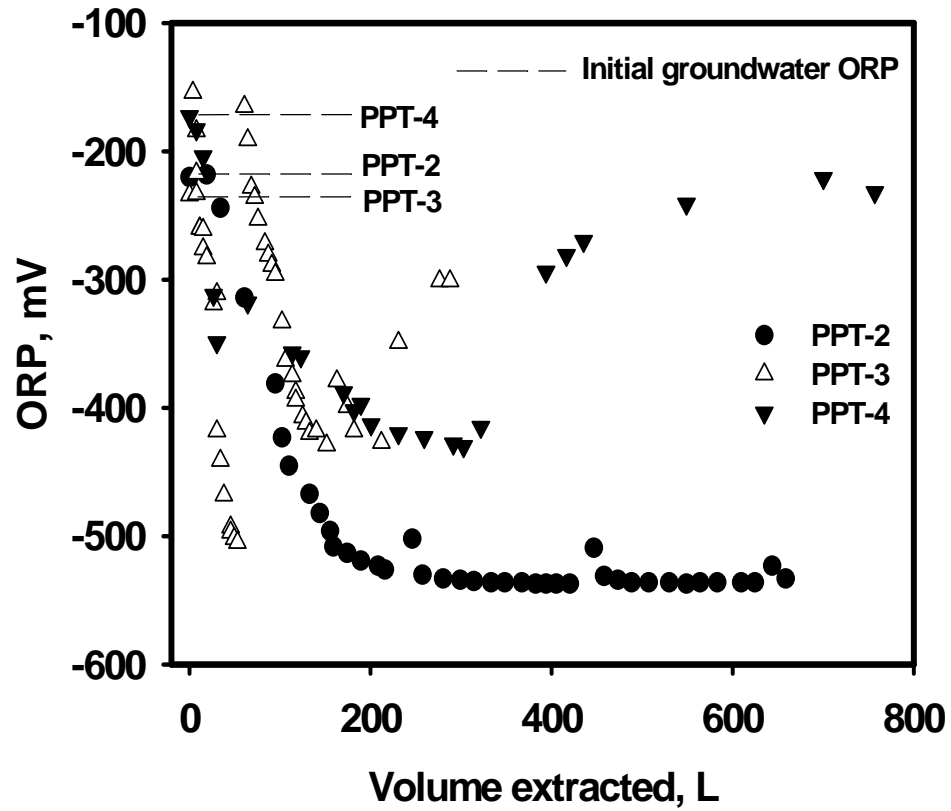
Figure 7-6. Changes of oxidation and reduction potential (ORP) of extracted groundwater during extraction phases of PPT-2, PPT-3, and PPT-4.
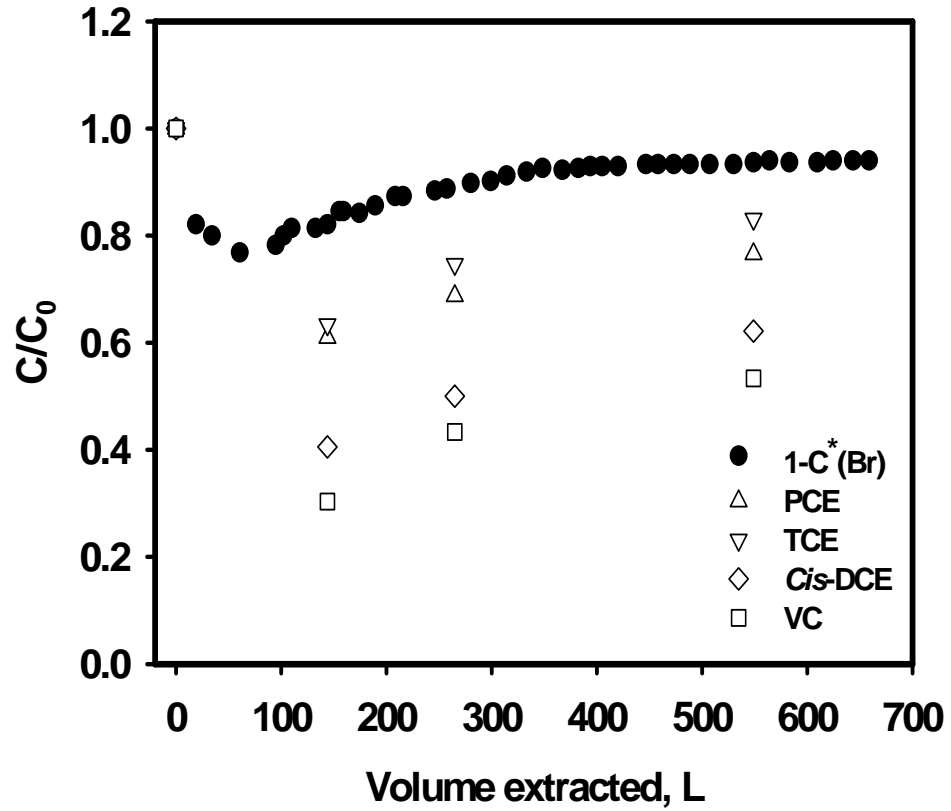
Figure 7-7. Changes of chlorinated contaminant and tracer concentrations in PPT-2 extracted groundwater samples.
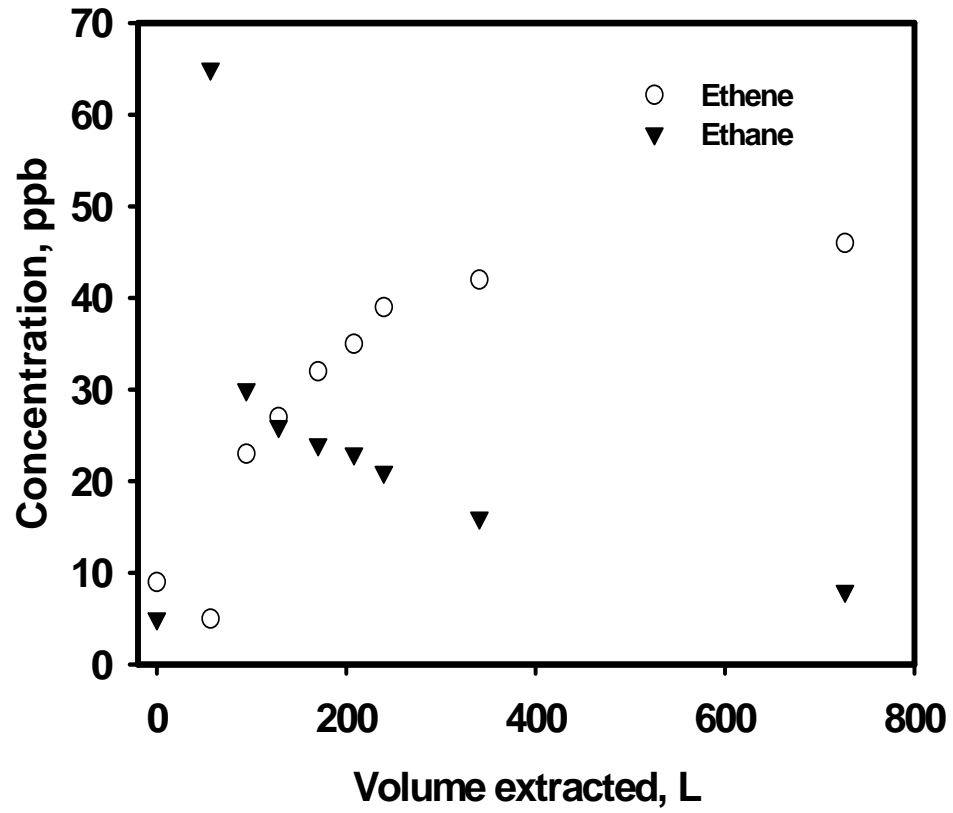
Figure 7-8. Evolution of ethane and ethene in PPT-4 extracted groundwater samples.

7.3.6 Assessment of nanoscale ZVI reactivity

Normalized concentration of chlorinated solvents (C/C_0) and $1\text{-}C_{Br}(t)/C_{Br}(0)$ versus time were plotted and compared to assess the reactivity of NZVI. Curve $1\text{-}C_{Br}(t)/C_{Br}(0)$ versus time represents the dilution of chlorinated solvents. If no degradation underwent, the PCE and TCE curves should match the dilution curve as indicated in the PPT-1 baseline test. The PPT-2 test was performed in the same zone as PPT-1. Therefore, same behavior of PCE and TCE curves were expected in PPT-2 if no degradation underwent. However, the PCE and TCE curves are apparently 10-20% under the dilution curve from PPT-2 as shown in **Figure 7-7**, which indicated about 10-20% degradation of PCE and TCE. The cis-DCE and VC curves are 10-20% more away from the dilution curve considering their retardation, which also indicates their degradation. These results demonstrated the reactivity of ZVI mono nanoparticles toward chlorinated solvents in groundwater. In PPT-3 and PPT-4, significantly higher concentrations of some chlorinated solvents, for example PCE in PPT-3 and c-DCE and VC in PPT-4 (data not shown), were observed in extracted water sample than the pre-injection groundwater, which indicates the change of groundwater chemistry after the pre-injection sampling. Moreover, the PPT-3 and PPT-4 were performed in the different zones compared to PPT-1. Both of these two factors make the comparison between dilution and degradation difficult and inclusive. However, in PPT-4, significant amount of ethane and ethene were detected in the extracted water as shown in **Figure 7-8**, which shows the fast dechlorination of the chlorinated contaminants. From **Figure 7-8**, ethane concentration in the extracted water exhibited a sharp increase from undetectable to 65 ppb during 0-25L extraction and gradually decreased. The ethane curve well matches the Fe elution curve

in **Figure 7-5** with higher ethane production at higher Fe concentration, which indicates the abiotic degradation of the chlorinated solvents. These observation is consistent to the lab results that ethane is the primary product of abiotic degradation of chlorinated solvents by nanoscale ZVI or Fe-Pd (Lien and Zhang, 2001; Liu et al., 2005b). Interestingly, ethene concentration underwent a slight dilution and continuously increased during the whole extraction period. Since ethene is the minor and intermediate product of abiotic degradation by nanoscale ZVI and the main product of biodegradation, these results may imply an incomplete abiotic degradation and a biologically enhanced reductive dechlorination of VOCs in the presence of nanoscale ZVI at later stage of extraction. The integration of the ethane and ethene curves gives the production of 3.7 mg ethane and 7.0 mg ethene in 756 L extracted water, which accounts for the complete removal of 63.5 ppb TCE in the absence of other chlorinated contaminants.

7.4 Conclusions

Based on the field testing results, it is concluded that:

- Preparation of stabilized ZVI nanoparticles can be accomplished in the field using a "batch reactor" for immediate injection to minimize losses in reactivity.

- The ZVI nanoparticles could be transported in the subsurface, but appeared to lose mobility over time such that greater than 50% of the particles could become immobile within a few hours of injection. Human exposure to Fe nanomaterials resulting from remediation application of nanoscale ZVI will be minimal.

- Freshly prepared stabilized suspensions of ZVI nanoparticles, with and without palladium catalyst, appear to have certain degree of reactivity toward VOCs in situ.

171

CHAPTER 8. FIELD ASSESSMENT OF CMC-STABILIZED FE-PD NANOPARTICLES FOR IN SITU CHLORINATED SOLVENT TREATMENT IN SOURCE ZONE

In the previous chapter, the soil mobility and reactivity of the Fe-Pd nanoparticles at a contaminated site were demonstrated by push-pull tests. However, push-pull tests can only investigate the short-term performance of the nanoparticles in the field. This chapter presents the results of a long-term field-scale assessment of CMC-stabilized Fe-Pd nanoparticles for source zone chlorinated solvent treatment. Two injections were performed in 1 month at a Northern Alabama site. The change of groundwater quality after injection was followed up to 4 months.

8.1 Introduction

Chlorinated hydrocarbons, such as polychlorinated biphenyls (PCBs), tetrachloroethylene (PCE) and trichloroethylene (TCE), are well-known potent toxins to human health and the environment (ATSDR, 2007). Although the uses of chlorinated hydrocarbons have now been either banned or highly restricted, the past massive production and applications have left an environmental legacy that high concentrations of chlorinated hydrocarbons are commonly detected in U.S. groundwater and soils.

Unfortunately, there have been no cost-effective and environmentally benign remediation technologies available for remediation of chlorinated solvents in soils and groundwater despite tremendous research efforts in the past three decades. To a great

172

extent, current remediation practices rely on pump and treat or excavation and landfill of contaminated soils, which are extremely costly and/or environmentally disruptive (Berti and Cunningham, 1997). Moreover, for cases like the sites located in the heavily populated area, engineered processes (e.g., excavation) are highly restricted.

Recently, our research group developed a new class of highly dispersed ZVI nanoparticles that were stabilized by low-cost and "green" carboxymethyl cellulose (CMC) (He et al., 2007; He and Zhao, 2007a, b). Our prior studies showed that these stabilized nanoparticles were highly reactive toward chlorinated solvents after coated with Pd (e.g. Fe-Pd bimetallic nanoparticles) and readily dispersible in the soil and therefore suitable for in situ injection. Column tests indicated that DNAPL dechlorination could be achieved with the injection of this new material into the porous media (Chapter 6). Therefore, it is expected that this technology can be applied in the field for source zone (e.g. hot spot) treatment, which has the potential to significantly cut down the remediation cost and time required for site cleanup.

In 2006, four push-pull tests were conducted by our research group and Geomatrix Consultants, Inc. in CA, which suggested that the CMC-stabilized ZVI and Fe-Pd nanoparticles were mobile in the soil and were reactive toward the chlorinated contaminants. However, the relatively low concentrations of chlorinated solvents in the test area (e.g. <2 ppm) implied that effectiveness of this technology for source zone remediation was not fully evaluated. Moreover, although push-pull test is simple and informative, it can only investigate the short-term (< 2d) performance of the nanoparticles. However, one potential advantage of this technology is its expected enhancement on long-term bioremediation of chlorinated solvents by acting as a long-

term H_2 source (Elliott and Zhang, 2001; Liu and Lowry, 2006). H_2 is the preferred electron donor for microorganisms that biodegrade chlorinated solvents (Seshadri et al., 2005).

Therefore, this field test aimed to pilot-test the field application of this cutting edge remediation technology for source zone chlorinated solvent treatment at a long term scale. The feasibility (dispersibility, reactivity, and reactive longevity) of the iron nanoparticles when applied under field conditions is evaluated.

8.2 Experimental Section

8.2.1 Site selection and test area description

The site selected for the pilot test is an abandoned metal processing plant site in northern Alabama. The test area is located within one of the relatively well-characterized source zones. The dimensions of the test area were approximately 15.0 ft by 9.0 ft, as shown in **Figure 8-1**. An injection well, denoted IW-1, was installed to inject the stabilized Fe suspension into the subsurface. The injection well was screened from 45 ft to 50 ft (right above the bed rock) below ground surface. The test area also contained three monitoring well with one (MW-3) at 5-ft up-gradient and two others (MW-1 and MW-2) located at 5ft and 10ft, respectively, down-gradient of the injection well along the groundwater flow direction. MW-1 and MW-3 were screened from 45 ft to 50 ft, while MW-2 was screened from 40 ft to 45 ft due to the change of bed rock level (from 50 ft to 45 ft). The hydraulic conductivity (K) of the aquifer within the test zone was determined to be 20 ft/day (i.e. 0.42 cm/min).

Nanoparticle
suspension

40ft

Submersible pump

45ft

45ft

50ft

MW-3   IW-1   MW-1   MW-2

5 ft   5 ft   5 ft
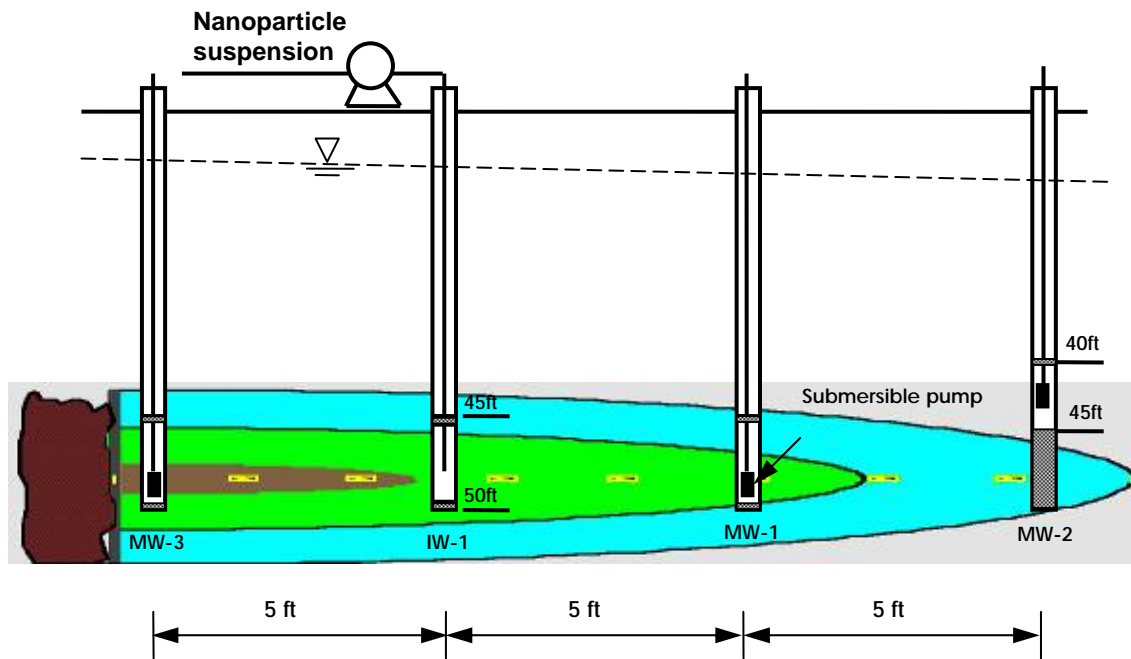
*: The plume schematic is adopted from Biochlor 2.2

Figure 8-1. A sectional view of the aquifer at the testing site and schematic of the in situ injection of CMC-stabilized Fe-Pd nanoparticles.

8.2.2 Groundwater quality in the test area

Groundwater quality within the test area has been monitored regularly for approximately a decade. Several chlorinated hydrocarbon contaminants including tetrachloroethene (PCE), trichloroethene (TCE), cis-dichloroethene (cis-DCE), trans-dichloroethene (trans-DCE), vinyl chloride (VC) and PCB1242 at levels ranging from ~ 1 ppb to 220 ppm have been recorded. The concentration of the primary contaminants PCE, TCE and PCB1242 in the test area ranged from 1.2 ppm to 12.0 ppm, 1.6 ppm to 23.8 ppm, and 6.9 ppb to 97.4 ppb, respectively, right before the field study.

8.2.3 Field preparation of stabilized nanoparticles

The preparation of ZVI nanoparticles was achieved by reducing ferrous ions with borohydride in aqueous phase on site. Two series of batches of Fe-Pd nanoparticle suspensions were prepared for injections conducted on 01/29/2007 (Injection #1) and 02/26/2007 (Injection #2), respectively. For injection #1, 1 batch of ~ 30 gallons Fe-Pd nanoparticle suspension (Fe = 1.0 g/L, Pd/Fe = 0.1 wt.%, NaCMC = 0.5 wt.%) was synthesis and diluted to ~ 150 gallons (e.g. Fe = 0.2 g/L, Pd/Fe = 0.1 wt.%, NaCMC = 0.1 wt.%) right before injection. For injection #2, four batches of ~ 37.5 gallons Fe-Pd nanoparticle suspensions (Fe = 1.0 g/L, Pd/Fe = 0.1 wt.%, NaCMC = 0.6 wt.%) were prepared in two identical batch reactors and injected into the ground continuously. The preparation of nanoparticles is briefed as follows.

Approximately 28 to 35.5 gallons of tap water were placed in a 65 gallon polyethylene reactor and rapidly stirred with a 1/3 horsepower motorized impeller. The polysaccharide powder (sodium carboxymethyl cellulose, NaCMC) 564 g to 844 g was

then added near the impeller while mixing, and the solution was mixed until no visible clumps were observed (~ 3 hours). During mixing, the nitrogen gas was also supplied to purge the oxygen out of the reactor and help mixing. After the completion of NaCMC dissolution, approximately 564 g to 705 g $FeSO_4 \cdot 7H_2O$ (Fisher, Fair Lawn, NJ) was dissolved in 1 gallon tap water and added into the reactor. As the stirring and N_2 purging continued, 146 g to 183 g $NaBH_4$ (98%, Acros Organics, Morris Plains, NJ) was dissolved in 1 gallon tap water. Then, the $NaBH_4$ solution was added into the reactor at a rate of 0.5 L/min. The solution in the tank turned from a milky white to inky black as the nanoparticles were formed. Finally, about 0.5 g to 0.6 g $Na_2PdCl_4 \cdot 3H_2O$ (Strem, Newburyport, MA) was dissolved in 100 ml tap water and slowly added into the reactor. In this way, Pd was coated on the surface of iron nanoparticles to form bimetallic ZVI nanoparticles. The expected NaCMC concentration was 0.5 wt.% for batch used in injection #1 and 0.6 wt.% for batches used in injection #2. The expected Fe concentration for all batches was 1 g/L with Pd/Fe = 0.1 wt.%.

For injection #1, the synthesized suspension was pumped into a 200 gallon reactor for dilution, in which 120 gallon tap water had been purged with N_2 for 3 hours. The diluted suspension had a Fe concentration of 0.2 g/L with a volume of 150 gallons. Before injection, ~ 34 g KBr (dissolved in 100 ml water) was added into the 200 gallon reactor to be used as a tracer. For injection #2, no dilution was conducted; ~ 14 g KBr (dissolved in 100 ml water) was added into each batch to be used as a tracer.

8.2.4 Iron suspension injection and groundwater monitoring

The nanoparticle suspension was injected into the screened interval of injection well IW-1 using a peristaltic pump. For injection #1, the injection rate was adjusted to

avoid the overflow of Fe suspension from the opened wellhead. The final injection rate was fixed at 0.67 gallon/min. The nanoparticle suspension was driven into the aquifer through the static hydraulic head only (the pump did not exert additional pressure). For injection #2, the well head of IW-1 was sealed and connected to a pressure gauge. The injection rate was fixed at 1.34 gallon/min. In this case, an injection pressure should be applied although no readings were distinguished from the gauge. For injection #1, groundwater samples were collected from two monitoring wells MW-1 and MW-2 before and after injection. However, for injection #2, groundwater samples were collected from both the monitoring wells MW-1, MW-2 and MW-3 and injection well IW-1. Particularly, the sampling from IW-1 started ~ 1 hr after the end of injection to make sure that the samples collected were not the injected suspension. Samples were collected without purging using 12V dedicated submersible pumps installed in each of the three monitoring wells. Samples from IW-1 were collected using the peristaltic pump, which was used for nanoparticle injection. A multi-parameter probe with a flow-through cell was used to collect pH, specific conductance, oxidation-reduction potential (ORP), dissolved oxygen (DO), and temperature readings during sampling activities.

8.2.5 Laboratory feasibility studies

Prior to the field test, laboratory feasibility studies were conducted using groundwater from the site. During the tests, 20 mL stabilized Fe-Pd nanoparticle suspension (Fe = 1.0 g/L, Pd/Fe = 0.1 wt.%, NaCMC = 0.5 wt.%) was mixed with 23 mL groundwater obtained from MW-3. The batch vials (43 mL) were then cap-sealed with Teflon-lined septa and placed on a rotary shaker at 50 rpm for degradation tests. Parallel experiments were also performed to degrade same amount of PCE and TCE in deionized

water solution. To test the change in particle reactivity with the particle age (i.e. storage time in water), replicate samples of 0.1g/L lab-synthesized Fe-Pd nanoparticle suspension were stored in sealed glass vials (with zero headspace) and kept in a refrigerator at 4 ^{o}C for up to 9 days before being tested. The particle reactivity was then evaluated through the degradation of TCE following the procedure described elsewhere (He et al., 2007).

8.2.6 Laboratory analyses

The analysis of primary contaminants PCE, TCE, and PCB1242 was carried out in the lab. In brief, 0.1 mL of the groundwater sample was withdrawn from the 43 mL vials using a 100 µL gas-tight syringe; then the sample was transferred into a 2 mL GC vial containing 1 mL of hexane for extraction of TCE; upon phase separation, the extract was analyzed for chlorinated solvents using a HP 6890 GC equipped with an RTX-624 capillary column (32 m long and 0.32 mm ID, Restek Co. Bellefonte, PA, USA) and an ECD. For PCBs analysis, 33 mL groundwater was extracted using 3 mL hexane in the 43 mL vials. PCBs in the hexane phase were then analyzed using an HP 6890 GC equipped with an HP5 capillary column (32 m long, 0.25 mm ID, Agilent, Santa Clara, CA, USA) and ECD.

For total iron tests, 1mL of the groundwater sample was withdrawn, dissolved in 4 mL HCl, diluted with DI water to 15 mL, and analyzed for total iron using a flame atomic-absorption spectrophotometer (AAS) (220FS, Varian, Palo Alto, CA). Bromide and sulfate were analyzed using a Dionex Ion Chromatography (DX-120, Dionex, Sunnyvale, CA) equipped with an AS14 column, an AG14 guard column and a 100 µL sample loop. Before analysis, groundwater sample was filtered through a 0.45 µm membrane filter to remove the colloids.

8.3 Results and Discussion

8.3.1 Laboratory testing results

Figures 8-2 depicts the reduction of PCE and TCE in batch tests with the field groundwater extracted from monitoring well MW-3 and with PCE/TCE solutions prepared using DI water. Complete destruction of TCE (C_0 = 15.0 ppm) was achieved within 3 hr for the groundwater sample containing 0.47 g/L Fe-Pd (Pd/Fe = 0.1 wt.%). More than 70% removal of PCE (C_0 = 9.6 ppm) in the groundwater sample was also achieved within the tested timeframe of 6 hr. Although it appears that PCE is more persistent than TCE to Fe-Pd reduction in groundwater, both of them are readily degradable by the stabilized Fe-Pd nanoparticles. Much more rapid degradation of both PCE and TCE was observed in lab-prepared PCE/TCE solution. Complete destruction of both PCE and TCE was achieved in 1 h. According to our prior studies, the reactivity of the stabilized Fe-Pd nanoparticles is essentially a function of solution pH, ionic strength and dissolved organic matters (DOM) (He and Zhao, 2007b). Since the pH and the ionic strength of the two studied samples were set to be similar, the reduced reactivity of the nanoparticles in groundwater is attributed to competitive effects of other oxidizing agents such as DO and sulfide, and to inhibitive effect due to adsorption of the groundwater DOM on the particle surface, which competes the reactive sites and hinder the dechlorination of the target chlorinated compounds.
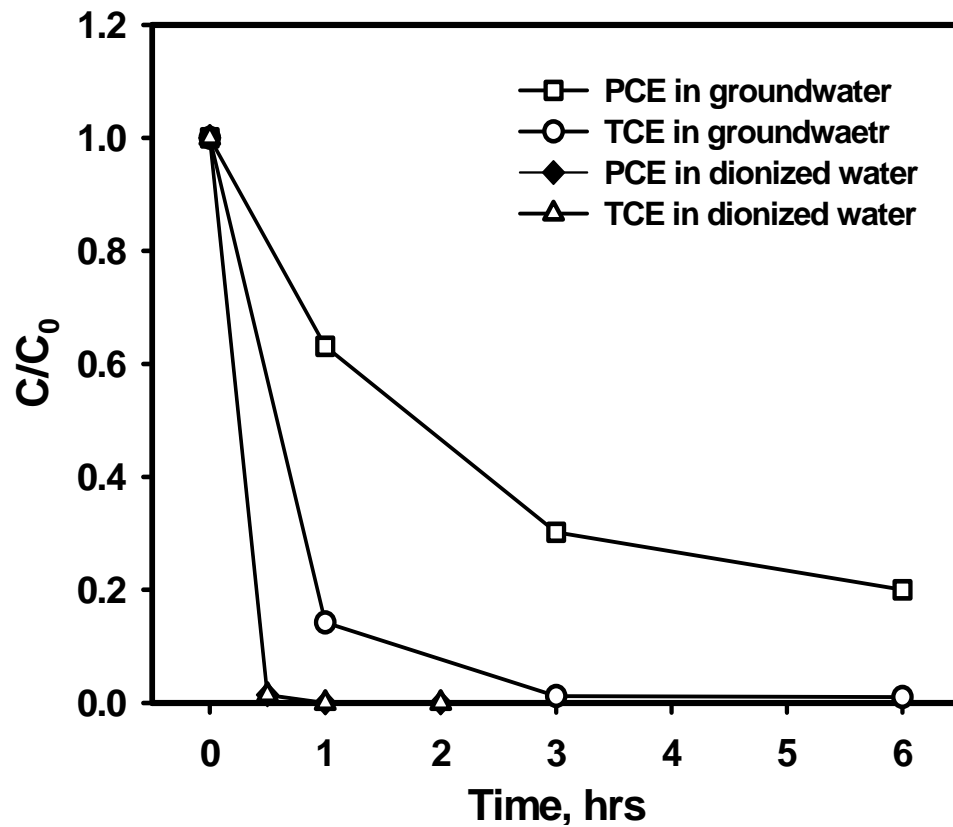
Figure 8-2. Reduction of PCE and TCE in a field groundwater and DI water with Fe-Pd nanoparticles synthesized in the lab. Iron dose was 0.47 g/L, Pd/Fe = 0.1 wt.%, NaCMC = 0.5 wt.%, $C_{PCE, 0}$ = 9.6 ppm, $C_{TCE, 0}$ = 15.0 ppm.

8.3.2 On-site nanoparticle preparation

The on site scale-up synthesis of CMC-stabilized Fe-Pd nanoparticles was successfully implemented. **Figure 8-3** presents the appearance of the field-prepared stabilized Pd-Fe nanoparticle suspension. The nanoparticle suspension appeared as black and inky liquid. Based on our prior lab tests, the resultant nanoparticles (Fe = 1.0 g/L; NaCMC = 0.5 wt.%) possessed a particle size around 22.8 ± 4.3 nm (He and Zhao, 2007a). A simple test carried out in the field showed that the nanoparticle suspension passed through a Fisher filter paper (P5) (particle interception: >1 μm) without obvious retention of solid particles observed. It is well known that Fe nanoparticles could continuously dissolve in water because of corrosion and lose reactivity. The successful synthesis of the nanoparticles on site maximally maintained the particle reactivity and therefore their lifetime for dechlorination.

8.3.3 Iron transport in the test area

Soil mobility is a critical characteristic of iron nanoparticles for their potential proactive destruction of chlorinated solvents in soil and groundwater. In order to monitor the migration of the nanoparticles, total iron concentration was measured at two down-gradient monitoring wells MW-1 and MW-2 for injection #1 and at monitoring wells MW-1, MW-2, and MW-3 and injection well IW-1 for injection #2 throughout the tests. **Figure 8-4** shows the injection of the nanoparticle suspension and the groundwater sample collection from monitoring well MW-1 during injection #1. The dark color of the gathered groundwater sample from MW-1 visually demonstrates the migration of the nanoparticles from the injection well IW-1 to the monitoring well MW-1.

Figure 8-3. A picture of the CMC-stabilized Fe-Pd particles (Fe = 1g/L) taken from the

reactor 5 min after preparation.

(a)

(b)

Figure 8-4. (a) Injection of the nanoparticle suspension and **(b)** groundwater sample collection from monitoring well MW-1.

Transport properties of the stabilized nanoparticles during injection #1 were then quantified by comparing the elution of injected Fe relative to SO_4^{2-} and tracer Br^- in monitoring wells MW-1 and MW-2, as shown in **Figure 8-5**. During the pilot test, Fe migration from injection well IW-1 to MW-3 was not visually observed. Therefore, the Fe concentration change in MW-3 was not followed. Following the injection, the gravity-fed Fe suspension was significantly diluted by the groundwater, as indicated by only ~ 27% of the injected Br^- concentration was observed in monitoring well MW-1. The peak concentration of the total Fe in MW-1, however, was determined to be ~ 15% of the injected concentration, which suggested that some portion of the Fe particles were retained in the aquifer between IW-1 and MW-1. The comparison between Fe and Br^- elution curves (e.g. area under the Concentration versus Time curves) suggested that ~37.4 % of the injected Fe transported to MW-1. Therefore, ~62.6% of the injected Fe was left in the soil between IW-1 and MW-1. In comparison, non-stabilized Fe particles would be completely intercepted on the injection well wall, as indicated by our prior studies. It is noteworthy that the breakthrough curves for Br^- and SO_4^{2-} almost coincide, which suggests that the SO_4^{2-} ions from particle preparation can also be used as a tracer in the field study. Much less Br^- and Fe concentrations were observed in MW-2. However, the presence of a peak Fe concentration of 6 mg/L (e.g. ~ 3% of the injected concentration) still suggests the migration of Fe particles from well MW-1 to MW-2 (Note: the background Fe concentration was < 1 mg/L). Interestingly, very low concentration of tracer ($C/C_0 < 3\%$) was detected in MW-2, which indicated that the nanoparticle suspension was either highly diluted in aquifer from MW-1 to MW-2 or bypassed the MW-2 as MW-2 and MW-1 were not in same elevation.

(a)

186
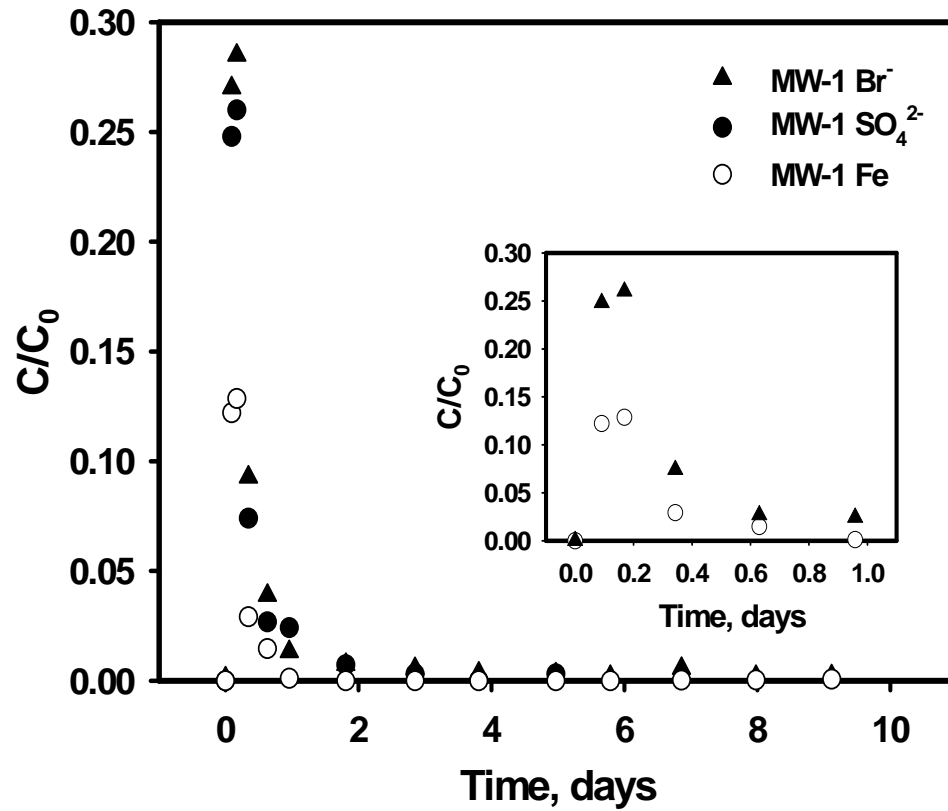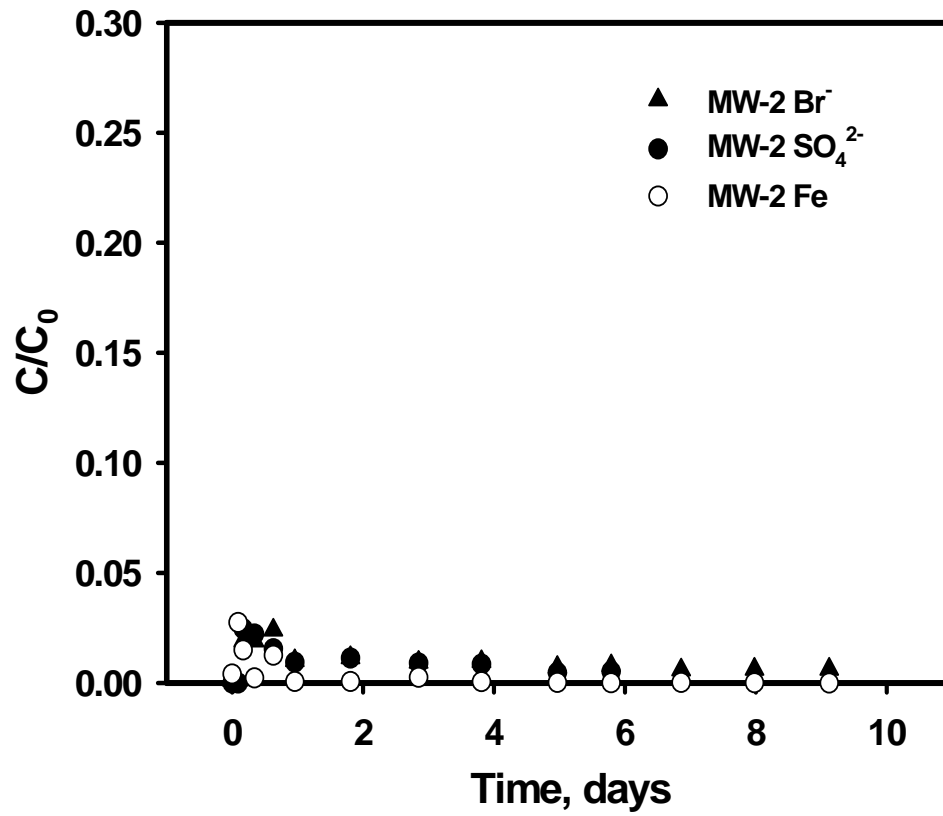
(b)

Figure 8-5. The transport of iron nanoparticles from injection well IW-1 to monitoring well MW-1 **(a)** and MW-2 **(b)** during injection #1. The inset in **(a)** shows the Fe migration in 1 day after injection (Note: Injection #1 ended 29 days after injection). The background total iron concentrations in MW-1 and MW-2 were less than 1 mg/L and the background SO_4^{2-} concentrations were less than 5 mg/L. Groundwater gradient head was 0.012 ft/ft.

During injection #2, ~ 100% of the injected Br^- concentration was observed in monitoring well MW-1 as shown in **Figure 8-6**, which indicated that the initial dilution of the nanoparticle suspension was minimal. This may be due to that the pressure-exerted nanoparticle suspension pushed the groundwater out of MW-1 without significant mixing. The peak concentration of the total Fe in MW-1 was determined to be ~ 84% of the injected concentration, which suggested that significant amount of the injected Fe particles past the aquifer between IW-1 and MW-1. Based on the areas under the elution curves, it is estimated that ~ 70% of injected Fe transported to MW-1. This result is consistent to our prior observation in column studies that iron nanoparticles past through sand column with much less retention at higher pressure (e.g. higher fluid velocity) (Chapter 6). On the other hand, only small amount of Br^- and Fe concentrations were observed in MW-2 despite the enhanced fluid pressure. Since the majority of Fe past MW-1, the Fe would stay in the aquifer between MW-1 and MW-2.

The Br^-, SO_4^{2-}, and total iron concentrations were also followed in MW-3 and IW-1 during injection #2. It is noteworthy that ~ 12% of the injected Br^- concentration and ~ 6% of the injected Fe concentration were observed in MW-3, indicating that the migration of injected suspension from IW-1 to MW-3 under the pressure, which overcame the groundwater head of ~ 0.06 ft. Therefore, the colloid barrier of Fe-Pd nanoparticles was extended to the aquifer between MW-3 and IW-1. Significantly high concentration of Fe was detected in injection well IW-1 up to 3 days after injection, which may be due to the moving back of the un-retained Fe from aquifer around IW-1 under groundwater flow after injection.
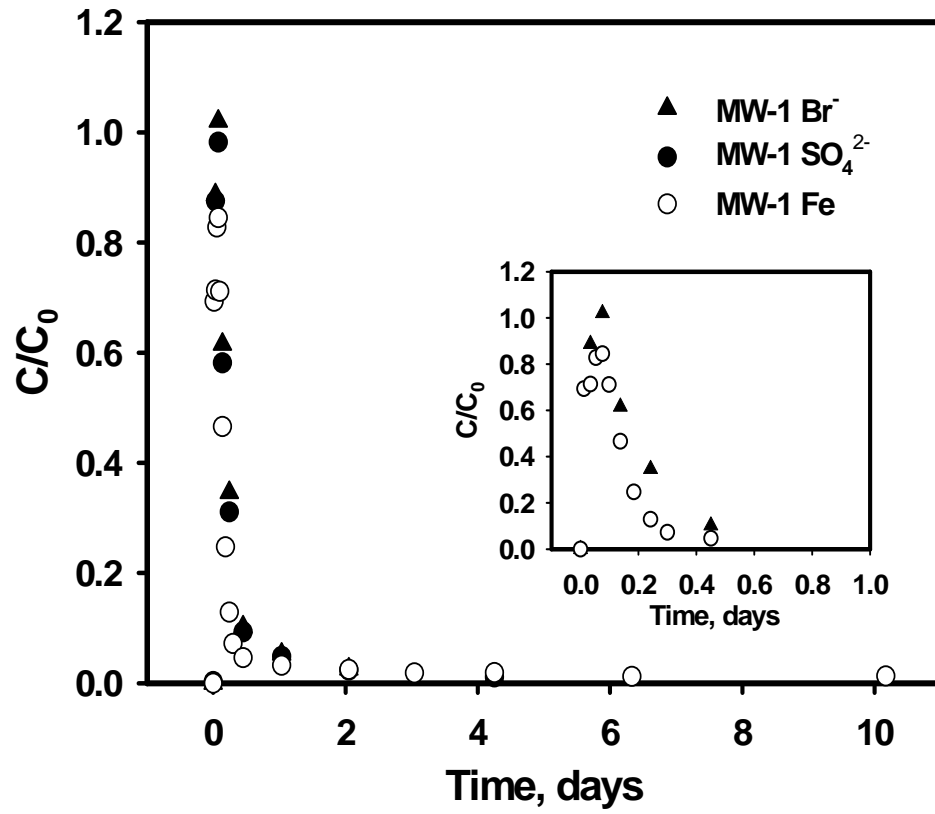
(a)
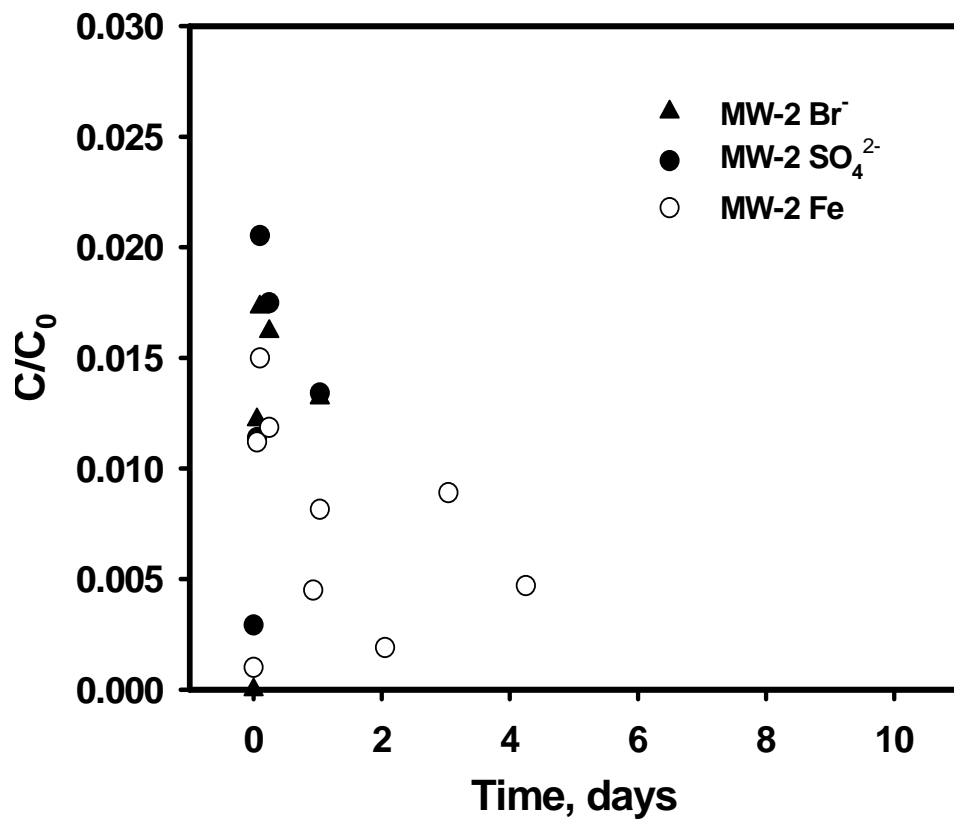
(b)
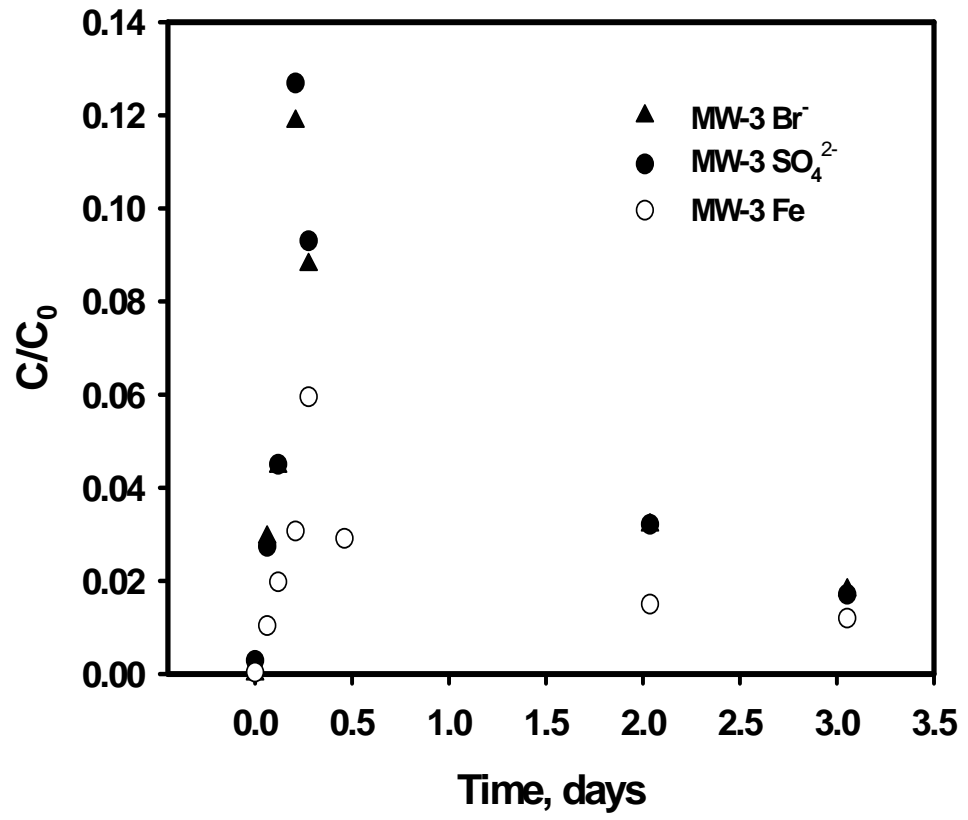
(c)
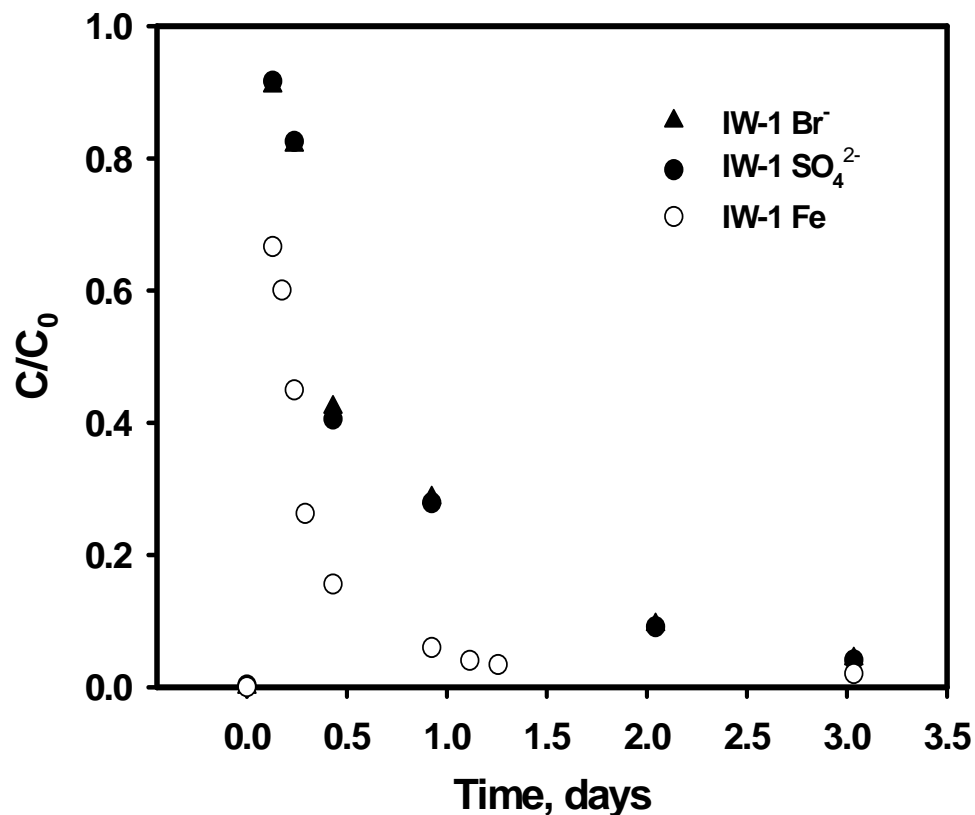
(d)

Figure 8-6. The transport of Fe-Pd nanoparticles from injection well IW-1 to monitoring

well MW-1 **(a)**, MW-2 **(b)**, and MW-3 **(c)** and the evolution of Fe concentration in IW-1

(d) during injection #2. The inset in **(a)** shows the Fe migration in 1 day after injection.

The background total iron concentrations in MW-1, MW-2, MW-3 and IW-1 were less

than 1 mg/L and the background SO_4^{2-} concentrations were less than 5 mg/L.

192

The hydrodynamic diameter of CMC-stabilized Fe nanoparticles was lab-determined to be ~ 22.8 nm with a percentage of 89%. As suggested by our prior studies, Brownian motion should be the primary mechanism of Fe nanoparticle filtration in the soil in this study. The soil-retained nanoparticles in the test area were expected to form a reactive barrier through the aquifer. This barrier could not only degrade the aqueous phase chlorinated hydrocarbon contaminants in groundwater but also proactively attack the contaminants adsorbed in the source zone soil.

8.3.4 Effects of nanoparticle injection on groundwater chemistry

The presence of nanoparticles temporarily altered the prevailing groundwater chemistry as they migrated through the subsurface. ORP is a measure of electron activity in a solution and indicates its relative tendency to accept or transfer electrons. Negative ORP values usually indicate reducing conditions which are beneficial for reductive dechlorination. In general, the ORP of groundwater extracted from monitoring wells significantly decreased following the injection and increased back to the pre-injection levels after several days. For example, during injection #2, the ORP of down-gradient monitoring wells MW-1 and MW-2 reduced from base line of -63 mv to $-$ 355 mv, and $-$ 73 mv to -179 mv, respectively, 2 hrs after the injection. The ORP remained low up to 6 days in both monitoring wells when negligible amounts of Fe were detected in extracted groundwater, as shown in **Figure 8-7**. After 8-10 days, the ORP in the monitoring wells increased back to the pre-injection values. The decrease of ORP is attributable to the consumption of oxidants by the nanoparticles as they migrated within the aquifer. For example, the DO in MW-1 during injection #2 decreased from 3.95 to 0 at 15 mins after injection and stayed at 0 level for 10 days.
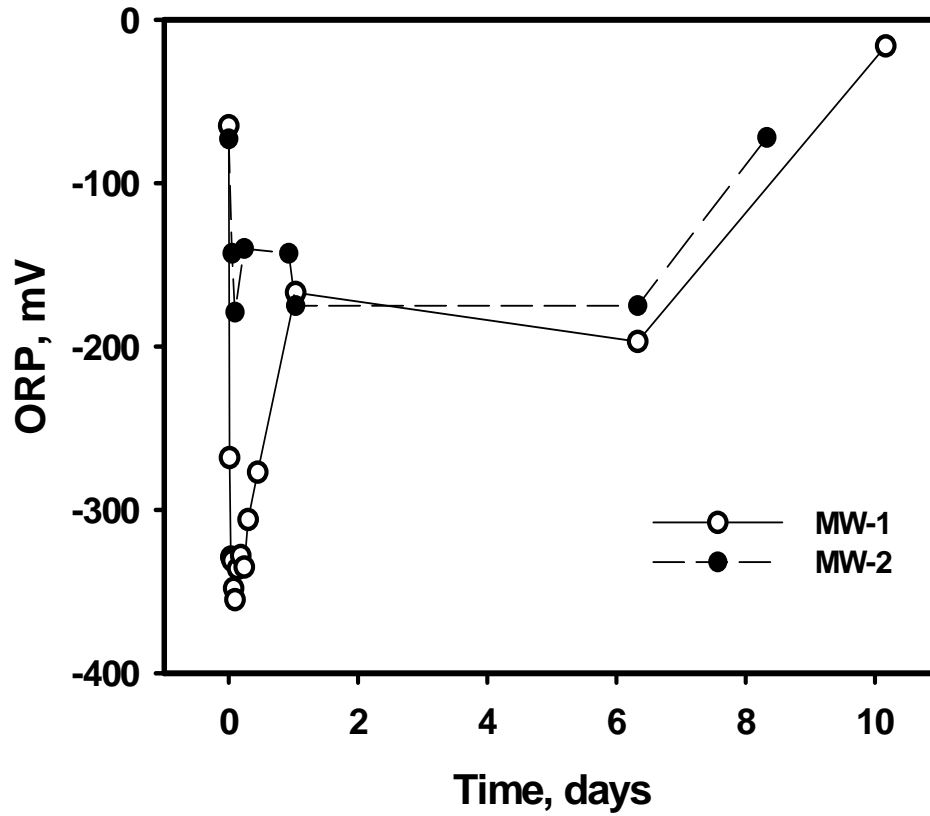
Figure 8-7. Change of oxidation and reduction potential (ORP) in monitoring well MW-1 and MW-2 during injection #2.

8.3.5 Chlorinated solvent transformation during the field test

Normalized concentration of chlorinated solvents (C/C_0) versus time were plotted to assess the reactivity of the stabilized nanoparticles during injection #1 and injection #2. As shown in **Figure 8-9**. During injection #1, PCE, TCE, and PCB 1242 concentrations in MW-1 increased significantly following the injection and then declined rapidly before exhibiting varying degrees of recovery. The increase of the chlorinated solvent concentrations in the beginning stage was also occasionally observed by other groups on conducting similar field studies (Mace, 2006). They explained this phenomenon as that the injection process remobilized the contaminants from the unsaturated zone. The later sharp decline of chlorinated contaminant concentrations clearly suggests the rapid degradation of the chlorinated hydrocarbon contaminants. However, caution should be taken here that the decrease of contaminant concentration could be caused by the dilution of groundwater with the injecting of Fe suspension. In **Figure 8-9**, the curve 1-$C_t(Br)/C_0(Br)$ versus time is used to represent the dilution effect of chlorinated solvents due to the injection. Clearly, much more decrease of PCE, TCE and PCB 1242 was obtained compared to the dilution at the first day after injection. After that, dilution did not exist while the chlorinated solvent concentrations remained at a very low level (C/C_0 < 0.25) for at least 4 days, indicating the significant chemical reduction of the contaminants. After 5 days, the concentrations of PCE, TCE and PCBs start to bounce back as the decrease of the Fe nanoparticle reactivity. This result is consistent with our lab findings that the reactivity of CMC-stabilized Fe-Pd nanoparticles exponentially decreased with time. For example, the TCE reduction rate with 9-day aged nanoparticles

was only 2.8% of that with fresh nanoparticles. The exponential decrease of Fe-Pd nanoparticle reactivity is shown in **Figure 8-10**.

It is noteworthy from **Figure 8-9** that the concentration of TCE and PCE started to decrease again after their recovery at 12 days after injection. For example, at 29 days after injection, the concentrations of PCE and TCE in MW-1 were 497 ppb and 72 ppb compared to the concentration of 1225 ppb and 1655 ppb before injection. This part of degradation can be attributed to the enhanced biodegradation of TCE and PCE. As well recognized, reactive Fe nanoparticles are a good H_2 source and H_2 is the preferred electron donor for microorganisms that biodegrade chlorinated solvents (Seshadri et al., 2005). Moreover, the CMC also provides an ideal nutrient for the growth of bacterial. The surprisingly good degradation of TCE and PCE demonstrated that the Fe left in the aquifer provided a steady-sate H_2 concentration that is suitable for biodegradation of TCE and PCE in the groundwater. However, the PCB 1242 concentration remained 90% of the pre-injection level after the recovery. This result conforms to the fact that PCB is much more persistent to biodegradation than PCE and TCE.
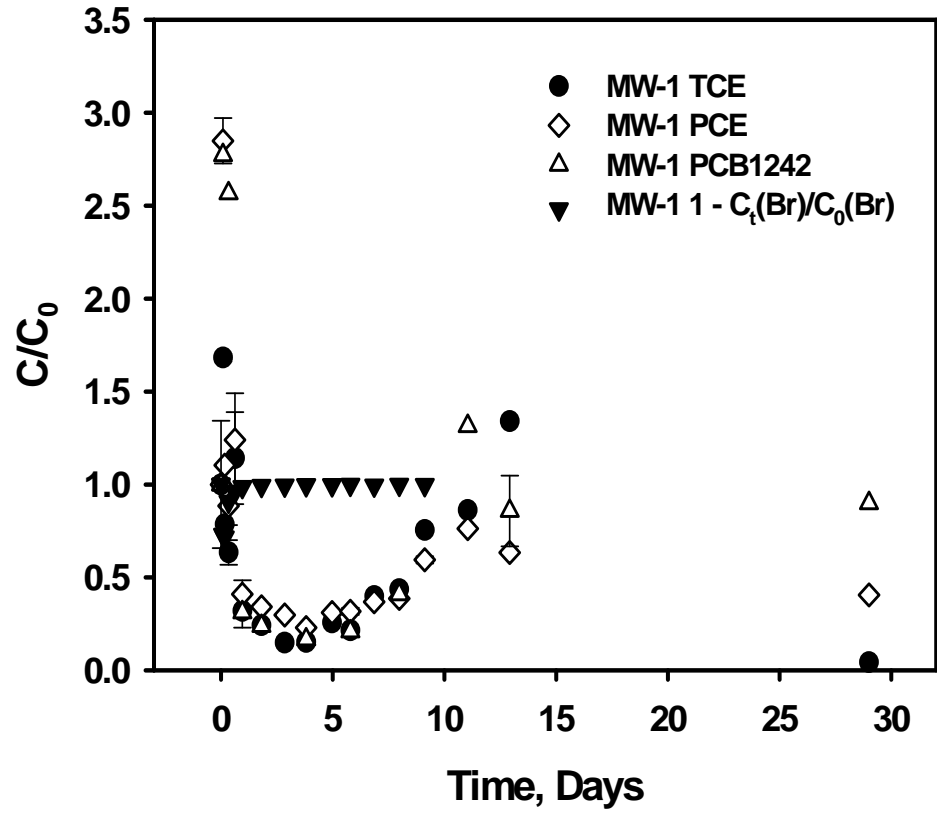
(a)
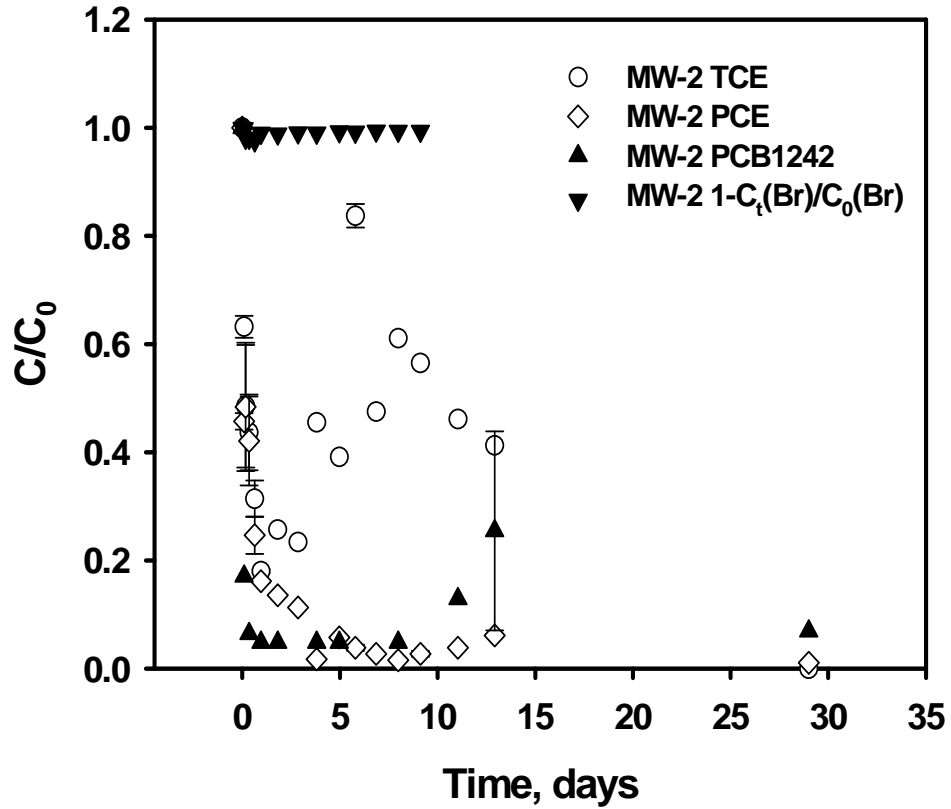
(b)

Figure 8-9. The concentration evolution of PCE, TCE and PCB 1242 in groundwater from MW-1 (a) and MW-2 (b) following injection #1. The pre-injection concentrations of PCE, TCE, and PCB1242 in MW-1 were 1225 ppb, 1655 ppb, and 21 ppb, respectively. The pre-injection concentrations of PCE, TCE, and PCB1242 in MW-2 were 4133 ppb, 3710 ppb and 62 ppb, respectively.
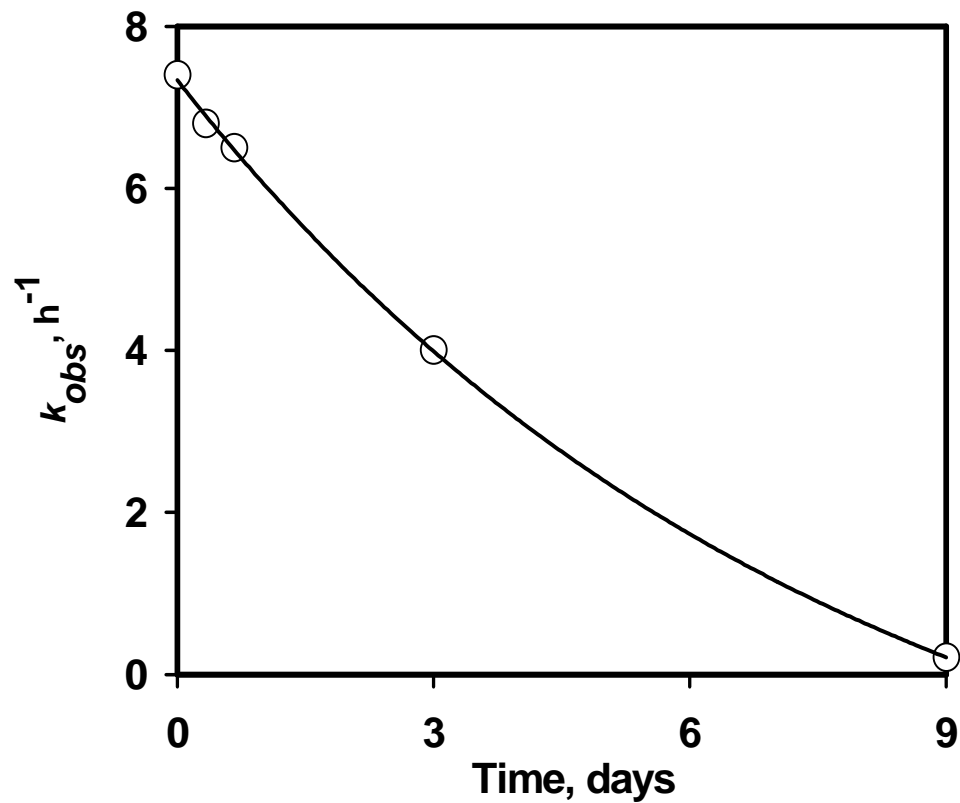
Figure 8-10. Exponential decrease of TCE degradation rate constant (k_{obs}) with particle age.

Figure 8-11 depicts the concentration evolution of PCE, TCE and PCB 1242 in groundwater from MW-2 following the nanoparticle injection. The concentrations of PCE, TCE and PCB 1242 declined rapidly following injection and later exhibited varying degrees of recovery. The PCE and TCE also underwent a second stage degradation after their recovery. The decrease of PCE and TCE in MW-2 can be attributed to: a) the reduced PCE, and TCE concentrations in the up-gradient monitoring well MW-1; b) further chemical reduction of the contaminants in groundwater flowing through MW-1 to MW-2 and proactive destruction of contaminants in the soil between MW-1 and MW-2; and c) enhanced biodegradation of chlorinated contaminants with H_2 generated from Fe corrosion. Interestingly, the PCB1242 concentration in MW-2 decreased to only ~7% of the pre-injection concentration. The cause of the significant degradation of PCB1242 in MW-2 is not known but could be attributed to the degradation of PCB1242 in soils near the vicinity of MW-2.

The long-term performance of Fe-Pd nanoparticles in subsurface was investigated in injection #2. In this case, the groundwater samples from all the monitoring wells and injection wells were monitored for up to 100 days. After first injection, the PCE, TCE, PCB1242 concentrations in MW-1 were 41%, 4%, and 90% of the pre-injection concentrations, respectively. Right after the second injection (< 1 d), the concentrations of PCE, TCE, and PCB1242 firstly increased and followed with rapid decreases, which was consistent to our prior observation in injection #1. After that, extensive degradation of PCE and TCE was observed. The concentrations of both contaminants stayed as low as less than 10% of the original concentrations up to 50 days. After 100 days, the concentrations of PCE and TCE started to increase back but still were as low as 20% and

35% of pre-injection concentrations, indicating the long-term degradation of both contaminants. The long-term degradation is likely attributed to biological reductive dechlorination of PCE and TCE. Compared to PCE and TCE, the degradation of persistent PCB1242 in MW-1 through the tested period was not obvious.

In monitoring well MW-2, the concentrations of PCE and TCE remained as low as less than 100 ppb up to 50 days following injection #2. After 100 days, the concentrations of PCE and TCE in MW-2 also exhibit a slight increase and were back to ~ 8% and 10% of pre-injection concentrations. Interestingly, the concentration of PCB1242 in MW-2 remained as low as undetectable up to 1 month after injection. Clearly, the chlorinated solvents in MW-2 underwent more extensive degradation than these in MW-1, which is consistent to the observation in injection #1.

The monitoring of contaminants of PCE, TCE, and PCB1242 was also followed in monitoring well MW-3 and injection well IW-1 as shown in **Figure 8-11(c)** and **(d)**. As only small amount of Fe-Pd nanoparticles had reached MW-3, no obvious degradation of the monitored contaminants was observed in this well. Similar degradation behavior of PCE and TCE was observed in IW-1 as that in MW-1 and MW-2. The concentrations of PCE and TCE declined rapidly following injection and recovered and then underwent a second stage degradation. At 98 days after second injection, the concentrations of PCE and TCE were 25% and 66% of the pre-injection concentrations, indicating the prolonged degradation of both contaminants in injection well IW-1. Significant degradation of PCB1242 was also observed in IW-1. For instance, at 21 days after second injection, the detected PCB1242 concentration in IW-1 was only ~ 13% of the pre-injection concentration. The comparison between the GC chromatograms of PCB1242 pre and post

injection (21 days later) further showed the left shift of the major peaks (**Figure 8-10**), which suggested that PCB1242 was transformed to some lower chlorinated compounds (He and Zhao, 2005).

8.4 Conclusions

The data from the field assessment of CMC-stabilized Fe-Pd nanoparticle technology at the North Alabama site demonstrated that effective chlorinated solvent remediation could be achieved using this technology although longer term groundwater monitoring is still needed. As it is clear that the natural degradation of CMC promoted the enhanced biodegradation of TCE, there are questions regarding the relative contributions of the abiotic and biological mechanisms of degradation of TCE. The stabilized nano-materials can be easily synthesized on site and gravity-fed or pressure-fed into contaminant source zones without disturbing the aquifer soil. The field-scale demonstration of the stabilized Fe-Pd nanoparticle technology for in situ destruction of chlorinated organic contaminants confirmed the potential of this technology for in situ remediation applications.
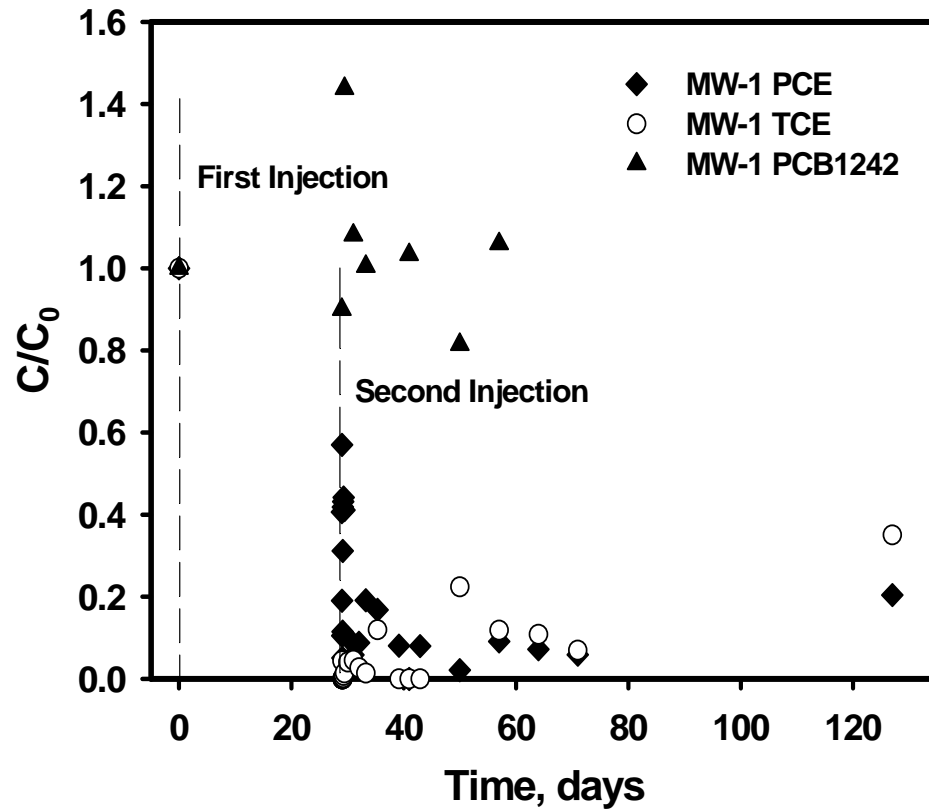
(a)
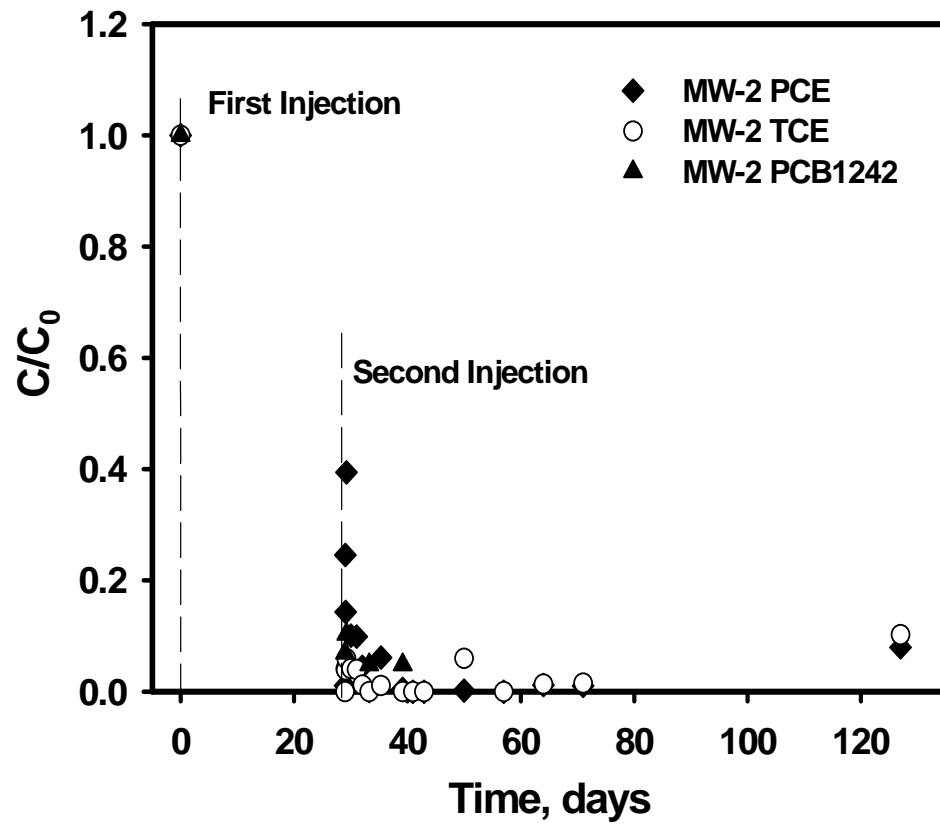
(b)
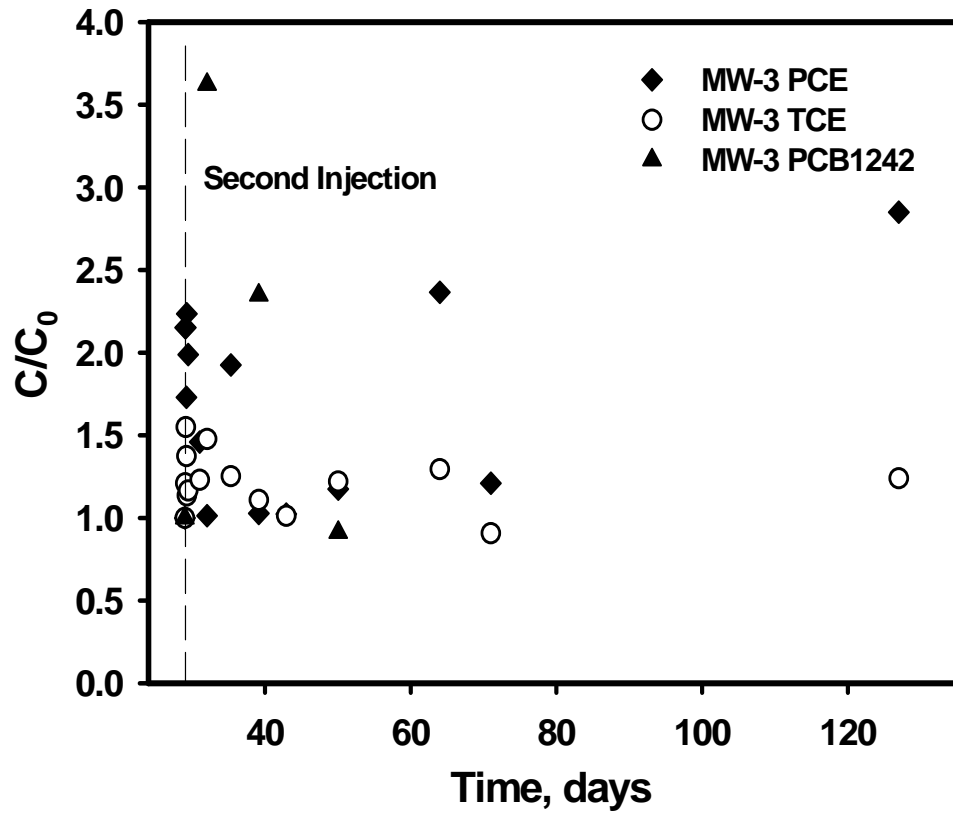
(c)
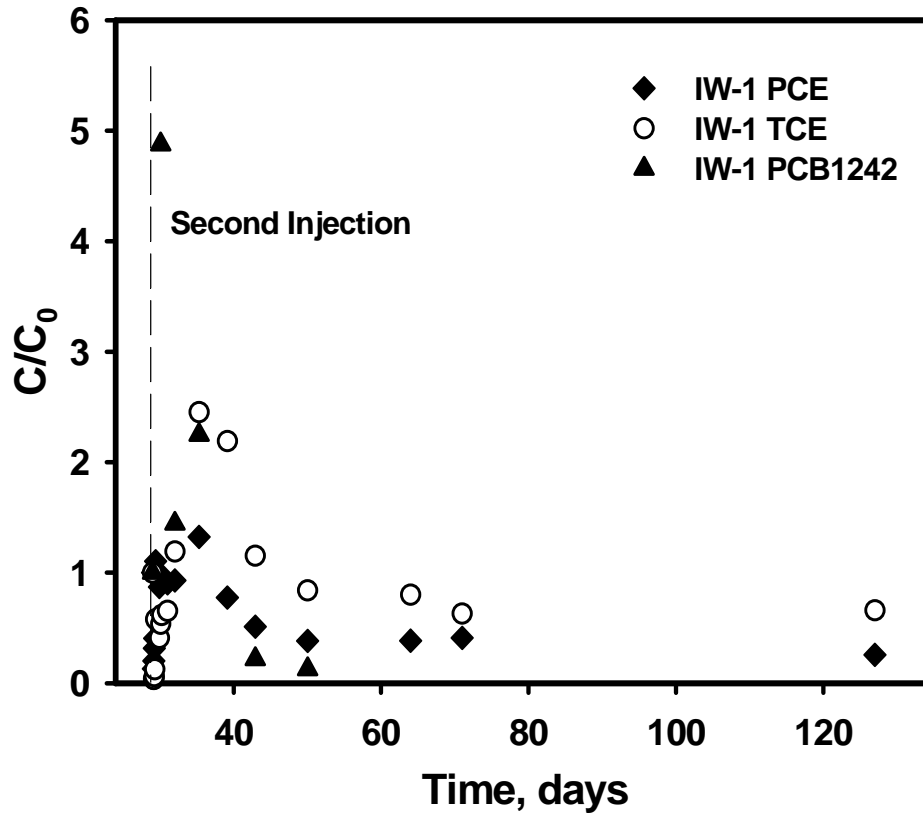
(d)

Figure 8-9. The concentration evolution of PCE, TCE and PCB 1242 in groundwater from MW-1 (a), MW-2 (b), MW-3 (c), and IW-1 (d) following injection #2. The pre-injection concentrations of PCE, TCE, and PCB1242 in MW-3 were 9128 ppb, 23803 ppb, and 7 ppb, respectively. The pre-injection concentrations of PCE, TCE, and PCB1242 in IW-1 were 11765 ppb, 7403 ppb and 97 ppb, respectively.

206
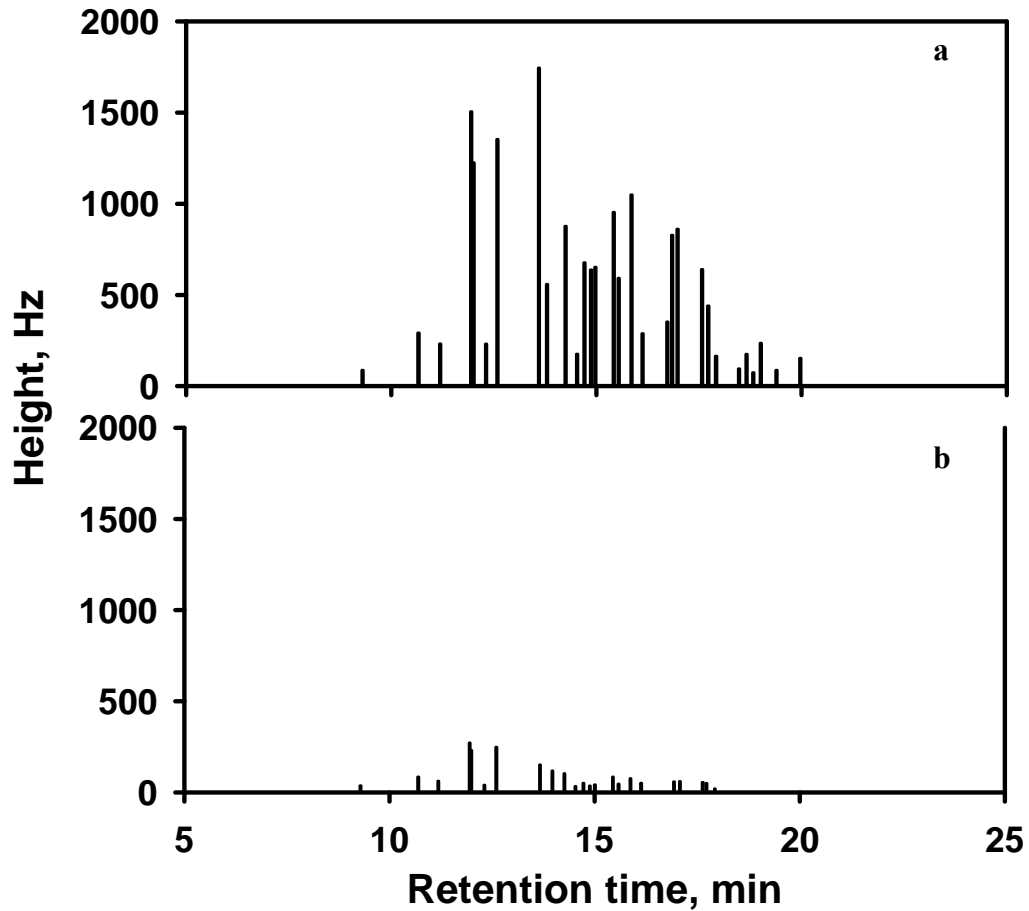
Figure 8-10. Comparing GC chromatograms for **(a)** PCB1242 in pre-injection groundwater, and **(b)** PCB1242 in post-injection groundwater (21 days after injection) in injection well IW-1. The pre-injection PCB1242 concentration was 97 ppb.

CHAPTER 9. CARBOXYMETHYL CELLULOSE STABILIZED PD NANOPARTICLES EXHIBITING HIGH CATALYTIC ACTIVITIES FOR HYDRODECHLORINATION OF TRICHLOROETHYLENE

Pd-catalyzed hydrodechlorination of chlorinated solvent is a promising technology for groundwater remediation. However, the amount and cost of the Pd catalyst may limit the applicability of this technology. One solution to this problem would be to design and engineer more active catalysts. In this chapter, one-step synthesis of highly dispersed Pd nanoparticles by employing "green" CMC as a capping agent is presented. This new type of Pd nanoparticles exhibited rather high catalytic activity for the hydrodechlorination of TCE in water.

9.1 Introduction

Catalytic hydrodechlorination is an innovative technology for the remediation of soil and groundwater contaminated with chlorinated hydrocarbon compounds (Lowry and Reinhard, 1999; Mcnab Jr. et al., 2000; Nutt et al., 2005; Schuth et al., 2004). Trichloroethylene (TCE) is one of the most detected chlorinated organic pollutants in US groundwater and a potent carcinogen (ATSDR, 2007). It is well recognized that TCE can undergo hydrodechlorination by H_2 in the presence of Pd catalysts, and ultimately be transformed into nontoxic ethane (Lowry and Reinhard, 1999). Since Pd catalytic hydrodechlorination of TCE is a surface-mediated process, an increase in surface area of

the Pd catalyst greatly enhances the reaction rate (Nutt et al., 2005; Nutt et al., 2006). Therefore, lowering the Pd particle size to the nanoscale is of great practical significance.

One key step to the synthesis of nanoscale particles is to employ a capping agent (e.g. stabilizer) during synthesis to passivate the surface and suppress the growth of the particles which would otherwise aggregate due to the high surface energy. The interactions of the functional molecular groups of the capping molecules with the nanoparticles play an important role in governing the particle size and size distribution. Typically, a capping agent that can interact strongly with the surface of nanoparticles may effectively stabilize the nanoparticles and result in small and monodisperse particles. On the other hand, for environmental applications, the capping agent should be low-cost, non-toxic, and biodegradable/biocompatible. Therefore, it is highly desirable to develop a "green" water-based process for synthesizing Pd nanoparticles with the aid of a low-cost, environmentally friendly and effective capping agent. The practical application of Pd nanoparticles usually requires the recovery and reuse of the nanoparticles through immobilizing them on a catalyst support. While the immobilization of nanoparticle catalysts is an area of ongoing research, the focus of the current study involves the controlled synthesis of highly dispersed Pd nanoparticles using "green" and low-cost capping agents as an initial step towards this goal.

Over the past decade or so, significant attention has been devoted to the synthesis of metal nanoparticles in aqueous phase using "green" stabilizers such as glucose (Liu et al., 2006a), starch (Raveendran et al., 2003; Raveendran et al., 2006), and carboxymethyl celluose (CMC) (He et al., 2007; Magdassi et al., 2003). Among the tested stabilizers, CMC is a bulky linear polymer that possesses carboxylate groups in addition to hydroxyl

209

groups. As a result, CMC exerts much stronger interactions with particles than starch or glucose that only possesses hydroxyl groups, and thus, serves as a more effective capping agent. For example, it was reported that the CMC-stabilized Fe nanoparticles were much more stable and had much smaller size than the starch-stabilized couterparts (He et al., 2007; He and Zhao, 2005). It is important to point out here that the particle reactivity varies with particle size; however, decreasing particle size does not always result in an increased reactivity. For example, Li et al. (2001) studied the size effects of PVP-Pd nanoparticles on the catalytic Suzuki reactions in aqueous solution and observed that the reactivity of Pd (3.9 nm) was higher than that of Pd (3.0 nm). Therefore, controlling the size of Pd nanoparticles is of profound importance for their practical application.

This work investigated the effectiveness of using CMC as a "green" and low-cost capping agent to synthesize highly dispersed Pd nanoparticles in aqueous solution for rapid TCE hydrodechlorination. Specifically, the size of the Pd nanoparticles was controlled through modifying the CMC/Pd^{2+} ratio during synthesis and the catalytic activity of the resultant nanoparticles was systematically investigated. The capping performance of the stabilizers on the Pd surface is also expected to affect the surface-mediated hydrodechlorination reaction. However, little has so far been reported for the dependence of capping performance on the metal nanoparticle catalysis (Stowell and Korgel, 2005). To evaluate both the effects of size and capping performance, the catalytic activity of CMC-stabilized Pd nanoparticles (CMC-Pd) was compared with that of β-D glucose stabilized Pd nanoparticles (glucose-Pd). The molecular mechanism under both effects was then discussed.

9.2 Experimental Section

9.2.1 Materials

$Na_2PdCl_4.3H_2O$ was purchased from Strem Chemicals. Carboxymethyl cellulose sodium salt (average M_w ~90,000), β-D glucose, sodium borohydride (Purity: 99.99%), and TCE with spectrophotometric grade (>99%) were obtained from Sigma-Aldrich. Deionized ultra-filtered water with specific conductance of 2.0μmhos/cm and hexane were obtained from Fisher Scientific.

9.2.2 Aqueous phase synthesis of Pd nanoparticles

The Pd nanoparticles were synthesized by reducing Pd^{2+} ions in a CMC or β-D glucose aqueous solution using sodium borohydride ($NaBH_4$). For the synthesis of glucose-Pd nanoparticles, a 1000 μL aliquot of a 0.05M $Na_2PdCl_4 \cdot 3H_2O$ aqueous solution was added to 250 mL of a β-D glucose aqueous solution (0.90 wt.%). Then, a 0.05 M $NaBH_4$ aqueous solution (around 3500 μL) was added to the mixture under constant stirring at room temperature (~ 23 °C). For a typical synthesis of CMC-Pd nanoparticles, a 1000 μL aliquot of a 0.05M $Na_2PdCl_4 \cdot 3H_2O$ aqueous solution was added to 250 mL of a CMC aqueous solution (concentrations varied from to 0.001 wt.% to 0.15 wt.%). Subsequently, a 0.05 M $NaBH_4$ aqueous solution (around 3500 μL) was added to the mixture under constant stirring at room temperature. After 24 hours, the resultant Pd nanoparticles were used for catalytic hydrodechlorination of TCE.

9.2.3 Transmission Electron Microscopy (TEM) characterization

For TEM analyses, samples of air-dried Pd nanoparticles were prepared by placing three droplets of aqueous Pd nanoparticle suspension onto a copper grid and

subsequently air-drying the samples overnight under ambient conditions. The morphology and size distribution of the Pd nanoparticles were determined by a Zeiss EM 10 TEM at an operating voltage of 60 kV.

9.2.4 Dynamic Light Scattering (DLS) measurement

The mean hydrodynamic diameter of the Pd nanoparticles stabilized by 0.90 wt.% β-D glucose or 0.15 wt.% CMC in aqueous solution were determined using a DLS spectrometer (Nicomp 380, PSS, Santa Barbara, CA) equipped with a He-Ne laser (wavelength 633 nm) at a measurement angle of 90°. The DLS data were processed with a software package CW380 to yield the volume-weighted size distributions.

9.2.5 Powder X-ray Diffraction (XRD) characterization

XRD patterns were collected with a Rigaku Miniflex powder X-ray diffractometer using Cu Kα (l = 1.54056 Å) radiation. Both the solid XRD samples of the β-D glucose-Pd and CMC-Pd nanoparticles were separated from the aqueous solution by centrifugation at a speed of 6000 rpm/4185 g while using ethanol as an antisolvent.

9.2.6 TCE hydrodechlorination experiments

Batch experiments were conducted using 127 mL serum bottles capped with Teflon Mininert valves. In a typical experiment, 4.5 mL of Pd nanoparticle suspension was initially mixed with 85 mL of deionized water under stirring. Then, the reactor was sparged with hydrogen gas for 20 min to displace dissolved oxygen (DO) and to fill the headspace with H_2 (1 atm). Then, 25 µL of a TCE stock solution (179 g/L TCE in methanol) was spiked into the suspension, resulting in an initial total TCE concentration of 50 mg/L. The catalytic dechlorination reaction was conducted at room temperature

under constant magnetic stirring and was monitored for about 10 min. At constant time intervals (2 min), 0.1 mL of each aqueous sample including the suspended Pd nanoparticles was withdrawn using a 100 µL gas-tight syringe. Then, the samples were transferred into 2 mL GC vials where the organic compounds were extracted into 1 mL hexane phase. Upon phase separation, TCE and the possible chlorinated reaction intermediates were analyzed using an HP 6890 GC equipped with an electron capture detector (ECD). The concentration of TCE in the headspace was obtained following Henry's law (Schwarzenbach et al., 1993). To examine the completeness of TCE hydrodechlorination, coupled TCE degradation and chloride production were followed by a separate set of batch experiments. At selected time intervals (2 min), the degradation reaction was ceased by rapidly sparging the suspension with N_2 gas to remove the residual TCE and H_2. Then, the solution was filtered through 0.22 µm membrane (Millipore, Billerica, MA) for chloride analysis using a Dionex Ion Chromatography (DX-120). All batch experiments were duplicated to assure data quality.

9.3 Results and Discussion

9.3.1 Synthesis and stability of CMC-Pd and glucose-Pd nanoparticles in aqueous solution

Upon addition of $NaBH_4$ into the CMC-Pd^{2+} or glucose-Pd^{2+} solution, the solution turned to transparent dark brown, visually indicating the formation of Pd nanoparticles. The Pd nanoparticles stabilized by 0.15 wt.% CMC were stable for prolonged periods (more than 9 months) and did not show any signs of aggregation and precipitation when stored in a 250 mL glass flask. In contrast, the Pd nanoparticles stabilized by 0.001wt.%

CMC could only be stable for two weeks before complete precipitation was observed, suggesting that the CMC concentration significantly influences the stability of the Pd nanoparticles.

9.3.2 Characterization of CMC-Pd and glucose-Pd nanoparticles

TEM images of the Pd nanoparticles stabilized by 0.15 wt.% CMC and 0.90 wt.% β-D glucose are presented in **Figure 9-1**. The Pd nanoparticles stabilized by 0.15 wt.% CMC had a mean diameter of 2.4 nm with a standard deviation, SD, of 0.5 nm, whereas the Pd nanoparticles stabilized by 0.90 wt.% β-D glucose showed a mean diameter of 4.3 nm with a SD of 1.0 nm. XRD analyses on the dried CMC-Pd and glucose-Pd samples showed the grain sizes of CMC-Pd and glucose-Pd were 1.9 nm and 5.2 nm, respectively, consistent to the TEM results. The XRD results also showed that both the CMC-Pd and glucose-Pd nanoparticles had a face-centered cubic (fcc) structure. The fact that much smaller and stable Pd nanoparticles were obtained using CMC with only 1/6 usage of β-D glucose clearly suggests the strong chelating ability of CMC for Pd nanoparticle stabilization. This observation conforms to our prior Fourier transform IR (FT-IR) results that CMC molecules can strongly interact with the metal nanoparticles via both carboxyl (COO$^-$) and hydroxyl (-OH) groups and exert effective stabilization (He et al., 2007), whereas the glucose molecules can only weekly interact with the metal nanoparticles via hydroxyl groups (Liu et al., 2006a).
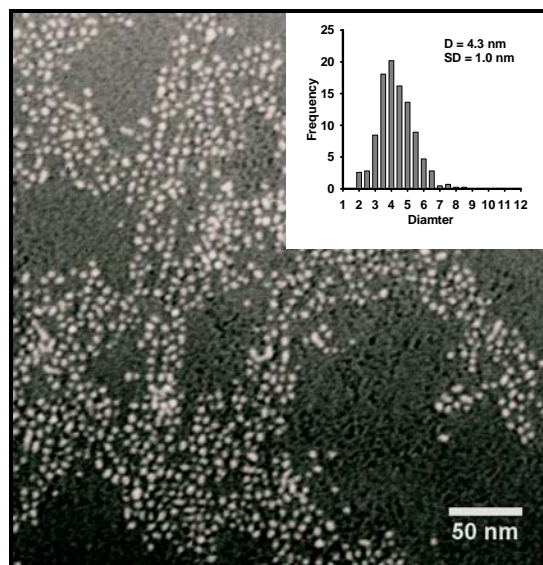
(a)
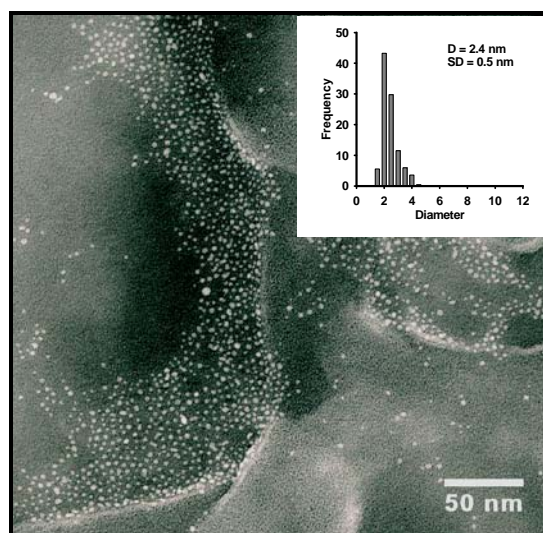
(b)

Figure 9-1. Representative TEM images of Pd nanoparticles synthesized using (a) 0.90 wt.% β-D glucose and (b) 0.15 wt.% CMC in aqueous phase system, along with the corresponding particle size distribution histograms.

To obtain the thickness of the polymer layer on the Pd nanoparticles, which is of interest for catalytic activity analysis, DLS measurements were performed to yield the hydrodynamic diameters. The mean hydrodynamic diameters of 0.15 wt.% CMC-Pd nanoparticles and 0.90 wt.% glucose-Pd were determined to be 12.7 nm with SD of 1.9 nm and 5.9 nm with SD of 0.7 nm, respectively. By subtracting the TEM radius from the hydrodynamic radius, we calculated the thickness of the CMC layer to be 5.2 nm and that of the glucose layer to be 0.8 nm. The bulkier and charged CMC layer provided more effective electrostatic stabilization of Pd nanoparticles than the thin neutral glucose layer to yield highly dispersed Pd nanoparticles.

When the concentration of β-D glucose and CMC was further increased beyond 0.90 wt.% β-D glucose or 0.15 wt.% CMC, respectively, no significant effect on the size of the Pd nanoparticles was observed. This suggests that the surface of Pd nanoparticles was saturated with either 0.90 wt.% β-D glucose or 0.15 wt.% CMC in the aqueous phase synthesis systems. On the other hand, upon decreasing the concentration of CMC, the size of Pd nanoparticles continuously increased. The TEM-based diameters of Pd nanoparticles synthesized at various CMC concentrations are summarized in **Table 9-1**. Clearly, through controlling the CMC concentration, the size-controlled synthesis of Pd nanoparticles was achieved. It is worth noting that Pd nanoparticles stabilized by 0.001 wt.% CMC had a diameter of 4.7 nm and can only be stable in aqueous phase for 2 weeks as mentioned before. Further decreasing of CMC concentration from 0.001 wt.% resulted in instant aggregation and precipitation of the Pd nanoparticles.

Table 9-1. Size and Composition of CMC and Glucose Stabilized Pd Nanoparticles and the Rate Constant and Turnover Frequency of the Hydrodechlorination of TCE for those Nanoparticles at Constant Pd Concentration.

	Pd nanoparticles synthesized with different concentrations of CMC and with glucose						
	0.15 wt.% CMC	0.10 wt.% CMC	0.05 wt.% CMC	0.01 wt.% CMC	0.005 wt.% CMC	0.001 wt.% CMC	0.90 wt.% glucose
TEM diameter (nm)	2.4 ± 0.5	2.5 ± 0.6	2.5 ± 0.8	2.9 ± 1.2	3.1 ± 1.4	4.7 ± 3.0	4.3 ± 1.0
Total No. of atoms	561	561	561	1415	1415	5083	3871
No. of surface atoms	252	252	252	492	492	1212	1002
No. of vertex and edge atoms	108	108	108	156	156	252	228
k_{app} (min^{-1})	0.775	0.878	0.831	0.491	0.482	0.237	0.161
k_{obs} ($L \cdot g_{pd}^{-1} \cdot min^{-1}$)	731	828	784	463	455	224	152
Initial TOF (mol TCE$\cdot$mol^{-1} Pd$\cdot$min^{-1})	65.9	74.7	70.7	53.9	53.0	38.0	23.8

9.3.3 Catalytic activity of the CMC-Pd and glucose-Pd nanoparticles

The catalytic activity of the Pd nanoparticles was investigated through the degradation of TCE. **Figure 9-2** presents the TCE degradation efficiencies using various Pd nanoparticles. The results of control test shown in **Figure 9-2** indicated that in the absence of the Pd nanoparticles, H_2 itself could not degrade TCE. In contrast, the presence of 1.06 mg/L of either glucose-Pd or CMC-Pd nanoparticles resulted in an effective degradation of TCE in the system. For example, after 10 mins of the reaction, approximately 80.9 % and 100 % of TCE was degraded by H_2 with 0.90 wt.% glucose-Pd and 0.15 wt.% CMC-Pd, respectively.

In the batch degradation tests, the H_2 in the system far exceeded the stoichiometric H_2 demand for the transformation of the TCE. Therefore, the H_2 concentration in the aqueous phase remained essentially constant during the reaction. The TCE degradation kinetics in **Figure 9-2** can be interpreted using a pseudo-first-order kinetic model as shown in eqn (9-1),

$$-\frac{d[TCE]}{dt} = k_{app} \cdot [TCE] = k_{obs} \cdot [Pd] \cdot [TCE] \qquad (9\text{-}1)$$

where the k_{app} is the apparent reaction rate constant. [Pd] is the concentration of Pd nanoparticles/catalyst. [TCE] is the concentration of TCE during the reaction. k_{app} is normalized by the catalyst concentration to yield the observed reaction rate constant, k_{obs}. The linear correlations of $\ln([TCE]_t/[TCE]_0)$ versus time were observed for all the cases as shown in **Figure 9-3**, through which the k_{app} and k_{obs} values for various Pd nanoparticles are obtained and summarized in **Table 9-1**.
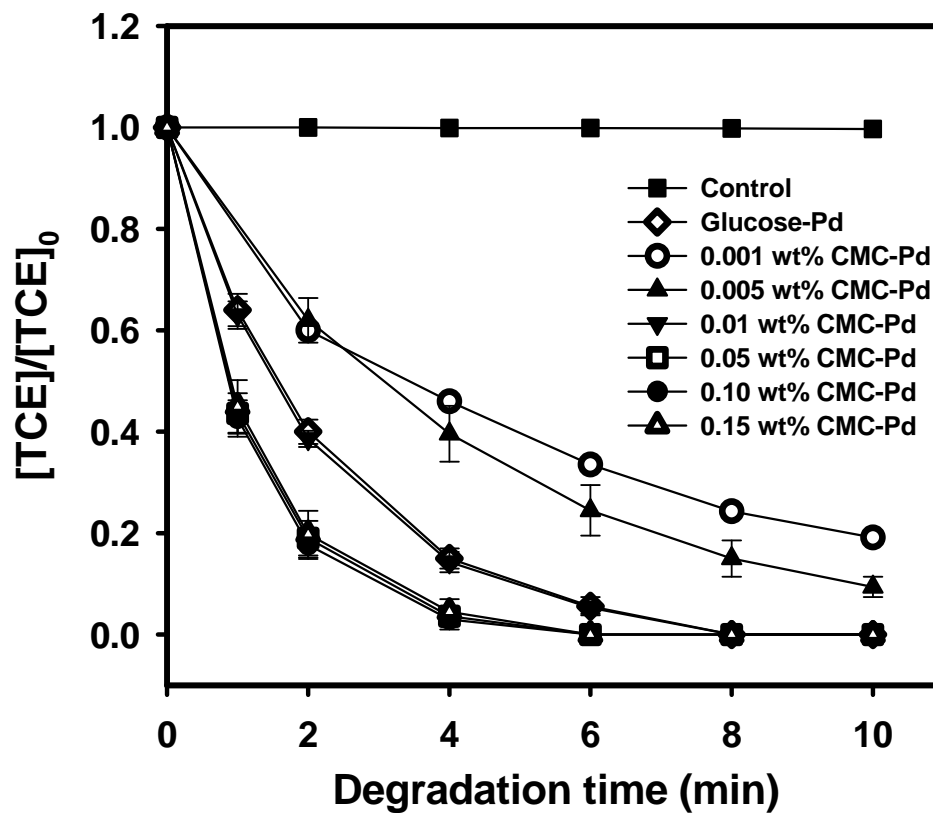
Figure 9-2. Hydrodechlorination of TCE catalyzed by glucose-Pd and CMC-Pd nanoparticles. The data of the control experiment (with no Pd nanoparticles but with CMC or β-D glucose in the system) are also presented for comparison. Initial total TCE concentration was 50 mg L^{-1}. Pd nanoparticles mass concentration was 1.06 mg/L.
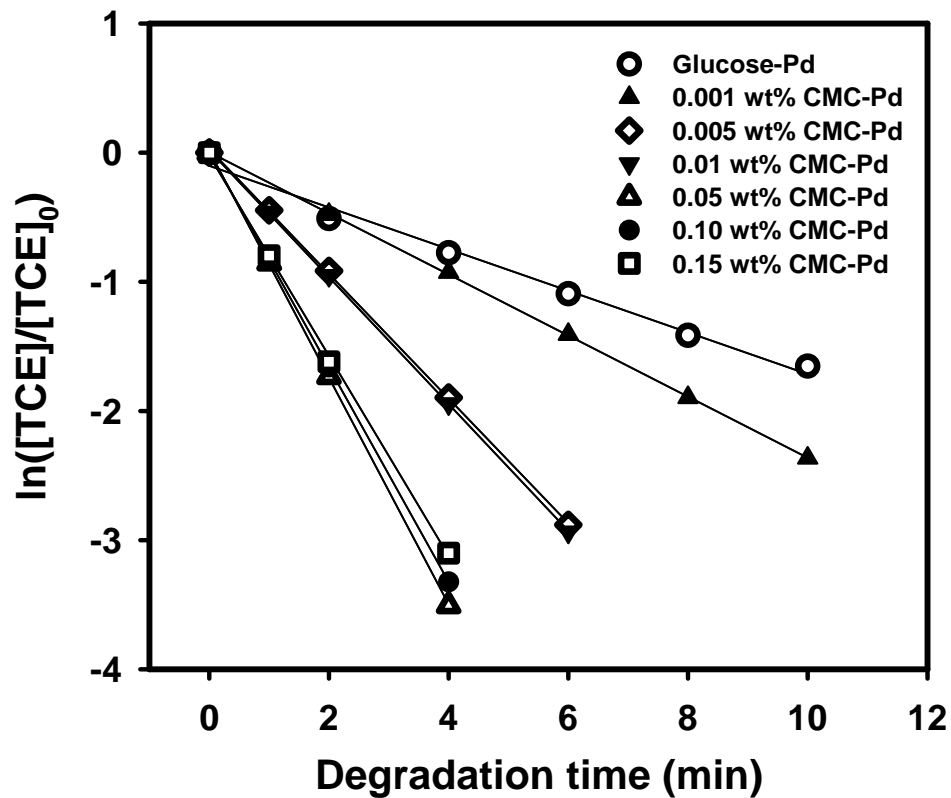
Figure 9-3. Plot of $\ln([TCE]_t/[TCE]_0)$ against time of hydrodechlorination of TCE catalyzed by glucose-Pd and CMC-Pd nanoparticles.

To assess the catalytic activity of Pd particles for TCE hydrodechlorination, the turnover frequency (TOF) is frequently used, which is defined as moles of TCE degraded per mole of surface Pd atom per min. The initial turnover frequencies (TOF$_{init}$) can be calculated using the following eqn (9-2):

$$TOF_{init} = -\left(\frac{d[TCE]}{dt}\right)_{t=o}\left(\frac{1}{[Pd]D_{Pd}}\right) \qquad (9\text{-}2)$$

where D_{Pd} is the ratio of the number of surface Pd atoms to the number of total Pd atoms of a nanoparticle, and [Pd] is the molar concentration of the Pd nanoparticles in the reaction system. To estimate the number of surface Pd atoms, we used the model of full-shell nanoparticles developed by Benfield (1992), knowing that the CMC-Pd and glucose-Pd are single crystallites with the face-center cubic (fcc) structure from XRD analyses. A Pd nanoparticle is treated as a central atom surrounded by concentric shells of atoms. The cuboctahedral surface sites are composed of five different types of surface atoms: interstitial (12-coordinate), vertex (5-coordinate), edge (7-coordinate), square face (8-coordinate), and triangular face (9-coordinate) atoms. With Benfield's model, the total number of atoms, the number of surface atoms, and the number of vertex and edge surface atoms for different size CMC-Pd or glucose-Pd nanoparticles are obtained and listed in **Table 9-1**. Here, the value of 0.138 nm is used as the radius of a Pd atom (Lide, 1994). After obtaining the number of surface atoms, the initial TOF can be calculated from eqn (9-2) and the results are summarized in **Table 9-1**.
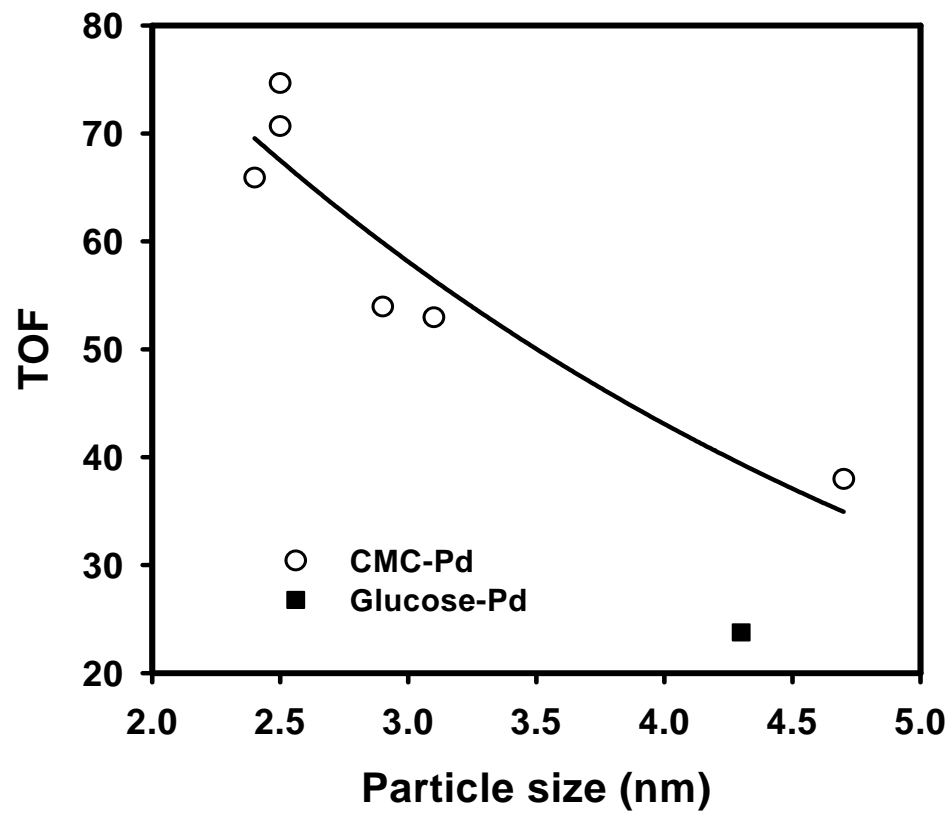
(a)
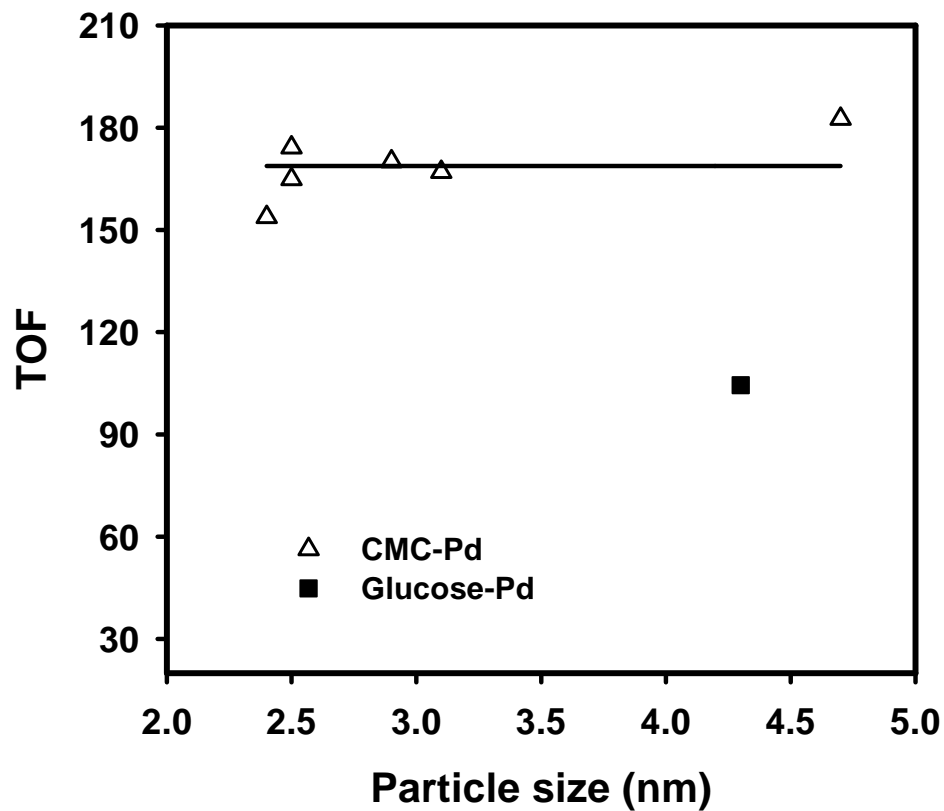
(b)

Figure 9-4. Turnover frequency (TOF) as a function of particle size for the CMC-Pd and glucose-Pd catalysts in the TCE hydrodechlorination reaction (Initial TCE concentration 50 mg/L, Pd colloidal solution containing 1.06 mg/L Pd nanoparticles). The TOF is calculated on the basis of **(a)** total number of surface atoms and **(b)** total number of vertex and edge surface atoms.

Figure 9-4(a) shows the TOF values versus the particle size and stabilizer. It is found that the catalytic activity of Pd nanoparticles decreased in the order of 0.15 wt.% CMC-Pd (2.4 nm) ≈ 0.10 wt.% CMC-Pd (2.5 nm) ≈ 0.05 wt.% CMC-Pd (2.5 nm) > 0.01 wt.% CMC-Pd (2.9 nm) ≈ 0.005 wt.% CMC-Pd (3.1 nm) > 0.001 wt.% CMC-Pd (4.7 nm) > 0.90 wt.% glucose-Pd (4.3 nm). The TOF value is increased by about a factor of 2 with the particle size decreased from 4.7 nm to 2.5 nm. Interestingly, the TOF values of CMC-Pd with same size but different CMC/Pd ratio are being equal, which indicates that the stabilizer effect does not play an important role in TCE hydrodechlorination. With excluding the stabilizer effect, if the reaction can be taking place over all of the surface Pd atoms (e.g. all the surface atoms were active sites), there would be no particle size dependence on the TOF. The fact that the smaller CMC-Pd nanoparticles have higher TOF values indicates higher fraction of active sites on the surface of smaller nanoparticles. As shown in **Table 9-1**, the fraction of different types of sites with respect to the total number of surface atoms depends on the particle size. The smaller the particle size the higher the fraction of the edge and vertex sites is, which suggests that the low-coordination vertex and edge atoms on the particle surface may be the active sites for catalysis. We calculated the TOF based on the number of vertex and edge atoms on the Pd surface (as shown in **Figure 9-4 (b)**), the dependent of TOF (expressed in terms of moles of TCE degraded per mole of vertex and edge surface Pd atoms per min) on the particle size disappears, which further supports the suggestion that the vertex and edge atoms on the Pd particle surface are the active sites for TCE hydrodechlorination.

Li et al. (2001) investigated the size effects of PVP-Pd nanoparticles on the catalytic Suzuki reactions in aqueous phase and also observed a general trend of increased catalytic activity with the decrease of particle size. They further suggested that the low-coordination vertex and edge atoms on the particle surface are active sites for the Suzuki reaction, consistent to the results from this study. Interestingly, they observed a decreased catalytic activity with the particle size decreased from 3.9 nm to 3.0 nm and attributed this change to the strong adsorption of reaction intermediates on the particle surface acting as a poison to the catalytic reaction. In this study, the decrease of catalytic activity for the smallest Pd nanoparticles was not observed, which suggests that the adsorption of intermediates from TCE hydrodechloriation on CMC-Pd nanoparticles may not be strong enough to impose a negative effect on reaction.

Interestingly, k_{app} and TOF values for glucose-Pd (4.3 nm) are lower than that for CMC-Pd (4.7nm), indicating that stabilizer effect becomes important as the stabilizer molecules are changed. This can be explained by the dense anchoring of β-D glucose on the Pd surface due to this small molecule's low degree of steric hindrance. In contrast, the much greater steric hindrance from the macromolecular CMC allows it adsorbed on the Pd surface in a much less compact way. The different adsorption of these two molecules on Pd surface was indicated by the DLS analyses that the thickness of the glucose layer was 0.8 nm whereas the thickness of the bulkier CMC layer was 5.2nm. Given that much higher glucose concentration (glucose = 0.90 wt.%) was used for Pd nanoparticle synthesis to obtain similar particle size as CMC-Pd (CMC = 0.001 wt.%), more β-D glucose molecules are expected to be adsorbed on the Pd surface in a denser way, which decreased the surface active sites for TCE hydrodechlorination. The bulkier layer of

CMC molecules also allows faster diffusion of the H_2 and TCE to access active sites on Pd surface, further increasing the rate of reaction.

It is worth noting that halogenated intermediates, such as VC and DCE, were not detected during the course of TCE hydrodechlorination catalyzed by 0.15 wt.% CMC-Pd nanoparticles, suggesting a one-step conversion of the environmentally deleterious TCE into biodegradable ethane. The completeness of the TCE hydrodechlorination catalyzed by CMC-Pd nanoparticles can be reflected by monitoring both the TCE degradation and chloride production rates. As shown in **Figure 9-5**, the chloride production rate is nearly stoichiometrically consistent with the degradation rate of TCE during the reaction. The nearly perfect chlorine mass balance indicates a nearly complete TCE degradation without the accumulation of chlorinated intermediates. This further confirms the results in the GC analysis where no VC and DCE were detected during reaction. The absence of chlorinated intermediates exhibits another key advantage of this highly effective catalysis technology since the intermediates such as VC are more toxic and persistent to natural attenuation processes than TCE itself in groundwater (He and Zhao, 2005).
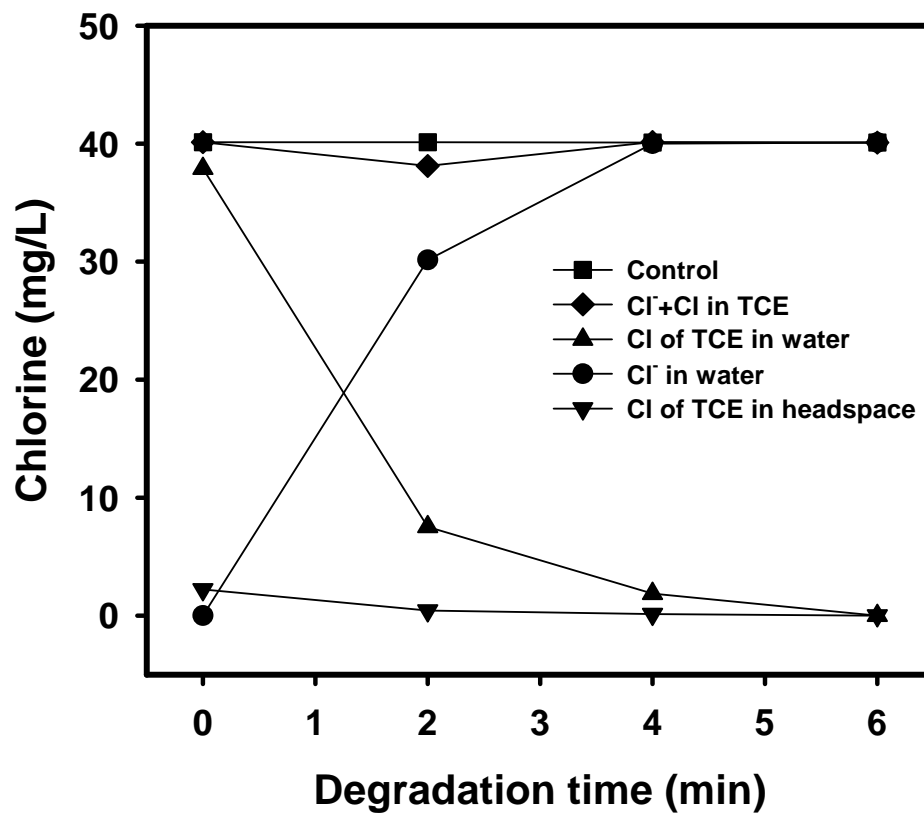
Figure 9-5. Evolution of chloride and TCE-Cl during hydrodechlorination of TCE catalyzed by CMC-Pd nanoparticles. Initial total TCE concentration = 50 mg L^{-1}. Pd nanoparticles mass concentration is 1.06 mg/L.

9.3.4 Implication of the CMC-Pd nanotechnology for groundwater remediation

Table 9-2 compares the catalytic activity of 0.1 wt.% CMC-Pd nanoparticles and other Pd-based catalysts for the TCE hydrodechorination based on the reaction rate constants and initial TOF. The k_{obs} of the CMC-Pd nanoparticles for the TCE hydrodeclorination is 13, 68, and 1971 times higher than those of PVP-Pd, Pd/Al$_2$O$_3$, and Pd black catalysts. Nutt et al. (2005) successfully synthesized Pd-Au alloys by adding controlled amounts of Pd salt and ascorbic acid (as reducing agent) to the Au sol. These Pd-Au alloys were highly ative to TCE hydrodechlorination, which might be due to an electronic inductive effect by the Au on the supported Pd particles. The CMC-Pd nanoparticles synthesized via a "green", cost-effective and straightforward way in the current work exhibited comparable k_{obs} to the Pd-Au alloys. CMC-Pd nanoparticles also exhibit much higher surface catalytic activity (TOF$_{init}$) than those of PVP-Pd, Pd/Al$_2$O$_3$, and Pd black catalysts for TCE degradation. We believe that both the fairly small particle size and the preferable adsorption nature of the CMC molecules on the Pd surface result in the highly active CMC-Pd nanoparticles for TCE degradation. The CMC-Pd nanoparticle technology holds promises for applications in groundwater remediation.

Table 9-2. Reaction Rate Constants and Initial TOF of TCE Hydrodechlorination for Pd-Based Catalysts.

Catalysts	Particle Size (nm)	k_{obs} ($L \cdot g_{pd}^{-1} \cdot min^{-1}$)	Initial TOF (mol TCE·mol^{-1} Pd·min^{-1})
Pd black[*]	8.2	0.42	0.4
Pd/Al$_2$O$_3$[*]		12.2	2.8
PVP-Pd[*]	6.1	62.0	13.6
Pd-Au alloy[*]	~ 20.0	~ 930	
0.90 wt.% glucose-Pd	4.3	152	23.8
0.10 wt.% CMC-Pd	2.5	828	74.7

*: Nutt et al. (2005)

CHAPTER 10. CONCLUSIONS AND SUGGESTIONS FOR FUTURE RESEARCH

10.1 Summary and Conclusions

In situ destruction of chlorinated solvents by directly injecting Fe-based (mono-Fe or Fe-Pd bimetal) nanoparticles into source zones has attracted great interests in recent years. However, the application of this promising technology has been held back by a key technical barrier that the nanoparticles tend to agglomerate to micron-scale or larger in minutes, thereby losing their soil mobility and chemical reactivity rapidly. For the first time, we synthesized a new class of highly dispersed iron nanoparticles using food-grade starch or carboxymethyl cellulose as "green" and low-cost stabilizers. Detailed experimental investigations were carried out to determine the morphology and the size of this new nanomaterial, the reactivity of these particles to trichloroethene and PCBs, their transport in porous media and application to DNAPL remediation, and the technical feasibility of applying this novel technology in the field for chlorinated solvent remediation.

The starched Fe-Pd nanoparticles displayed much less agglomeration but greater dechlorination power than those prepared without a stabilizer. TEM analyses indicated that the starched nanoparticles were present as discrete particles as opposed to dendritic

flocs for non-starched particles. The mean particle size was estimated to be 14.1 nm with a standard deviation of 11.7 nm, which translated to a surface area of ~55 m^2 g^{-1}. While starched nano-particles remained suspended in water for days, non-starched particles agglomerated and precipitated within minutes. The starched nanoparticles exhibited markedly greater reactivity when used for dechlorination of TCE or PCBs in water. At a dose of 0.1 g L^{-1}, the starched particles were able to destroy 98% of TCE ($C_0 = 25$ mg L^{-1}) within 1 h. While trace amounts (<25 µg L^{-1}) of 1,1-DCE were detected in the initial stage (<20 minutes) of degradation, no other intermediate by-products such as vinyl chloride, *cis*- or *trans*-dichloroethene were detected. The starched nanoparticles at ~1 g L^{-1} were able to transform over 80% of PCBs ($C_0 = 2.5$ mg L^{-1}) in less than 100 hours, compared to only 24% with non-starched Fe-Pd nanoparticles.

As starch could only stabilize the Fe nanoparticles for ~ 2 days, carboxymethyl cellulose (CMC) was selected as a better stabilizer. The CMC-stabilized Fe nanoparticles did not show any signs of precipitation over a 7-day period, after which the 0.1g/L nanoparticles were nearly completely oxidized by water under ambient conditions. Transmission Electron Microscope (TEM) and Dynamic Light Scattering (DLS) analyses indicated that the CMC-stabilized nanoparticles were highly dispersed in water with a diameter <11.0 nm. Fourier Transform Infrared Spectroscopy (FTIR) results suggested that CMC molecules were adsorbed to iron nanoparticles primarily through the carboxylate groups through monodentate complexation. In addition, –OH groups in CMC were also involved in interacting with iron particles to exert effective stabilization. Batch dechlorination tests demonstrated that the CMC-stabilized nanoparticles degraded TCE

17 times faster than non-stabilized counterparts based on the initial pseudo first-order rate constant.

To facilitate the effective application of iron nanoparticles for in situ chlorinated solvent remediation, the size-controlled synthesis of iron nanoparticles is desired. Iron nanoparticles of various size were synthesized by applying various types of carboxymethyl cellulose (CMC) as a stabilizer. At an initial Fe^{2+} concentration of 0.1 g/L and with 0.2% (w/w) of a CMC (M.W. = 90k), nanoparticles with a hydrodynamic diameter of 18.6 nm were obtained. Smaller nanoparticles were obtained as the CMC-to-Fe^{2+} molar ratio was increased. When the initial Fe^{2+} concentration was increased to 1 g/L, only 1/4 of the CMC was needed to obtain similar nanoparticles. On an equal weight basis, CMC with greater M.W. or higher D.S. (degree of substitution) gave smaller nanoparticles, and lower synthesizing temperature favored formation of smaller nanoparticles. It is proposed that CMC stabilizes the nanoparticles through accelerating nucleation of Fe atoms during formation of ZVI nanoparticles, and subsequently, forming a bulky and negatively charged layer via sorption of CMC molecules on the ZVI nanoparticles, thereby preventing the nanoparticles from agglomeration through electrosteric stabilization. In accord with the classical coagulation theory, the presence of high concentrations of cations (Na^+ and Ca^{2+}) promoted agglomeration of the nanoparticles.

The surface modification of Fe-Pd nanoparticles with CMC stabilizers also affected their reactivity toward chlorinated solvents. Overall, the particle stabilization prevented particle agglomeration and resulted in greater particle reactivity. However, the presence of CMC may inhibit TCE degradation at a stabilizer-to-Fe molar ratio greater

than 0.0124. Within the same homologous series, CMC of greater molecular weight resulted in more reactive nanoparticles for TCE hydrodechlorination. Hydrogen (either residual hydrogen from zero-valent iron (ZVI) nanoparticle synthesis or hydrogen evolved from ZVI corrosion) can serve as effective electron donors for TCE dechlorination in the presence of Pd (either coated on ZVI or as separate nanoparticles). Decreasing reaction pH from 9.0 to 6.0 increased the TCE reduction rate by 11.5 times, but enhanced the Fe corrosion rate by 31.4 times based on the pseudo-first order rate constant. Decreasing pH also shifted the rate controlling step of TCE reduction from Fe corrosion to hydrodechlorination. Ionic strength ($< 0.51M$) did not significantly affect the TCE reduction.

Lab column tests showed significant mobility of the CMC-stabilized Fe nanoparticles in four different porous media: coarse and fine glass bead, silica sand, and loamy sand soil. The attachment efficiency α of CMC-stabilized Fe nanoparticles in silica sand was ~ 0.0025, which is 1-2 magnitude lower than the reported α for other surface-modified Fe nanoparticles, indicating the relatively high mobility of this new class of nanoparticles. With pumping the Fe-Pd nanoparticle suspension through a TCE DNAPL-contained silica sand column, $\sim 39.5\%$ of the TCE was completely dechlorinated to chloride. The successful destruction of DNAPL in porous media indicated the future application of this technology to DNAPL remediation in source zones.

To demonstrate the effectiveness of CMC-stabilized Fe nanoparticles as a potential remediation technology, two field-scale pilot tests were carried out in California and Alabama, respectively. Preparation of stabilized ZVI nanoparticles on site was accomplished using a "batch reactor" for immediate injection to minimize losses in

reactivity. Significant mobility and reactivity of the stabilized particles were observed in both California and Alabama sites. The push-pull tests performed in California site demonstrated that the particles lost their mobility with time in the subsurface and thereby may not pose potential environmental risk to human. The injection of the nanoparticles altered the geochemistry of the groundwater and created a favorable condition for reductive dechlorination. The continuous releasing of H_2 from Fe corrosion and natural degradation of CMC significantly promoted the enhanced biodegradation of chlorinated solvent contaminants such as PCE and TCE in the Alabama site. For example, the concentration of PCE in the injection well IW-1, monitoring well MW-1 (5ft down-gradient of IW-1), and monitoring well MW-2 (10ft down-gradient of IW-1) was only 25%, 20%, and 8% of the pre-injection concentrations at ~ 100 days after nanoparticle (568 g Fe-Pd) injection. The successful field demonstration of the stabilized Fe-Pd nanoparticle technology confirmed the great promise of this technology for in situ groundwater and soil remediation.

The application of CMC as an effective stabilizer was extended to the synthesis of highly dispersed Pd nanoparticles. The CMC-Pd nanoparticles exhibited rather high catalytic activity (observed pseudo-first-order rate constant, k_{obs}, is up to $828\,L \cdot g_{Pd}^{-1}\,\mathrm{min}^{-1}$) for the hydrodechlorination of TCE in water. The effect of stabilizer and particle size on TCE hydrodechlornation was investigated by the use of six CMC-Pd catalysts stabilized by 0.15 wt.%, 0.10 wt.%, 0.05 wt.%, 0.01 wt.%, 0.005 wt.%, and 0.001 wt.% CMC, respectively, and one glucose-Pd catalysts stabilized by 0.090 wt.% glucose. The catalytic activity of the Pd nanoparticles expressed in terms of the initial turnover frequency is found to be in the order of 0.15 wt.% CMC-Pd (2.4 nm) ≈ 0.10

wt.% CMC-Pd (2.5 nm) ≈ 0.05 wt.% CMC-Pd (2.5 nm) > 0.10 wt.% CMC-Pd (2.9 nm) ≈ 0.005 wt.% CMC-Pd (3.1 nm) > 0.001 wt.% CMC-Pd (4.7 nm) > glucose-Pd (4.3 nm), indicating that surface Pd atoms do not all have the same reactivity in this reaction. The trend of increased catalytic activity with the decrease in the CMC-Pd particle size suggests that the low-coordination number vertex and edge atoms on the particle surface are active sites for the TCE hydrodechlorination. The lower catalytic activity for glucose-Pd nanoparticles might be due to the dense adsorption of glucose on the particle surface, which decreases the active sites for TCE hydrodechlorination. Due to the high catalytic activity, the usage of CMC-Pd could be significantly cut down to achieve same remediation goal as using commercial Pd black or Pd/Al_2O_3. This technology holds promises for applications in groundwater remediation.

10.2 Suggestions for Future Work

The chlorinated solvent degradation by stabilized Fe-based nanoparticles has been extensively studied in this research. However, the chlorinated solvents in source zone are usually adsorbed in the soil or present as a separate DNAPL phase. The degradation behavior of soil-related chlorinated solvents or DNAPL using stabilized Fe-based nanoparticles may significantly differ from their degradation behavior in water. For example, the strong adsorption of chlorinated solvent by the NOM in the soil could retard the effective degradation of chlorinated solvents in the soil, and the degradation of DNAPL could be limited by the relatively low affinity of the nanoparticles to the NAPL/water interface. To facilitate the effective application of this technology for source zone remediation, all these questions must be asked and answered and should be an emphasis in the future research.

One solution to the above problem would be to use surfactants as the co-stabilizer with CMC (Note: Sole surfactants themselves are not effective enough to stabilize iron nanoparticles). The further adsorption of surfactants onto CMC-Fe particle surface would not only increase the particle stability but also enhance the dissolution of chlorinated solvents from the soil or increase the particle affinity to the NAPL/water phase when the nanoparticles are applied for degradation. The selection and the amount of surfactants used to best promote dechlorination in soil need to be optimized and should be an interesting and important topic for future research.

Untill recently, the evaluation of the nanoparticle transport in porous media is usually performed in 1-D column experiments. However, 1-D column may not represent the subsurface conditions as real as 2-D box. Therefore, the 2-D investigation on transport of iron nanoparticles or other nanoparticles are important for predicting their transport and eventually the fate in the real subsurface. Another interesting research topic here is to investigate the DNAPL degradation in 2-D box when the stabilized nanoparticles are applied. The knowledge from this experiment would help predicting the performance of this technology in field DNAPL remediation.

In order to gain regulatory and public acceptance for using nanomaterials in environmental remediation, information on toxicology and fate of iron nanoparticles is needed. Although research on nanoparticle toxicology and their fate and transport have been two of the common research priorities for nanotechnology environment and safety research (Dunphy Guzman et al. 2006), researchers have focused mainly on the nanoparticulate aerosols by the atmospheric toxicologists and ultrafine particles (UFP) by toxicologists (Biswas and Wu, 2005). No investigations on toxicology and fate of the iron

naoparticles have been reported. Therefore, future work should consider the transport and fate of nanoparticles in environment.

The practical application of Pd nanoparticles usually requires the recovery and reuse of the nanoparticles through immobilizing them on a catalyst support. Nutt et al. (2006) deposited the pre-synthesized Pd/Au nanoparticles on oxide supports through mechanical mixing followed by evaporation. This strategy was based on electrostatic interactions between the Pd/Au nanoparticles and the porous support. Therefore, the stability of the nanoparticles in the porous support is highly affected by the groundwater chemistry. If thermal treatment is used to remove the stabilizer ligands, the nanoparticles tend to sinter. In the future research, a new strategy needs to be developed to homogeneously disperse nanoparticles in the support, through which the wide application of this technology is expected.

REFERENCES

Agency for Toxic Substance and Disease Registry (ATSDR). ToxFAQ for Trichloroethylene. http://www.atsdr.cdc.gov/tfacts19.html.

Alford-Stevens, A. L., 1986. Analyzing PCBs. Environ. Sci. Technol. 20 (12), 1194-1199.

Arnold, W. A., Roberts, A. L., 2000. Pathways and kinetics of chlorinated ethylene and chlorinated acetylene reaction with Fe(0) particles. Environ. Sci. Technol. 34 (9), 1794-1805.

Bellamy, L. J., 1975. The infrared spectra of complex molecules, Chapman and Hall: London.

Benfield, R. E., 1992. Mean coordination numbers and the non-metal-metal transition in clusters. J. Chem. Soc. Faraday Trans. 88 (8), 1107-1110.

Berti, W. R., Cunnimgham, S. D., 1997. In-place inactivation of Pb in Pb-contaminated soils. Environ. Sci. Technol. 31 (5), 1359-1364.

Biswas, P., Wu, C. Y., 2005. Nanoparticles and the environment. J. Air Waste Manage. Assoc. 55(6), 708-746.

Bransfield, S. J., Cwiertny, D. M., Roberts, A. L., Fairbrother, D. H., 2006. Influence of copper loading and surface coverage on the reactivity of granular iron toward 1,1,1-trichloroethane. Environ. Sci. Technol. 40, 1485-1490.

Brown, D. W., Floyd, A. J., Sainsbury, M., 1988. Organic spectroscopy, John Wiley &

Sons: Bath.

Chen, K. L., Mylon, S. E., Elimelech, M., 2006. Aggregation kinetics of alginate-coated hematite nanoparticles in monovalent and divalent electrolytes. Environ. Sci. Technol. 40 (5), 1516-1523.

Chuang, F. W., Larson, R. A., Wessman, M. S., 1995. Zero-valent iron-promoted dechlorination of polychlorinated biphenyls. Environ. Sci. Technol. 29 (9), 2460-2463.

Chu, Y., Jin, Y., Yates, M. V., 2000. Virus transport through saturated sand columns as affected by different buffer solutions. J. Environ. Qual. 29 (4), 1103-1110.

Ciesielski, W., Lii, C. Y., Yen, M. T., Tomasik, P., 2003. Interactions of starch with salts of metals from the transition groups. Carbohydr. Polym. 51 (1), 47-56.

Ciesielski, W., Tomasik, P., 2003. Thermal properties of complexes of amaranthus starch with selected metal salts. Thermochim. Acta 403 (2), 161-171.

Creighton, J. A., Eadon, D. G., 1991. Ultraviolet-visible absorption spectra of the colloidal metallic elements. J. Chem. Soc. FARADAY TRANS. 87 (24), 3881-3891.

Cushing, B. L., Kolesnichenko V. L., O'Connor C. J., 2004. Recent advances in the liquid-phase syntheses of inorganic nanoparticles. Chem. Rev. 104 (9), 3893-3946.

Cwiertny, D. M., Bransfield, S. J., Livi, K. J. T., Fairbrother, D. H., Roberts, A. L., 2006. Exploring the influence of granular iron additives on 1,1,1-trichloroethane reduction. Environ. Sci. Technol. 40 (21), 6837-6843.

Deacon, G. B., Phillips, R. J., 1980. Relationship between the carbon-oxygen stretching frequencies of carboxylate complexes and the type of carboxylato coordination.

Coord. Chem. Rev. 33 (3), 227-250.

Ditsch, A., Laibinis, P. E., Wang, D. I. C., Hatton, T. A., 2005. Controlled clustering and enhanced stability of polymer-coated magnetic nanoparticles. Langmuir 21 (13), 6006-6018.

Doong, R. A., Lai, Y. J., 2005. Dechlorination of tetrachloroethylene by palladized iron in the presence of humic acid. Water Res. 39 (11), 2309-2318.

Dunphy Guzman, K. A., Taylor, M. R., Banfield, J. F., 2006. Environmental risks of nanotechnology: National nanotechnology initiative funding, 2000-2004. Environ. Sci. Technol. 40(5), 1401-1407.

Elliott, D. W., Zhang, W. X., 2001. Field assessment of nanoscale bimetallic particles for groundwater treatment. Environ. Sci. Technol. 35 (24), 4922-4926.

Field, J. A., Istok, J. D., Schroth, M. H., Sawyer, T. E., Humphrey, M. D., 1999. Laboratory investigation of surfactant-enhanced trichloroethene solubilization using single-well, "push-pull" tests. Ground Water 37 (4), 581-588.

Gavaskar, A. R., Gupta, N., Sass, B. M., Janosy, R. J., O'Sullivan, D., 1998. Permeable barriers for groundwater remediation: Design, construction, and monitoring; Battelle Press: Columbus.

Gavaskar, A., Tatar, L., Condit, W., 2005. Cost and performance report: Nanoscale zero-valent iron technologies for source remediation, Naval Facilities Engineering Service Center: Port Hueneme, CA.

Gilbert, R. D., 1994. Cellulosic polymers, blends, and composites, Hanser/Gardner Publications: Cincinnati.

Gillham, R. W., Win 2003. Discussion of nano-scale iron for dehalogenation. Ground

Water Monit. Rem. 23 (1), 6-8.

Glavee, G. N., Klabunde, K. J., Sorensen, C. M., Hadjipanayis, G. C., 1995 Chemistry of borohydride reduction of iron(II) and iron(III) ions in aqueous and nonaqueous media. Formation of nanoscale Fe, FeB, and Fe_2B powders. Inorg. Chem. 34 (1), 28-35.

Grittini, C., Malcomson, M., Fernando, Q., Korte, N., 1995. Rapid dechlorination of polychlorinated biphenyls on the surface of a Pd/Fe bimetallic system. Environ. Sci. Technol. 29 (11), 2898-2900.

Guven, O., Falta, R. W., Molz, F. J., Melville, J. G., 1985. Analysis and interpretation of single-well tracer tests in stratified aquifers. Water Resour. Res. 21 (5), 676-684.

Haggerty, R., Schroth, M. H., Istok, J. D., 1998. Simplified method of "push-pull" test data analysis for determining in-situ reaction rate coefficients. Ground Water 36 (2), 314-324.

Hall, S. H., Luttrell, S. P., Cronin, W. E., 1991. A method for estimating effective porosity and groundwater velocity. Ground Water 29 (2), 171-174.

He, F., Zhao, D., 2005. Preparation and characterization of a new class of starch-stabilized bimetallic nanoparticles for degradation of chlorinated hydrocarbons in water. Environ. Sci. Technol. 39 (9), 3314-3320.

He, F., Zhao, D., 2007a. Manipulating the size and dispersibility of zero-valent iron nanoparticles by use of carboxymethyl cellulose stabilizers. Environ. Sci. Technol. 41 (17), 6216-6221.

He, F., Zhao, D., 2007b, Hydrodechlorination of trichloroethene using stabilized Fe-Pd nanoparticles: Reaction mechanism and effects of stabilizers, catalysts and

reaction conditions. Appl. Catl., B, in review.

He, F., Zhao, D., Liu, J., Roberts, C. B., 2007. Stabilization of Fe-Pd nanoparticles with sodium carboxymethyl cellulose for enhanced transport and dechlorination of trichloroethylene in soil and groundwater. Ind. Eng. Chem. Res. 46 (1), 29-34.

Hogue, C., 2002. Assessing Anniston. Chem. Eng. News, 13 (19), 27-32.

Hogue, C., 2002. Monsanto, Solutia shell out on PCBs. Chem. Eng. News, 13 (19), 27-32.

Image J: Image processing and analysis in Java. http://rsb.info.nih.gov/ij.

Interstate Technology & Regulatory Council (ITRC), 2005. Permeable reactive barriers: Lessons learned/new directions. Washington, DC: ITRC.

Istok, J. D., Field, J. A., Schroth, M. H., Davis, B. M., Dwarakanath, V., 2002. Single-well "push-pull" partitioning tracer test for NAPL detection in the subsurface. Environ. Sci. Technol. 36 (12), 2708-2716.

Johnson, P. R., Sun, N., Elimelech, M., 1996a. Colloid transport in geochemically heterogeneous porous media: Modeling and measurements. Environ. Sci. Technol. 30 (11), 3284-3293.

Johnson, T. L., Scherer, M. M., Tratnyek, P. G., 1996b. Kinetics of halogenated organic compound degradation by iron metal. Environ. Sci. Technol. 30 (8), 2634-2640.

Jones, F., Farrow, J. B., Bronswijk, W. V., 1998. An infrared study of a polyacrylate flocculant adsorbed on hematite. Langmuir 14 (22), 6512-6517.

Jorgensen, J. M., Erlacher, K., Pedersen, J. S., Gothelf, K. V., 2005. Preparation temperature dependence of size and polydispersity of alkylthiol monolayer protected gold clusters. Langmuir 21 (23), 10320-10323.

Jovanovic, G. N., Znidarsic-Plazl, P., Sakrittichai, P., Al-Khaldi, K., 2005.

Dechlorination of *p*-chlorophenol in a microreactor with bimetallic Pd/Fe catalyst. Ind. Eng. Chem. Res. 44 (14), 5099 - 5106.

Kanel, S. R., Greneche, J. M., Choi, H., 2006. Arsenic(V) removal from groundwater using nano scale zero-valent iron as a colloidal reactive barrier material. Environ. Sci. Technol. 40 (6), 2045-2050.

Kanel, S. R., Manning, B., Charlet, L., Choi, H., 2005. Removal of arsenic(III) from groundwater by nanoscale zero-valent iron. Environ. Sci. Technol. 39 (5), 1291-1298.

Kanel, S. R., Nepal, D., Manning, B., Choi, H., 2007. Transport of surface-modified iron nanoparticle in porous media and application to arsenic (III) remediation. J. Nanopart. Res. 9 (5), 725-735.

Kataby, G., Cojocaru, M., Prozorov, R., Gedanken, A., 1999. Coating carboxylic acids on amorphous iron nanoparticles. Langmuir 15 (5), 1703-1708.

Kataby, G., Prozorov, T., Koltypin, Y., Cohen, H., Sukenik, C. N., Ulman, A., Gedanken, A., 1997. Self-assembled monolayer coatings on amorphous iron and iron oxide nanoparticles: Thermal stability and chemical reactivity studies. Langmuir 13 (23), 6151-6158.

Kecskes, L. J., Woodman, R. H., Trevino, S. F., Klotz, B. R., Hirsch, S. G., Gersten, B. L., 2003. Characterization of a nanosized iron powder by comparative methods. KONA 21, 143-150.

Khalil, H., Mahajan, D., Rafailovich, M., Gelfer, M., Pandya, K., 2004. Synthesis of zerovalent nanophase metal particles stabilized with poly(ethylene glycol). Langmuir 20 (16), 6896-6903.

Kim, D. K., Mikhaylova, M., Zhang, Y., Muhammed, M., 2003. Protective coating of superparamagnetic iron oxide nanoparticles. Chem. Mater. 15 (8), 1617-1627.

Kim, Y. H., Carraway, E. R., 2003a. Reductive dechlorination of TCE by zero valent bimetals. Environ. Technol. 24 (1), 69-75.

Kim, Y. H., Carraway, E. R., 2003b. Dechlorination of chlorinated ethenes and acetylenes by palladized iron. Environ. Technol. 24 (7), 809-819.

Korte, N. E., West, O. R., Liang, L., Gu, B., Zutman, J. L., Fernando, Q., 2002. The effect of solvent concentration on the use of palladized-iron for the step-wise dechlorination of polychlorinated biphenyls in soil extracts. Waste Manage. 22 (3), 343-349.

Kreibig, U., Vollmer, M., 1995. Optical properties of metal clusters, Spring-Verlag: Berlin.

Kretzschmar, R., Borkovec, M., Grolimund, D., Elimelech, M., 1999. Mobile subsurface colloids and their role in contaminant transport. Adv. Agron. 66, 121-193.

Kretzschmar R., Sticher, H., 1997. Transport of humic-coated iron oxide colloids in a sandy soil: Influence of Ca^{2+} and trace metals. Environ. Sci. Technol. 31 (12), 3497-3504.

Kubatova, A., Herman, J., Steckler, T. S., Veij, M. D., Miller, D. J., Klunder, E. B., Wai, C. M., Hawthorne, S. B., 2003. Subcritical (hot/liquid) water dechlorination of PCBs (Aroclor 1254) with metal additives and in waste paint. Environ. Sci. Technol. 37 (24), 5757-5762.

Lecoanet, H. F., Wiesner, M. R., 2004. Velocity effects on fullerene and oxide nanoparticle deposition in porous media. Environ. Sci. Technol. 38 (16), 4377-

4382.

Lehman, J., 1998. Carbohydrates: Structure and biology, Thieme: Stuttgart.

Lide, D.R., 1994. CRC Handbook of Chemistry and Physics, 75th ed., CRC Press, Boca Raton, FL.

Lien, H. L., Zhang, W. X., 2001. Nanoscale iron particles for complete reduction of chlorinated ethenes. Colloids Surf., A 191 (1-2), 97-105.

Li, F., Vipulanandan, C., Mohanty, K. K., 2003. Microemulsion and solution approaches to nanoparticle iron production for degradation of trichloroethylene. Colloids Surf., A 223 (1-3), 103-112.

Lin, C. J., Lo, S. L., Liou, Y. H., 2004. Dechlorination of trichloroethylene in aqueous solution by noble metal-modified iron. J. Hazard. Mater. 116 (3), 219-228.

Liou, Y. H., Lo, S. L., Kuan, W. H., Lin, C. J., Weng, S. C., 2006. Effect of precursor concentration on the characteristics of nanoscale zerovalent iron and its reactivity of nitrate. Water Res. 40 (13), 2485-2492.

Liu, J., He, F., Durham, J. E., Zhao, D., Roberts, C. B., 2007. Sugar stabilized Pd nanoparticles exhibiting high catalytic activities for the hydrodechlorination of environmentally deleterious trichloroethylene. Langmuir Submitted.

Liu, J. C., Qin. G. W., Raveendran, P., Ikushima, Y., 2006a. Facile "green" synthesis, characterization, and catalytic function of β-D-glucose-stabilized Au nanocrystals. Chem. Eur. J. 12 (8), 2132-2138.

Liu, Y., Choi, H., Dionysiou, D., Lowry, G. V., 2005a. Trichloroethene hydrodechlorination in water by highly disordered monometallic nanoiron. Chem. Mater. 17 (21), 5315-5322.

Liu, Y., Huang, C., Chen, Y., 2006b. Liquid-phase selective hydrogenation of p-chloronitrobenzene on Ni-P-B nanocatalysts. Ind. Eng. Chem. Res. 45 (1), 62-69.

Liu, Y., Lowry, G. V., 2006. Effect of particle age (Fe^0 Content) and solution pH on NZVI reactivity: H_2 evolution and TCE dechlorination. Environ. Sci. Technol. 40 (19): 6085-6090.

Liu, Y., Majetich, S. A., Tilton, R. D., Sholl, D. S., Lowry, G. V., 2005b. TCE dechlorination rates, pathways, and efficiency of nanoscale iron particles with different properties. Environ. Sci. Technol. 39 (5), 1338-1345.

Li, X. Q., Elliott, D. W., Zhang, W. X., 2006. Zero-valent iron nanoparticles for abatement of environmental pollutants: Materials and engineering aspects. Crit. Rev. Solid State Mater. Sci. 31 (4), 111-122.

Li, Y., Boone, E., EI-Sayed, M. A., 2002. Size effects of PVP-Pd nanoparticles on the catalytic Suzuki reactions in aqueous solution. Langmuir 18 (12), 4921-4925.

Lowry, G. V., Reinhard, M., 1999. Hydrodehalogenation of 1-to 3-carbon halogenated organic compounds in water using a palladium catalyst and hydrogen gas. Environ. Sci. Technol. 33 (11), 1905-1910.

Mace, C., 2006. Controlling groundwater VOCs: Do nanoscale ZVI particles have any advantages over microscale ZVI or BNP. Pollut. Eng. April issue, 24-27.

Magar, V. S., 2003. PCB treatment alternatives and research directions. J. of Environ. Eng. 129 (11), 961-965.

Magdassi, S., Bassa, A., Vinetsky, Y., Kamyshny, A., 2003. Silver nanoparticles as pigments for water-based ink-jet inks. Chem. Mater. 15 (11), 2208-2217.

Matheson, L. J., Tratnyek, P. G., 1994. Reductive dehalogenation of chlorinated

methanes by iron metal. Environ. Sci. Technol. 28 (12), 2045-2053.

Mcnab, Jr., W. W., Ruiz, R., Reinhard, M., 2000. In-situ destruction of chlorinated hydrocarbons in groundwater using catalytic reductive dehalogenation in a reactive well: Testing and operational experiences. Environ. Sci. Technol. 34 (1), 149-153.

Mondal, K., Jegadeesan, G., Lalvani, S. B., 2004. Removal of selenate by Fe and NiFe nanosized particles. Ind. Eng. Chem. Res. 43 (16), 4922-4934.

Moran, M. J., Zogorski, J. S., Squillace, P. J., 2007. Chlorinated solvents in groundwater of United Stats. Environ. Sci. Technol. 41 (1), 74-81.

Moran, T., 2004. New technology revolutionizing groundwater clean-up. E-Wire Press Release, http://www.ewire.com.

Nationtal Research Council (NRC), 1994. Alternative for groundwater cleanup. National Academy Press: Washington, DC.

Nationtal Research Council (NRC), 2001. Risk-management strategy for PCB-contaminated sediments. National Academy Press: Washington, DC.

Nurmi, J. T., Tratnyek, P. G., Sarathy, V., Baer, D. R., Amonette, J. E., Pecher, K., Wang, C. M., Linehan, J. C., Matson, D. W., Penn, R. L., Driessen, M. D., 2005. Characterization and properties of metallic iron nanoparticles: Spectroscopy, electrochemistry, and kinetics. Environ. Sci. Technol. 39 (5), 1221-1230.

Nutt, M. O., Heck, K. N., Alvarez, P., Wong, M. S., 2006. Improved Pd-on-Au bimetallic nanoparticle catalysts for aqueous-phase trichloroethene hydrodechlorination. Appl. Catal., B. 69 (1-2), 115-125.

Nutt, M. O., Hughes, J. B., Wong, M. S., 2005. Designing Pd-on-Au bimetallic

nanoparticle catalysts for trichloroethene hydrodechlorination. Environ. Sci. Technol. 39 (5), 1346-1353.

O'Melia, C. R., 1972. In physicochemical processes for water quality control, Weber, W. J., JR., Ed., Wiley: New York.

Orth, W. S., Gillham, R. W., 1996. Dechlorination of trichloroethene in aqueous solution using Fe^0. Environ. Sci. Technol. 30 (1), 66-71.

Pitterle, M. T., Andersen, R. G., Novak, J. T., Widdowson, M. A., 2005. Push-pull tests to quantify in situ degradation rates at a phytoremediation site. Environ. Sci. Technol. 2005, 39 (23), 9317-9323.

Ponder, S. M., Darab, J. G., Bucher, J., Caulder, D., Craig, I., Davis, L., Edelstein, N., Lukens, W., Nitsche, H., Rao, L., Shuh, D. K., Mallouk, T. E., 2001. Surface chemistry and electrochemistry of supported zerovalent iron nanoparticles in the remediation of aqueous metal contaminants. Chem. Mater. 13 (2), 479-486.

Ponder, S. M., Darab, J. G., Mallouk, T. E., 2000. Remediation of Cr(VI) and Pb(II) aqueous solutions using supported, nanoscale zero-valent iron. Environ. Sci. Technol. 34 (12), 2564-2569.

Quinn, J., Geiger, C., Clausen, C., Brooks, K., Coon, C., O'Hara, S., Krug, T., Major, D., Yoon, W.-S., Gavaskar, A., Holdsworth, T., 2005. Field demonstration of DNAPL dehalogenation using emulsified zero-valent iron. Environ. Sci. Technol. 39 (5), 1309-1318.

Raveendran, P., Fu, J., Wallen, S. L., 2003. Complete "green" synthesis and stabilization of metal nanoparticles. J. Am. Chem. Soc. 125 (46), 13940-13941.

Raveendran, P., Fu, J., Wallen, S. L., 2006. A simple and "green" method for the

synthesis of Au, Ag, and Au-Ag alloy nanoparticles. Green Chem. 8 (1), 34-38.

Reinhard, M., Shang, S., Kitanidis, P. K., Orwin, E., Hopkins, G. D., Lebron, C. A., 1997. In situ BTEX biotransformation under enhanced nitrate- and sulfate-reducing conditions. Environ. Sci. Technol. 31 (1), 28-36.

Reynolds, G. W., Hoff, J. T., Gillham, R. W., 1990. Sampling bias caused by materials used to monitor halocarbons in groundwater. Environ. Sci. Technol. 24 (1), 135-142.

Saleh, N., Phenrat, T., Sirk, K., Dufour, B., Ok, J., Sarbu, T., Matyiaszewski, K., Tilton, R. D., Lowry, G. V., 2005. Adsorbed triblock copolymers deliver reactive iron nanoparticles to the oil/water interface. Nano Lett. 5 (12): 2489-2494.

Saleh, N., Sirk, K., Liu, Y. Q., Phenrat, T., Dufour, B., Matyjaszewski, K., Tilton, R. D., Lowry, G. V., 2007. Surface modifications enhance nanoiron transport and NAPL targeting in saturated porous media. Environ. Eng. Sci. 24 (1), 45-57.

Sayles, G. D., You, G., Wang, M., Kupferle, M. J., 1997. DDT, DDD, and DDE dechlorination by zero-valent iron. Environ. Sci. Technol. 31 (12), 3448-3454.

Schrick, B., Blough, J. L., Jones, A. D., Mallouk, T. E., 2002. Hydrodechlorination of trichloroethylene to hydrocarbons using bimetallic nickel-iron nanoparticles. Chem. Mater. 14 (12), 5140-5147.

Schrick, B., Hydutsky, B. W., Jones, A. D., Mallouk, T. E., 2004. Delivery vehicles for zerovalent metal nanoparticles in soil and groundwater. Chem. Mater. 16 (11), 2187-2193.

Schroth, M. H., Istok, J. D., Conner, G. T., Hyman, M. R., Haggerty, R., O'Reilly, K. T., 1998. Spatial variability in in-situ aerobic respiration and denitrification rates in a

petroleum-contaminated aquifer. Ground Water 36 (6), 924-937.

Schuth, C., Kummer, N. A., Weidenthaler, C., Schad, H., 2004. Field application of a tailored catalyst for hydrodechlorinating chlorinated hydrocarbon contaminants in groundwater. Appl. Catal. B. 52 (3), 197-203.

Schwarzenbach, R. P., Gschwend, P. M., Imboden, D. M., 1993. Environmental organic chemistry, John Wiley & Sons: New York.

Seshadri, R., Adrian, L., Fouts, D. E., Eisen, J. A., 2005. Genome sequence of the PCE-dechlorinating bacterium dehalococcoides ethenogenes. Science 307, 105-108.

Shen, J., Li, Z., Yan, Q., Chen, Y., 1993. Reactions of bivalent metal ions with borohydride in aqueous solution for the preparation of ultrafine amorphous alloy particles. J. Phys. Chem. 97 (32), 8504-8511.

Shimmin, R. G., Schoch, A. B., Barun, P. V., 2004. Polymer size and concentration effects on the size of gold nanoparticles capped by polymeric thiols. Langmuir 20 (13), 5613-5620.

Si, S., Kotal, A., Mandal, T., Giri, S., Nakamura, H., Kohara, T., 2004. Size-controlled synthesis of magnetite nanoparticles in the presence of polyelectrolytes. Chem. Mater. 16 (18), 3489-3496.

Snodgrass, M. F., Kitanidis, P. K., 1998. A method to infer in-situ reaction rates from push-pull experiments. Ground Water 36 (4), 645-650.

Sondi, I.; Goia, D. V.; Matijevic, E., 2003. Preparation of highly concentrated stable dispersions of uniform silver nanoparticles. J. Colloid Interface Sci. 260 (1), 75-81.

Song, H., Carraway, E. R., 2005. Reduction of chlorinated ethanes by nanosized zero-

valent iron: Kinetics, pathways, and effects of reaction conditions. Environ. Sci. Technol. 39 (16), 6237-6245.

Stowell, C. A., Korgel, B. A., 2005. Iridium nanocrystal synthesis and surface coating-dependent catalytic activity. Nano Lett. 5 (7), 1203-1207.

Su, C., Puls, R.W., 1999. Kinetics of trichloroethene reduction by zerovalent iron and tin: pretreatment effect, apparent activation energy, and intermediate products. Environ. Sci. Technol. 33 (1), 163-168.

Sun, S., Zeng, H., 2002. Size-controlled synthesis of magnetite nanoparticles. J. Am. Chem. Soc. 124 (28), 8204-8205.

Suslick, K. S., Fang, M., Hyeon, T., 1996. Sonochemical synthesis of iron colloids. J. Am. Chem. Soc. 118 (47), 11960-11961.

Suthersan, S. S., 1997. Remediation engineering: Design concepts. Lewis Publishers: Boca Raton, Florida.

Sylvestre, J. P., Poulin, S., Kabashin, A. V., Sacher, E., Meunier, M., Luong, J. H. T., 2004. Surface chemistry of gold nanoparticles produced by laser ablation in aqueous media. J. Phys. Chem. B 108 (43), 16864-16869.

Tilley, R. J. D., 2004. Understanding solids: The science of materials, John Wiley & Sons, New York.

Tufenkji, N., Elimelech, M., 2004. Correlation equation for predicting single-collector efficiency in physicochemical filtration in saturated porous media. Environ. Sci. Technol. 38 (2), 529-536.

U.S. EPA., 1997. Cleanup of the nation's waste sites: Markets and technology trends, EPA524-R-96-005, U.S. EPA: Washington, DC.

U.S. EPA, 1999. Field application of in situ remediation technologies: permeable reactive barriers, EPA 542-R-99-002, U. S. EPA: Washington, DC.

U.S. EPA, 2000. EPA Region 4 Alabama NPL/NPL Caliber Cleanup Site Summaries-Capital City Plume. http://www.epa.gov/region4/waste/npl/nplal/caplumal.htm.

Vance, D. B., 2005. Nanoscale iron colloids: The maturation of the technology for field scale applications. Pollut. Eng. 37(7), 16-18.

Wang, C. B., Zhang, W. X., 1997. Synthesizing nanoscale iron particles for rapid and complete dechlorination of TCE and PCBs. Environ. Sci. Technol. 31(7), 2154-2156.

Wei, J., Xu, X., Liu, Y., Wang, D., 2006. Catalytic hydrodechlorination of 2, 4-dichlorophenol over nanoscale Pd/Fe: Reaction pathway and some experimental parameters. Water Res. 40 (2), 348-354.

Wong, J. H. C., Lim, C. H., Nolen, G. L., 1997. Design of Remediation Systems; CRC Press/Lewis Publishers: Boca Raton, FL.

Wonterghem, J. V., Morup, S., Charles, S. W., Wells, S., Villadsen, J., 1985. Formation of a metallic glass by thermal decomposition of $Fe(CO)_5$. Phys. Rev. Lett. 55 (4), 410-413.

Wu, L., Ritchie, S. M. C., 2006. Removal of trichloroethylene from water by cellulose acetate supported bimetallic Ni/Fe nanoparticles. Chemosphere 63 (2), 285-292.

Wu, N., Fu, L., Su, M., Aslam, M., Wong, K. C., Dravid, V. P., 2004. Interaction of fatty acid monolayers with cobalt nanoparticles. Nano Lett. 4 (2), 383-386.

Xu, J., Bhattacharyya, D., 2007. Fe/Pd nanoparticle immobilization in microfiltration membrane pores: Synthesis, characterization, and application in the

dechlorination of polychlorinated biphenyls. Ind. Eng. Chem. Res. 46 (8): 2348-2359.

Xu, Y., Zhang, W. X., 2000. Subcolloidal Fe/Ag particles for reductive dehalogenation of chlorinated benzenes. Ind. Eng. Chem. Res. 39 (7), 2238-2244.

Xu, Y., Zhao, D., 2007. Reductive immobilization of chromate in water and soil using stabilized iron nanoparticles. Water Res. 41 (10), 2101-2108.

Xiong, Z., Zhao, D., Pan, G., 2007. Rapid and complete destruction of perchlorate in water and ion-exchange brine using stabilized zero-valent iron nanoparticles. Water Res. 41 (15), 3497-3505.

Yak, H. K., Wenclawiak, B. W., Cheng, I. F., Doyle, J. G., Wai, C. M., 1999. Reductive dechlorination of polychlorinated biphenyls by zerovalent iron in subcritical water. Environ. Sci. Technol. 33 (8), 1307-1310.

Zhang, L., Manthiram, A., 1997. Chains composed of nanosize metal particles and identifying the factors driving their formation. Appl. Phys. Lett. 70 (18), 2469-2471.

Zhang, P., Tao, X., Li, Z., Bowman, R. S., 2002. Enhanced perchloroethylene reduction in column systems using surfactant-modified zeolite/zero-valent iron pellets. Environ. Sci. Technol. 36 (16), 3597-3603.

Zhang, W. X., 2005. Dispersed zero-valent iron colloids. U. S. Patent Application 20050199556.

Zhang, W. X., Wang, C. B., Lien, H. L., 1998. Treatment of chlorinated organic contaminants with nanoscale bimetallic particles. Catalysis Today 40 (4), 387-395.

Zhao, M., Sun, L., Crooks, R. M., 1998. Preparation of Cu nanoclusters within dendrimer

templates. J. Am. Chem. Soc. 120 (19), 4877-4878.

Zheng, J., Stevenson, M. S., Hikida, R. S., Van Patten, P. G., 2002. Influence of pH on dendrimer-protected nanoparticles. J. Phys. Chem. B 106 (6), 1252-1255.

Zhou, Y., Itoh, H., Uemura, T., Naka, K., Chujo, Y., 2002. Synthesis of novel stable nanometer-sized metal (M = Pd, Au, Pt) colloids protected by a π-conjugated polymer. Langmuir 18 (1), 277-283.

Zhuang, J., Qi, J., Jin, Y., 2005. Retention and transport of amphiphilic colloids under unsaturated flow conditions: Effect of particle size and surface property. Environ. Sci. Technol. 39 (20), 7853-7859.